

Generation of pure iron nanostructures via electron-beam induced deposition in UHV

Erzeugung von reinen Eisen-Nanostrukturen mittels
elektronenstrahlinduzierter Abscheidung im UHV

Der Naturwissenschaftlichen Fakultät der
Friedrich-Alexander-Universität Erlangen-Nürnberg

zur Erlangung des Doktorgrades Dr. rer. nat.

vorgelegt von

Thomas Lukasczyk

aus Erlangen

Als Dissertation genehmigt

durch die Naturwissenschaftliche Fakultät

der Friedrich-Alexander-Universität Erlangen-Nürnberg

Tag der mündlichen Prüfung: _____

Vorsitzende/r der Promotionskommission: Prof. Dr. Bänsch

Erstberichterstatter/in: Prof. Dr. Steinrück

Zweitberichterstatter/in: Prof. Dr. Diwald

Table of contents

List of abbreviations	IV
1 Introduction.....	1
2 Fundamentals and techniques	5
2.1 Scanning electron microscopy (SEM)	5
2.2 Auger electron spectroscopy (AES)	12
2.3 Scanning Auger electron microscopy (SAM) and Auger line scans.....	16
2.4 Scanning tunneling microscopy (STM).....	18
2.5 Quadrupole mass spectrometry (QMS)	19
2.6 Low energy electron diffraction (LEED)	20
2.7 Electron-beam induced deposition (EBID)	21
2.8 The precursor iron pentacarbonyl.....	32
3 Experimental setup	37
3.1 Vacuum system.....	37
3.1.1 Preparation chamber and fast entry lock chamber	42
3.1.2 Analysis chamber.....	46
3.1.3 Gas dosage system	53
3.1.4 Gas Purification and Monitoring (GPM) chamber	56
3.2 Lithographic attachment	59
3.3 Applied materials	61
3.4 Experimental details and data processing.....	63
4 Testing the Instrument: first EBID experiments	77
4.1 Introduction.....	77
4.2 Electron-beam lithography with PMMA	77
4.2.1 Basic principles of lithography with resist samples.....	78
4.2.2 Results and discussion	82
4.3 EBID of carbonaceous structures	85
4.3.1 Characterization of the precursor.....	85
4.3.2 Results and discussion	86
4.4 Summary and conclusions	96

5	Iron pentacarbonyl on Rh(110)	99
5.1	Introduction.....	99
5.2	The Rh(110) surface	100
5.3	Preparation of Rh(110) in an UHV-SEM	104
5.4	Visualizing reduction fronts on Rh(110)	109
5.5	Influence of additional gas dosage.....	118
5.6	Surface quality determines the selectivity of EBID	124
5.6.1	Iron deposition on different sample states	125
5.6.2	Reduction of the autocatalytic behavior via a thin titanium layer	133
5.6.3	Summary.....	140
5.7	Effect of the electron dose on the EBID process	142
5.8	Thermal stability of iron structures.....	148
5.9	Selective oxidation of the iron structures	154
5.10	Summary and conclusions	157
6	Iron pentacarbonyl on silicon single crystal surfaces	161
6.1	Introduction.....	161
6.2	The substrates: Si(111) and Si(100)	162
6.3	Influence of the beam energy on the electron exit area.....	166
6.4	Material parameters in EBID with Fe(CO) ₅ on silicon	170
6.4.1	Deposition of iron on Si(100) at room temperature	171
6.4.2	Influence of the precursor gas purity	179
6.4.3	Deposition under clean conditions at 200 K.....	186
6.4.4	EBID with Fe(CO) ₅ on Si(111)	193
6.5	Influence of the electron dose on the iron cluster density	196
6.6	Thermal stability of iron clusters on silicon	204
6.7	Application: carbon nanotube growth on iron deposits.....	211
6.8	Summary and conclusions	220
7	Summary	223
8	Zusammenfassung	227
9	Appendixes	231
9.1	Appendix to Chapter 3.....	231

9.1.1 Electron filament setup in the preparation chamber	231
9.1.2 Characteristics of the different sample holder setups	232
9.1.3 Scheme of the preparation chamber with port designation.....	234
9.1.4 Modification of the preparation chamber manipulator	236
9.1.5 Scheme of the analysis chamber with port designation	239
9.1.6 Gas doser design	242
9.1.7 Precursor storage device	243
9.1.8 Images of GPM-chamber	243
9.1.9 Manipulator positions in the preparation chamber	244
9.1.10 Experimental parameters	245
9.1.11 Reference values for carbon and oxygen contaminations.....	247
9.2 Appendix to Chapter 5.....	249
9.2.1 Auger line scans on Sample III and Sample III-Ti	249
9.3 List of applied data	251
References	255

List of abbreviations

AE	Auger electron
AES	Auger Electron Spectroscopy
AFM	Atomic Force Microscopy
BSE	Backscattered electron
CCM	Constant Current Mode
CEM	Channel Electron Multiplier
CHM	Constant Height Mode
CMA	Cylindrical Mirror Analyzer
CNT	Carbon Nanotube
CVD	Chemical Vapor Deposition
DD	Dipolar Dissociation
DEA	Dissociative Electron Attachment
DI	Dipolar Ionization
EBID	Electron-Beam Induced Deposition
EBIE	Electron-Beam Induced Etching
EBIP	Electron-Beam Induced Processing
EBL	Electron-Beam Lithography
EDX	Energy Dispersive X-ray analysis
EELS	Electron-Energy Loss Spectroscopy
ESD	Electron Stimulated Desorption
ESEM	Environmental Scanning Electron Microscope
fcc	Face centered cubic
FEL	Fast Entry Lock (chamber)
FSE	Forward scattered electrons
GPM	Gas Purification and Monitoring (chamber)
HSA	Hemispherical Energy Analyzer
HV	High vacuum
IMFP	Inelastic Mean Free Path
IPA	Isopropanol
LDOS	Local Density of States
LEED	Low Energy Electron Diffraction
LLE	Low-loss electrons

MIBK	Methyl isobutyl ketone
PBN	Pyrolytic Boron Nitride
PE	Primary electron
PEEM	Photoemission Electron Microscopy
PMMA	Polymethyl methacrylate
QMS	Quadrupol Mass Spectrometry
SAM	Scanning Auger Microscopy
SE	Secondary electron
SEM	Scanning Electron Microscopy
STM	Scanning Tunneling Microscopy
SWCNT	Single Walled Carbon Nanotube
TEM	Transmission Electron Microscope
TPD	Temperature Programmed Desorption
UHV	Ultra-high vacuum
VT	Variable temperature
XPS	X-ray Photoelectron Spectroscopy

1 Introduction

Nowadays, the term “nanotechnology” is a common concept in many scientific fields, ranging from surface chemistry to semiconductor physics and even to food technology. Also in daily life this topic plays an important role, like, e.g., the utilization of nanomaterials as pigments and other additives for colors or as composites in clothing. Other important applications with a high industrial relevance lie in the field of nanoelectronics, particularly in the generation of transistors and microprocessors. Already in 1965, Gordon E. Moore, a co-founder of Intel, proposed a trend, nowadays denoted as “*Moore’s Law*”, which predicted a doubling of the number of transistors on integrated circuits every two years [1].

Richard Feynman is commonly considered as the father of nanotechnology, due to his lecture with the title “*There’s Plenty of Room at the Bottom*” in 1959 [2]. In this famous talk he considered the possibility of direct manipulation of individual atoms and a number of consequences resulting from it. Yet, the term “nanotechnology” was used for the first time by Norio Taniguchi in 1974 [3]:

"Nano-technology mainly consists of the processing of separation, consolidation, and deformation of materials by one atom or one molecule."

Since that time, the definition was extended to objects with a size below 100 nm, at least in one dimension [4]. As the surface to volume ratio of arbitrary objects increases with decreasing size, the surface of nanosized structures becomes increasingly important for their properties. Additionally, quantum mechanical effects come into play and may be exploited in advanced functional devices (e.g., quantum dots in light-emitting diodes [5]).

For the fabrication of nanostructures on surfaces two main concepts can be distinguished: the bottom-up and the top-down approach. In the bottom-up approach small components are arranged into larger and more complex conformations. One example is molecular self-assembly, in which molecules (e.g., porphyrins) adopt a defined arrangement due to intermolecular interactions [6]. On the other hand, top-down approaches generate smaller devices from larger components via various structuring techniques. This concept is, e.g., realized in standard lithography techniques.

One important top-down lithography technique is electron-beam induced deposition (EBID). Initially known as a side effect in electron microscopy [7], the first intended generation of metal-containing structures by EBID [8] led to numerous efforts to exploit this

technique for the fabrication of spatially and chemically well-defined deposits [9-20]. In this direct-write method a focused electron-beam (e.g., from a scanning electron microscope) is used to locally induce the dissociation of chemical compounds (so called precursors) adsorbed on a surface. The generated non-volatile fragments are deposited on the surface, while the volatile parts are pumped out of the system. The ultimate goal is to produce deposits consisting of a specified composition, which is determined by the used molecule. One advantage of EBID is that the dimension of the generated deposits can be varied down to below 20 nm [21]. Another advantage is the large variety of chemical compounds that can be used, leading to the generation of, e.g., tungsten [11-13], cobalt [16, 22], chromium [15] or platinum [17, 23] containing structures.

The fabrication of clean metallic deposits is one of the major challenges in EBID. For example, structures generated from metal organic precursor molecules exhibit typical metal contents of < 60 %, with carbon and oxygen being the main contaminations (e.g., compare references [11, 15-18, 22, 24-31]). This observation is partly attributed to electron induced dissociation of the corresponding molecules, leading to the co-deposition of carbon and oxygen containing fragments. Another important factor is that EBID experiments are usually performed under high vacuum (HV) conditions, where a certain background pressure of water and other compounds (e.g., hydrocarbons) is unavoidable [32]. Additionally, these residual gases may have a direct influence on the specimen properties.

In the “surface science” approach presented in the work at hand, the experiments are performed in an ultra-high vacuum (UHV) environment. In UHV, the pressure of residual gases is strongly reduced, which should result in a lower amount of contaminations in the deposits; furthermore a well-defined, clean specimen surface can be maintained. The main goals of the present thesis are:

- I) To examine the **impact of UHV on the EBID process** itself
- II) To investigate the possibilities to generate **clean metallic nanostructures** with **arbitrary shape**.

The experiments aim mainly at the fabrication of iron nanostructures from the metal organic compound iron pentacarbonyl ($\text{Fe}(\text{CO})_5$), which is a well-known precursor for EBID (compare references [33-37]). In the following the major goals and challenges of the thesis at hand are described.

The UHV system (base pressure of $< 2.0 \cdot 10^{-10}$ mbar) used in this thesis is equipped with a UHV-compatible SEM column and is described in Chapter 3. It was purchased in June 2005 and dedicated to the EBID project. One of the major challenges at the beginning of this work was to modify the instrument according to the requirements of the EBID process. Thereby, the main focus lied on the construction of a gas injection system for the dosage of gaseous compounds onto the specimen surface. Other necessary modifications mainly concerned sample handling and preparation.

The generation of arbitrarily shaped deposits requires a precise control of the position of the electron-beam on the surface. For that purpose a commercially available lithographic module is attached to the system. The possibilities of this attachment had to be tested by electron-beam lithography (EBL) on a resist sample and, in combination with the gas dosage system, via EBID with the precursor ethene on Si(111) single crystals (Chapter 4). Ethene was chosen for these experiments, since it is comparably easy to handle. Important parameters that had to be studied are the primary beam voltage and the electron dose.

The deposition of iron structures with the precursor iron pentacarbonyl should be performed on metal as well as semiconductor samples. In the case of the metal the novel aspect for EBID was the application of a catalytically active surface, namely Rh(110) (Chapter 5); up to now, only inert specimens like, e.g., Au were used [34, 38]. In this context, an interesting goal was to study the influence of the surface condition on the deposition process. Furthermore, the thermal stability of the generated structures and the possibility to transform iron into iron oxide was of interest. A successful in situ oxidation would expand the potential to fabricate tailored nanostructures with a defined chemical composition.

Silicon is a widely used substrate material for EBID (compare references [11, 22, 33, 39]) with high relevance in the semiconductor industry. However, the electron-beam induced deposition under ultra-clean and defined, i.e., UHV, conditions was only marginally studied so far. One goal of this work was therefore to investigate EBID with $\text{Fe}(\text{CO})_5$ on Si(100) and Si(111). Specific emphasis should be given on the influence of the applied EBID parameters, e.g., sample temperature and precursor gas composition (Chapter 6). Other topics that should be studied were the dependence of the amount of deposited material on the applied electron dose and the thermal stability of the resulting iron structures. As a possible application, the potential to use the iron deposits as catalytic seeds for the locally selective fabrication of carbon nanotubes should be explored.

2 Fundamentals and techniques

In the work at hand different surface analysis techniques, namely scanning electron microscopy (SEM), Auger electron spectroscopy (AES), Auger electron microscopy (SAM) and line scans, scanning tunneling microscopy (STM), quadrupol mass spectrometry (QMS) and low energy electron diffraction (LEED), were applied, which are described in the following chapters.

The description of the analysis techniques is followed by an overview of the EBID process (Chapter 2.7). Thereby, the main focus is on the effects and interactions that are important for the work at hand. For a comprehensive summary of all relevant topics concerning the EBID process the reader is referred to the excellent review articles of Utke et al. [40], van Dorp and Hagen [32], Silvis-Cividjian and Hagen [41], Randolph et al. [42] and Botman et al. [21].

A short description of the metal organic precursor iron pentacarbonyl ($\text{Fe}(\text{CO})_5$), which was used for most of the EBID experiments in this work, is given in Chapter 2.8. Attached to this chapter is also a literature review of EBID experiments performed with this compound.

2.1 Scanning electron microscopy (SEM)

Scanning electron microscopy is a powerful analysis tool for imaging samples with a high spatial and lateral resolution. Historically, the first SEM image was already obtained in 1935 by Max Knoll [43], followed by some pioneering work of Manfred Ardenne [44, 45]. Yet, another 30 years and some further developing by Charles Oatley and Gary Stewart were necessary to build the first commercially available microscope (*Stereoscan*; Cambridge Instrument Company; 1965).

The basic working principle of an SEM is the linear scanning of a sample surface with a highly focused electron-beam, resulting in the emission of electrons that can be detected for the acquisition of an image. Its main advantage compared to optical microscopy is the significantly higher resolution. The resolution of a microscope can be defined as the minimal distance between two separately distinguishable points on a sample. Amongst other parameters it is determined by the wavelength of the applied radiation, with the maximum resolution being in the range of one wavelength of the used radiation (law of Abbé) [46]. In the case of optical microscopes, visible light with a wavelength between 400 and 750 nm is typically used, resulting in a maximum resolution of 0.5 to 1 μm . In electron microscopy

(scanning or transmission electron microscopy (TEM)), electron beams with energies between a few hundred eV and several hundred keV are applied; according to the de Broglie relation (Equation 2.1, with the Planck constant h , the momentum p_e , the electron mass m_e and the electron velocity v) these energies correspond to the so called de Broglie wavelength λ [47].

$$\lambda = \frac{h}{p_e} = \frac{h}{m_e \cdot v} = \frac{h}{\sqrt{2 \cdot m_e \cdot E}} \quad (2.1)$$

For example, the typical electron energy used for the experiments in this work is 15 keV, which corresponds to a wavelength of ~ 0.01 nm. However, the resolution of our instrument is restricted to < 3 nm, which is mostly due limitations of the setup (e.g., of the electron optics).

Imaging modes of scanning electron microscopes

The irradiation of a sample with the primary electron-beam of an electron microscope leads to certain interaction processes. A variety of different electrons and photons are generated in a teardrop-shaped interaction volume, which are sketched in Fig. 2.1 (a), together with their typical escape depths. Fig. 2.1 (b) shows the corresponding schematic energy spectrum of the emitted electrons, including secondary electrons (SE), backscattered electrons (BSE) and Auger electrons (AE). By convention, secondary electrons are defined as electrons with an energy below 50 eV; they exhibit a large peak for the most probable energy between 2 – 5 eV [48]. The broad spectrum of BSEs between 50 eV and the primary electron energy E is caused by the deceleration of primary electrons that have suffered (multiple) energy losses and undergone large angle scattering. Auger electrons, with their respective energies being characteristic for the irradiated material, are generated during the relaxation of inner shell electron vacancies caused by incident PEs. The hole is filled by an outer shell electron, while the gained energy is transferred to another electron, which is emitted as an AE (compare Chapter 2.2).

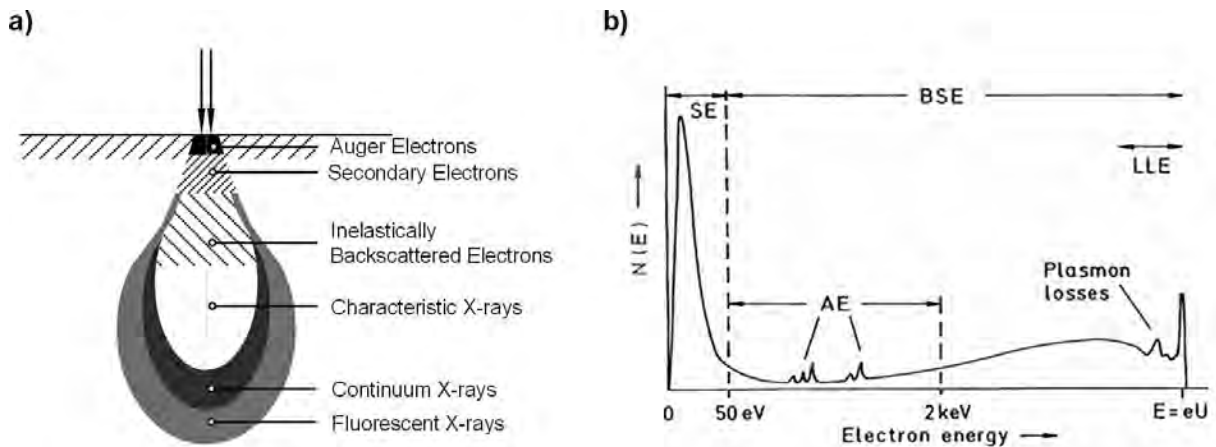


Fig. 2.1: a) Schematic drawing of the teardrop-shaped interaction volume of the primary electrons with the sample material; different regions of signal generation with respect to their corresponding escape depths are included. The image is adapted from reference [49]. b) Schematic energy spectrum of electrons, emitted by the irradiation with a primary electron-beam [48].

SEs and AEs are highly susceptible to elastic and inelastic scattering processes, which is the reason why their escape depth is only in the order of a few nanometers (AEs: three times the inelastic mean free path (IMFP), which is mainly dependent on sample material and electron energy [50]; SEs: 0.5 - 1.5 nm for metals and 10 – 20 nm for insulators [51]). AEs generated deeper in the solid have a high probability to lose energy on their way out of the target and therefore no longer contribute to the characteristic Auger peak. This effect explains the very low escape depth of the AEs schematically depicted in Fig. 2.1 (a).

Furthermore, AEs and SEs are also generated by BSEs on their way through the sample material. Since the latter typically undergo multiple scatterings, their interaction volume is larger compared to the primary electrons; the lateral region, from which BSEs, SEs, and AEs leave the surface, therefore exceeds significantly the area irradiated by the primary electron-beam. The size and shape of this BSE interaction volume is strongly depending on the sample material and beam voltage, as it will be discussed in detail in Chapter 2.7. In order to differentiate the secondary electrons that are generated by primary and backscattered electrons, they are typically denoted as SE I and SE II, respectively [51]. The spectrum in Fig. 2.1 (b) also shows pronounced peaks close to the applied primary electron energy E ; these so-called low-loss electrons (LLE) are the result of inelastic scattering processes in the sample material, such as the excitation of plasmons.

Beside the described generation of different types of electrons, also a certain amount of characteristic and continuum X-rays is produced (compare Fig. 2.1 (a)); the latter is

Bremsstrahlung, which is emitted from electrons that are decelerated, while the characteristic X-rays are the result of the de-excitation of a core hole by an outer shell electron (X-ray fluorescence). Characteristic X-rays with a sufficiently high energy can also lead to the photoionization of other atoms and thus to a secondary x-ray fluorescence.

Principally, any of the generated electrons (BSE, SE, AE) as well as the characteristic X-rays can be used for image formation, which leads to different microscopy techniques [48]. For the Auger electrons this results in an elemental mapping of the surface, as their energy is characteristic for their respective material. This technique is referred to as scanning electron microscopy (SAM) and will be discussed in detail in Chapter 2.2.

For imaging in the SEM, backscattered electrons and secondary electrons are used. The main advantages of the SEs are that they can easily be collected by means of an electrostatic field, they exhibit a higher surface sensitivity compared to BSEs due to their lower energy (< 50 eV) and that the resulting images show a pronounced topography contrast (see below). On the other hand, image acquisition via BSEs requires detectors with a large solid angle of collection, as their trajectories are less influenced by electrostatic fields due to their higher kinetic energy; in this case the actual material determines the contrast (see below).

The SEM images depicted in this work were solely acquired with the In-Lens detector of the applied apparatus (see Chapter 3.1.2). Its setup enables image acquisition only in the SE mode. The following description of contrast mechanisms in an SEM will therefore mainly be performed with respect to secondary electrons.

Contrast modes in the secondary electron imaging

As it has been already mentioned, the images acquired in the SE mode are sensitive to topography, which is caused by several contrast mechanisms. The most important of them are summarized in Fig. 2.2. At the top of Fig. 2.2 a schematic surface profile is depicted, while the resulting line scans of SE signals, with respect to the corresponding contrast mechanisms, are depicted in Fig. 2.2 (a) to (c) and are discussed in the following.

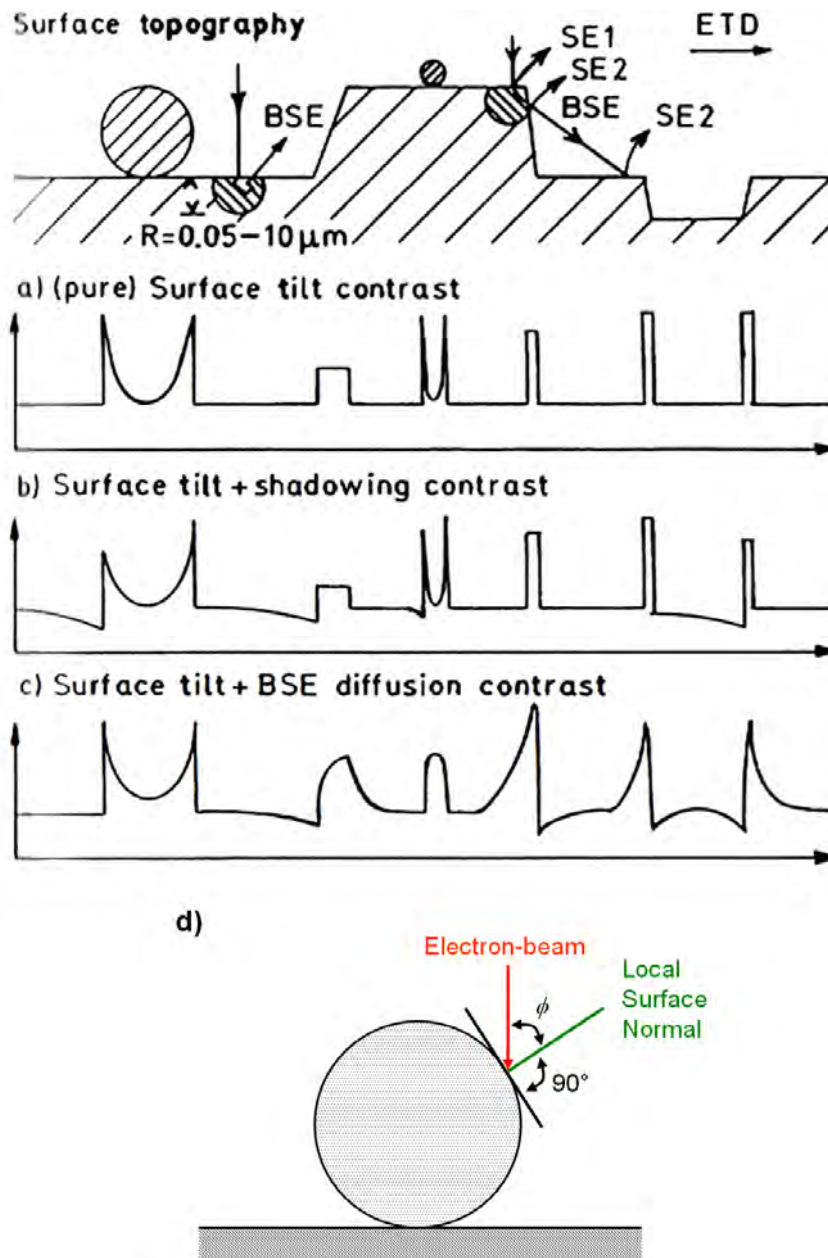


Fig. 2.2: Contributions to the topographic contrast, demonstrated schematically by surface contours (top) and line scans of SE signals: a) surface tilt contrast, b) shadowing contrast and c) BSE diffusion contrast. d) Side view of a spherical feature with the tilt angle ϕ . The images in (a), (b) and (c) were taken from reference [48].

a) The **surface tilt contrast** (Fig. 2.2 (a)) results from the dependence of the secondary electron yield δ (current of SEs divided by the incident electron-probe current) on the tilt angle ϕ between the local surface normal and the incident electron-beam (compare Fig. 2.2 (d)). According to Equation 2.2

$$\delta \propto \sec \phi = \frac{1}{\cos \phi} \quad (2.2)$$

δ is increasing with an increasing ϕ , which is mainly attributed to an increase of the path length of the primary electrons inside the exit depth of the SEs [48]. This effect leads therefore to an increase in the locally observed brightness of SE images at edges, protrusions and circumferences.

b) A different mechanism, which is directly associated to the surface tilt contrast, is the **shadowing contrast** (Fig. 2.2 (b)). It is based on the fact that on the side of a surface feature opposite to the detector, the increase of the SE signal due to high tilt angles (surface tilt contrast) is lower, as more SE have momenta in opposite direction and do not reach the detector [48]. This effect is visible in the schematic line scan in Fig. 2.2 (b), which shows a lower increase of the SE yield at the edges averted to the detector (ETD; on the right side in the schematic surface profile) compared to the ones that are directed towards it. Furthermore, the shadowing contrast blocks the imaging of structures inside deep holes and surface cracks. In order to reduce this contrast mechanism and thereby to observe a “pure” surface tilt contrast, e.g., an In-Lens detector in the electron column can be used, with the surface normal of the sample aligned parallel to the incident electron-beam.

c) Another mechanism that is superposed with the surface tilt contrast is the **BSE diffusion contrast** (Fig. 2.2 (c)). It is caused by an increase of the ratio of SE II / SE I at positions where forward or lateral scattered electrons can leave the side walls (BSEs), i.e., at small particles and edges [48]. If the dimension of a surface particle becomes comparable with or smaller than the range of these electrons, their SE II emission overlaps and the secondary electron emission becomes greatest at the center of the particle (compare the small, spherical structure in the center of Fig. 2.2). At larger surface features (size larger than the range of the scattered electrons), a higher amount of the diffusely scattered BSEs may leave the surface at the edges and generates therefore a higher amount of SE II in the corresponding regions. Furthermore, electrons that are emerging at the edges can hit the specimen again (multiple irradiation) and thereby excite further SE far from the point of the primary electron-beam impact. From these effects it is evident, that even though a secondary electron imaging mode is applied, the backscattered electrons might exhibit a large influence on the local contrast of the resulting micrographs. Also possible is an SE diffusion contrast, which becomes apparent when the electron-probe diameter is in the order of the exit depth of the

secondary electrons; in this case particles with dimensions below one nanometer will show an increased SE signal and even monoatomic surface steps can be imaged at high tilt angles [48].

The topography contrast of the SE images is further complicated, as all the described mechanisms may appear simultaneously. Additionally, the micrographs exhibit also a certain material contrast. Fig. 2.3 shows a plot of the SE yield δ and the backscattering coefficient η (current of BSEs divided by the incident electron-probe current) versus the atomic number Z of the applied sample material for primary electrons with an energy of 25 – 30 keV. It can be observed that δ increases monotonically with an increasing Z , even though it is less rapid compared to the growth of η . The main contribution to the increase of the SE yield can be attributed to the SE II, which are generated by the BSEs on their trajectories through the surface layer and are therefore directly related to η . Yet, this effect can only be observed for a primary electron energy higher than 5 keV, since otherwise the backscattering coefficient shows a maximum at a medium Z . Additional material differences in the SE yield due to variations in the work function may also exhibit a specific influence in certain systems, even though they are more pronounced at primary energies of a few hundreds of eV [48]. It has to be noted, that the material contrast in the SE micrograph contains information not only from an exit depth of the secondary electrons, as they might be generated from BSEs as well.

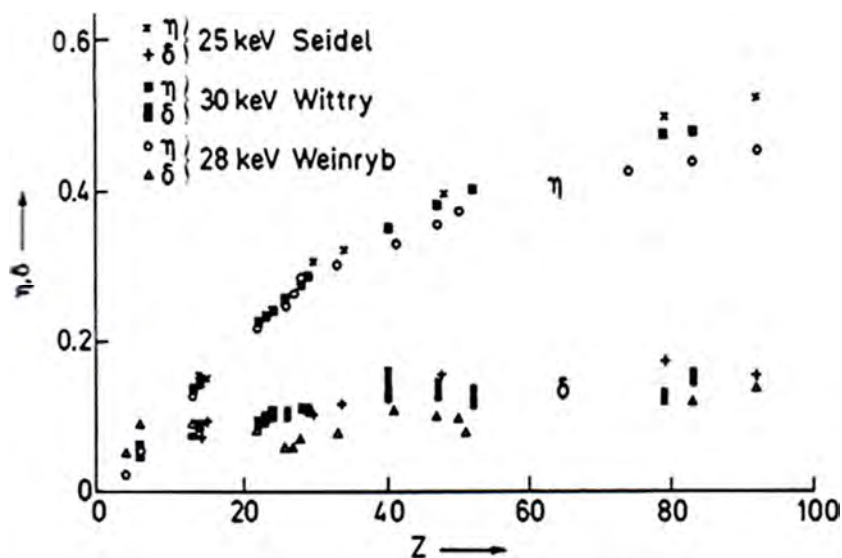


Fig. 2.3: Increase of the backscattering coefficient η and the secondary electron yield δ for primary electrons with an energy of 25 – 30 keV with an increasing number of Z [48].

Beside the described topography and material contrasts, some other types of contrast mechanism exist (e.g., crystal orientation contrast, magnetic contrast, etc.), which are not discussed in detail in this chapter. The interested reader is therefore referred to reference [48].

The main advantage of an SEM compared to a TEM is the possibility to analyze bulk specimens, as the imaging is realized via electrons (BSE or SE) emitted from the surface; in case of a TEM the image formation is performed by detecting transmitted primary electrons, resulting in the necessity of thin samples (< 100 nm). Yet, the latter exhibits a significantly higher resolution, as the energy of the applied primary electrons is typically between 80 and 400 keV and a completely different beam optic is applied. In order to avoid charging effects in an SEM only conductive or semiconducting samples can be analyzed, if not some special setups are used (e.g., environmental SEM (ESEM)).

The experimental setup of an SEM column is described in detail in Chapter 3.1.2.

2.2 Auger electron spectroscopy (AES)

Auger electron spectroscopy is a method to determine the surface composition of specimens. It is based on the Auger process, which was discovered by Pierre Auger in the 1920s [52] and is one of the possible processes that occur upon the interaction of a highly energetic primary electron-beam of an SEM with the sample material (compare Fig. 2.1).

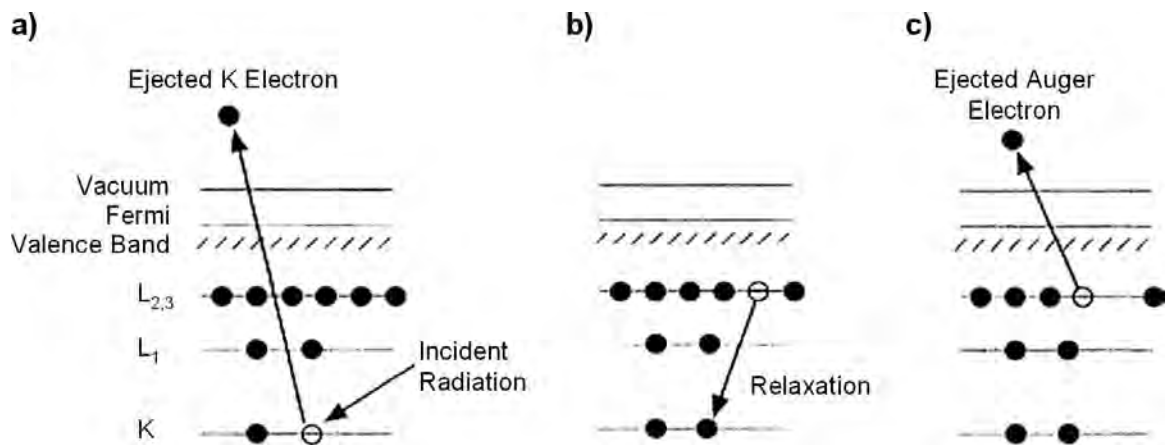


Fig. 2.4: Scheme, summarizing the Auger process. a) Generation of a core level vacancy by an incident radiation. b) Filling of the core hole by an electron from a higher level ($L_{2,3}$). c) Emission of the Auger electron ($L_{2,3}$ electron). The image was adapted from reference [50].

The scheme in Fig. 2.4 summarizes the important steps of the emission of an Auger electron (AE). Due to the irradiation with electrons (or by ions or photons), sample atoms are ionized by the creation of a core hole (Fig. 2.4 (a)). The resulting ion is in an excited state and will rapidly relax back to a lower energy state by the filling of the core hole with an electron from an outer shell (Fig. 2.4 (b)). Thereby, a certain amount of energy is released, which

equals in a simplified picture the difference between the orbital energies of the observed transition. This energy may result in two different processes. The first possibility is the transfer of the released energy to another outer shell electron (non-radiative transition; Fig. 2.4 (c)), called Auger electron, if the transferred energy is higher than the electron orbital binding energy [52]. As the transferred energy and the binding energy of the Auger electron are both discrete and characteristic for each chemical element, the observation of Auger electron energies represents a method for elemental characterization. The second possibility is the emission of X-ray photons (radiative transition; compare Fig. 2.1).

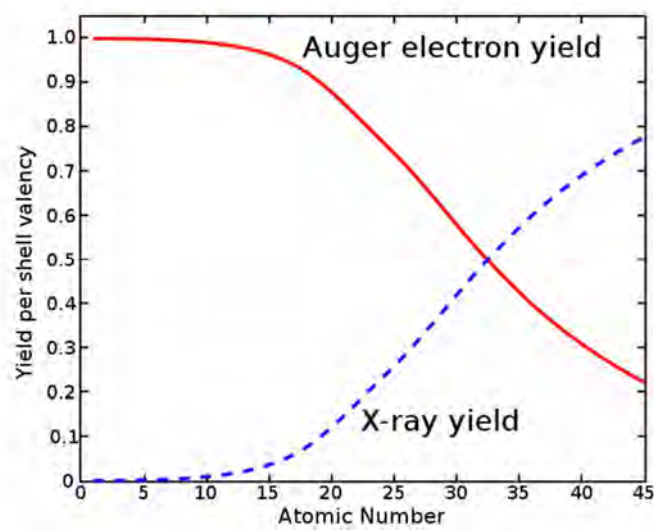


Fig. 2.5: X-ray (blue dotted curve) and Auger electron yields (red curve) as a function of atomic number for K shell vacancies [53].

The emission of Auger electrons and the emission of X-rays are complementary processes. The probability of these processes depends on the atomic number Z of the element; Fig. 2.5 shows plots of the corresponding Auger electron and X-ray yields as a function of Z for initial K-shell vacancies. It can be clearly observed that for elements with a lower atomic number (< 15) the emission of Auger electrons is the dominant relaxation process, while X-ray emission becomes negligible. This behavior is attributed to the relatively low binding energies of the core levels of the corresponding elements [54]. Higher atomic number elements (≥ 15) are more likely to release their energy from K-level based transitions in the form of characteristic X-rays (compare Fig. 2.5). For L- and M-level transitions a similar behavior can be observed, i.e., the X-ray emission probability is increasing for higher atomic number elements; however, in these cases the AE emission is dominating until $Z > 50$ [55].

The different Auger transitions within an atom are described by three letters, which are indicating the orbitals relevant for the corresponding Auger process: the first letter describes the core shell containing the initial hole, while the second letter represents the shell of the electron that fills the vacancy; the third letter describes the orbital from which the AE is released. Thereby, the assignment of the letters follows the X-ray notation. For the Auger process depicted in Fig. 2.4, the corresponding notation is therefore $KL_{2,3}L_{2,3}$ [50]. This means that the initial core hole is located in the K level (1s in the spectroscopic notation), the electron that fills this vacancy is from the level $L_{2,3}$ (2p) and the emitted Auger electron is a $L_{2,3}$ (2p) electron.

The energy, which is transferred to the Auger electron, is present in form of the kinetic energy. In a first approximation this energy can be estimated from the binding energies of the involved levels, as it is denoted in Equation 2.1 for the example given in Fig. 2.4 ($KL_{2,3}L_{2,3}$ transition); in this formula E_K and $E_{L_{2,3}}$ are the binding energies of the core level and the first and second outer shell, respectively, while $\Phi = E_{vacuum} - E_{fermi}$ is the work function of the material [56].

$$E_{KL_{2,3}L_{2,3}} = E_K - E_{L_{2,3}} - E_{L_{2,3}} - \Phi \quad (2.3)$$

Equation 2.3 neither takes into account the interaction energies between the core holes ($L_{2,3}$ and $L_{2,3}$) in the final atomic state nor the inter- and extra-atomic relaxation energies, which are the result of an additional core screening needed. These problems can be satisfactorily addressed by an empirical approach that considers the energies of the atomic levels involved (Z) and those of the next element in the periodic table ($Z+1$); thereby, Equation 2.3 is modified to Equation 2.4 [50].

$$E_{KL_{2,3}L_{2,3}}(Z) = E_K(Z) - E_{L_{2,3}}(Z) - E_{L_{2,3}}(Z+1) - \Phi \quad (2.4)$$

An alternative to this approach can be seen in Equation 2.5, with the effective potential U_{Eff} that takes the coulomb interaction between the two vacancies in the final state into account [57].

$$E_{KL_{2,3}L_{2,3}}(Z) = E_K(Z) - E_{L_{2,3}}(Z) - E_{L_{2,3}}(Z) - U_{Eff} \quad (2.5)$$

All three Equations (2.3, 2.4 and 2.5) also reflect the fact that the kinetic energy of the Auger electron is independent from the type of the primary irradiation probe (e.g., electrons) and its energy, as it is only depending on the binding energies of the involved atomic levels. Furthermore, Auger electrons exhibit a rather low escape depth (three times the IMFP [50]), as their characteristic energy is lost by an inelastic collision (compare Chapter 2.1); AES is therefore attributed as a highly surface sensitive analysis method.

The detection of the emitted AEs is performed via an electron energy analyzer. Typical examples for such detectors are the cylindrical mirror analyzer (CMA), the hemispherical sector analyzer (HSA) and the four-grid retarding field analyzer (LEED-AES device). For the work at hand a HSA was applied; the setup of this analyzer and its position on the analysis chamber will be discussed in Chapter 3.1.2.

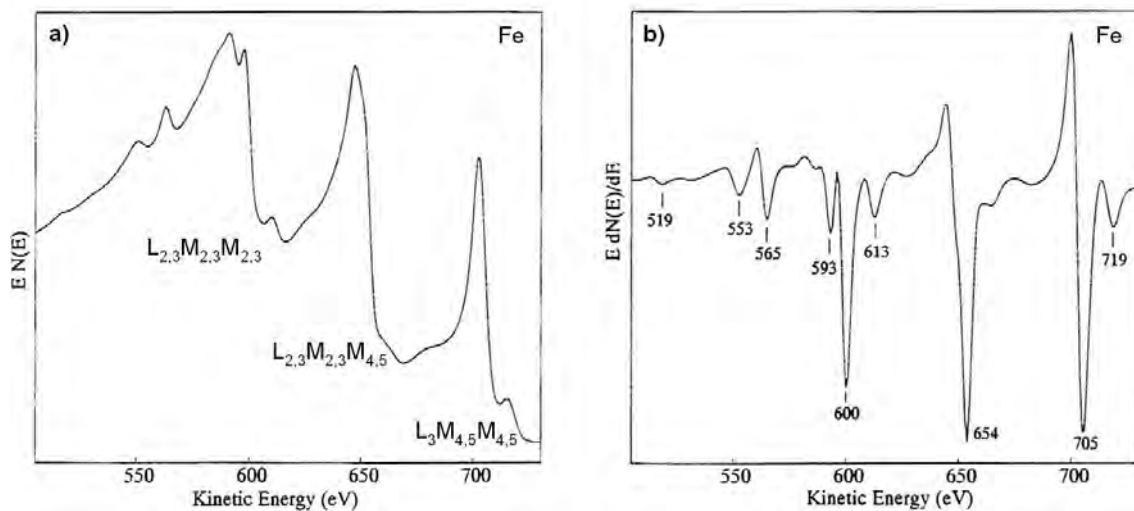


Fig. 2.6: a) Non-derivative and b) derivative AE spectra with an identical kinetic energy region for the element iron. The images were adapted from reference [58].

The recorded Auger spectrum (plot of the amount of AEs $N(E)$ versus the electron energy) shows relatively small Auger signals, which are superposed on a high background resulting from other SEs. To suppress the large background and therefore to improve peak visibility, Auger spectra are often recorded in a derivative mode $dN(E)/dE$. Fig. 2.6 shows a non-derivative spectrum ((a)) in comparison to a derivative spectrum $dN(E)/dE$ ((b)) for the element iron. In the non-derivative spectrum three main peaks for the $L_{2,3}M_{2,3}M_{2,3}$ (~ 591 eV), $L_{2,3}M_{2,3}M_{4,5}$ (~ 647 eV) and $L_3M_{4,5}M_{4,5}$ (~ 703 eV) Auger transitions are visible, which are accompanied by smaller signals. In the derivative spectrum the peaks can be mainly observed as rather sharp minima; especially the smaller signals exhibit in this case a superior visibility.

Note, that in the derivative spectrum the position of the minimum is used to define the energetic position of the corresponding Auger peak, as it is depicted in Fig. 2.6 (b). In the work at hand, all AE spectra were acquired and are displayed as non-derivative spectra ($N(E)$ versus E).

As it has been already described, elemental identification from an AE spectrum is possible from the energy positions of the Auger peaks. Corresponding reference values are widely tabulated for all elements of the periodic table (except for H and He, since they have less than three electrons), for example in references [58] and [59]. It has to be noted, that the experimental setup might have a specific influence on the measured Auger energies; extremely accurate reference values can therefore only be achieved by the acquisition in the same system. In addition, the Auger spectrum contains information about the chemical bonding states of the atoms. The specific chemical environment of an atom changes the binding energies (“chemical shift”) and leads to a redistribution of the electron density of states in the valence band [56]. These changes are reflected in the change of the Auger peak position and / or the peak shape and can therefore be used to differentiate between different chemical compounds.

Besides the high surface sensitivity, one of the major advantages of AES with a highly focused electron-beam as irradiation probe is the spatial resolution, as the Auger electrons originate in close proximity of the beam. In the applied system it is therefore possible to perform local AES with an ultimate spatial resolution < 10 nm. In contrast to that, X-rays are emitted on a much larger scale (compare Fig. 2.1 (a)), which significantly reduces the lateral resolution and surface sensitivity of EDX.

2.3 Scanning Auger electron microscopy (SAM) and Auger line scans

In the previous chapter it was discussed, how local AES with an electron-beam as irradiation source, i.e., via a point analysis, can be used to study the chemical composition of a surface area. Yet, the high spatial resolution of this technique can also be exploited for two other modes of operation.

One of these is the scanning Auger electron microscopy (SAM), which combines element characterization with a two dimensional imaging and thus enables elemental mapping of a sample surface. In this case the energy analyzer of an AES instrument is used to monitor a single, predefined energy, e.g., of an Auger peak, while the primary electron-beam is scanning across the specimen surface. The measured intensities of the emitted electrons are recorded as a function of electron beam position; this results in a micrograph with grayscale

values that represent the intensity distribution for every point along the path of the beam. By using an Auger energy, which is characteristic for a certain element, the intensity distribution in the image also reflects the distribution of the chemical element on the surface: a high intensity, i.e., a bright area in the micrograph, corresponds to a high amount of the corresponding element. In order to improve the signal to noise ratio of the SA micrographs, a background map (*Bkg*) can be recorded by selecting a nearby non-characteristic energy, which is subtracted from the Auger peak map (*Peak*).

The Auger electron yield is very sensitive to the electron take-off angle; a SAM image will therefore invariably reflect the surface topography of the specimen, possibly even more strongly than the chemical variations. This should be considered if objects with a rather three-dimensional appearance are analyzed. A correction for the effects of surface topography can be achieved by applying a simple algorithm such as $(Peak-Bkg)/Bkg$, resulting in a pure chemical information image [50].

Fig. 2.7 (a) shows a SAM image for the element titanium, which was acquired from a silicon surface covered with a certain amount of titanium oxide nanotubes. The TiO_x -tubes appear bright in the SAM image compared to the rest of the surface, which represents the high amount of titanium in these features. For comparison, Fig. 2.7 (b) shows an SEM image of the same surface region.

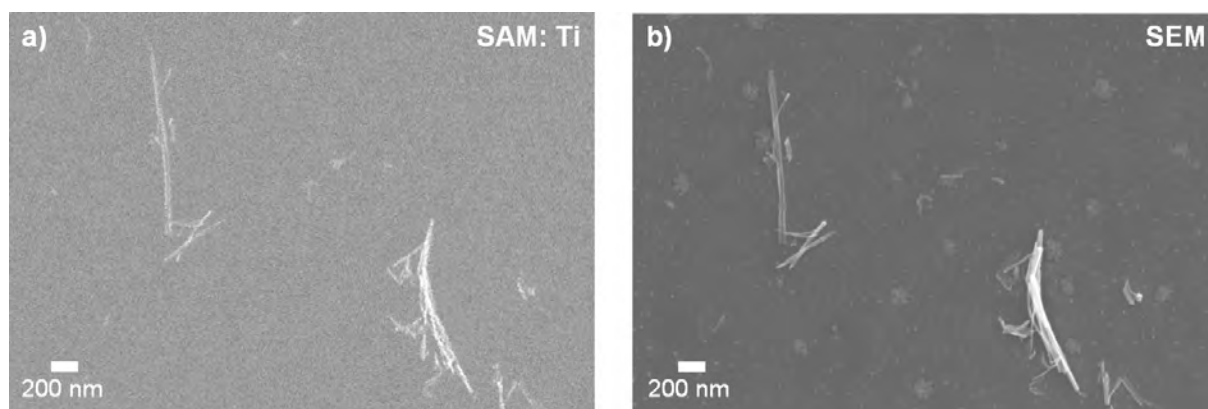


Fig. 2.7: a) Titanium SAM image of TiO_x -nanotubes on a silicon support ($E_{Peak} = 383.5$ eV; $E_{Bkg} = 397$ eV; $t_{Dwell} = 6.55$ ms). b) SEM image of the same surface region ($U = 15$ kV; $I = 3$ nA; tilted sample).

Another measurement mode based on the Auger process is the so called Auger line scan. In this method the primary electron-beam is scanning the sample along a predefined, linear path, while the electron analyzer is used to record the intensity of a characteristic Auger

peak and background intensity as a function of the beam position. By subtracting the background measurement from the Auger peak measurement, a profile of the respective Auger intensity is acquired, which represents therefore the elemental distribution along this path. Examples for Auger line scans can be found in the appendix to Chapter 5 (see Fig. 9.9)

In summary, a SAM image shows the two dimensional distribution of an element on a surface, while an Auger line scan provides a profile of an elemental distribution along a predefined path (one dimensional distribution of element).

2.4 Scanning tunneling microscopy (STM)

The scanning tunneling microscope was developed by Binnig and Rohrer in 1981. It represented the first technique to image atomic surface structures on a flat surface in a non-destructive way. In the following only a rough overview of this technique is presented; the interested reader is therefore referred to references [60] and [61].

The measurement principle of an STM is based on the quantum mechanical tunneling effect. It allows a particle to overcome a potential barrier that is higher than the energy the particle possess with a certain probability, which is in contrast to the classic Newtonian dynamics and therefore not encountered in the macroscopic world. For STM, the tunneling effect is exploited by scanning over a sample surface with a sharp metal tip (consisting of one atom, in the idealized case) in a distance of a few Ångströms. While applying a bias voltage U_{Bias} between the tip and the sample, a tunneling current I_{Tunnel} can be measured, which is exponentially depending on the distance d between the tip and the sample according to Equation 2.6 [62].

$$I_{Tunnel} \propto U_{Bias} \cdot \exp(-A\sqrt{\Phi} \cdot d) \quad (2.6)$$

In this case, $A = 1.025 \text{ \AA}^{-1} \text{eV}^{-1/2}$ is a constant and Φ represents the height of the potential barrier, which corresponds to the mean work function between tip and sample. As obvious from Equation 2.6, the tunneling current is directly depending on the topography of the sample via the distance d . Furthermore, it is related to the local density of states (LDOS); therefore, the structural and electronic information of the sample surface are superposed in an STM image.

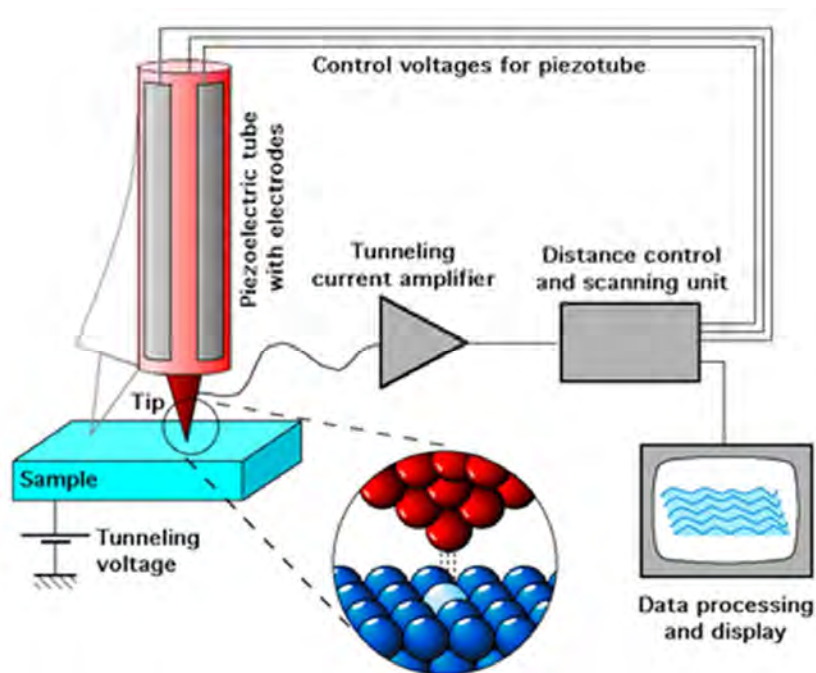


Fig. 2.8: Working principle of a scanning tunneling microscope [63].

Technical implementation of an STM is realized by mounting the tip to one (or more) finely adjustable piezo-electric actuators, enabling the controlled modification of the x,y,z -direction of the tip. The z -position, i.e., the distance between the tip and the sample, can either be kept constant (constant height mode (CHM)) or controlled by a feedback loop in order to maintain a preset tunneling current (constant current mode (CCM)).

Fig. 2.8 summarizes the working principle of a scanning tunneling microscope.

2.5 Quadrupole mass spectrometry (QMS)

Mass spectrometry is a method for analyzing the chemical composition of a gas phase. Generally, this is performed by the ionization of molecules within a vacuum environment (e.g., by means of electron impact ionization), which are subsequently accelerated by a high voltage towards a mass filtering device. The latter enables only ionic fragments with a specific mass-to-charge ratio (m/z) to pass through; at the end of this filtering device the amount of generated ions is detected. A sweep of all possible mass-to-charge ratios provides an intensity spectrum of all fragments. By analyzing these intensity plots the composition of the gas phase can be determined.

Several types of mass spectrometers exist that vary mainly in the utilized method of ionization and mass filtering. For the quadrupole mass spectrometer (QMS) the special

feature is its mass filter; it relies on four metal rods that are connected individually to a current that is produced by a radio frequency (RF) generator and thereby produce an alternating electrical quadrupole field. Ionic fragments that are entering this filter can only pass through on stable paths if they are in resonance with the electric field. All other fragments move on unstable paths and are deflected. For the detection of the ionized masses, e.g., a channeltron (channel electron multiplier, CEM) can be used. The resulting signals of the detected, ionized fragments are plotted versus the m/z -ratio. The main advantage of this setup is that it allows for small and relatively light designs, while still giving accurate measurements; it is therefore ideally suited for the analysis of gas compositions in HV and UHV systems. Fig. 2.9 shows a scheme of the main components of a QMS.

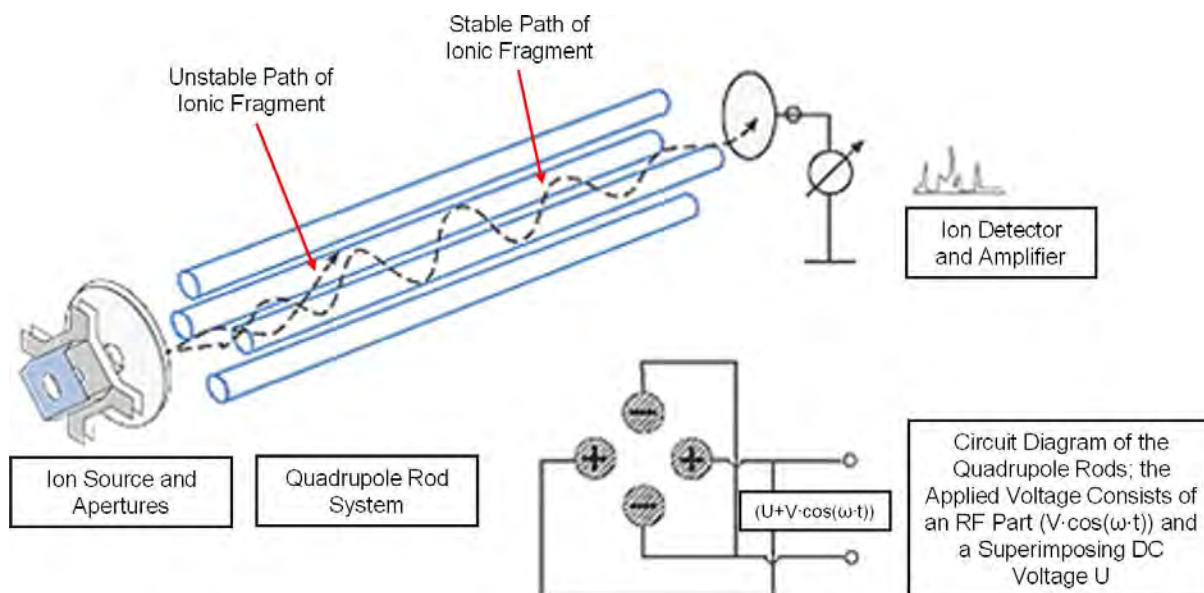


Fig. 2.9: Schematic drawing of a quadrupole mass spectrometer [64].

2.6 Low energy electron diffraction (LEED)

The diffraction of low-energetic electrons is a standard method in surface science, which enables the determination of the long range atomic order of a sample surface or an adsorbed layer. In the following a short overview of LEED is presented; the interested reader is referred to references [47] and [65].

LEED is based on the wave properties of rather “slow” electrons with a kinetic energy E between 5 and 500 eV. The corresponding wave lengths can be calculated according to Equation 2.1 (de-Broglie relation) to be between 5.5 Å and 0.6 Å, which is in the range of atomic distances. Due to the very low penetration depth of these electrons, the diffraction

process (according to Bragg's diffraction law) is regarded to be highly surface sensitive and in first approximation to be two-dimensional.

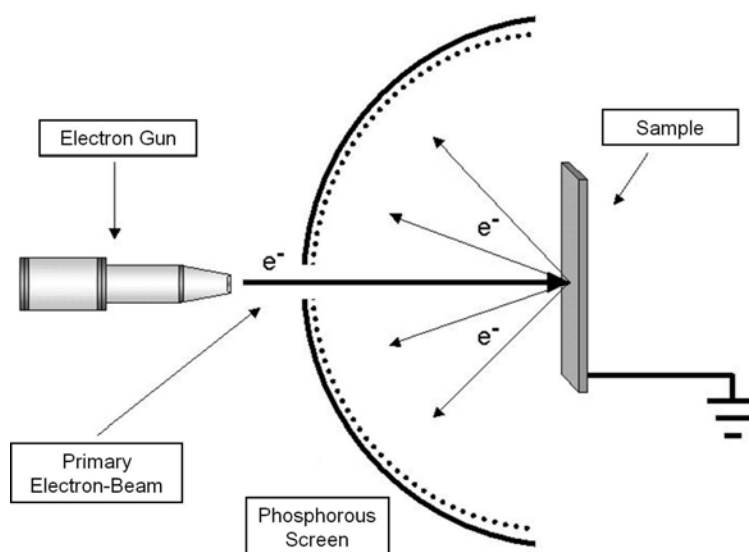


Fig. 2.10: Schematic drawing of a LEED optic [64].

The resulting intensity maxima of the interference pattern are observed as point reflexes on a phosphorous screen. The diffraction pattern is a reciprocal representation of the surface lattice, i.e., that smaller atomic distances on the surface are represented by larger distances on the screen and vice versa. Information about the long range order of the surface atoms and thus of the quality of the surface can be extracted from the size and position of the reflexes with respect to the (00)-reflex (direct reflection of the incident electron-beam). Additional information about the geometry of the surface unit cell can be derived from the dependence of the intensity of the reflexes from the applied primary electron energy (LEED-IV); since the latter was not used for the work at hand, it will not be discussed any further. A scheme of the setup of a LEED optic is depicted in Fig. 2.10.

2.7 Electron-beam induced deposition (EBID)

Electron-beam induced deposition is a direct-write lithography technique, in which an electron-beam from an SEM or TEM (transmission electron microscope) is focused onto a substrate in the presence of a so-called precursor-gas. Thereby, the precursor-molecules are locally dissociated into volatile and non-volatile fragments. The latter directly adsorb to the surface and form a deposit with a composition that depends on the nature of the applied precursor; e.g., hydrocarbons, like methane [66, 67], result in the generation of carbonaceous

deposits, while the utilization of metal organic precursor (e.g., CpPtMe₃ [17, 68]) or inorganic precursors (e.g., WF₆ [15, 69, 70] and TiCl₄ [71]) result in metal containing structures. A schematic representation of the most important steps of the electron-beam induced deposition process with the precursor iron pentacarbonyl (Fe(CO)₅) is depicted in Fig. 2.11.

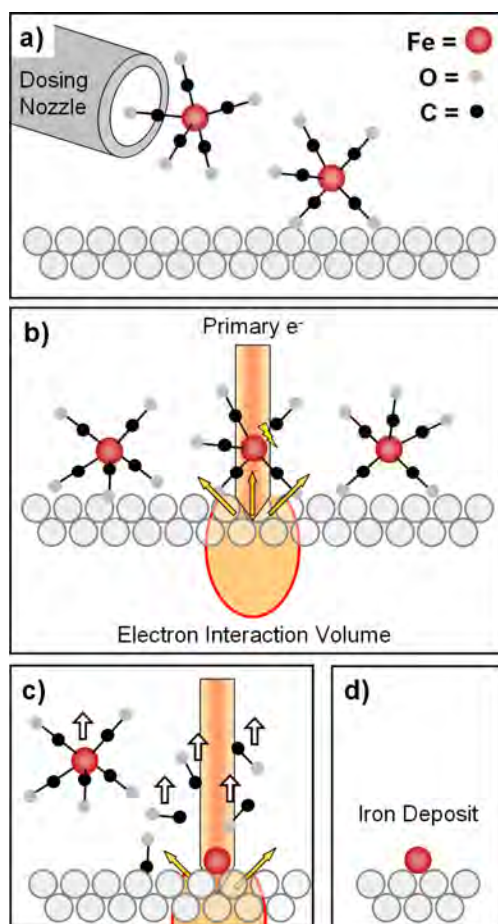


Fig. 2.11: Scheme, summarizing the ideal EBID process with the precursor molecule Fe(CO)₅. a) Dosage and adsorption of the precursor molecule Fe(CO)₅. b) Local exposure of adsorbed molecule to the primary electron-beam and electrons, which are subsequently emitted from the surface. c) Decomposition of the Fe(CO)₅ molecule exposed to electrons and desorption of the unexposed Fe(CO)₅ and the volatile fragments (e.g., CO). d) Pure iron deposit at the electron exposed position after the EBID process.

Important requirements for the applied precursor molecules are that they should adsorb and reside long enough on the surface to be dissociated for the deposition and that the resulting, undesired fragments are desorbing readily; both factors are difficult to combine in the same precursor compound, which should also exhibit a sufficient vapor pressure to enable a rather good handling [40]. The basic idea is to find suitable compounds for the deposition of

a broad variety of elements. There now exist precursors to generate structures containing, e.g., Cr [15, 33], Co [16, 22], Cu [17, 30, 72], Mo [17, 19], Rh [24, 73], Pt [17, 18, 74] and Au [17-20, 75]. For a comprehensive summary of applied precursor molecules for EBID the reader is referred to the review articles of Utke et al. [40] and Silvis-Cividjian and Hagen [41].

Beside the described possibility to tune the chemical composition of the deposits by choosing the precursor compound, another major advantage of EBID is that it can be performed on flat as well as structured surfaces (e.g., on an AFM probe [16]), as long as it is possible to focus the electron-beam on the sample. Furthermore, since electron-beams can be focused into spots down to the sub-Ångström level, this process is well suited for the generation of structures in the nanometer regime. With a minimum structure size of < 1 nm achieved up to now it is therefore superior in terms of deposit resolution compared to other maskless-techniques like light lithography or electron-beam lithography (EBL) on resist samples [12]. By controlling the scan pattern, e.g., via a lithographic attachment, it is also possible to generate two- and even three-dimensional structures [19]. A disadvantage of EBID compared to the other lithography techniques is a rather low deposition rate [32].

Due to its partly unique properties, EBID is ideally suited for a broad variety of applications in the field of nanotechnology. Industrially relevant applications are, e.g., the generation of high-aspect ratio tips for scanning probe techniques like AFM (atomic force microscopy) [16, 76] and the rewiring of integrated circuits in the prototyping phase [77]. Furthermore, EBID is now established as a state of the art repair tool for new generation lithographic UV masks for the semiconductor industry (45 nm node technology [78-80]), an application field that was formerly dominated by focused ion beam (FIB) processing.

One of the major challenges here is to generate clean EBID structures. Typical deposits generated from metal organic precursors exhibit a metal content of 10 to 60 at. % [11, 15-18, 22, 24-31] and consist of a nanocomposite material containing metal crystals with a size of a few nanometers embedded in a matrix of amorphous carbon [81]. Higher metal contents can be achieved, e.g., with inorganic precursors, like fluorine-based compounds; therefore, with the precursor WF_6 a metal purity of 85 at. % was achieved [70] and gold crystals with a purity > 95 % could be deposited from $AuCIPF_3$ [20]. It is also possible to increase the metal content by the utilization of higher beam currents. Utke et al. have shown that the Co content of deposits generated with $Co_2(CO)_8$ is increasing with an increasing beam current up to a maximum value of 80 % (at a beam current of 3 μA) [82, 83]; this observation is mainly attributed to an increase in the molecule fragmentation due to the higher current

density. Other possibilities to achieve higher deposit purities are heating of the specimen during the EBID process (leading to a reduction of the residence time of carbonaceous fragments) [21, 23] and the application of lower primary beam energies (resulting in differences in the PE scattering) [17].

The rather low metal content of typical EBID deposits described before can be attributed to the applied experimental conditions, as most EBID experiments were performed in high vacuum (HV) systems. In the corresponding chambers contaminations like hydrocarbons (mainly residual gases from pump oil) or water are present, which are simultaneously deposited and thereby significantly contribute to the deposit composition. Moreover, they can adsorb on the specimen surface and thus influence the adsorption of the precursor molecules [21, 40]. An obvious way to avoid these problems is the utilization of better vacuum conditions, namely UHV conditions, as it was applied for the work at hand. Influences of residual gases should therefore be minimized.

EBID belongs to a larger family of electron-beam induced processes (EBIP), which all incorporate the use of a highly focused electron-beam. Other techniques from this group are, e.g., electron-beam induced etching (EBIE) or electron-beam induced heating. In literature the EBID process is also known by a multitude of other names, which are listed in the following [84]:

- electron-beam induced resist (EBIR),
- electron-beam induced metal formation (EBIM),
- electron-beam induced selective etching and deposition (EBISED),
- electron-beam induced chemical vapor deposition (EB-CVD),
- electron-beam stimulated deposition,
- electron-beam induced surface reaction,
- electron-beam writing,
- environmental electron-beam deposition,
- electron-beam assisted direct-write nanolithography,
- contamination lithography (generation of carbonaceous structures),
- additive lithography.

In order to keep things simple for the work at hand, only the term EBID (electron-beam induced deposition) will be used.

Interaction mechanisms between electrons and precursor molecules

Despite the long history of EBID, the underlying physical and chemical processes are not yet fully understood. In Chapter 2.1 it was described that the interaction of the primary electron-beam with the sample material results in the emission of additional electrons, e.g., SE and BSE, with a broad energy distribution from the surface; in principle, any of these electrons may contribute to the EBID process. The probability that an electron induces the scission of a bond in a precursor molecule depends on the electron energy and is generally expressed as a cross section σ_E (in cm^2), which is increasing with an increasing bond breaking probability. This cross section depends on many parameters, like, e.g., the energy of the bonds within the molecule, the adsorption geometry on the surface and the available reaction paths for the dissociation event [32]. Yet, only a relatively low data on electron impact cross sections exist for molecules in the gas phase or adsorbed on a surface. In Fig. 2.12 cross sections for different precursor molecules, namely $\text{Fe}(\text{CO})_5$, WF_6 , $\text{W}(\text{CO})_6$ and C_2H_5 , are plotted against the corresponding electron energies [32].

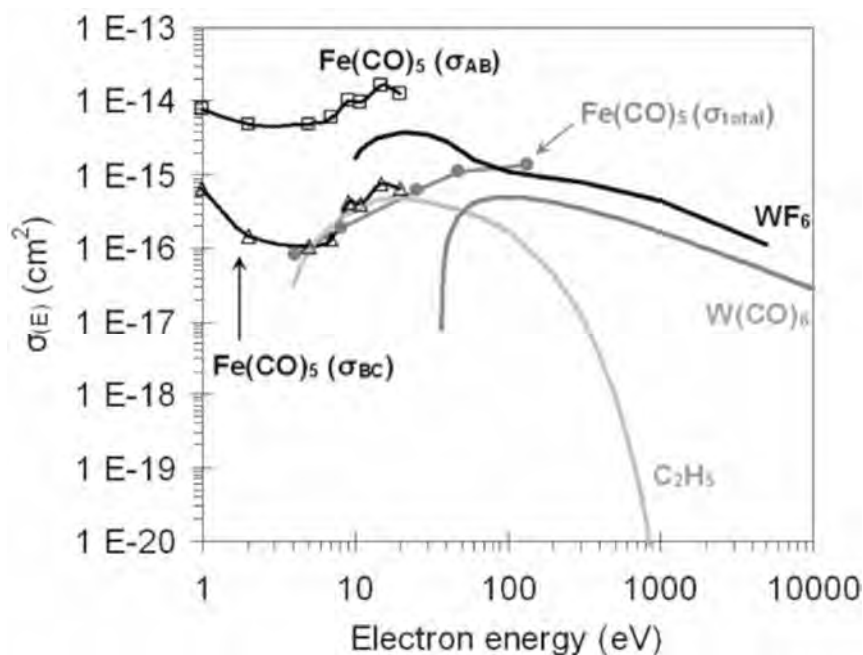


Fig. 2.12: Measured and estimated cross sections for different precursors in EBID [32].

The three cross sections for the low-energy dissociation of $\text{Fe}(\text{CO})_5$ were measured by Rowntree (σ_{AB} and σ_{BC}) [85] and Henderson et al. (σ_{total}) [86]; Henderson reported the total cross section for the dissociation of a monolayer of adsorbed $\text{Fe}(\text{CO})_5$, while Rowntree presented two values for a two-step dissociation from the original molecule (A) via an intermediate species (B) into the final material (C). The cross sections for the other three

precursor molecules in Fig. 2.12 were determined via Monte-Carlo simulations by Silvis-Cividjian et al. (C_2H_5), Fowlkes et al. (WF_6) and Mitsuishi et al. ($W(CO)_6$) [87-89].

In literature, four different dissociation mechanisms for the interaction of electrons with molecules are discussed [32, 40]. These reaction paths were mainly identified in gas phase measurements and are listed in the following; it has to be noted, that due to additional relaxation paths on the surface, the dissociation cross sections of these reaction mechanisms might be reduced for adsorbed molecules.

A) The **dissociative electron attachment** (DEA) is a resonant interaction, where a molecule combines with a free electron to give a superexcited anion, which subsequently dissociates into molecular fragments (one anionic and one neutral). It has a peak value for the cross section when the electron energy matches the energy of the lowest unoccupied molecular orbital (LUMO), which is typically at energies up to ~ 15 eV [90].

B) The **dipolar dissociation** (DD) is a nonresonant electronic excitation process that results in the production of a stable anion and cation from a neutral excited state of the initial molecule [91]. Typically, this mechanism can be already induced by electrons with an energy of a few eV, as it was shown, e.g., for the dissociation of polystyrene [91].

C) In the **dissociative ionization** (DI) the interaction with the impinging electron results in an ionization of the molecule, which subsequently dissociates into a cation and neutral fragment [91]. The peak value of the cross section is in this case situated between 70 and 100 eV and decays with an increasing electron energy [40].

D) Another possibility is the **dissociation into neutrals**. It exhibits a similar distribution of the cross section as observed for the DI, with a peak value at an electron energy around 50 eV [40].

The described dissociation mechanisms all have cross sections that have their peak value well below 1 keV. One might therefore conclude, that the dissociation of precursor molecules in EBID is mainly performed by the secondary electrons (SE I and SE II) and low energetic BSEs. Yet, the current density of the high-energy electrons at the area of the impinging electron-beam (PEs and BSEs) is very high compared to the current density of the low-energy electrons. That means, that although the absolute cross sections for high-energy electrons might be small, their absolute number may be high enough to make a significant contribution to the deposition process [32]. In effect, any type of electron present on the surface (PE, SE, BSE) may contribute to the dissociation of the precursor molecules.

BSE exit area and proximity effects

Another topic concerning the deposition of material due to BSEs and their resulting SEs (SE II; compare Chapter 2.1) is the range of the backscattered electrons in the sample material. Due to the relatively high energy of the BSEs, they might exhibit multiple scattering processes in a certain volume of the solid below the irradiated area. From this volume a certain amount of secondary (SE II) and backscattered electrons can leave the surface and thus significantly increase the size of the electron interaction area compared to the one, which is defined by the primary electron impact. The shape and size of this volume depends on the applied primary electron energy, the atomic number of the specimen and the specimen's density. Thereby, the size of the interaction volume increases with an increase of the primary electron energy and a decrease of the atomic number and density of the sample material [48]. Fig. 2.13 shows simulations of BSE trajectories in two different materials, namely silicon ((a), (c)) and rhodium ((b), (d)), for primary electron-beams with a beam voltage of 15 ((a), (b)) and 8 kV ((c), (d)); they were calculated with a Monte Carlo simulation using the software *CASINO V 2.42* [92].

For both materials a reduction of the size of the interaction volume with a decrease of the primary electron energy from 15 to 8 kV is clearly visible. Another observation is that at a given PE energy the interaction volume is significantly smaller for rhodium compared to silicon, which is associated with the higher atomic number and density of rhodium. A smaller size of the interaction volume results also in a smaller BSE exit area at the surface, as it is indicated by the trajectories in Fig. 2.13 that reach the surface (red trajectories); i.e., for a given primary electron energy the surface area of the electron – precursor interaction is smaller for rhodium than for silicon. Additionally, a smaller interaction volume is associated with a higher local electron density, as it is evident from the density of the trajectories in Fig. 2.13.

One possibility to reduce the scattering of BSEs in the sample material is to use very thin specimens (< 0.1 mm) and high primary beam voltages (few hundred keV), as it is typical for a TEM setup. Thereby, the BSE interaction volume is effectively “cut-off” and the size of the electron interaction area is significantly reduced. EBID deposits generated under these conditions exhibit typically a smaller size; van Dorp et al. even reported a size of < 1 nm for point deposits generated in a TEM with the precursor $W(CO)_6$ [12].

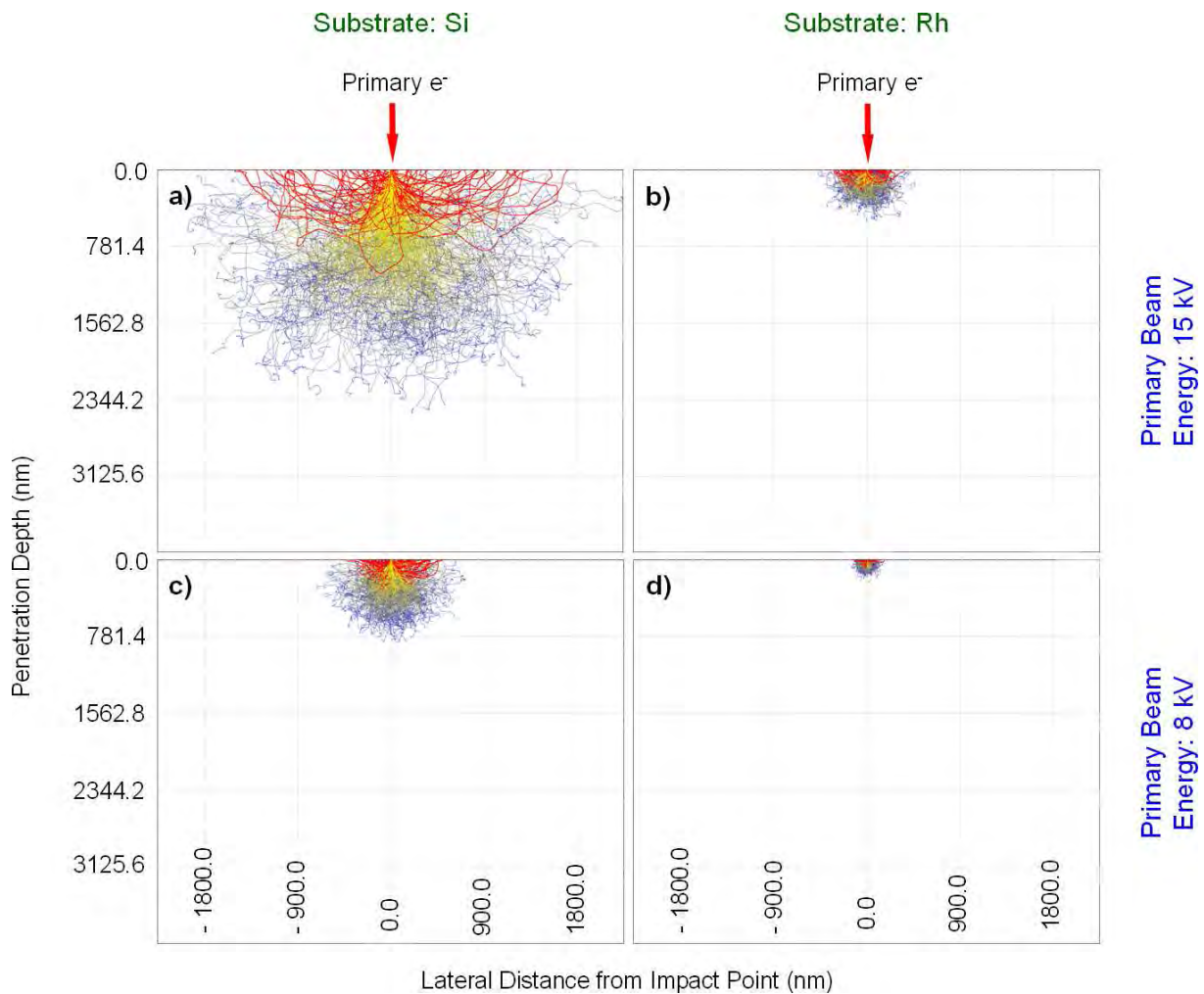


Fig. 2.13: Monte Carlo simulations of BSE trajectories in silicon (left) and rhodium (right) with the software CASINO V2.42 [92]. Simulated were 200,000 backscattered electrons resulting from a a), b) 15 kV and c), d) 8 kV primary electron-beam with a beam diameter of 3.0 nm and 3.8 nm, respectively; for better visualization only 500 BSEs are depicted in the images. The red trajectories correspond to BSEs that are able to reach the surface.

It also has to be considered that the shape and composition of the specimen changes during the EBID experiment, due to the deposition of material. An example is the growth of a pillar, which leads to an electron scattering volume that becomes more confined to the pillar as it becomes higher; thereby, impinging primary electrons might also be scattered in a direction where they leave the pillar and hit the surface at a certain distance from the primary electron impact point (forward scattered electron (FSE)).

From the topics discussed so far it is evident, that the interaction between the primary electrons and the target material leads to an unintentional exposure of the regions surrounding the irradiated areas. The resulting effects on the EBID process are known as proximity effects; the most prominent of them are discussed in the following.

A) The **BSE proximity effect** was reported, e.g., by Lau et al. and Bret [16, 93]; it is visible as a halo in the surrounding of the generated structures, resulting from an extra deposition of material due to the irradiation with BSEs and their resulting SEs (SE II). The size of the halo is therefore directly related to the size of the BSE exit area (see above); Bret demonstrated that on Au pads the width of the halo is significantly smaller than on SiO₂, which is consistent with the larger backscattering range of the BSEs in SiO₂ [93].

B) Similar in result to the BSE proximity effect is the **FSE proximity effect**, except for the fact that it causes unintended deposition on a larger length scale. It is mainly observed during the irradiation of rather high structures or deposits, resulting in a certain amount of forward scattered electrons. These electrons have a much larger range than BSEs and will be blocked by surface features in their path, as it was shown by Bret et al. [94].

C) Aristov et al., Mølhave et al. and Lau et al. reported a type of proximity effect where unintended deposition occurred on already existing, self-standing rods, tips and dots, respectively, when new deposits were generated in the close vicinity [16, 95, 96]. Aristov attributed this extra deposition to the scattering of SEs from the structure that is being fabricated; therefore, this effect is called the **SE proximity effect**. It has to be noted, that the energy of the electrons was not measured and that this unintentional growth might also be caused by electrons with an energy > 50 eV. It is therefore possible that there is no fundamental difference between the FSE and SE proximity effect [84].

D) A proximity effect that affects the structures that are being generated instead of the structures that are already present at the time of irradiation is the **slope dependent proximity effect**. Hiroshima et al. and van Dorp et al. observed an increase of the amount of deposited material on the side of an already existing structure compared to the irradiation of a flat area [97, 98]. This observation was attributed to the enhanced SE emission from the sidewall of the irradiated structure (compare the topography contrast mechanisms in Chapter 2.1), even though a specific influence of the PEs, due to an enhanced path length through the adsorbant layer, cannot be ruled out.

Two additional proximity effects are reported in literature, which are referring to the growth of EBID deposits due to surface plasmons and the deformation of tips in close vicinity due to charging effects. Both effects will not be discussed in detail in this chapter; the interested reader is referred to the review article of van Dorp and Hagen and the references cited within [84].

It was also observed, that the composition, morphology and conductivity of the material deposited via proximity effects can be significantly different from the deposit in the

directly irradiated area. In doing so, the differences of the observed compositions are strongly depending on the applied precursor molecule. Certain indications are given that mechanisms such as electron-beam induced heating and autocatalytic decomposition are involved in these observations, but conclusive evidence is missing.

Precursor and electron limited regime

Of practical interest for the EBID process is how much material is deposited under given experimental conditions. To address this topic, a simple theoretical model can be applied, which was presented by van Dorp and Hagen [84]. It is based on a rate equation describing the precursor molecule coverage N (cm^{-2}) on the surface. This equation (Equation 2.7) considers three processes, namely the number of molecules that adsorb from the gas phase, the number of molecules that are decomposed by the electron-beam and the number of molecules that desorb to the gas phase.

$$\frac{dN}{dt} = \underbrace{gF \left(1 - \frac{N}{N_0}\right)}_{\text{Adsorption}} - \underbrace{\sigma NJ}_{\text{Decomposition}} - \underbrace{\frac{N}{\tau}}_{\text{Desorption}} \quad (2.7)$$

The adsorption term in Equation 2.7 describes a nondissociative Langmuir adsorption, with the available adsorption site density in a monolayer N_0 (cm^{-2}), the sticking factor g and the gas flux arriving on the surface F ($\text{cm}^{-2} \text{ s}^{-1}$). The desorption term is depending on the residence time τ (s) of the precursor molecules on the surface, while the electron induced decomposition is depending on the dissociation cross section σ (see above; integral over all electron energies) and the current density J (electrons $\text{cm}^{-2} \text{ s}^{-1}$). In reality J is a combination of the current densities of the PEs, BSEs and SEs. As a simplification it is assumed that J equals J_{PE} , since J_{BSE} and J_{SE} are usually not measured during the experiments.

A steady state situation for the coverage N is reached when $dN/dt = 0$, which results in Equation 2.8.

$$N = N_0 \left(\frac{\frac{gF}{N_0}}{\frac{gF}{N_0} + \sigma J + \frac{1}{\tau}} \right) \quad (2.8)$$

The vertical deposition rate R (cm/s) for a steady state situation is defined as

$$R = V_{Molecule} N \sigma J \quad (2.9)$$

with the volume of a deposited precursor fragment $V_{Molecule}$. A combination of Equations 2.8 and 2.9 leads to Equation 2.10.

$$R = V_{Molecule} N_0 \left(\frac{\left(\frac{gF}{N_0} \right) \sigma J}{\frac{gF}{N_0} + \sigma J + \frac{1}{\tau}} \right) \quad (2.10)$$

In a further simplification, the desorption term ($1/\tau$) in Equation 2.10 will be ignored. In the resulting Equation 2.11 two distinguishable regimes can be defined (Equation 2.11 (a) and (b)).

$$R = V_{Molecule} N_0 \left(\frac{\left(\frac{gF}{N_0} \right) \sigma J}{\frac{gF}{N_0} + \sigma J} \right) \quad (2.11)$$

$$\left(\frac{gF}{N_0} \right) \gg \sigma J \quad \Rightarrow \quad R = V_{Molecule} N_0 \sigma J \quad (2.11 \text{ (a)})$$

$$\left(\frac{gF}{N_0} \right) \ll \sigma J \quad \Rightarrow \quad R = V_{Molecule} gF \quad (2.11 \text{ (b)})$$

In the first regime (Equation 2.11 (a)) the growth rate has become independent from the gas flux F and is restricted by the applied current density J . This regime is defined as the **electron-limited regime**. In the second regime (Equation 2.11 (b)) the situation is reversed, i.e., the growth rate is limited by the gas flux F and is independent from the current density J . Therefore, this regime is defined as the **precursor-limited regime**. Both regimes have a large influence on the EBID process, not only in terms of deposition rate; for example, the ratio of electrons per deposited molecule fragment may influence the degree of fragmentation and thus results in a certain influence on the deposit composition.

An important question is how both regimes can be differentiated in an experiment. One possibility is to plot the deposit height h or the deposit volume $V_{Deposit}$ versus the current density J . The corresponding plots exhibit a linear dependence of h or V on J for the electron-limited regime and a value that is independent of J for the precursor-limited regime. It is important to mention, that by definition the deposition rate is higher in the electron-limited regime than in the precursor-limited regime.

The theoretical model presented by van Dorp and Hagen considers the replenishment of molecules in the irradiated area only by precursor adsorption from the gas phase. Another important replenishment process that was neglected is surface diffusion from the surrounding region into the irradiated area. By taking this process into account Equation 2.7 would be extended to Equation 2.12, with the diffusion coefficient D and a diffusion gradient [40].

$$\frac{dN}{dt} = gF \left(1 - \frac{N}{N_0} \right) - \sigma NJ - \frac{N}{\tau} + \underbrace{D \left(\frac{\partial^2 N}{\partial r^2} + \frac{1}{r} \frac{\partial N}{\partial r} \right)}_{\text{Diffusion}} \quad (2.12)$$

A more profound theoretical model that includes this diffusion term was presented by Utke et al [40]. Due to the complexity of the treatment it will not be discussed in depth in the work at hand. The interested reader is referred to reference [40]. An important result is that they identified an additional molecule-limited regime, which is characterized by a dominance of the molecule replenishment by surface diffusion with respect to precursor adsorption from the gas phase. This regime is defined as the **diffusion-enhanced regime**. This deposition regime may result in a significant change of the resulting structure shape, as the diffusing precursor molecules are already fixed at the periphery of the irradiated area.

2.8 The precursor iron pentacarbonyl

The metal organic complex iron pentacarbonyl ($\text{Fe}(\text{CO})_5$) belongs to the metal carbonyls, which are defined as a class of metal complexes with carbon monoxide ligands according to the molecular formula $\text{M}_n(\text{CO})_m$ [99]. The first metal carbonyl (nickel tetracarbonyl ($\text{Ni}(\text{CO})_4$)) was discovered in 1890 by Mond et al.. Since then this group of molecules has attributed a high significance as catalysts for organic processes, like, e.g., hydrogenation

reactions and oxo-syntheses, and as starting materials for the synthesis of other metal complexes [99].

Molar Mass	195.90 g/mol	Melting Point	253 K
Density	1.45 g/ml	Boiling Point	376 K
Bond Length Fe-C_{axial}	181 pm	Ignition Temp.	323 K
Bond Length Fe-C_{equa.}	183 pm	Vapor Pressure (303 K)	53 mbar

Table 2.1: Physical properties of iron pentacarbonyl ($Fe(CO)_5$) [99-101].

Three different iron carbonyl species exist, which differ in the number of iron atoms and CO ligands in the complex: iron pentacarbonyl ($Fe(CO)_5$), diiron nonacarbonyl ($Fe_2(CO)_9$) and triiron dodecacarbonyl ($Fe_3(CO)_{12}$). Iron pentacarbonyl was chosen for the work at hand, as it exhibits a high vapor pressure combined with a good handling compared to other metal carbonyls. Under atmospheric conditions it is a yellow liquid, which is stable, but sensitive to light, heat and air. Some additional physical properties of $Fe(CO)_5$ are summarized in Table 2.1.

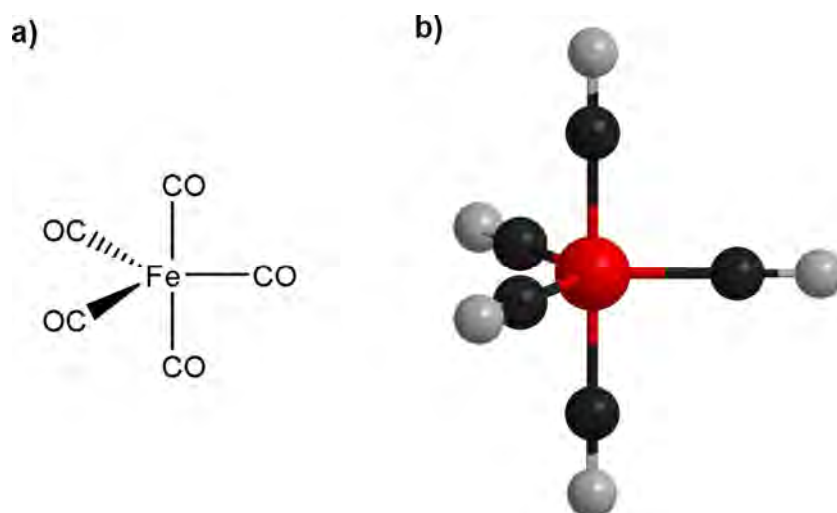
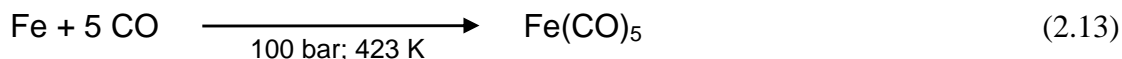


Fig. 2.14: a) Structural formula and b) ball & stick model of iron pentacarbonyl ($Fe(CO)_5$).

The synthesis of $Fe(CO)_5$ is typically performed via the reaction in Equation 2.13, which applies a high pressure and temperature.



$\text{Fe}(\text{CO})_5$ shows a trigonal bipyramidal structure, as it is illustrated in Fig. 2.14. A specialty of this molecule as well as of all metal carbonyls is the bonding mechanism of the carbon atoms of the CO ligands to the metal atom. This mechanism can be described as a synergetic σ -donor/ π -acceptor-interaction, which leads to an electron delocalization and thereby to an energetic stabilization of the complex. Furthermore, the π -acceptor back-bonding results in a simultaneous weakening of the C-O bond in the ligand (the degree of the back-bonding is dependent on the type and charge of the metal atom) [102].

EBID with iron pentacarbonyl: literature overview

In the following a short literature review of EBID experiments with the precursor iron pentacarbonyl will be given.

$\text{Fe}(\text{CO})_5$ is one of the most popular metal organic precursors for EBID [32]. The first aimed generation of electron-induced deposits with iron pentacarbonyl, to the best of my knowledge, was performed by Kunz and Mayer in 1987. They reported the selective deposition of 100 – 400 nm wide iron lines via a focused 3 and 1 kV electron beam on silicon at 398 K [34, 39]. The lines exhibited a polycrystalline morphology, which was attributed to the selective thermal decomposition of $\text{Fe}(\text{CO})_5$ on a thin iron layer, generated via the electron irradiation. Later they have shown, that the autocatalytic decomposition (sample temperature 383 – 413 K) results in a linear increase of the Fe film thickness with time after film nucleation has been achieved via electron irradiation [33]; during the electron irradiation the iron film growth was even faster, while virtually no iron was deposited on the silicon surface in the absence of the electron beam. In the same experiment the chemical composition of the iron structures was determined via AES. The corresponding spectra displayed only minor contaminations of oxygen and argon; the latter was the result of an argon ion sputter procedure, which was necessary as the deposits were exposed to air prior to the Auger analysis. It is noteworthy, that both experiments were performed in a HV-instrument (base pressure $1.0 \cdot 10^{-6}$ mbar) and that a rather high pressure of the iron pentacarbonyl was applied ($5.3 \cdot 10^{-5}$ – $2.7 \cdot 10^{-4}$ mbar).

Zhang et al. used an HV-SEM (base pressure $2.0 \cdot 10^{-8}$ mbar) to generate tips [35] and dots [103] on a carbon microgrid film. In the surrounding of these deposits, the growth of nanocrystals could be observed, which is attributed to the scattering of electrons in the target structure (compare proximity effects described in Chapter 2.7). The crystals were identified as

pure α -Fe (determined via TEM measurements), while the generated tips were amorphous, containing Fe, C and O. The authors attributed this observation to the higher electron density in the irradiated area compared to the one in the surrounding [35]. Utke et al. mentioned that these observations might also result from an electron-induced heating of the specimen, as heat dissipation in membranes is significantly reduced compared to bulk substrates [40]; resulting from this might be a thermal decomposition of $\text{Fe}(\text{CO})_5$, similar as it was observed by Kunz and Mayer [33, 34].

Another example for the electron-induced thermal decomposition of iron pentacarbonyl was recently reported by Hochleitner et al. for the generation of freestanding pillars on silicon samples with a native oxide layer (SEM with base pressure $1.4 \cdot 10^{-6}$ mbar) [36]. After depositing a pillar with a certain height, a radial growth of dendritic structures was starting at the tip and progressed towards the bottom of the stem. This observation was attributed to thermal heating of the pillar by the electron-beam and thus to an autocatalytic growth of the structures (compare references [33, 34]). It was also reported, that this growth process depends strongly on the applied beam current (0.97 and 1.97 nA) and precursor pressure ($6.0 \cdot 10^{-6} - 1.2 \cdot 10^{-5}$ mbar). The iron content of the pillars deposited via EBID was measured to be 48 %, while for the dendritic deposits generated by the thermal decomposition a value of 84 % was determined via EDX.

Tanaka et al. used a UHV-TEM (base pressure $< 5.0 \cdot 10^{-10}$ mbar; 200 kV) to generate thin iron silicide islands on Si(111) and Si(100) at a sample temperature of 673 – 873 K [104]. On Si(111) cubic silicide nano-rods of different aspect ratio were locally formed by a focused electron-beam (beam diameter ~ 1 nm), while the formation of β - FeSi_2 islands was mainly observed on Si(100), when the electron beam was broadly spread (beam diameter ~ 200 nm). It was suggested that the type of the generated iron silicide depends significantly on the size and the intensity of the applied electron-beam. Furthermore, it was shown that the nano-rods, which were fabricated on Si(111) at a sample temperature of 850 – 900 K, are aligned along one of the $\langle 110 \rangle$ directions of the silicon surface and that their length could be controlled by the irradiation time [105].

The same research team generated dots (30 nm in diameter) and free standing rods (width ~ 25 nm) on 10 nm thick carbon micro-grid films via an SEM (base pressure $2.0 \cdot 10^{-8}$ mbar) [37]. The deposited structures were amorphous containing Fe, C and O, as it was determined from electron diffraction and electron-energy loss spectroscopy (EELS) in a UHV-TEM; the oxygen contamination was attributed to the exposure to air before the analysis. After heating the structures for 1 h at 873 K in UHV, the deposits were crystallized;

thereby, several phases were formed, which could be identified as α -Fe, Fe_5C_2 , Fe_7C_3 and Fe_2C . In contrast to that, post-deposition annealing (2 h at 873 K in UHV) of amorphous, freestanding iron rods that were generated on a thin Si substrate resulted in the generation of single-crystal α -Fe, as it was shown by Takeguchi et al. [106]; it is important to mention, that in this case the shape of the rods was almost maintained.

Shimojo et al. succeeded in forming free standing, crystalline Fe_3O_4 nanostructures with different shape (wires, rings, etc.) by mixing water vapor with iron pentacarbonyl [10]. The experiments were performed on a thin molybdenum substrate in an SEM (base pressure $2.0 \cdot 10^{-8}$ mbar) at room temperature, while the generated deposits were analyzed in an UHV-TEM with EELS apparatus. The addition of the water vapor resulted also in a reduction of the carbon content of the deposits; depending on the ratio of the applied partial pressures $p(\text{H}_2\text{O})/p(\text{Fe}(\text{CO})_5)$ the relative composition Fe:C (atomic ratio) of the structures varied from 1:0.45 ($p(\text{H}_2\text{O})/p(\text{Fe}(\text{CO})_5) = 0.0$) to 1:0.0 ($p(\text{H}_2\text{O})/p(\text{Fe}(\text{CO})_5) = 1.5$).

Different co-dosage experiments were performed by Takeguchi et al. on a molybdenum substrate in an SEM (base pressure $< 1.0 \cdot 10^{-8}$ mbar) [9]. By dosing a combination of iron pentacarbonyl and ferrocene ($\text{Fe}(\text{C}_5\text{H}_5)_2$) they were able to fabricate nanorods with varying compositional ratios of iron to carbon, which could be controlled by changing the partial pressure of these compounds. Via this technique it was possible to generate structures with an iron purity of 30 – 70 %, as it was determined by EDX in combination with previously performed EELS measurements. It has to be noted, that the partial pressure of ferrocene was kept constant for the generation of the rods ($1.0 \cdot 10^{-7}$ mbar), while the partial pressure of iron pentacarbonyl was varied ($2.0 \cdot 10^{-7} - 11.0 \cdot 10^{-7}$ mbar), resulting in a difference of the applied total pressure.

3 Experimental setup

The experiments have been performed in an ultra-high vacuum (UHV) system that houses all the surface analysis techniques described in the previous chapter. By definition UHV means pressures lower than 10^{-8} mbar [47]. Nowadays, this pressure region is achieved in bakeable stainless-steel chambers. For the work at hand, a system purchased from Omicron NanoTechnology (*Multiscan LAB*) was used, which was delivered in June 2005 and customized by the author and his co-workers according to the guidelines of the project. The capabilities of this instrument as well as the implemented modifications will be described in detail in Chapter 3.1.

An additional modification that is not directly related to the vacuum system itself is the lithographic attachment. Due to its importance for the deposition of arbitrarily shaped patterns, further information about it will be given in Chapter 3.2.

Finally, Chapter 3.3 will deal with specifications about the applied precursor gases and substrates, while Chapter 3.4 will describe the experimental details and data processing for the experiments.

3.1 Vacuum system

The UHV setup consists mainly of four parts: (I) preparation chamber, (II) analysis chamber, (III) fast entry lock (FEL) chamber or load lock chamber and (IV) gas dosage system. Fig. 3.1 shows an overview of the apparatus, without the gas dosage system and the normally plugged cables and wires. Denoted are the positions of the different chambers, which are separated by manual gate valves (VAT / CF-40).

Samples can be transferred between the chambers via two linear translators (see Fig. 3.1 (a) and (b)). The one with the longer travel (VG / *MLRM209* / 914 mm) connects the preparation with the analysis chamber, while the other (VG / *MLRM204* / 457 mm) is necessary for sample entry in the FEL chamber and transfer into the preparation chamber.

Since the main techniques of the system are sensitive to mechanical vibrations, the whole setup is decoupled from the floor by a self leveling damping system (IDE). The corresponding four “elephant legs” are located at the edges of the rack, raising it slightly from the ground via an air cushion.

The whole setup has a base pressure in the low 10^{-10} mbar region, which is achieved after baking the system at 410 K for roughly 48 h. For that purpose three heaters are directly mounted on the rack of the apparatus (see Fig. 3.1 (b)).

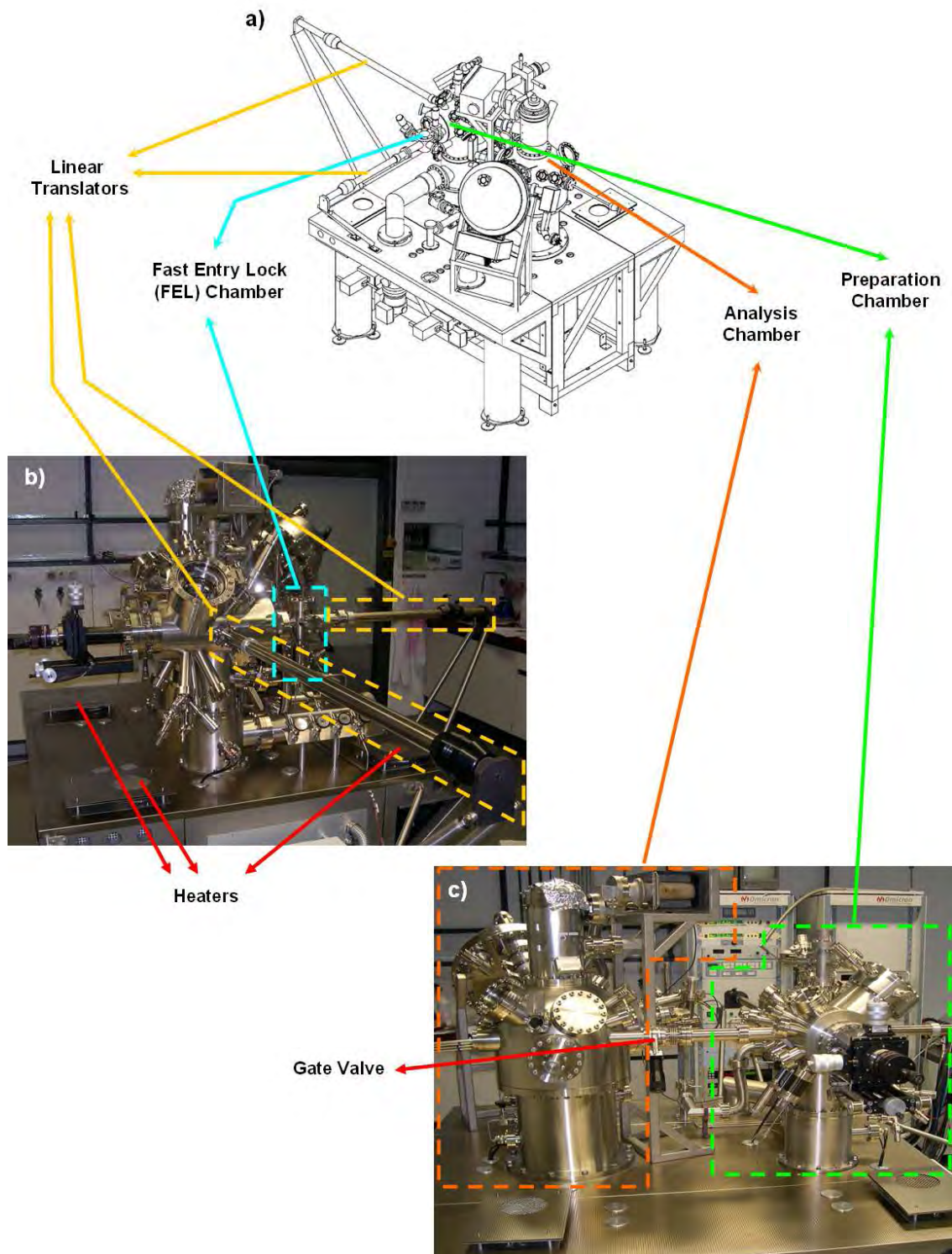


Fig. 3.1: Presentation of the chamber with description of the most important sections. a) Isometric drawing of the complete system [107]. b) Picture of the setup from the side of the preparation chamber. c) Picture from front view.

A schematic drawing of the vacuum system is depicted in Fig. 3.2. Components added in the course of the work at hand are colored red, while the section used for venting the apparatus is colored blue. Vacuum maintenance in the analysis and preparation chamber

during normal operation is realized by ion getter pumps of 400 l/s (Varian / *VacIon Plus 500*) and 120 l/s (Varian / *VacIon Plus 150*; the given values are the specified pumping speeds, referring to the volume flow rate at the inlet), respectively, accompanied by titanium sublimation pumps (VG / *ZST22*). For bake out and after experiments with a high gas load additional pumping can be employed via a turbo molecular pump (Pfeiffer / *TMU261* / ~ 200 l/s) in combination with a rotary pump (Boc Edwards / *RV3*). The pressure at the exhaust ports of the turbo molecular pumps is measured via pirani gauge heads (VG / *PVG5KF*), while in the chambers it is controlled by ion gauge heads (VG / *VIG-18*).

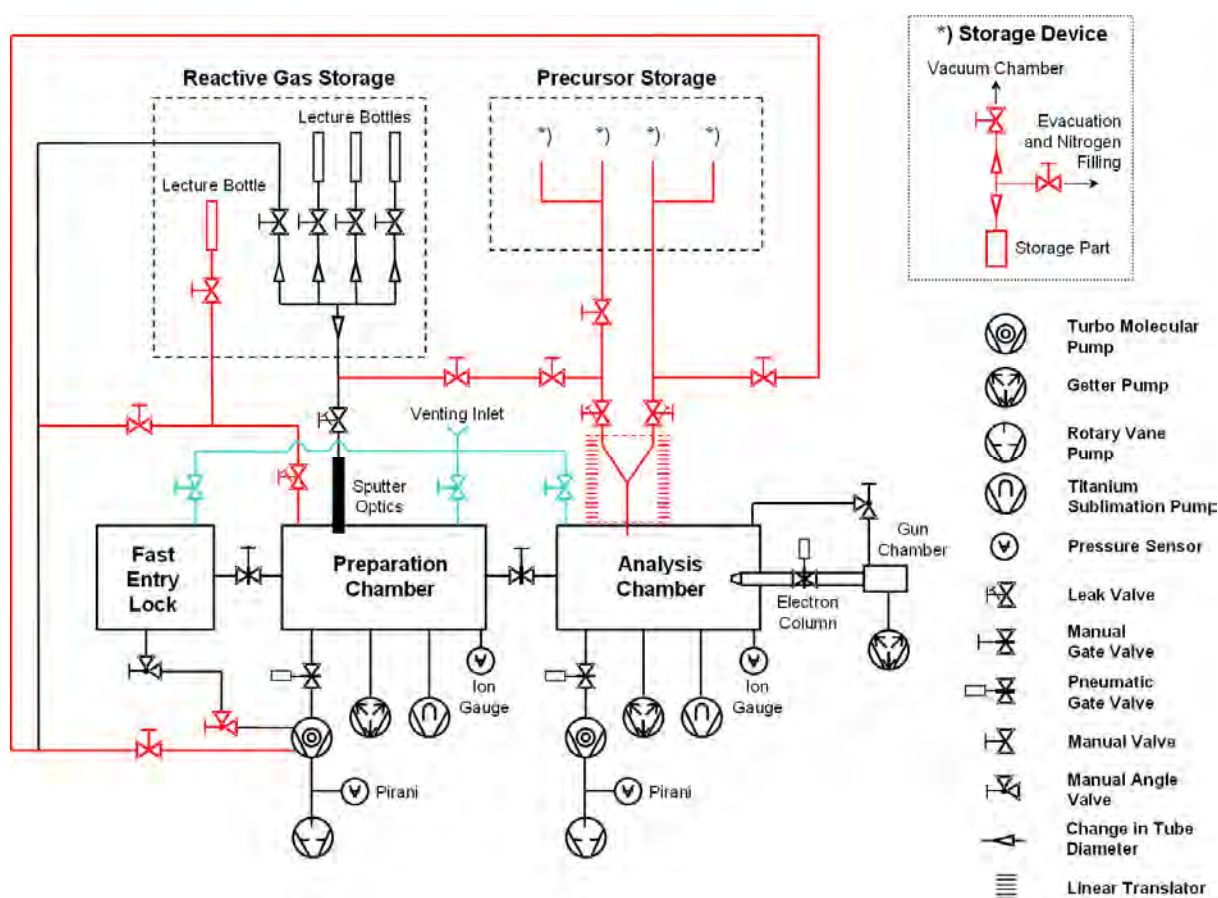


Fig. 3.2: Schematic drawing of the vacuum system with a legend of the vacuum components on the right. Red colored components were added during the work at hand. The blue ones belong to the venting system.

The turbo molecular pump connected to the preparation chamber is also used to evacuate the FEL chamber and the gas dosage system. For the latter a complex system of valves allows for specific sections being evacuated and filled with reactive or precursor gases. In the case of the FEL chamber evacuation via the turbo molecular pump is only applied after sample entry or removal. During normal operation, vacuum maintenance is achieved by the

ion getter and titanium sublimation pump of the preparation chamber through the open gate valve, in order to avoid mechanical vibrations..

An additional ion getter pump is directly connected to the electron gun, housed in the analysis chamber. It is used to maintain the vacuum in the electron gun, which is during normal operation connected to the rest of the vacuum system by a small aperture in the electron column and can be separated by a pneumatic gate valve.

The vacuum pumps, pneumatic gate valves and electronic devices in the chamber are connected to an interlock system that protects the apparatus in case of emergency (e.g., low vacuum in the chamber, low rotational speed of the turbo molecular pump). Venting of the system can be performed separately for the FEL, the preparation and the analysis chamber as well as the gas dosage system, which allows, e.g., modifications without breaking the vacuum for the whole setup.

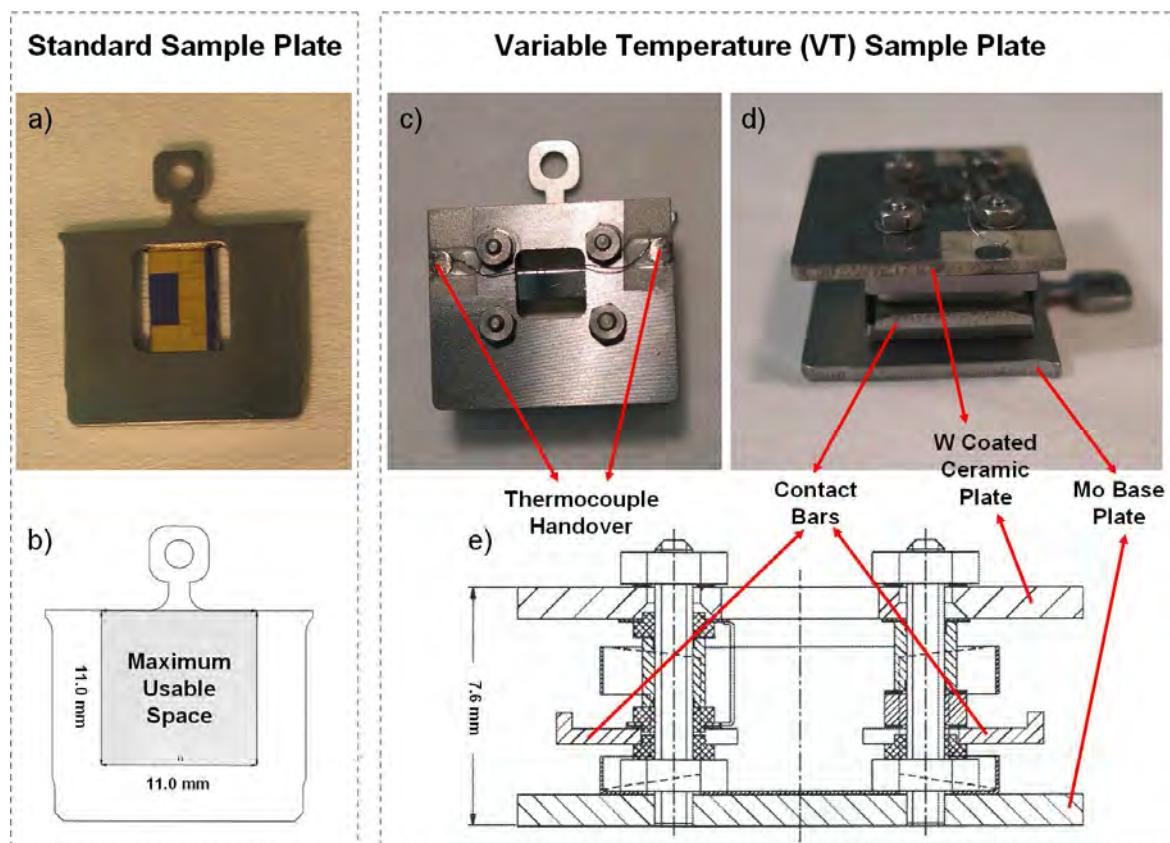


Fig. 3.3: Sample holder setups. a) Standard sample plate with a four point measurement specimen mounted below the window. b) Schematic drawing of a standard sample plate [108]. c) Top view of a VT sample plate with mounted Rh(110) crystal. d) Side view of the sample holder in (c). e) Schematic drawing of a VT sample holder from a side view [108].

In order to transfer the specimens in the apparatus they were mounted on sample holders. As depicted in Fig. 3.3 two different setups are possible: the standard sample plate and the variable temperature (VT) sample plate. The standard sample plate is a 1 mm thick tantalum or stainless steel sheet with a shape as depicted in Fig. 3.3 (a) and (b). The main advantages of this setup are that it is easy to handle and that comparably “large” specimens with a maximum size of $10 \cdot 10 \text{ mm}^2$ can be fixed on the plate (see Fig. 3.3 (b)). Heating with this rather simple type of sample holder is only possible in the preparation chamber via electron bombardment of the sample holder from below. By implementing a window in the plate, top mounted samples can be directly heated. On the other hand, mounting the specimen below the window (see Fig. 3.3 (a)) results in a fixed height in relation to the electron analyzer in the analysis chamber, which is important for AES measurements (see Chapter 3.1.2), but inhibits completely the heating of the sample.

The VT sample plate has a more complex setup, as shown in Fig. 3.3 (c), (d), and (e). It consists of a molybdenum base plate and a tungsten coated ceramic plate with a window at the top. Both are connected via four molybdenum studs. Between the plates the studs are covered by metal and ceramic parts, among others two contact bars that realize the electrical contact, e.g., for heating the sample in the analysis and preparation chamber. The types and alignments of the other components determine the functions of the sample holder, e.g., the applied heating technique; this can be direct current heating of the specimen, radiative heating via a pyrolytic boron nitride (PBN) heater or electron bombardment heating by a specially modified sample plate with an integrated filament (see Chapter 3.1.1). For temperature readout of the specimen two thermocouple handover spots are integrated in the ceramic plate, which allow to transfer the measured thermovoltage to a system connected to the outside of the apparatus. The sample is clamped to the top plate from below, resulting in a fixed distance between the surface and the tip during STM experiments with varying specimen temperatures. Additionally, the distance between the sample surface and the electron analyzer is kept constant regardless of the thickness of the specimen. This setup leads to some geometrical limitations of the applied samples, i.e., that only specimens with a maximum size of $(9 \cdot 3 \cdot 2) \text{ mm}^3$ can be used. The eyelet at the back of the base plate, which is also attached to the standard sample plate, is necessary for sample transfer by the linear translators and the wobble stick in the analysis chamber.

A complete overview of the heating and cooling possibilities of the different sample holder designs can be found in the appendix to Chapter 3.

3.1.1 Preparation chamber and fast entry lock chamber

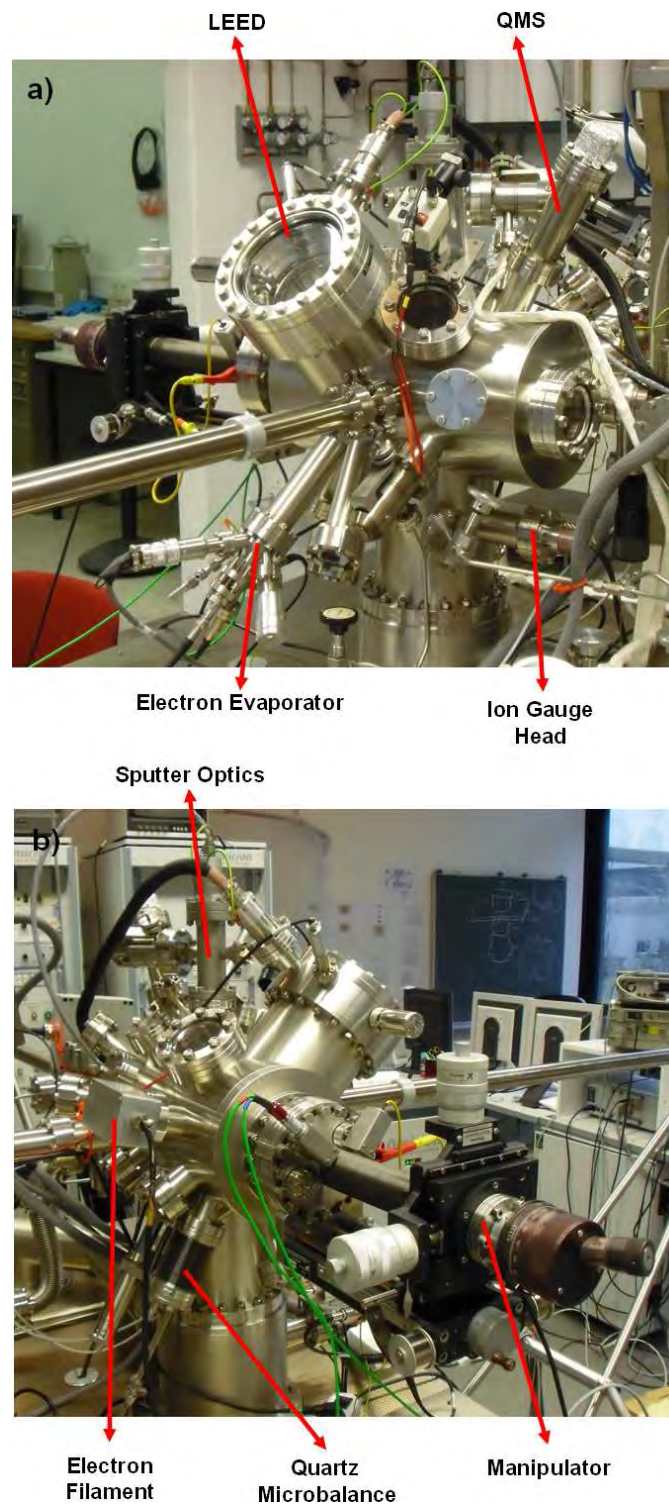


Fig. 3.4: Pictures of the preparation chamber with descriptions of the most important parts.

The preparation chamber of the apparatus is depicted in detail in Fig. 3.4. It houses a set of instruments mainly used for sample preparation, which are listed in the following:

- Sputter gun (Omicron NanoTechnology / *ISE 10*)
- Electron evaporator (Focus / *EFM 3i*)
- Quartz microbalance (Syscon / *OSC-100A*)
- Retractable LEED optics (Omicron NanoTechnology / *SPECTALEED*)
- Quadrupol mass spectrometer (QMS) (Pfeiffer Vacuum / *Prisma QMS 200 M2*).

A description of the flange positions, where the components were mounted on the chamber, can be found in the appendix to Chapter 3.

Sample access to the focus points of the attached instruments is achieved via a X,Y,Z – Φ, φ manipulator (Omicron NanoTechnology / *RX1515*). It enables a Z travel of 150 mm and an X and Y transfer of ± 12.5 mm each. Additionally, it has a rotary drive that allows turning the manipulator 360° around the Z axis (Φ) and another one for the rotation of the manipulator head in the Y / Z plane with $\pm 90^\circ$ (φ) (note: for a coordinate system with respect to the manipulator head see Fig. 3.5 (a)). For the purposes of electric contact and thermocouple readout, two four point feedthroughs are integrated in the base flange.

The original design of the manipulator head was modified, as the necessity of a second contact brush arose to utilize sample holders with an integrated filament for electron beam heating. The resulting setup is depicted in Fig. 3.5, while an exact description of the performed modifications can be found in the appendix to Chapter 3.

Cooling of the sample is possible by a cryostat mounted below the manipulator, with a copper braid realizing the thermal contact to the sample stage (see Fig. 3.5 (a)); by this method a temperature of 160 K can be reached for the sample holders with liquid nitrogen. For the heating of standard sample plates a tungsten filament ($\varnothing = 0.2$ mm) is directly integrated in the sample stage. As already mentioned before, the heating possibilities of the VT sample holders depend on their integrated components. For each type the electrical contact to the manipulator is realized by two contact brushes (see Fig. 3.5 (b)), which connect to the contact bars of an inserted sample holder (see Fig. 3.5 (d)). The right contact brush is important for the utilization of VT sample holders with an integrated e-beam heater, since a variable negative bias has to be applied to the filament and the surrounding Wehnelt cup.

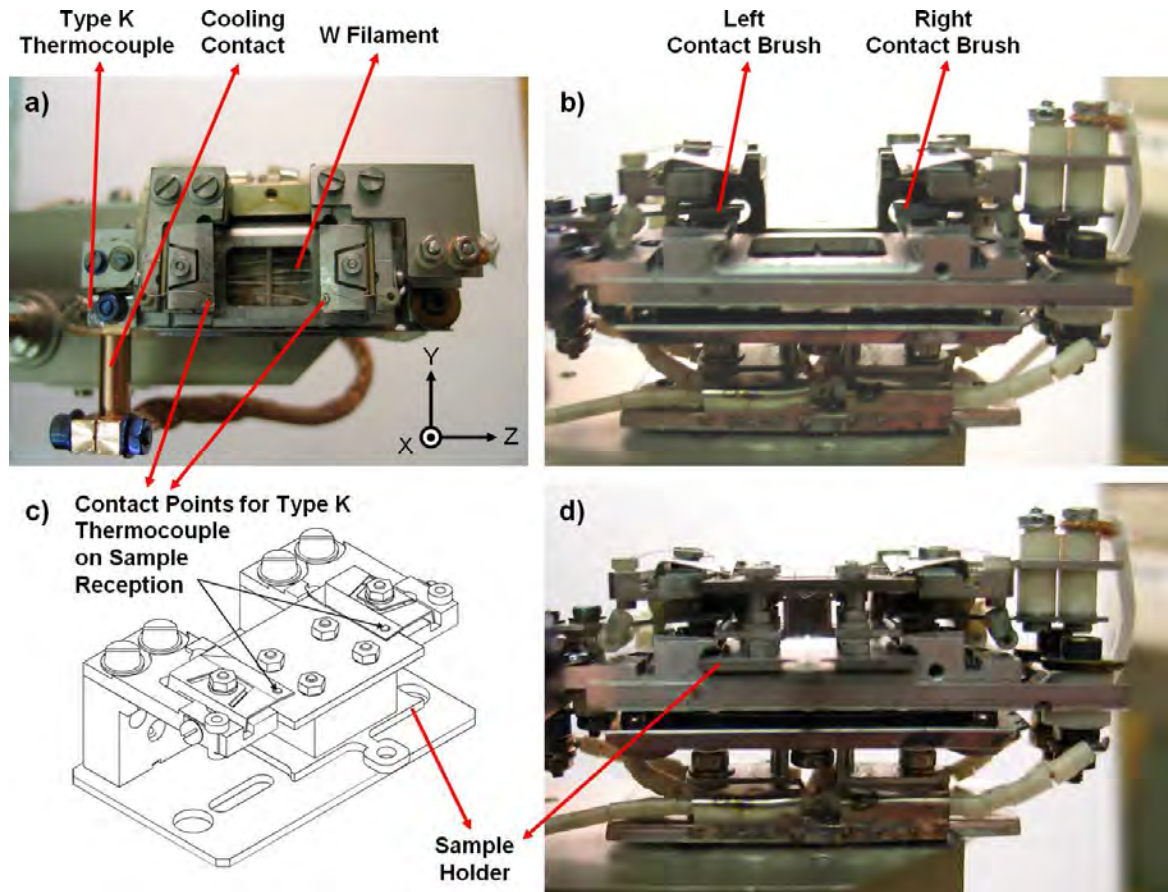


Fig. 3.5: Modified manipulator head with descriptions of the most important components. a) Picture from top view. b) Picture from side view. c) Scheme of the sample reception with thermocouple handover [107]. d) Picture from side view with an inserted VT sample holder with integrated filament.

The temperature of the sample stage is measured via a type K thermocouple fixed to the connection point of the cooling contact (temperature baseplate; see Fig. 3.5 (a)). Direct temperature readout of the specimen is only possible on a VT sample holder; the electrical contact to the thermocouple mounted to the sample is in this case realized by two clamping springs at the sample reception, which are connecting to the handover spots on the top ceramic plate of the sample holder (see Fig. 3.5 (a) and (c)).

Another component that was attached to the preparation chamber during the work at hand, is a self constructed electron filament. As depicted in Fig. 3.6 it is a simple setup, which consists of three vacuum feedthroughs with two thoriated tungsten filaments, each spot welded to two of the metal rods (filament 1 between rod I and rod II; filament 2 between rod II and rod III). Via this design it is possible to heat the filaments separately or combined. Detailed information about the metrics of the setup can be found in the appendix to Chapter 3.

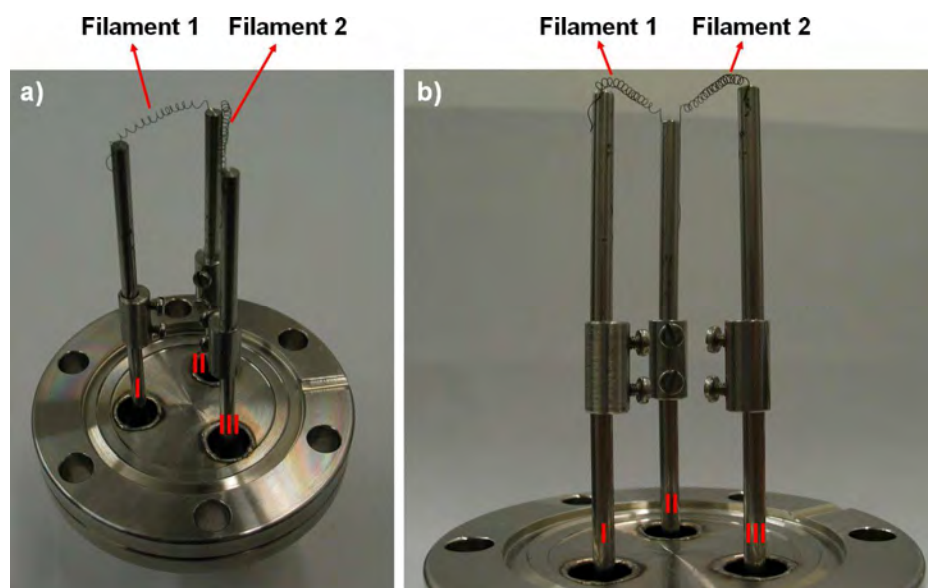


Fig. 3.6: Electron filament setup. a) Picture from bird's eye view. b) Picture from side view.

The intention of this component is to provide a steady flow of low energy electrons and thus to perform EBID not localized, but on the whole specimen area. A problem is that a variable negative bias has to be applied to the filaments, which results in the acceleration of the generated electrons towards every grounded part of the preparation chamber. Therefore, by applying a bias of -90 V only a maximum current density of $\sim 23 \mu\text{A}/\text{cm}^2$ was achieved with one filament, as measured by a specially modified sample holder with a mounted Si(100) sample. A possible improvement would be to attach a Wehnelt grid around the filaments in order to focus the electrons towards the specimen position.

Sample entry into the system is realized via the fast entry lock (FEL) or load-lock chamber, which is shown in the picture in Fig. 3.7. The design is a 6-way cross UHV fitting with five CF 40 and one CF 63 ports. The latter is normally used as a viewport; for specimen and tip loading and unloading the corresponding window is removed and the holders are inserted into a sample sledge with three receptions, mounted at the front of the shorter linear translator. This translator is seen in Fig. 3.7, situated on the right side of the load-lock, and enables the transfer into the preparation chamber. The two chambers can be separated via a manual gate valve. For evacuation after sample introduction a bypass to the turbo molecular pump of the preparation chamber is opened. Therefore, it is possible to achieve a pressure in the low 10^{-8} mbar range after roughly one hour of pumping.

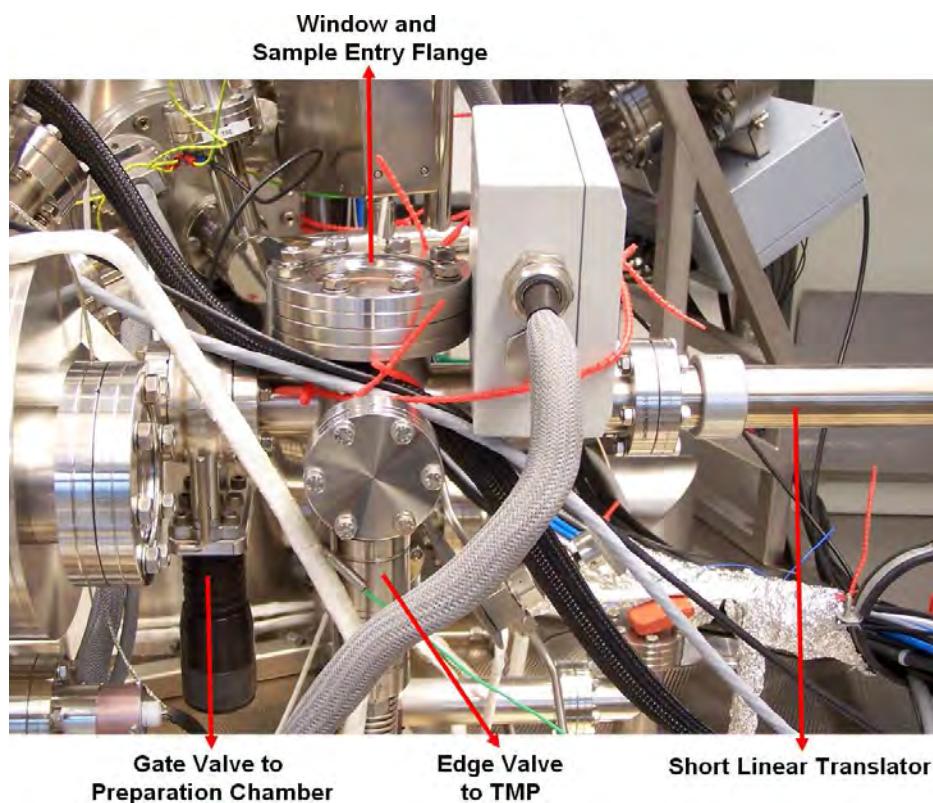


Fig. 3.7: Picture of the fast entry lock (FEL) chamber.

3.1.2 Analysis chamber

The analysis chamber is shown in Fig. 3.8. Sample entry from the preparation chamber can be performed via the longer linear translator onto the sample carousel (see Figure 3.8 (a)). The latter has two identical floors, each capable for the storage of six sample plates and / or tip holders. Sample transfer between the carousel and the sample stage is realized via a wobble stick.

Since the composition of the residual gases and the applied precursor or reactive compounds play a vital role in the performed experiments, another QMS (Pfeiffer Vacuum / *Quadrupol Prisma QMS 200*) was directly attached to this chamber. For a detailed description of the respective flange positions I refer to the appendix to Chapter 3.

The main component of the analysis chamber is the top mounted UHV compatible electron column (Zeiss / *UHV Gemini*). It is designed to enable scanning electron microscopy with a high spatial resolution, even at low beam voltages and energies. The ultimate resolution is < 3 nm at 15 kV and with a beam current of 400 pA (according to the 20 / 80 criteria, as determined on a gold coated mica sample). One of the main reasons for the resolution limitation in the given setup is the relatively high working distance of ~ 8 mm

between the exit of the column and the sample holder, which is necessary for the functionality of the other measurement techniques.

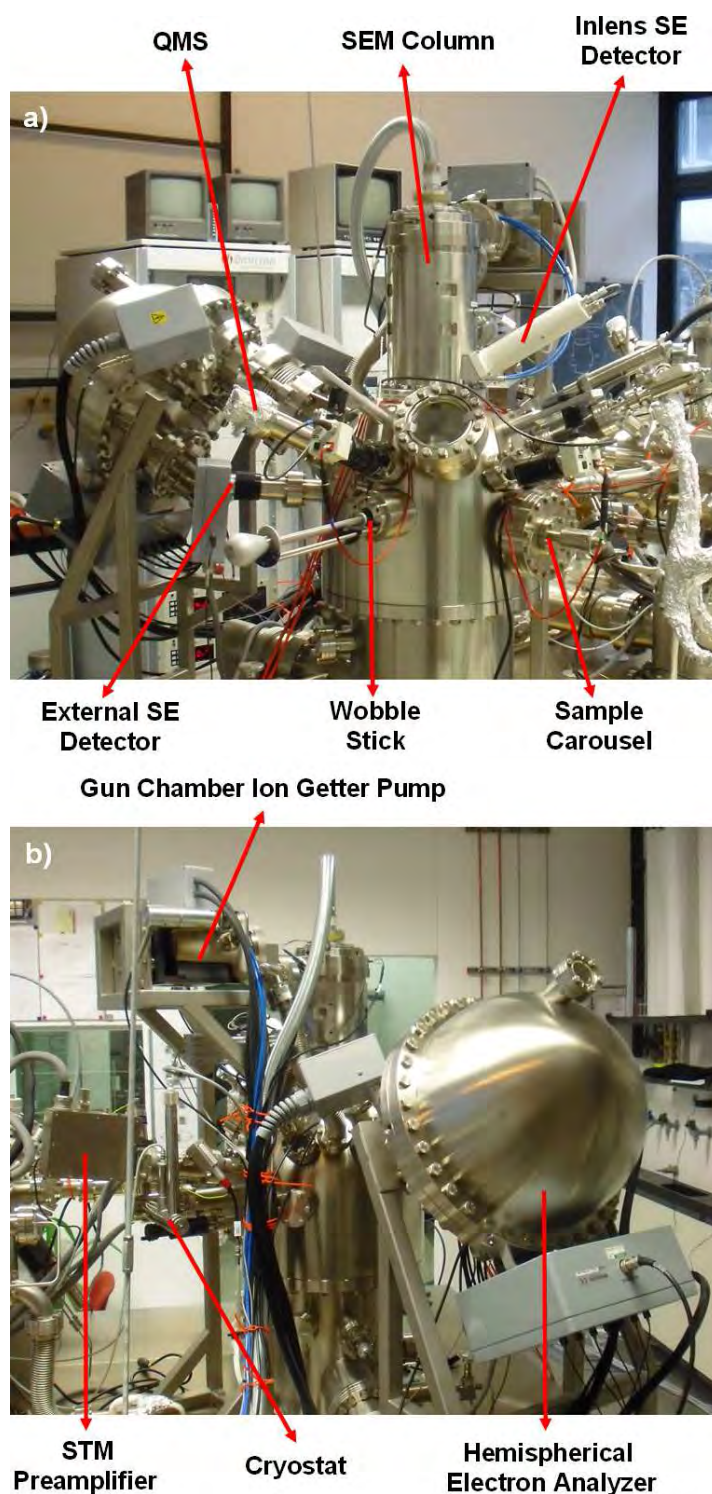


Fig. 3.8: Pictures of the analysis chamber with descriptions of the most important parts.

The electron beam generated by the *Gemini* column is also used as the probe for locally resolved AES and SAM measurements. In this case a higher beam current is required

for a good signal to noise ratio. The resolution is correspondingly lowered to < 6 nm (at 15 kV and 3 nA) [109].

A schematic profile of the *Gemini* is depicted in Fig. 3.9. Electron generation is realized via a Schottky field emitter, located at the top of the column in the source chamber (see Fig. 3.9 (b)). The filament is a (100) oriented tungsten single crystal tip with a zirconium oxide (ZrO) reservoir at the barrel. By heating it to 1800 K and applying a voltage of 4-8 kV to the extractor electrode, the ZrO diffuses to the tip end, generating a sharp apex of ~ 0.3 nm. Additionally, the metal oxide coating of the tungsten filament leads to a decrease of the electron work function from 4.5 eV to 2.7 eV, which is further reduced by the applied extractor voltage ($\Delta \sim 0.4$ eV). Due to the lowered work function, the thermal energy of the electrons is sufficient for them to leave the filament, resulting in a stable emission of the source and high gun brightness. A suppressor or Wehnelt grid is used for a controlled emission only at the position of the tip apex, which leads to a more defined energy distribution of the electrons ($\Delta E \sim 0.5$ eV). The emitted electrons are accelerated through the hole of an anode, located directly below the extractor electrode (see Fig. 3.9 (b)). The applied acceleration voltage is given by the operator, with typical values between 0.1 and 50 kV [48, 110].

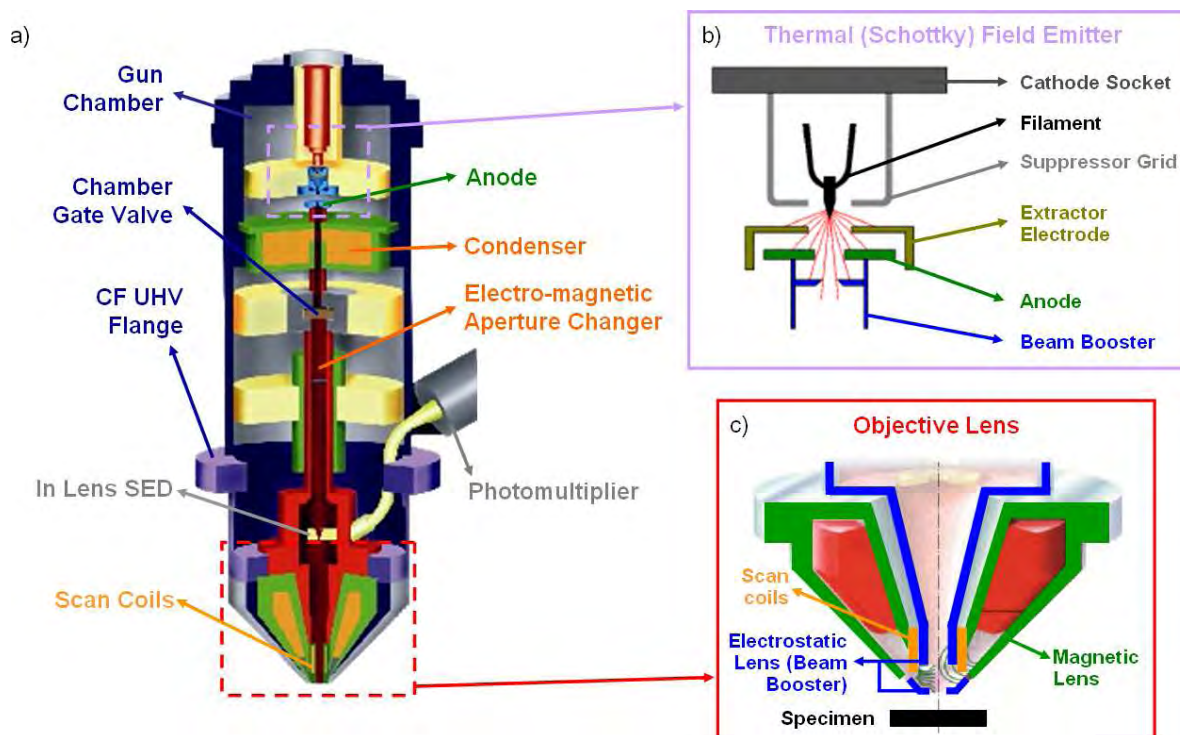


Fig. 3.9: *Gemini* column setup. a) Schematic profile of the column with blow ups of b) the thermal field emitter gun and c) the objective lens. The images were adapted from references [110] and [111].

Directly below the anode starts one of the electrodes of the beam booster, which extends through the whole column and is also an essential part of the objective lens. For acceleration voltages ≤ 20 kV a potential of 8 kV is applied to the electrode, leading to a higher electron energy in the column and thus decreasing the influence of lens errors and magnetic and electrostatic stray fields. The deceleration to their originally applied energy is realized in the objective lens, directly in front of the column exit (see below) [110].

The beam current can be chosen via an aperture with six different hole sizes, integrated in the middle of the column. A change in the transit hole is performed via electromagnetic deviation of the electrons before the aperture and back to the optical axis afterwards.

Distribution, focusing and control of the electron beam in the column is performed via a set of electrostatic and magnetic lenses. In the *Gemini*, this process is achieved with a cross-over free electron path. Situated below the field emitter gun is the condenser lens; it is designed to bring the divergent electrons emitted by the cathode back to a parallel stream along the optical axis of the column. Responsible for the final probe-forming and focusing is the objective lens, housed at the end of the column (see Fig. 3.9 (c)). For the *Gemini* this is a combined magnetic and electrostatic lens, with the latter also being a part of the beam booster (marked blue). Therefore, at beam voltages ≤ 20 kV the inner electrode is on an acceleration potential of 8 kV; the outer one is on ground potential, which means that deceleration of the electrons back to the original applied beam voltage takes place in the gap between the electrodes. Also integrated in the aperture lens is the scan coil system, which is used for the controlled beam deflection at the end of the column and hence for the scanning process [48, 110].

In the case of the *Gemini* the aperture lens is not only important for the primary electron beam, but also for the secondary electrons emitted by the specimen: due to the electric field of the integrated electrostatic lens, they are collected, accelerated towards the inner electrode and focused by the magnetic lens towards the In Lens SE detector, situated before the objective lens. This guarantees a high signal to noise ratio for beam voltages ≤ 20 kV (otherwise the objective lens exhibits no electrical field). At the detector the electrons (almost exclusively SE I and SE II) are impinging on a scintillator, which converts them into photons. These are transported via a light pipe out of the optical axis of the microscope to a photomultiplier that amplifies the information and finally converts it into an electrical signal. Combination of the individual signals to an image is performed via an attached electronic system, necessary for the synchronization between the scan coils and the SE detector. This

scan electronics also realizes the power supply of the column as well as the voltage settings for the lenses.

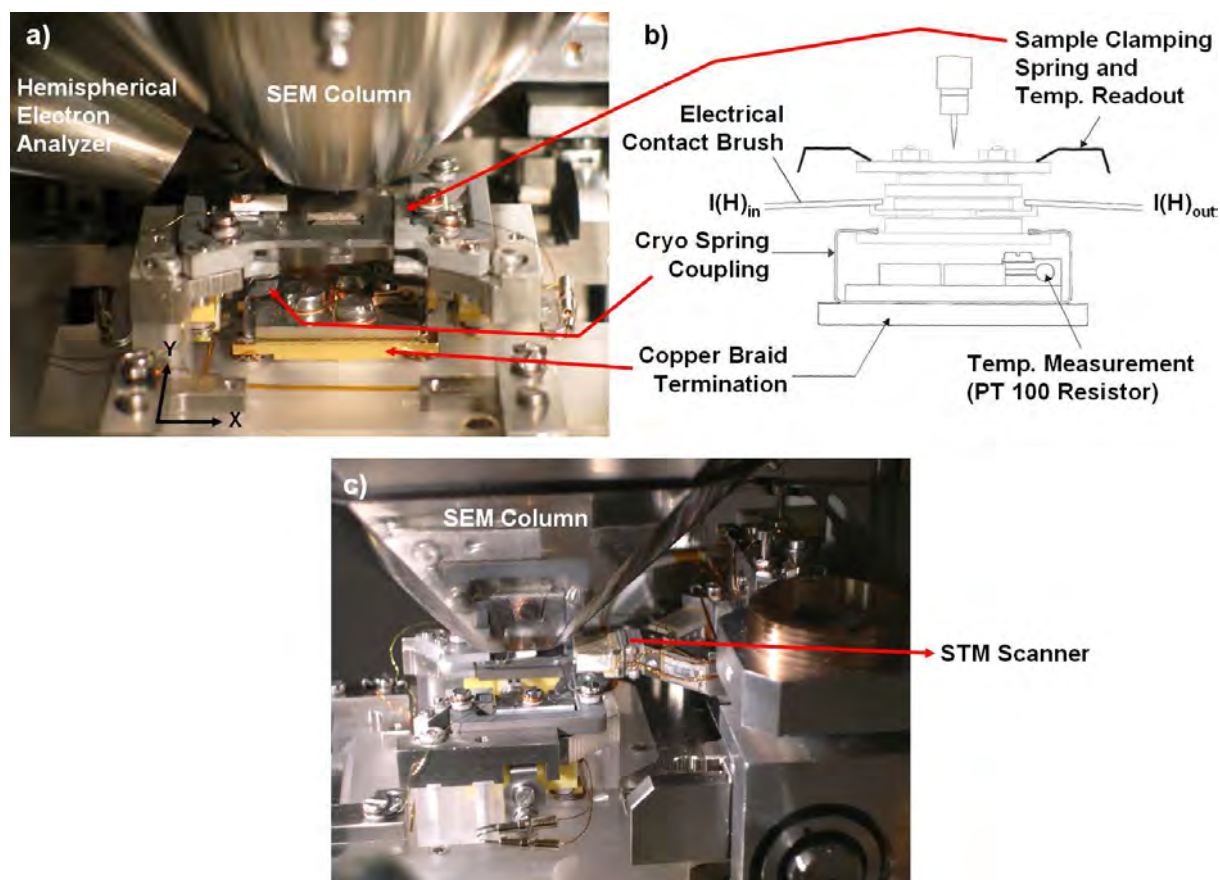


Fig. 3.10: Sample stage setup of the analysis chamber. a) Picture from a front view, with an inserted standard sample plate. b) Schematic drawing of the electrical and thermal contacts to a VT sample holder. c) Picture of the stage from a side view.

Additionally, the chamber houses an external SE detector that can be utilized for the generation of images from a flat angle (see Fig. 3.8 (a)). In contrast to the In Lens detector, signal amplification is in this case realized via a channeltron. It has also a prefixed detectors grid that enables, depending on the applied potential, to collect or repel secondary electrons emitted by the specimen and thus to increase the signal to noise ratio or to obtain images generated solely by BSEs, respectively. Since it was only barely used for the work at hand, no detailed descriptions will be given.

Fig. 3.10 shows pictures of the sample stage, which is situated directly below the electron column. The sample holders are inserted with the wobble stick at the position of the splints, located in the middle of the stage. The latter have some integrated clamping springs for the fixing of the holder (see Fig. 3.10 (a) and (b)). For a standard sample plate this is

shown in Fig. 3.9 (a). In the case of VT sample holders the top ceramic plate is inserted. Except for top mounted specimens on a standard sample holder this leads to a roughly constant working distance of ~ 9.3 mm between the specimen surface and the exit of the SEM column (as the sample is in these cases mounted below the inserted plate). Position changes of the holders under the column are performed by a two axis linear piezo motor, which allows for x,y-movements parallel to the sample surface with a travel range of 10 mm in both directions.

Heating and cooling during experiments can only be performed for a specimen mounted on a VT sample holder. Fig. 3.10 (b) shows a schematic drawing of the electrical and thermal contact points of the sample stage. Two brushes realize the contacting to the contact bars of the sample holders and thus also to the integrated heating components (except for the special cooling setup, which has no contact bars). Due to certain heat-sensitive parts integrated in the stage, the maximum applicable heating temperature is limited to ~ 1000 K for direct current heating and ~ 650 K for radiative heating via a PBN heater (see Appendix 9.1.1.).

For low temperature experiments (down to 70 K) the sample stage houses a flow cryostat that can be used for liquid or gaseous helium and nitrogen cooling. The entry and exit tube are localized at the back of the stage flange, with the latter normally connected to a rotary vane pump to drag the coolant through (see Fig. 3.8 (b)). Temperature control is realized via two regulation valves situated before and after the cryostat and by an integral heater element for counter heating of the coolant. The heating power is adjusted by a microprocessor based PID controller (Lakeshore / *331 Temperature Controller*), according to the temperature measured by a silicon diode at the heater position. Thermal contacting to the sample reception is realized by a cooper braid that ends in a copper block with direct connection to the VT sample holder via coupling springs (see Fig. 3.10 (a) and (b)).

Temperature measurements are taken directly at the spring coupling stage by means of a PT 100 resistor (see Fig. 3.10 (b)). The offset temperature between the measured value and the real sample temperature is, according to Omicron NanoTechnology, between 33 K and 22 K (with an error of ± 5 K), depending on the temperature measured by the resistor [108]. Additionally, temperature readout of a thermocouple directly connected to the specimen is possible via electric contacts integrated in the sample clamping springs, which are pressing on the handover spots of the top ceramic plate.

The sample stage houses also a STM, as illustrated in the picture in Fig. 3.10 (c). The associated scanner design is very flat, enabling the operation in the ~ 8 mm gap between the

column exit and the sample holder. Another advantage of this setup is that the position of the STM tip can be controlled by the SEM. Since STM was only barely used for the work at hand, no detailed description of this component will be given.

The whole sample stage is mounted on a goniometer, which allows turning up to 25° into counter-clockwise direction. For the In Lens detector this means a change in the point of view of the specimen, resulting in images acquired at a flat angle and with a higher surface topography sensitivity; the disadvantage of this acquisition method is a distortion in the micrograph along the tilting direction.

Turning of the stage is also important for AES and SAM applications, as the hemispherical electron analyzer (Omicron NanoTechnology / *NanoSAM*), depicted in Fig. 3.8 (b), is mounted at an angle of 60° with respect to the untilted surface normal (see appendix to Chapter 3). The reduction of this angle results in a larger number of electrons with trajectories towards the entry tube and therefore in higher count rates (see Fig. 3.10 (a)). In combination with the electron source this *NanoSAM* setup enables the performance of local Auger spectroscopy on features with a minimum size of 50 nm and SAM measurements with a resolution of < 10 nm.

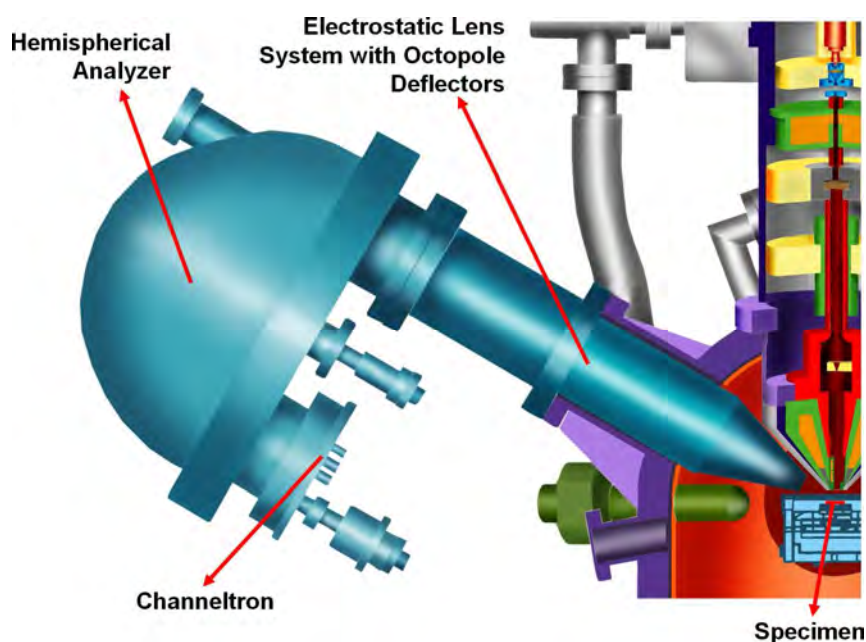


Fig. 3.11: Drawing of the electron analyzer system. The image was adapted from reference [111].

Fig. 3.11 shows a schematic drawing of the analyzer. Directly connected to the chamber is a stack of three electrostatic lenses that collect the emitted electrons from the surface, focus them on the adjustable analyzer entrance slit and decelerates them to the chosen

pass energy of the analyzer. The first lens is also important for the functionality of the whole system, since it prevents field penetration into the analysis chamber and thus an influence on the SEM. Located between the second and third lens are two sets of octopole deflector electrodes, which enable the compensation of the effects of stray fields in dependence of the kinetic energy of the electrons. The voltages applied to the electrodes have to be calibrated by a test sample. Setup changes in the analysis chamber and altered sample holder geometries have strong influences on the exact positioning of the sample in the electrical fields and thus on the performance of the octopole correction. One way to guarantee high detection efficiency is therefore to utilize samples with the same reference height as for the test sample.

The electrostatic hemispherical deflection analyzer with a mean radius of 125 mm is situated after the lens system [112]. It consists of two concentric hemispheres biased negatively and positively with respect to the chosen pass energy. Electrons with a specific energy are directed into a circular path and impinge on a seven channel electron multiplier (channeltron), situated after the adjustable exit slit of the analyzer. There, the incoming electrons are accelerated and multiplied until they are measured as a pulse at the output. Via a subsequent preamplifier the pulse is converted into an optical signal. This signal is transmitted to the multichannel receiver, where it is evaluated and sent to the measurement computer. Additionally, for SAM applications a synchronization between the SEM scan generator and the receiver is established to convert the single point measurements into an image.

3.1.3 Gas dosage system

Originally, the gas dosage system consisted of a reactive gas storage with a connection to the leak dosage valve of the sputter optics. Several components were added, as illustrated in the schematic drawing of the vacuum system in Fig. 3.2. An additional leak dosage valve with a separate gas supply port was attached to the preparation chamber and two separate lines were added to the analysis chamber. The latter are linked to the reactive gas storage as well as to the precursor storage part of the system. The additional connections were constructed by stainless steel tubes with an outer diameter of 6 mm and a wall thickness of 1 mm. Separations, which were necessary in certain positions, were realized via bellows sealed full metal valves (Swagelok). The whole gas dosage system can be evacuated by the turbo molecular and rotary vane pump of the preparation chamber.

The utilization of less volatile compounds proved to be problematic for the subsequent evacuation and purification of the dosage system. Therefore, two 10 m long heating strings were attached to the tubes and thermally insulated by a glass fiber ribbon (Heinz). This

enables the heating of the dosage system to ~ 410 K, separately from the rest of the apparatus. To prevent adsorption of the compounds in the turbo molecular pump, it is simultaneously heated to ~ 330 K by a heating tape.

Dosage of the precursor molecules on the surface is realized via a self-constructed, retractable doser. Pictures of the design are depicted in Figs. 3.12 and 3.13, while a detailed description about the metrics can be found in the appendix to Chapter 3. By the utilization of this doser setup it is possible to bring the exit of the dosing nozzle closer than 10 mm to the specimen surface (see Fig. 3.12 (d)), resulting in a higher effective surface pressure during the EBID process. The nozzle approaches parallel to the x-axis of the sample stage, with an angle of 26° with respect to the specimen surface plane. During normal operation, it is typically retracted by additional 30 mm from the sample position in order to minimize the influence on the measurement techniques.

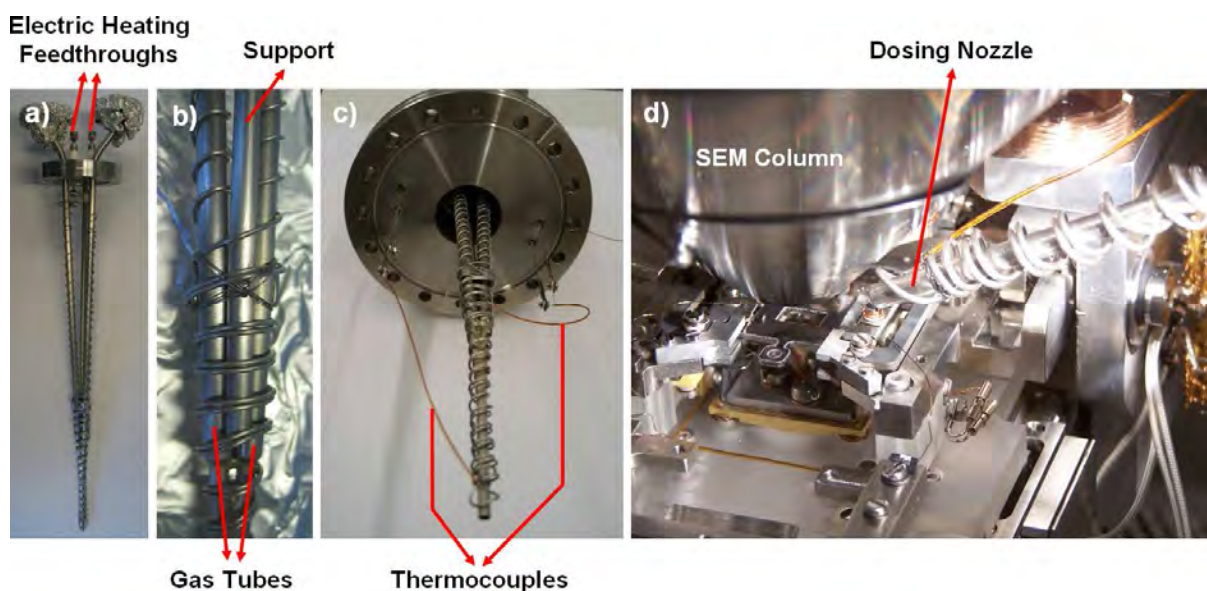


Fig. 3.12: Pictures of the gas dosage nozzle. a) Top view of the nozzle integrated in the flange. b) Blow up of the dosing nozzle with the heating wire wrapped around. c) Frontal view of the dosing nozzle that is mounted on the adapter flange. d) Sample stage with dosing nozzle in approached position.

For the construction of the dosing nozzle two stainless steel tubes with an inner diameter of 3 mm were integrated in a CF 40 flange (see Fig. 3.12 (a)), in order to enable the simultaneous dosage of up to two precursor and / or reactive gases. After a certain distance from the flange the two tubes are merging into one. Mechanical stabilization is realized via an additional support rod that is fixed to the flange. In order to clean the dosing nozzle from less

volatile compounds, a special heating wire was wrapped around the tubes (Thermocoax / *NcAc10*) (see Fig. 3.12 (b)). It consists of a current carrying NiCr core insulated by highly compacted MgO powder and kept in a stainless steel tube. The advantages are that the heating wire is comparably flexible and can be directly attached to the metal object. Heating power can be applied to the wire by two electrical feedthroughs integrated in the flange.

To enable movement of the dosing nozzle towards or away from the specimen it was mounted on a linear translator with a maximum range of 100 mm (VG / *ZLTM100*) (see Fig. 3.13 (a)). Connection of the two integrated tubes to the exterior gas dosage system and control of the gas flow into the analysis chamber is realized via two leak dosage valves (VG / *LVM940*). The attached tubes of the gas lines were partly bent into circular spirals, in order to create a more flexible connection and therefore to avoid mechanical tensions due to the movements of the doser (see Fig. 3.13 (b)).

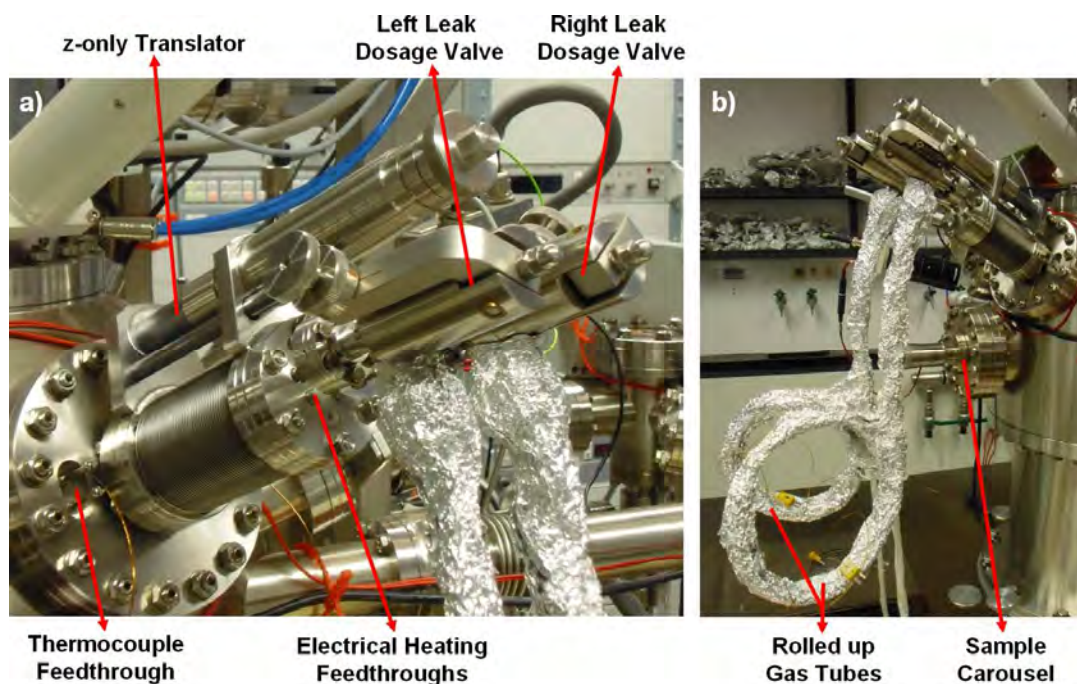


Fig. 3.13: Pictures of the gas doser. a) Setup from a close point of view. b) Overview image of the mounted position on the analysis chamber.

The device was mounted to the analysis chamber directly opposite to the electron analyzer on a modified CF 100 flange (see appendix to Chapter 3). The latter has also four integrated thermocouple feedthroughs for the temperature readout of thermocouples attached to the front of the dosing nozzle and the position of the tube mержence, respectively (see Figs. 3.12 (c) and 3.13 (a)).

Another challenge was the attachment of the precursor compounds to the gas dosage system. Therefore, a storage device was constructed, which is depicted in Fig. 3.14. The precursor is normally kept in the cylindrical stainless steel part at the bottom. Detailed information about the dimensions of this part can be found in the appendix to Chapter 3. Attached to it are two full metal valves (Swagelok) via a cross- or T-shaped fitting. The top mounted valve connects the storage device with one of the dosage lines of the analysis chamber, while the right valve is used for evacuation and nitrogen filling before the precursor is introduced. This enables the attachment of the precursor to the system without exposing the compound to ambient conditions. If precursors with a low vapor pressure are used, the storage part can also be heated by an oven. Up to two storage devices can be connected to each dosage line of the gas dosage system, i.e., four storage devices can be mounted simultaneously.

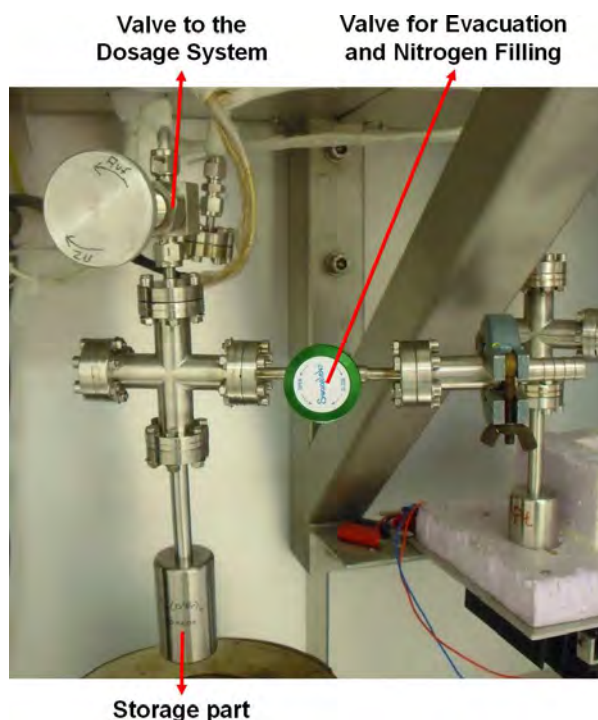


Fig. 3.14: Picture of one precursor storage device.

3.1.4 Gas Purification and Monitoring (GPM) chamber

One disadvantage of the gas dosage system described in Chapter 3.1.3 is associated with the utilization of precursor compounds with a low vapor pressure (e.g., titanium(IV) tetraisopropoxide). These materials tend to form deposits in the gas handling system: for sensible parts like, e.g., fine dosage valves this can lead to malfunction. Another drawback is the necessity to perform the verification of the gas compound by QMS measurements in the

experimental chamber, which can lead to significant contaminations in the system. In order to reduce the gas load to the chamber and to contain the inevitable contaminations within a separable and maintainable section of the apparatus, an additional chamber with its own pumping system and QMS was constructed. The vacuum system of this GPM chamber (**G**as **P**urification and **M**onitoring chamber) is schematically depicted in Fig. 3.15. It is attached to the rest of the system at the position labeled as “Precursor Storage” in Fig. 3.2, i.e., it is directly connected to the two separate tubes of the gas doser (compare Figs. 3.12 and 3.13). Two images of this chamber in its assembly rack, which was used as a mounting device during the construction, are depicted in Fig. 3.16. Some additional drawings of the GPM chamber can be found in the appendix to Chapter 3.

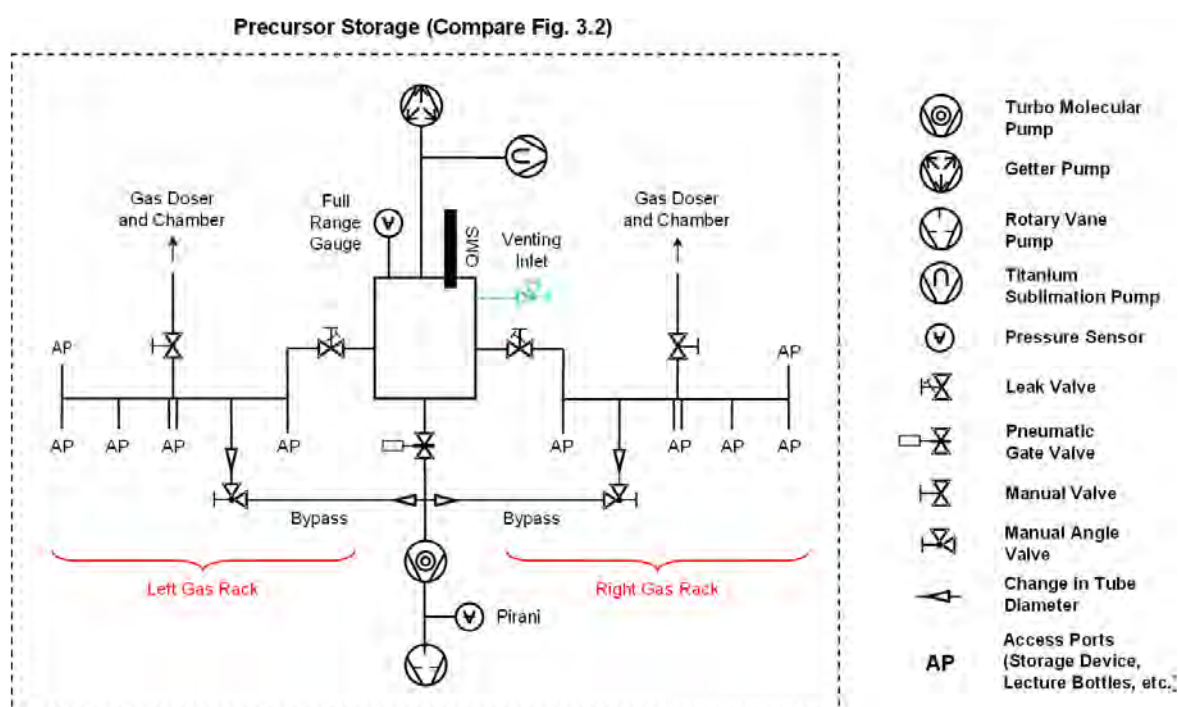


Fig. 3.15: Schematic drawing of the vacuum system of the GPM chamber with a legend of the vacuum components on the right. With respect to the vacuum system of the whole apparatus in Fig. 3.2, this chamber is attached at the position denoted as “Precursor Storage”. The valve depicted in blue is used for venting purposes.

The main part of the GPM chamber is a 6-way cross UHV fitting with five CF 40 and one CF 63 ports. It houses a quadrupole mass spectrometer (QMS) (Pfeiffer / *Prisma QMS 200 M*; compare Fig. 3.16 (a)) and a compact full range gauge head (Pfeiffer / *PBR 260*; compare Fig. 3.16), which combines a Pirani and a Bayard-Alpert sensor for pressure measurements. During normal operation the vacuum in the chamber is maintained by an 8 l/s ion getter pump

(Varian / *VacIon*; compare Fig. 3.16 (b)) and a titanium sublimation pump (self-constructed; two U-shaped filaments), which results in a base pressure of $< 5.0 \cdot 10^{-10}$ mbar (lowest value that can be measured by the full range gauge). For experiments with a high gas load and bake-out purposes, additional pumping can be employed via a turbo molecular pump (Pfeiffer / *TMU071P* / ~ 59 l/s; compare Fig. 3.16) in combination with a rotary pump (Edwards / *E2M2*), which can be separated from the rest of the chamber by a gate valve (compare Fig. 3.16). The pressure at the exhaust port of the turbo molecular pump is additionally measured via a Pirani gauge head (Pfeiffer / *TPR280*). Venting of the chamber can be realized by a full metal angle valve (see Fig. 3.16 (a)).

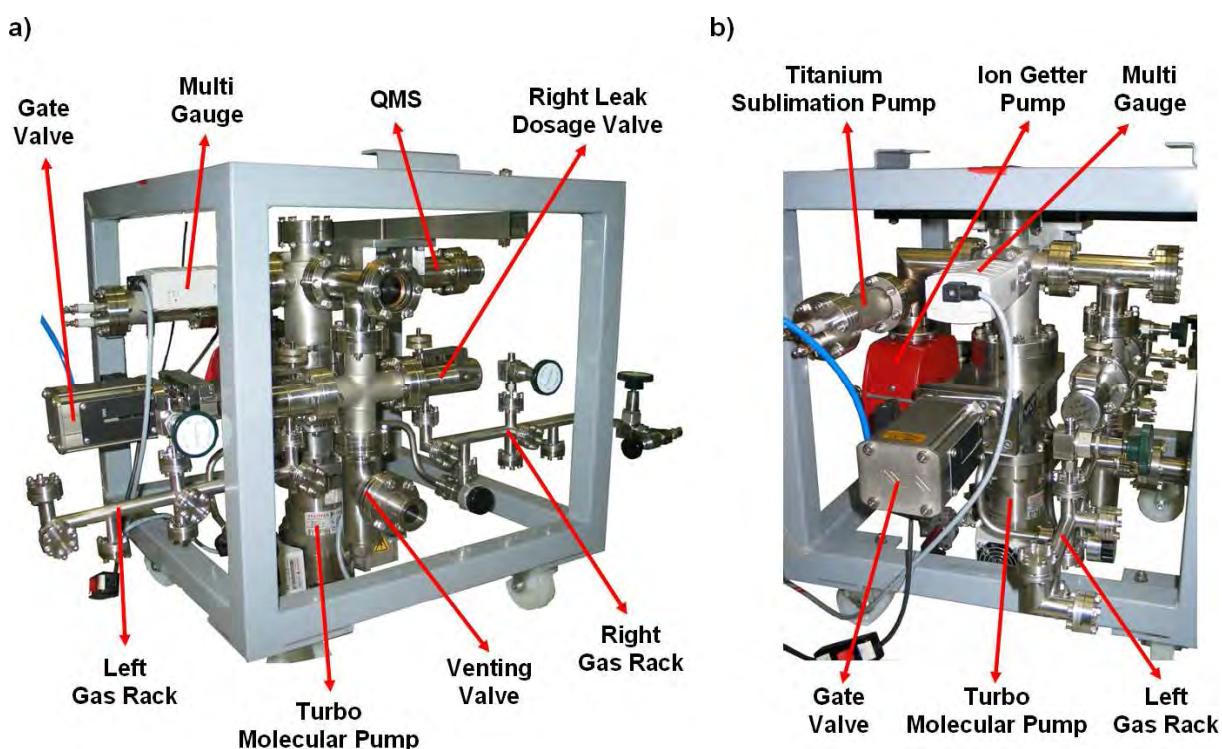


Fig. 3.16: Pictures of the GPM chamber in its assembly rack, with descriptions of the most important components.

Directly connected to the chamber are two gas racks (compare Figs. 3.15 and 3.16), which were constructed by stainless steel tubes with an outer diameter of 16 mm and a wall thickness of 1 mm. Each of them has six CF 16 ports for the attachment of precursor storage devices (compare Fig. 3.14), lecture bottles and other components. Furthermore, via bellow sealed full metal valves (Swagelok) they can be directly attached to the two tubes leading to the gas doser of the analysis chamber (separated tubes for both racks). Vacuum generation and gas purification in the racks is realized by the turbo molecular pump, which can be

separately connected by a bypass (outer diameter: 10 mm; wall thickness: 1 mm) via opening an angle valve; for the racks this results in a base pressure of lower than $9.0 \cdot 10^{-10}$ mbar (measured in the chamber via an open gate valve with both racks connected by the bypasses). The attachment of the racks to the remaining part of the GPM chamber is realized via leak dosage valves (Varian / *Model 1000*; see Fig. 3.16 (a)), which are also used to control the gas flow for QMS measurements and other experiments.

Via the described setup, it is possible to purify the precursor gases in the racks via vacuum pumping with the turbo molecular pump, to monitor their composition via QMS measurements in the main part of the chamber and afterwards to connect them to the gas doser at the analysis chamber. The relatively small volume of the GPM chamber should also reduce the longsome pumping of the system after gas introduction. Another advantage is the bake-out system, which is realized via heating tapes (Horst) and attached such that the main part of the chamber as well as both racks can be baked separately. Furthermore, it is also possible to perform experiments directly in this chamber by mounting additional components (e.g., a sample stage).

The completion of the GPM chamber took place during the final stage of the work at hand. Therefore, it was not applied for the results presented in the Chapters 4 to 6; for all the presented experiments the gas dosage system was in the state described in Chapter 3.1.3.

3.2 Lithographic attachment

For the control of the electron-beam position on the surface and hence the irradiation of patterns with arbitrary shapes the *ELPHY Quantum* nanolithography system (Raith) was attached to the setup. It consists of a PC with integrated PCI 16 bit DAC board and the *ELPHY* software [113].

The beam deflection in the column is realized by the scan coils in the objective lens that can be controlled by an analog external scan-interface integrated in the scan electronics. By applying voltage input signals with maximum values of ± 5 V to the x- and y-direction ports any position in a square surface area referred to as the writefield can be reached in a controlled way. The size of the writefield depends on the magnification of the electron microscope and has to be calibrated for each size. Communication between the *ELPHY* and the *SmartSEM* software is realized by a remote control program (*Zeiss / REMCON*), installed on the SEM measurement computer. This software setup regulates also the on and off switching of the external scan-interface and thus the change between lithographic exposure and normal electron microscopy.

Supply and control of the voltage signals for the beam deflection is realized via the PCI board housed in the lithographic computer. It enables the exposure of separated points with a minimum distance of 0.8 nm and an ultimate pixel to pixel frequency of 2.5 MHz [113]. The dwell time at each spot can therefore be varied between values from 0.4 μ s up to several seconds. In order to minimize the influence on already finished structures, the PC board applies a voltage of roughly - 5 V to the scan-interface when there is no pattern exposure (both, x- and y-direction ports) and thus parks the beam at a position in the top left corner of the writefield. Automatic blanking of the electron-beam via the lithographic attachment is not possible, since the *Gemini* has no dedicated beam blarker.

The *ELPHY* software has an integrated graphical interface for the generation of arbitrarily shaped structures. Additionally, images and patterns in different file formats (e.g., ASCII) can be integrated. The arrangement of particular structures into different layers enables principally the fabrication of complex, 3-dimensional structures or the assembly of the deposit from different materials [114]. The software uses its own coordinate system (UV), which compensates also for any misalignments of the mounted specimen.

Irradiation of area and line structures is realized in a point by point fashion with a predefined step size (area step size (S_A) or line step size (S_L)) between the individually exposed spots. The particular electron doses for area, line and dot structures (D_A , D_L or D_D , respectively) can be determined by the specification of the dwell time at each spot (T_A , T_L or T_D , respectively), the applied electron-beam current (I_B) and eventually the step size (in the case of area and line structures). Alternatively, the electron dose and two of the other variables can be predefined to calculate the missing value. Variations of the electron dose within a template can be realized by the allocation of a dose factor (F) to individual structures; this value counts as a multiplier for the respective dwell time at each spot and therefore also directly for the applied electron dose. The connections between the different lithography parameters are summarized by the following Equations 4.1 to 4.3.

$$D_A = \frac{(F \cdot T_A) \cdot I_B}{(S_A)^2} \quad (4.1)$$

$$D_L = \frac{(F \cdot T_L) \cdot I_B}{S_L} \quad (4.2)$$

$$D_D = (F \cdot T_D) \cdot I_B \quad (4.3)$$

For the irradiation of rectangular and square areas either a “meander” or “line” mode can be chosen (menu “Exposure Details / Area Mode”); both settings perform the exposure by consecutive irradiation of lines. For the “meander” sequence, the exposure of the second line starts on the side where the one of the first ends, leading to a zig-zag pattern of the electron path (see Fig. 3.17 (a)). In the case of the “line” mode irradiation of each line starts at the same side, resulting in a sawtooth-like movement of the electron-beam (see Fig. 3.17 (b)). The exposure of circular areas is performed in a completely different way: the activation of a “circular” mode (menu “Exposure Details / Advanced Details”) leads to the irradiation of concentric rings with a decreasing radius from the outside to the center (see Fig. 3.17 (c)); when this option is turned off the circle is divided into triangles, rectangles and trapezes, which leads to a rather inhomogeneous exposure of the corresponding structures.

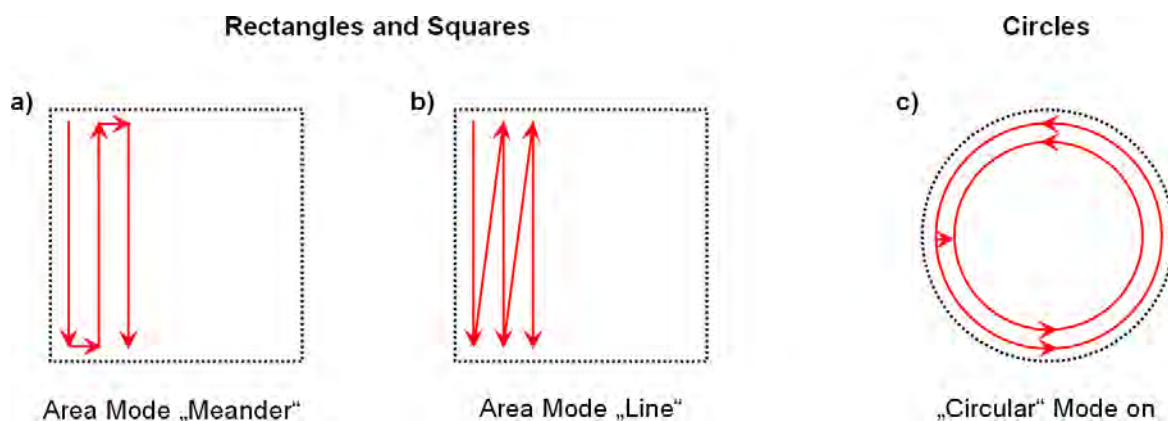


Fig. 3.17: Schematic drawing of the different modes for the area exposure with the software *ELPHY Quantum*: rectangles and squares in a) “meander” mode and b) “line” mode and c) circles with “circular” mode turned on.

A major problem of the *ELPHY Quantum* system is the repeated irradiation of patterns; between each loop a certain computing time is necessary, in which the position of the electron-beam cannot be predicted (most presumably it will be parked in the top left corner of the writefield). The exposure of patterns with high loop numbers and defined electron doses is therefore not possible.

3.3 Applied materials

Table 3.1 lists the applied precursor and reactive gas compounds together with their suppliers and indicated purities.

Iron pentacarbonyl ($\text{Fe}(\text{CO})_5$) was filled into the precursor storage device (see Chapter 3.1.3) under nitrogen atmosphere and directly attached to the gas dosage system. Purification of the compound and nitrogen removal was achieved via flushing of the gas lines and partly by directly pumping the storage device.

Ethene (C_2H_4), argon (Ar), oxygen (O_2) and hydrogen (H_2) were attached to system via 12 liters lecture bottles and only slightly purified by the flushing of the attached gas tubes.

Compound	Formula	Supplier	Purity
Iron pentacarbonyl	$\text{Fe}(\text{CO})_5$	ABCR GmbH & Co.	99.5 %
		Sigma-Aldrich	99.5 %
		Acros Organics	99.5 %
Ethene	C_2H_2	Linde	99.8 %
Hydrogen	H_2	Messer	99.999 %
Argon	Ar	Linde	99.999 %
		Messer	99.999 %
Oxygen	O_2	Linde	99.995 %
		Messer	99.998 %

Table 3.1: Applied precursor and reactive gas compounds.

The applied sample types and their suppliers are summarized in Table 3.2. The PMMA (polymethyl methacrylate) samples were mounted on top of a standard sample plate without window via two tantalum stripes; the stripes were placed on the sample and spot welded to the holder on each side. Removal of the irradiated material was achieved by a developer solution (3 : 1 mixture of methyl isobutyl ketone (MIBK) and isopropanol (IPA)) and a stopper solution (pure IPA), which were also supplied by Raith.

The applied silicon wafers were laser cut into individual samples with a size of 10 mm · 1 mm. They were typically mounted on a VT sample plate configured for direct resistive heating.

The Rh(110) crystal was initially mounted on a VT sample holder with integrated PBN heater; later, it was assembled on top of a standard sample plate with integrated window.

The crystal has a drill hole in the middle of one of the 9 mm · 1 mm sides, in order to attach a thermocouple.

Sample	Supplier	Important Parameters
PMMA (950,000 u) on Silicon Support	Raith	<i>Thickness PMMA: 100 nm</i>
Si(111)	Institute of Electronic Materials Technology (Warszawa, Poland)	<i>2" Wafers</i> <i>Thickness: 0.5 ± 0.025 mm</i> <i>Boron Doped:</i> <i>3.2 · 10¹⁸ to 8.5 · 10¹⁸ at / cm³</i> <i>Resistivity: 0.01 to 0.02 Ω cm</i>
Si(100)		<i>2" Wafers</i> <i>Thickness: 0.5 ± 0.025 mm</i> <i>Boron Doped:</i> <i>4.5 · 10¹⁷ to 5.4 · 10¹⁷ at / cm³</i> <i>Resistivity: 0.065 to 0.074 Ω cm</i>
Rh(110)	MaTeck	<i>Size: 9 mm · 2 mm · 1 mm</i> <i>Polished on one 9 · 2 mm² Side with a</i> <i>Roughness < 0.03 μm</i> <i>Accuracy Surface Orientation: < 0.1°</i>

Table 3.2: Applied specimens.

3.4 Experimental details and data processing

Pressure values

All partial gas pressures given in this work were adjusted via the background pressure in the chamber and are based on uncorrected ion gauge readings.

Determination of sample temperatures

In Chapter 3.1 it was reported that the manipulator in the preparation chamber as well as the sample stage in the analysis chamber have a thermo voltage handover for direct temperature readout of the specimen. The corresponding setup turned out to deliver unreliable readouts, which was mainly attributed to a bending of the clamping springs (see Figs. 3.5 and 3.10) induced by thermal (e.g., during bakeout) or mechanical stress (e.g., due to repeated sample

entry). Another problem is that the thermo voltage handover can only be applied for VT sample holders (compare Fig. 3.3).

Due to the described problems, the sample temperatures denoted in this work were mainly determined by other methods, depending on sample type and sample holder setup, as listed below:

I. Rh(110) mounted on VT sample holder with integrated PBN-heater:

In this case, the denoted sample temperatures for heating in the preparation chamber to temperatures above 600 K were determined using a pyrometer (Impac Elektronik GmbH / *IP 120*) through a quartz window (viewport at flange number 14; see Fig. 9.2 in the appendix to Chapter 3). Fig. 3.18 shows a plot of the sample temperature against the PBN heating power. Two sets of measurement values are presented: the points indicated by dark blue squares were measured while the sample was heated up stepwise to a maximum temperature of ~ 970 K, while the light blue triangles were acquired during the reverse cooling process. For each measurement the heating power was kept constant for roughly 30 min to enable the specimen to reach an equilibrium temperature. For both measurement sets (heating up and cooling) also the corresponding temperatures at the baseplate are depicted in Fig. 3.18 (determined via the thermocouple, which is attached at the connection point of the cooling contact; see Fig. 3.5). A logarithmic trend line was applied to each of the temperature sets. For both measurements (heating up and cooling) the respective curves are reproducible for the sample as well as the baseplate. Since the pyrometer measurements were performed through a quartz window and the sample surface could not be positioned completely perpendicular to the optical axis of the pyrometer (the corresponding manipulator settings can be found in the appendix to Chapter 3), an error value of ± 50 K can be assumed for the absolute sample temperature (indicated by the error bars in Fig. 3.18). Temperatures below 600 K could not be determined reliably via the applied pyrometer.

Heating of this setup (Rh(110) mounted on VT sample holder) in the preparation chamber below 600 K and in the analysis chamber below 610 K was performed according to a reference curve given by Omicron (Figure 42 on page 86 in reference [108]; the error was specified to be ± 25 K). The accuracy of this curve at lower temperatures was verified by measurements via a thermocouple attached to the sample, while the thermo voltage handover was functioning properly.

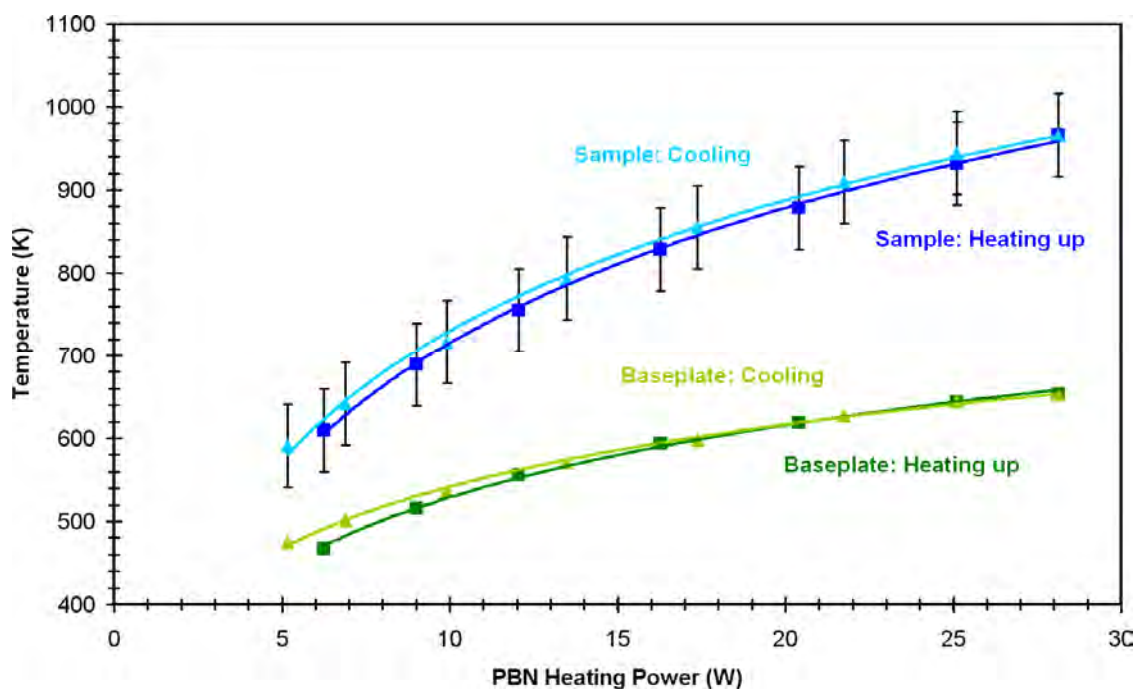


Fig. 3.18: Plots of sample and baseplate temperature vs. the heating power of a PBN heater, integrated in a VT sample holder with mounted Rh(110) crystal. The sample temperatures (blue curves) were measured using a pyrometer through a quartz window, while the temperatures of the baseplate (green curves) were acquired via a thermocouple.

II. Rh(110) mounted on standard sample holder with integrated window (e-beam heating):

Heating of this specimen setup could only be performed in the preparation chamber. In this case, the temperatures of the sample were again determined using a pyrometer with the same setup as described for the VT sample holder (see above). For e-beam heating with the filament integrated in the manipulator head, adjustment of the filament current for a certain temperature is realized by a regulator unit (VG / EBHC with integrated Eurotherm / 2408) based on a temperature readout at the baseplate (determined via the thermocouple attached to the connection point of the cooling contact; see Fig. 3.5). In Fig. 3.19 a plot of the sample temperature (measured via pyrometer; error of approximately ± 50 K for the absolute sample temperature) against the temperature at the baseplate (measured via thermocouple at the connection point of the cooling contact) is depicted. The sample temperature shows an exponential dependence to the temperature of the baseplate, as indicated by the exponential trend line in Fig. 3.19. All values were measured while heating the sample with the high voltage turned on (- 650 V applied to the filament) and after the temperature at the baseplate reached the setpoint and stayed constant. Higher temperatures were not applied due to a limitation of the filament current (2 A) and the temperature at the copper bread.

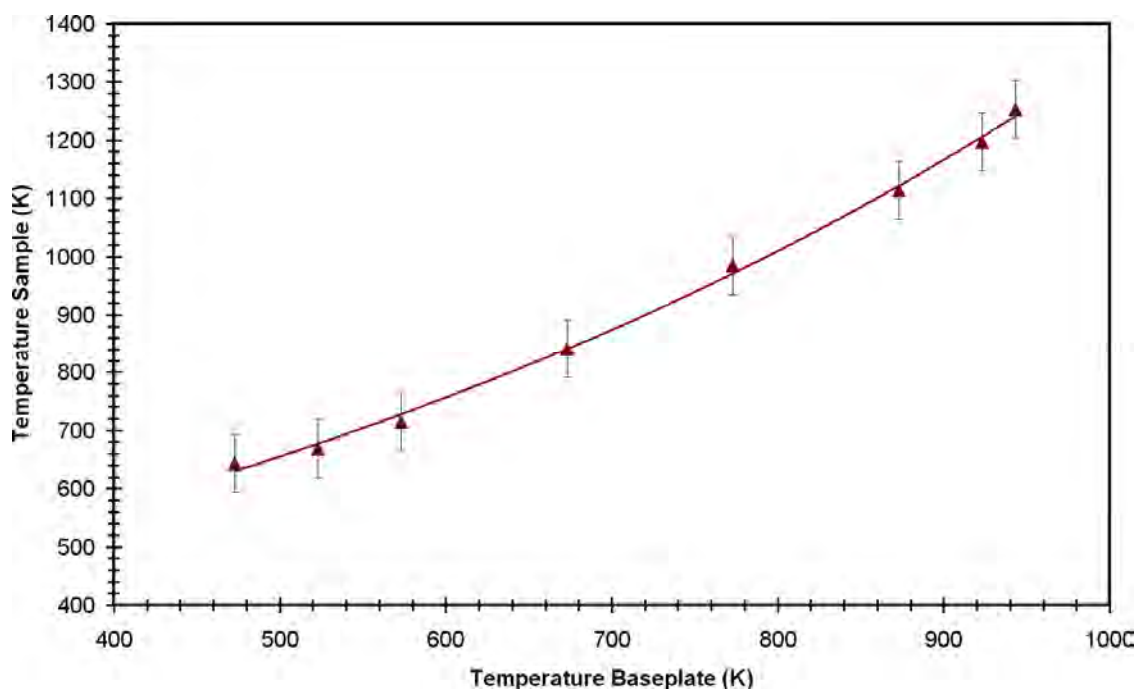


Fig. 3.19: Plot of sample temperature vs. temperature of the baseplate, while e-beam heating of the Rh(110) crystal mounted on a standard sample plate. The sample temperatures were measured using a pyrometer through a quartz window, while the temperatures of the baseplate were acquired via a thermocouple.

Observation of oxidation / reduction cycles in front of the LEED optics while heating the sample to ~ 600 K could not be performed with the high voltage of the filament turned on (strong influence of the emitted electrons on the phosphorescent screen). The temperature was therefore achieved without a potential difference between the filament and the sample, which made a higher filament current necessary to reach the setpoint.

III. Si(111) and Si(100) mounted on VT sample holder:

The denoted sample temperatures for resistive heating in the preparation and analysis chamber were again determined by a pyrometer measurement, similar as it was described for the rhodium sample (see above; error of roughly ± 50 K). Fig. 3.20 shows plots of the sample temperature for Si(100) (blue) and Si(111) (green). Two sets of measurement values are presented for each specimen: the points indicated by squares (dark blue squares for Si(100) and dark green squares for Si(111)) were measured while the sample was heated up stepwise to a maximum temperature of ~ 1180 K, while the triangles (light blue for Si(100) and light green for Si(111)) were acquired during the reverse cooling process. For each measurement the heating current was kept constant for roughly 5 min to enable the specimen to reach an

equilibrium temperature. The differences between the heating up and cooling curves for each specimen are very small, indicating the high reproducibility of the temperature measurements.

Temperatures below 600 K could not be determined reliably via the applied pyrometer. Thus, denoted temperatures below 600 K were extrapolated from the trendlines of the data sets depicted in Fig. 3.20.

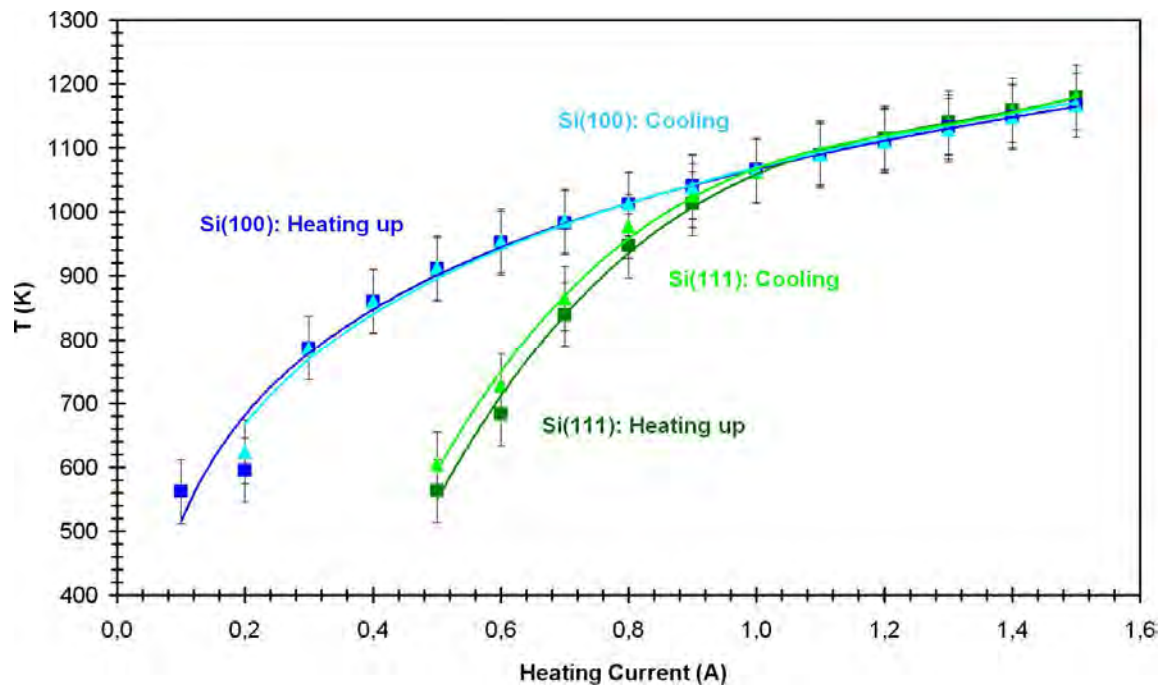


Fig. 3.20: Plots of sample temperature vs. heating current for Si(100) (blue) and Si(111) (green), mounted on a VT sample holder. The sample temperatures were measured using a pyrometer through a quartz window.

Preparation of the Rh(110) surface

For the initial cleaning procedures and experiments the rhodium crystal was mounted on a VT sample holder with integrated PBN heater (see Chapter 3.1); a maximum sample temperature of ~ 1000 K was possible via this setup. To achieve a higher surface quality, additional cleaning procedures were performed with the crystal mounted on top of a standard sample plate with integrated window, enabling heating to ~ 1250 K via electron bombardment in the preparation chamber. The sample was cleaned under UHV conditions by the following standard procedure [115-117]:

- **Ar⁺ ion sputtering** ($p(\text{Ar}) = 4.0 \cdot 10^{-6}$ mbar; $E(\text{Ar}^+) = 1$ keV) at ~ 800 K for 10 – 60 min

- **Annealing** of the sample for 10 – 20 min at ~ 1000 K for the VT sample holder setup and 2.5 – 3 min at ~ 1250 K for the standard sample plate
- **Oxidation** ($p(\text{O}_2) = 2.0 \cdot 10^{-6}$ mbar) at ~ 1000 K for 10 min
- **Annealing** of the crystal; the parameters are identical to the ones of the other annealing step.

As both annealing temperatures are lower than those typically used in the literature [115-117], additional cleaning and improvement of the surface reconstruction was achieved via oxidation / reduction cycles at sample temperatures between 600 K and 700 K by dosing oxygen and hydrogen ($p(\text{O}_2) / p(\text{H}_2) = 5.0 \cdot 10^{-8} - 4.0 \cdot 10^{-6}$ mbar). The surface condition of the Rh(110) sample was periodically monitored using SEM, AES and LEED (discussed in detail in Chapter 5.3). Additional information on the quality of the surface was derived from the observation of oxygen-induced superstructures via LEED. For a well-prepared clean Rh(110) surface a sequence of ordered phases (reconstructions) form upon increasing oxygen coverage at ~ 600 K: (2x2)_{p2mg}, c(2x6) and c(2x8); the formation of the latter indicates a very good surface quality (compare Chapters 5.2 and 5.3).

The dosage of oxygen and hydrogen during in-situ observation with the electron microscope lead to the observation of reduction fronts on the Rh(110) surface (see Chapter 5.4). During the corresponding experiments the sample was heated to ~ 610 K, while gas dosage was performed through the retracted dosing nozzle (exit of the nozzle roughly 40 mm away from the sample; position 55 of the linear transfer scale bar).

Preparation of the Si(100) and Si(111) surfaces

The preparation of silicon single crystals with the surface orientations (100) and (111) was performed by resistive heating in UHV. If not mentioned otherwise, fresh, i.e., unexposed samples were used, which were treated according to the following procedure:

- **Heating of the sample** for at least 30 min (typically for **one night**) at a temperature of ~ **1010 K** (heating current: 0.8 A)
- **Flashing of the sample** (5 times; ~ 5 s each) at a temperature of ~ **1200** and ~ **1210 K** for Si(100) and Si(111), respectively (heating current: 1.5 A)

- **Flashing of the sample** (5 times; ~ 5 s each) at a temperature of ~ 1330 and ~ 1340 K for Si(100) and Si(111), respectively (heating current: 2.4 A)
- **Flashing of the sample** (5 times; ~ 5 s each) at a temperature of ~ 1430 and ~ 1450 K for Si(100) and Si(111), respectively (heating current: 3.5 A)
- **Flashing of the sample** (5 times; ~ 5 s each) at a temperature of ~ 1500 and ~ 1510 K for Si(100) and Si(111), respectively (heating current: 4.2 A)
- **Quick reduction of the heating current to 1.5 A** after the last flashing step
- **Stepwise reduction of the heating current from 1.5 to 0 A** (~ 0.1 A every 10 s). Thereby, the sample temperature is reduced from ~ 1180 to ~ 600 K for Si(100) and from ~ 1170 to < 500 K for Si(111).

The denoted sample temperatures were measured via a pyrometer in the preparation chamber (see above) during one of these preparation procedures. The resulting surface quality was mainly monitored using LEED and SEM, and partially via AES. If any obvious problems with the surface condition were observed (e.g., weak and diffuse reflexes in LEED), the described preparation procedure was repeated; thereby, the time for the first step (heating at ~ 1010 K) was reduced.

The surface reconstruction of the Si(100) and Si(111) surface was considered to be good, if sharp and intense reflexes of a (2x1) and (7x7) pattern, respectively, could be observed via LEED, as it is visible in the images in Fig. 3.21.

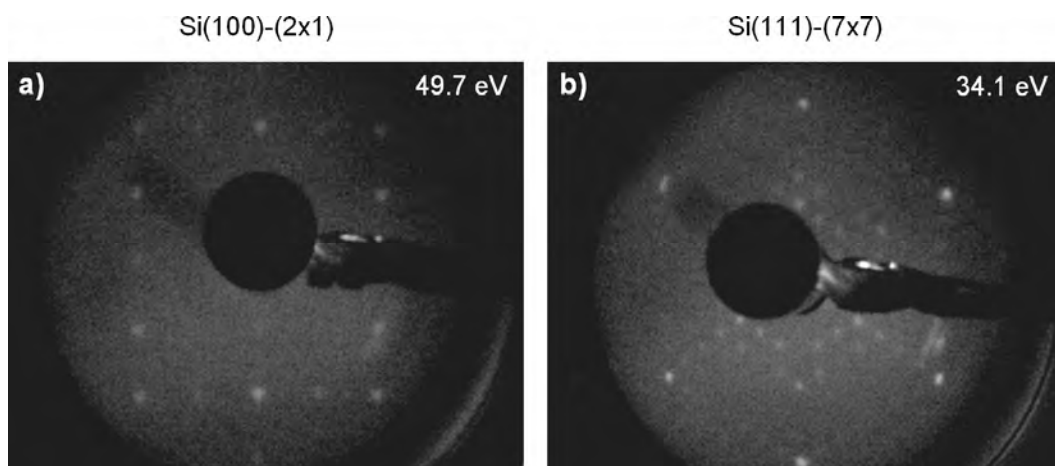


Fig. 3.21: LEED images of a) (2x1)-reconstructed Si(100) and b) (7x7)-reconstructed Si(111).

SEM images

The SEM images were acquired with the software *SmartSEM* (Zeiss / V 05.00.08). If not stated differently, they are reproduced with minor contrast and brightness adjustments. Beam current, acceleration voltage and sample pitch (plane sample: surface normal parallel to electron-beam; tilted sample: 25° between surface normal and electron-beam) applied for the acquisition of each image are denoted in the corresponding figure captions. Typical image acquisition times for the SE micrographs shown are 2.7 min. In the case of in-situ observations of rather rapid processes (e.g., the propagation of reduction fronts in Chapter 5.3) a higher scan speed and thus a faster image acquisition time of 40 s was applied, resulting in a slightly reduced signal-to-noise ratio of the corresponding images.

AE spectra, SAM images and Auger line scans

For these measurements techniques, the sample had to be tilted (25° between surface normal and incident electron-beam) and an electron-beam with a primary beam voltage of 15 kV and a beam current of 3 nA was applied.

Local Auger spectra were acquired with the software *EIS* (Omicron / V 2.4.16). If not stated differently, they were measured via electron irradiation of a spot with the focused electron-beam. Adjustment of the measurement position was performed via the software *ISEM* (Omicron / V 1.0.2.2).

In some cases a different scan method was applied: instead of only one spot, a certain surface area was repeatedly scanned while the AE spectrum was acquired (“area scan”). Thereby, the electron dose necessary for acquiring the spectrum was spread over the whole scanned area, i.e., the local electron dose was reduced and thus electron induced effects should also be minimized.

Regardless of the applied scan method, all measured spectra were processed via *Igor Pro* (WaveMetrics / V 5.02). If not described differently, they are shown without any modifications (e.g., smoothing). In the case of several spectra being plotted in one frame, an offset was applied to the count-rate values of each spectrum in order to improve visibility.

SAM images were acquired via the software *ISEM* by the predefinition of peak energy, background energy¹ and dwell time (dwell time for each point and each energy). The respective values for each image are given in the corresponding figure captions. The measurement position and magnification level of the SAM image could be directly controlled by the SEM (via *SmartSEM*).

¹ Background energy describes the energy position of the subtracted background signal.

Auger line scans were acquired in a similar way, also via the software *ISEM*. The definition of the measurement position was realized in the same software in a previously scanned electron microscopy image, acquired via *SmartSEM* (menu: “File/New/ISEM/SED Image”). The values for the applied peak energy, background energy, dwell time (dwell time for each point and each energy) and the number of measured points for each scan are denoted in the corresponding figure captions. Auger line scans for multiple elements depicted in one figure were acquired during the same measurement (to guarantee position stability). All spectra were processed via *Igor Pro* and are shown without any modifications (e.g., smoothing). The x-axis shows the respective distance from the starting point of the line scan.

Other typical parameters used for the acquisition of AE spectra, SAM images and Auger line scans are given in the appendix to Chapter 3.

LEED measurements

Low energy electron diffraction was mainly performed to determine the long range atomic order and hence to obtain an important characteristic of the specimen quality. The corresponding measurements were performed with the sample attached to the manipulator of the preparation chamber (the corresponding manipulator settings can be found in the appendix to Chapter 3). The beam energies that were applied to generate the LEED patterns are denoted in the corresponding images.

Images of LEED patterns shown in this work were recorded by a commercial digital camera (*PowerShot G3 / Canon*) or a CCD video camera (*CSB-175 / Framos*). The resulting pictures (except the ones in Fig. 3.21) were aligned according to the setup of the optics, with the electron-gun mounting utilized as an orientation feature (setup: $\sim 5^\circ$ clockwise rotation between the electron-gun mounting and the z-axis of the manipulator). From the LEED images of the Rh(110) surface (compare Chapter 5.3) the orientation of the crystallographic axes of the sample was determined.

Typical measurement parameters used for LEED are denoted in the appendix to Chapter 3.

QMS measurements

The QMS measurements in Chapter 6.4.2 were performed in the preparation chamber during the dosage of iron pentacarbonyl with a background pressure of $3.0 \cdot 10^{-7}$ mbar. A secondary electron multiplier voltage of 2150 V and a scan speed of 0.2 s was applied.

STM measurements

Scanning tunneling microscopy was performed with a commercial tungsten tip (purchased from Omicron). The applied tunneling parameters are denoted in the corresponding figure captions.

EBID experiments

If not stated otherwise, all EBID experiments were performed at room temperature on a plane sample with a beam current of 400 pA and a primary beam energy of 15 kV. Some of the experiments presented in Chapter 4.3.2 (“Influence of the primary beam energy”) and Chapter 6.3 were performed with beam energies of 8 or 3 kV. If not denoted differently, the background pressure of the precursor in the chamber was adjusted to $3.0 \cdot 10^{-7}$ mbar for iron pentacarbonyl and $1.0 \cdot 10^{-8} - 2.0 \cdot 10^{-8}$ mbar for ethene.

The EBI deposits presented in this work were mainly generated via the *Elphy Quantum* lithography attachment (compare Chapter 3.2; writefield size: $(2 \mu\text{m})^2$). The step sizes and electron doses specified in the software are summarized in Table 3.3, while the total electron doses applied for each structure are given in the corresponding figure captions or during the description of the respective experiments. Area structures with the shape of a square were irradiated in the “meander” mode, while for circles the “circular” mode was activated (compare Chapter 3.2).

Some additional EBID experiments were performed via the image acquisition mode of the SEM (under control of the *SmartSEM* software). The respective exposure parameters are denoted in the corresponding chapters.

	Ethene	Iron Pentacarbonyl
Area Step Size (S_A)	16 nm	16 nm
Area Dose (D_A)	0.5 C/cm ²	1.33 C/cm ²
Line Step Size (S_L)	5 nm	5 nm
Line Dose (D_L)	1.5 $\mu\text{C}/\text{cm}$	4 $\mu\text{C}/\text{cm}$
Dot Dose (D_D)	0.05 nC	0.12 nC

Table 3.3: *Lithographic parameters for EBID experiments with the Elphy Quantum software.*

Low temperature EBID experiments on Si(100)

The low temperature EBID experiments presented in Chapter 6.4.3 were performed by cooling the sample with gaseous nitrogen to ~ 200 K. The nitrogen gas flow through the cryostat was adjusted by the regulation valve at the Dewar vessel (opened by roughly seven turns) and the valve in front of the rotary vane pump (~ 13.0 mm). The temperature control was realized by a PID controller in combination with the heater element integrated in the cryostat (compare Chapter 3.1.2).

The applied EBID parameters were identical to the above described ones (experiments at room temperature). The applied parameters for the PID controller are given in the appendix to Chapter 3.

EBL experiments on PMMA

The electron-beam lithography experiments in Chapter 4.2.1 were performed with a 100 nm thick PMMA (polymethyl methacrylate) layer on a silicon support. A 10 kV electron-beam with a beam current of 200 pA was applied for the generation of the patterns.

The *Elphy Quantum* lithography attachment was used for the fabrication of the structures (compare Chapter 3.2; writefield size: $(100 \mu\text{m})^2$). The step sizes and electron doses specified in the software are listed in Table 3.4. The total electron doses applied for the generation of each structure are given in the corresponding figure captions or during the description of the experiments.

The development of the sample was performed by a developer solution, consisting of a 3 : 1 mixture of methyl isobutyl ketone (MIBK) and isopropanol (IPA), and a pure IPA stopper solution (both supplied by Raith), according to the parameters given in Chapter 4.2.1.

Area Step Size (S_A)	20 nm
Area Dose (D_A)	100 $\mu\text{C}/\text{cm}^2$
Line Step Size (S_L)	10 nm
Line Dose (D_L)	300 pC/cm
Dot Dose (D_D)	0.1 pC

Table 3.4: Lithographic parameters for the electron-beam lithography in Chapter 4.2.1.

Determination of the lateral size of deposits and surface features

If not stated otherwise, the determination of the lateral size of the structures was performed via the software *analySIS* (Soft Imaging System / V3.2): two lines were positioned by eye and the software determined their distance according to a size information incorporated in the image. To increase the accuracy of the value, the measurement was repeated multiple times and a mean value was estimated.

In the case of structures that exhibited a low contrast in the SEM compared to the rest of the surface (e.g., the carbonaceous deposits in Chapter 4.3) the measurement was performed via the software *ImageJ* (National Institutes of Health USA / V 1.40g) in combination with a suitable plug-in (delivered by Omicron). Via this software it is possible to generate gray value profiles of defined sections of the SEM image. The lateral size of specific features was determined by averaging several line scans across the corresponding structure; in the resulting profile plot the full width of the structure was measured (distance on the x-axis). When the lateral size was determined according to this method, it is specially denoted in the text.

Estimation of the deposit thickness

The estimation of layer thicknesses d was performed using the modified straight-line approximation model according to Equation 4.4, with the intensity of the electrons from the substrate I_B , the intensity observed from a pure substrate I_B^∞ (e.g., the clean surface before the EBID experiment), the attenuation length of electrons with energy E_B in the overlayer material A ($\lambda_{AL}^A(E_B)$) and the angle of emission of the electrons with respect to the surface normal θ (35° for the applied instrument) [118].

$$I_B = I_B^\infty \cdot \exp\left(-\frac{d}{\lambda_{AL}^A(E_B) \cdot \cos \theta}\right) \quad (4.4)$$

This model is supposed to be reliable, if the surface coverage of A is higher than one monolayer and if the intensity of the substrate peak I_B can be measured sufficiently accurate (I_B at least 5 % of I_B^∞). The attenuation length $\lambda_{AL}^A(E_B)$ was calculated according to a semi-empirical equation developed by Cumpson and Seah (Equation 15 in reference [118]).

Quantitative analysis of Auger spectra

Auger peak intensities, i.e., the areas of the Auger peaks, were determined after a linear background subtraction. The determination of the composition of the generated deposits (in %) was performed via a comparison of the carbon and oxygen peak intensities with reference values that were self-determined for both elements and are described in the following.

For carbon the reference value was acquired from a spectrum of a thick carbon layer on a SiO_x (300 nm) / Si support; note, that the substrate signals were in this case completely damped due to the overlying carbon. In some cases the estimated deposit thickness (see above) has to be taken into account for the carbon reference value; this was performed via a consideration of the peak intensity as a function of depth, i.e., the reference value was calculated for a pure carbon layer with the corresponding thickness (according to Equation 4.4).

For oxygen no measured reference value was available. Therefore, a reference value was estimated from the iron oxidation experiment presented in Chapter 5.9. Based on the damping of the iron signal at 647 eV (due to the oxidation), the thickness of the adsorbed oxygen layer was determined (according to the model described above). The resulting thickness d was used to calculate a reference value for a “pure oxygen specimen” I_A^∞ according to Equation 4.5 (based on the modified straight-line approximation model), with the intensity of the electrons from the overlayer I_A , the attenuation length of electrons with energy E_A in the material A ($\lambda_{AL}^A(E_A)$) and the angle of emission of the electrons with respect to the surface normal θ (35° for the applied instrument) [118]. The attenuation length $\lambda_{AL}^A(E_A)$ was again calculated according to Equation 15 in reference [118].

$$I_A = I_A^\infty \left[1 - \exp\left(-\frac{d}{\lambda_{AL}^A(E_A) \cdot \cos \theta}\right) \right] \quad (4.5)$$

A major problem of this consideration is the assumption that the oxygen is situated only on top of the iron deposit. Additionally, electron-beam induced effects during the measurement (e.g., electron induced desorption of oxygen) cannot be completely ruled out. The determination of the oxygen content of the deposits should therefore be considered as a rough approximation.

The reference values determined for carbon and oxygen are given in the appendix to Chapter 3.

4 Testing the Instrument: first EBID experiments

4.1 Introduction

Prior to studying the electron induced deposition of metal structures it was important to validate the possibilities of the modified *Multiscan LAB* system. Especially the capabilities of the lithographic attachment (i.e., control of the electron-beam position on the surface) to generate arbitrarily shaped structures and the functionality of the modified instrument in terms of the EBID process had to be validated. Therefore, two projects were conducted:

I) A widely used method for the local generation of nanostructures is electron-beam lithography (EBL). In this top-down approach a position controllable electron-beam from a SEM or TEM can be used to irradiate an electron-sensitive resist, which is afterwards developed in a solvent. The basic principles of EBL are explained in Chapter 4.2.1, while a corresponding experiment with the applied instrument is described and discussed in Chapter 4.2.2.

II) Since its discovery as an unintended side effect in electron microscopy [7], the generation of carbon deposits has become the most investigated product for EBID [119]. Different types of hydrocarbon precursors, ranging from n-alkanes like methane [66, 67] and propane [120] to ketones like acetone and cyclohexanone [93], have been used; for a detailed overview of the studied compounds the reader is referred to reference [40]. The first EBID experiments performed during the work at hand aimed at the generation of carbonaceous deposits with the precursor ethene (ethylene; C_2H_4), which has been already utilized for EBID by Guise et al. and Schirmer [121, 122]. Some important parameters of this molecule are described in Chapter 4.3.1. As specimens, silicon single crystals with the surface orientation (111) were applied. The corresponding experiments are described and discussed in Chapter 4.3.2.

4.2 Electron-beam lithography with PMMA

Since the introduction of the first electron-beam lithography machines (based on the scanning electron microscope) in the late 1960s [123], this method has become an important technique of modern electronics industry. Mainly used for the generation of photomasks and the manufacturing of special high resolution devices, it can also be combined with other methods like, e.g., metal deposition and subsequent lift-off to fabricate metallic nanostructures. One of the major drawbacks of this method for large scale industrial applications is the low

throughput; recent developments in the field of multi-beam systems might be able to overcome this problem [124].

4.2.1 Basic principles of lithography with resist samples

The technique of EBL uses an electron-beam to locally expose an electron-sensitive resist, thus transferring energy in a desired pattern in the resist film [123]. The main steps of the process are depicted in Fig. 4.1.

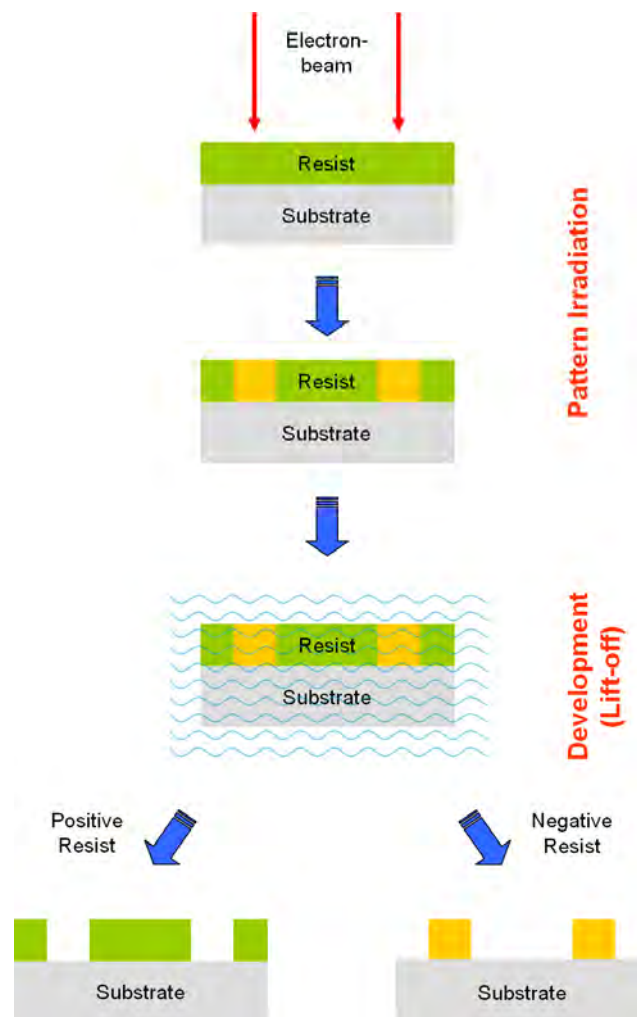


Fig. 4.1: Scheme of the electron-beam lithography (EBL) process. The resist covered substrate is locally irradiated with an electron-beam. Development of the sample in a liquid leads to a dissolution of the exposed areas in the case of a positive resist, while for a negative resist the non-exposed material is removed.

Prior to the irradiation, the resist film is deposited on a supporting substrate with a defined thickness, which is typically prepared via spin-coating. Local irradiation with the

electron-beam (see top part of Fig. 4.1) generates a cascade of secondary electrons, also with relatively low energies (due to inelastic collisions), which form free radicals and radical cations in the resist. Deactivation of these intermediate species through fragmentation or reaction with the matrix is the basis for the resulting chemical change [125]. Depending on the type of the actual resist this can either occur through main chain scission (positive resist) or interchain linkages, which generate a cross-linked network (negative resist). The electron exposure is followed by the development of the sample, which is usually realized in a solution (developer). Depending on the utilized resist type the irradiated areas are more or less soluble in the developer, leading to the dissolving of the material either in the exposed (positive resist) or non-exposed regions (negative resist), respectively (lift-off; see middle part of Fig. 4.1).

More commonly used are positive resists, since they exhibit a better process control for small geometries. Negative resists on the other side have the advantage of almost no unintended removal of material (material only removed in desired areas, i.e. non-exposed areas), which cannot be completely ruled out for positive resists; problems are caused in this case by soluble residues in the exposed area, which lead to swelling of the structures during the development. Parameters used to define the performance of a resist material for EBL are resolution (achievable lateral size of the structures) and sensitivity (response of the resist to electron irradiation and the efficiency of the visualization of the resulting radiochemical conversions); usually, these factors develop contrary, i.e. a resist with a low electron sensitivity enables the generation of structures with a high resolution [123].

Theoretically, the resolution of EBL is only limited by the diameter of the electron-beam (few nanometers). However, similar to EBID is the electron interaction volume influenced by several factors, mainly the scattering of primary electrons in the irradiated material. Fig. 4.2 shows Monte Carlo simulations of electron trajectories in a typical EBL specimen based on a 1 μm thick resist on an infinitely thick silicon substrate; the shape and density of the resulting distribution varies strongly with the applied energy of the primary electrons. Two types of scattering occur during the irradiation and contribute to the calculations in Fig. 4.2: forward scattering and backscattering. Forward scattering is the result of multiple small angle scattering events ($< 90^\circ$) in the resist material, which are spreading the electrons as they penetrate the surface and lead to an increase of the effective beamwidth at the bottom of the resist [123, 126]. This can be avoided by the utilization of thin resists ($< 0.1 \mu\text{m}$) and high energy electrons ($> 50 \text{ kV}$). Penetration of the electrons through the resist and into the substrate leads to large angle scattering events, and therefore to the generation of

backscattered electrons (BSEs) with a distribution that is also depending on the atomic number and density of the supporting material (compare Chapters 2.1 and 2.6). These BSEs generate additional secondary electrons (by inelastic collisions) and return into the resist at a significant distance from the incident point of the primary electron-beam, causing additional resist exposure. This unintentional resist irradiation is commonly referred to as the proximity effect [123], similar as for the unintended deposition via electron scattering described for EBID (see Chapter 2.7). It is especially problematic for patterns with structures in close proximity, where the electron dose that a feature receives is affected by electrons scattering from other features nearby. To avoid this problem, thin substrates can be used as a support in order to reduce the interaction volume with the primary electrons [124]. Due to the described scattering processes and the range of the secondary electrons in the sample material (few nanometers), the minimum resolution attainable via EBL is limited to > 10 nm [124, 125].

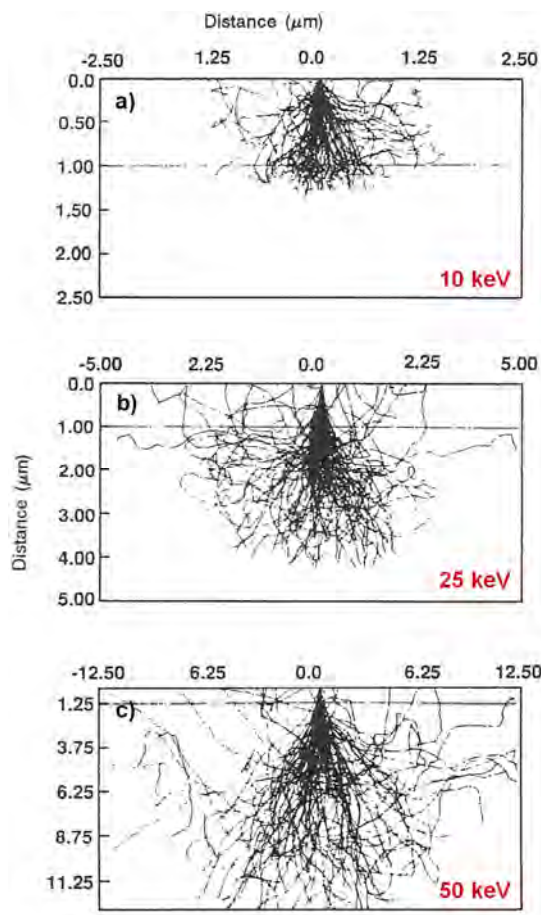


Fig. 4.2: Monte Carlo simulated trajectories of 100 electrons with different energies, penetrating a 1 μm thick resist (above the horizontal line) on an infinitely thick silicon support. The figure was adapted from reference [126].

For the experiments described in Chapter 4.2.2 a positive resist sample consisting of a 100 nm thick layer of polymethyl methacrylate (PMMA), with an average polymer weight of 950,000 u, on a silicon support was applied. PMMA (see left side in Fig. 4.3) was one of the first polymers recognized to exhibit sensitivity to electron-beam radiation and represents also the most frequently used resist in EBL [125]. It is synthesized by a radical-initiated polymerization of commercially available methyl methacrylate monomer. The main advantages of this positive resist is a high resolution, ease of handling, a wide range of applications, a good availability and low costs. One drawback of the material is its relatively low sensitivity, requiring therefore higher exposure doses and thus makes it unprofitable for large scale industrial applications due to longer irradiation times [127].

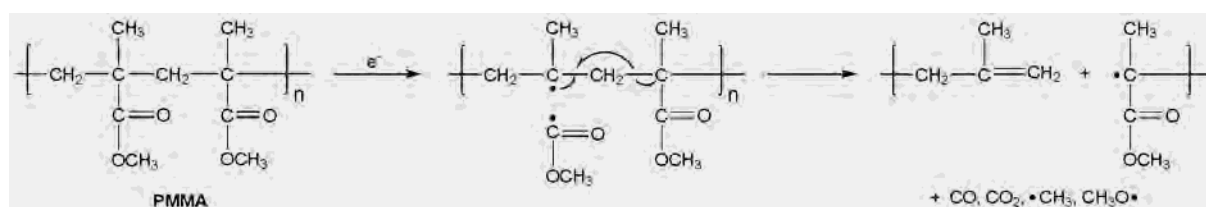


Fig. 4.3: Mechanism of electron induced chain scission in PMMA [127, 128].

The supposed main-mechanism for the electron induced chain scission in PMMA is depicted in Fig. 4.3. According to literature, the initial radiochemical event appears to be a homolysis of the main-chain carbon to carbonyl bond (also a homolysis of the carbon to oxygen σ -bond is possible). The resulting main-chain radical undergoes rearrangement through β -scission to cleave the chain and generate an acyl-stabilized, tertiary radical. Additionally, carbon monoxide, carbon dioxide and methyl and methoxyl radicals are generated [127, 128]. The resulting fragments can be preferentially dissolved by a suitable developer or are desorbing volatilyly (e.g. CO, CO₂). In the experiments in Chapter 4.2.2 this was performed with methyl isobutyl ketone (MIBK). Since pure MIBK is too strong for the development of PMMA (removal of some of the unexposed resist) it was diluted with isopropanol (IPA) to a ratio of 3:1. The irradiated sample was removed from the instrument and dipped into this mixture for 30 s. Immediately afterwards it was dipped into a stopper solution of pure isopropanol for 15 s to remove the developer. Re-entry into the instrument enabled the characterization of the irradiated patterns via SEM.

4.2.2 Results and discussion

Fig. 4.4 shows SEM images of two different patterns, which were irradiated on a PMMA sample and developed afterwards. The corresponding templates are described in the following:

- **Template I (Fig. 4.4 (a))** consists of line and area structures. The lines (located at the top of the template) are arranged as letters and were irradiated with an electron dose of $6.0 \mu\text{C}/\text{cm}$. Below the letters were two ellipses, each with a diameter of $11.8 \mu\text{m}$ from left to right and $12.8 \mu\text{m}$ from bottom to top; they were both irradiated with an electron dose of $2.0 \text{mC}/\text{cm}^2$. Located at the bottom of the template are eleven rectangles ($10 \mu\text{m} \times 4 \mu\text{m}$), aligned in two rows (five in the top row, six in the bottom row). The rectangles in the bottom row were all irradiated with an electron dose of $1.0 \text{mC}/\text{cm}^2$, while the electron dose for the ones at the top row was increased from the right ($2.2 \text{mC}/\text{cm}^2$) to the left ($3.0 \text{mC}/\text{cm}^2$).
- **Template II (Fig. 4.4 (b))** consisted of a (5x5) dot matrix. The electron dose was increased by multiplication with a constant factor of 1.5 from left to right and 2.0 from bottom to top, resulting in a lowest electron dose of 0.1 pC for the bottom left dot and a highest one of 8.1 pC for the top right one.

The features in both patterns (Fig. 4.4 (a) and (b)) appear bright in the SEM after the development. This is interpreted as due a higher SE yield of the underlying silicon support in the irradiated areas compared to the polymer covered regions.

A blow-up of the letters of Template I (Fig. 4.4 (a)) is depicted in Fig. 4.4 (c); separated lines of the text feature appear spatially well defined with a line width of roughly $0.3 \mu\text{m}$. At locations where multiple lines of the letters merge the structures appear significantly broader and less defined. This is mainly attributed to the proximity effects described in the previous Chapter, i.e. exposure of regions close to the irradiated structures due to electron scattering in the sample material [126]. As described before, this effect is especially problematic for structures in close proximity, where the unintendedly irradiated areas overlap, leading locally to a higher electron dose and therefore to the removal of additional resist material, as visible for the structures in Fig. 4.4 (c). The edges of the line structures exhibit also weak vibrational features, which are supposed to be the result of electron-beam vibrations during the irradiation process.

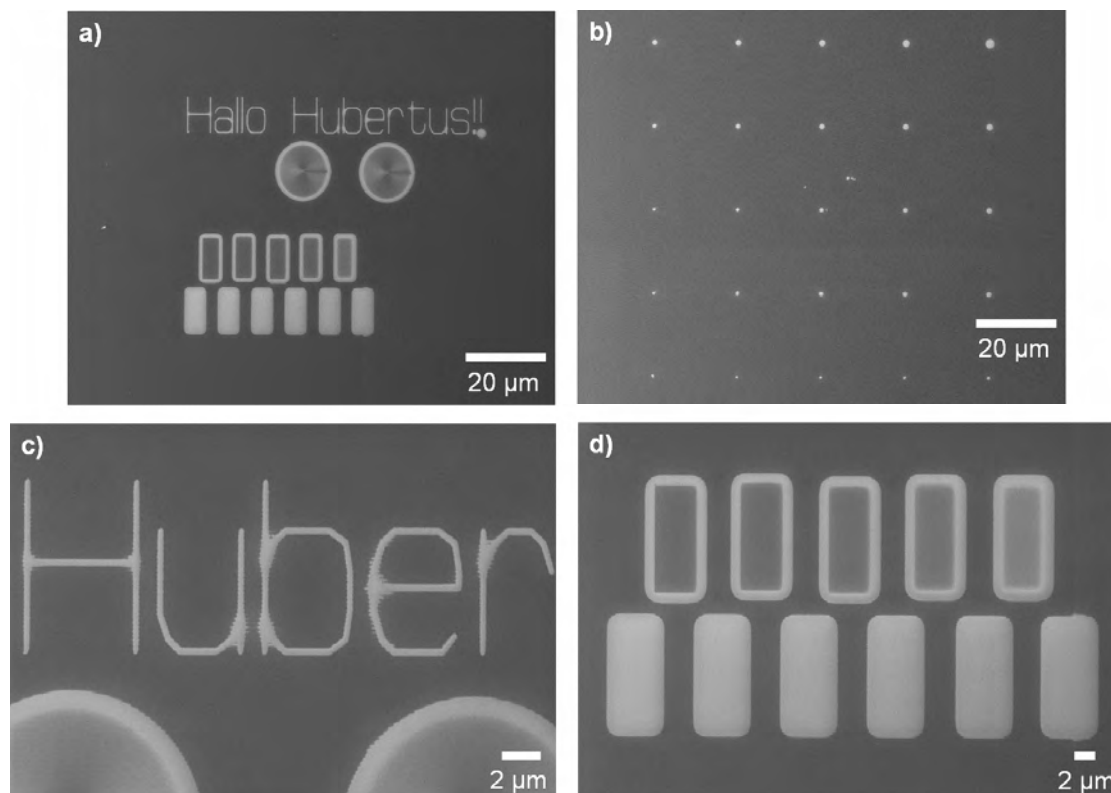


Fig. 4.4: Structures generated by local electron irradiation of PMMA and subsequent development. a) Pattern generated by irradiation of template I. b) Pattern generated by irradiation of template II. c) Blow-up of the letters in (a). d) Blow-up of the rectangles in (a).

Fig. 4.4 (d) displays an image of the irradiated rectangular areas in the lower part of Template I (see Fig. 4.4 (a)). In this case the morphology of the structures is different in the top row compared to the bottom row: the six rectangles at the bottom appear all uniformly bright, while the five in the top row consist of a dark rectangle in the center surrounded by a bright area with rounded corners. For the upper ones it is also observed, that the brightness of the central region is decreasing from right to left. These differences in the morphology and brightness of the structures observed in the SEM are attributed to variations in the applied electron dose and the resulting distribution of the electron density in the resist material. The six rectangles in the bottom row were all irradiated with an identical electron dose of 1.0 mC/cm^2 , resulting in a similar contrast and shape of the deposits. The size of the structures ($11.7 \mu\text{m} \times 5.5 \mu\text{m}$) is larger than the one expected from the template ($10 \mu\text{m} \times 4 \mu\text{m}$), which is attributed to the unintended exposure of PMMA in the direct surrounding of the irradiated area due to electron scattering (proximity effect). In the top row the applied electron dose was stepwise increased from the right (2.2 mC/cm^2) to the left (3.0 mC/cm^2). The overall size of the rectangles appears to be rather independent ($\sim 12.1 \mu\text{m} \times 6.0 \mu\text{m}$) of the electron dose,

while the size of the dark central rectangles is slightly increasing with an increase of the applied dose (from $9.8 \mu\text{m} \times 3.6 \mu\text{m}$ for the right one to $10.3 \mu\text{m} \times 4.0 \mu\text{m}$ for the left one). Since the dimensions of the latter fit quite well to the ones of the rectangles in the template, it is obvious that these regions correspond to the originally exposed areas. Therefore, the dark central rectangles can be attributed to primary electron irradiation, while the bright regions in the surrounding area are generated due to proximity effects. An explanation for the different contrasts of the exposed areas is given by the literature: when exposed to more than ten times the optimal electron dose, PMMA is starting to crosslink, forming effectively a negative resist, which is not removed by subsequent developing. Obviously, this is the case for the irradiated areas of the rectangles in the top row of Template I, while the electron density in the direct surrounding (due to proximity effects) is too low for the crosslinking, which results in a positive resist behavior [123]. A similar morphology can also be observed for the two circles in Template I (see Fig. 4.4 (a)). The small variations in the size of the central rectangles in the top row of Fig. 4.4 (d) can be attributed to the electron distribution in the surrounding of the exposed area (e.g., see the Monte Carlo simulations in Fig. 4.2). With an increasing distance from the incident point of the primary electron-beam is the electron density steadily decreasing. Therefore, an increase of the electron dose applied to the exposed area is directly associated with a further reaching cross-linking of the resist material, visible by the increasing size of the central rectangles in the top row of Fig. 4.4 (d)..

In the case of the dot matrix in Fig. 4.4 (b) (generated by the irradiation of Template II) it can be observed that the lateral size of the structures is significantly increasing with an increase of the applied electron dose; the dot with the lowest dose (bottom left; 0.1 pC) exhibits a size of $\sim 0.75 \mu\text{m}$, while the one with the highest (top right; 8.1 pC) has a diameter of $\sim 2.52 \mu\text{m}$. Similar as for the structures in Template I this effect is attributed to electron scattering in the sample material (proximity effects); an increasing electron dose leads also to an increasing number of scattered electrons and therefore to a higher electron density in the region surrounding the primary electron impact. Subsequent removal of the exposed material leads to the observed increase of the dot size.

Summarizing the data presented in this chapter, it can be stated that the lithographic attachment of the applied instrument is capable of generating arbitrarily shaped structures at defined positions. Via electron-beam lithography on a PMMA layer it was possible to generate spatially well-defined line features with a size of $0.3 \mu\text{m}$ and dots with a minimum size of $\sim 0.75 \mu\text{m}$. The lateral extent of the generated structures is strongly influenced by the scattering of electrons in the sample material (proximity effects). Furthermore, variations of

the applied electron dose have a strong influence on the morphology (crosslinking of PMMA at higher doses) and size of the resulting features (increasing proximity effects with increasing dose).

4.3 EBID of carbonaceous structures

After successfully testing the lithographic attachment, it was necessary to combine it with the self-constructed dosage system and therefore to perform electron-beam induced deposition in the applied apparatus. For these initial experiments the compound ethene was used for the generation of carbonaceous deposits. The precursor was chosen for several reasons: I) it is easy to handle (e.g. volatile), II) it is cheap and readily available and III) the utilization of hydrocarbons for the targeted generation of nanostructures via electron irradiation is known since the 1970s [129] and thus well studied in literature [66, 67, 93, 120, 121]. An application for the local deposition of carbon nanostructures is, e.g., the fabrication of masks for subsequent ion milling [130].

For the experiments described in this chapter, silicon single crystal samples with the surface orientation (111) were applied. A detailed description of this surface is given in Chapter 6.2.

4.3.1 Characterization of the precursor

Ethene (C_2H_4) is under atmospheric conditions a colorless gas of slightly sweet smell [131]. It is the simplest representative of the unsaturated hydrocarbons and belongs to the group of the alkenes. Fig. 4.5 shows the structural formula (a) and a ball & stick model (b) of C_2H_4 . The dominating structural element of the planar molecule, which is also mainly responsible for the chemical reactivity, is the double bond connecting the two carbon atoms.

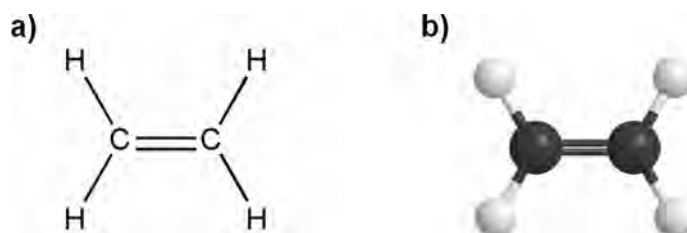


Fig. 4.5: a) Structural formula and b) ball & stick model of ethene (C_2H_4).

Ethene is obtained from natural gas or coal gas using fractional distillation followed by steam cracking; a different source is the dehydration of ethanol [132]. In industrial applications, it is important for the synthesis of other chemical compounds, e.g. oxirane (ethylene oxide) and vinyl acetate, and for the manufacturing of polymers such as polyethylene (polyethene, polythene, PE), polyvinyl chloride (PVC), polystyrene (PS) or polyvinyl acetate (PVA). A different application field is the utilization in greenhouses, as it accelerates the ripening of crops and fruits.

The most important physical properties of C_2H_4 are summarized in Table 4.1.

Molar Mass	28.05 g/mol	Melting Point	104 K
Rel. Density (to Air)	0.975	Boiling Point	169 K
Bond Length C-C	133 pm	Ignition Temp.	698 K
Bond Length C-H	108 pm		

Table 4.1: Physical properties of ethene (C_2H_4) [131, 132].

For EBID, ethene has been applied by Guise et al. for the deposition of hydrogenated carbon structures with variable thicknesses on Si(100) [121]; additionally, the effect of post-deposition annealing was studied. Further experiments for EBID with ethene on Si(111) and Si(100) were performed by Schirmer [122]; in this case also the generation of carbonaceous structures with the aromatic compound benzene was studied.

4.3.2 Results and discussion

In this chapter, some important results for the electron-beam induced deposition of carbon structures via the precursor ethene will be presented. The chemical composition of the generated structures was not determined during these experiments. Guise et al. studied the composition of structures generated via EBID with ethene on Si(100) at room temperature [121]; via AES, XPS and TPD measurements the deposits could be characterized as an amorphous, hydrogenated carbon film (C_yH_x). Heating this film to 720 K leads to a dehydrogenation process and to the production of additional C-C bonds, while at 900 – 950 K the structure is converted into SiC. Furthermore, it was postulated that the electron-beam induced deposit contains a higher fraction of multiple C-C bonds (C=C, C≡C) compared to a

thermally-produced carbon film, as the latter shows a reduced thermal stability towards SiC formation. Based on these results, it can be assumed that the EBID structures presented in the following consist of an amorphous layer of hydrogenated carbon.

Deposition of arbitrarily shaped structures

To achieve the main goal of arbitrarily shaped deposits via EBID, control of the electron-beam has to be granted to the lithographic attachment. Fig. 4.6 shows two examples of structures deposited with the precursor ethene (background pressure in the chamber $2.0 \cdot 10^{-8}$ mbar). The deposit in Fig. 4.6 (a) was fabricated using the emblem (logo of the Friedrich-Alexander-University Erlangen-Nuremberg) in Fig. 4.6 (b) as a template; the logo was imported in the *ELPHY Quantum* software and converted into a dot pattern via the *Image 2 Ascii* converter (Raith). The resulting deposit in Fig. 4.6 (a) appears dark in the SEM, which is attributed to the lower SE yield of carbon compared to silicon associated with the lower atomic number [48].

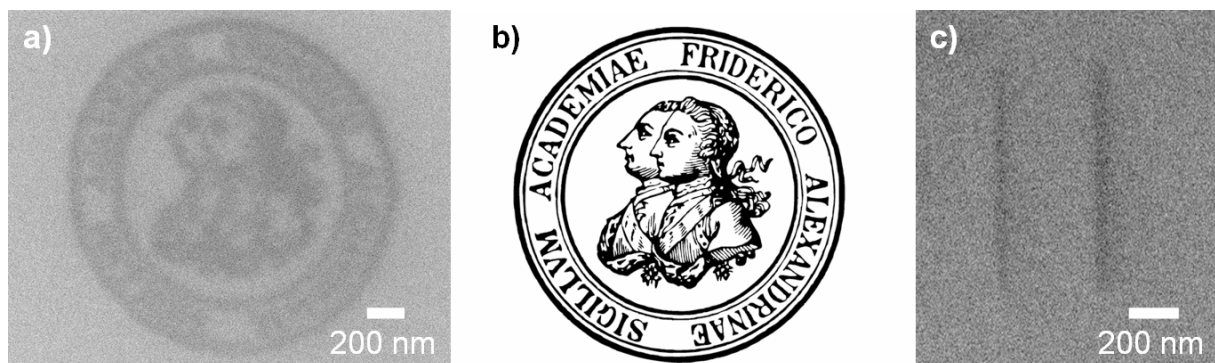


Fig. 4.6: EBI deposits generated with the precursor ethene on Si(111). a) Deposit, using the emblem in b) as template. The structure was generated by the irradiation of multiple dots with an electron dose of 0.1 nC each and a step size of ~ 12 nm. c) Two line structures deposited with an electron dose of 432 $\mu\text{C}/\text{cm}$ (left) and 864 $\mu\text{C}/\text{cm}$ (right). Contrast and brightness of the SEM images in (a) and (c) were strongly varied to improve visibility. ($U = 15$ kV; $I = 400$ pA; plane sample)

The overall shape of the emblem in Fig. 4.6 (a) is clearly recognizable, while individual features are hardly distinguishable. The latter is supposed to result from a too densely packed dot matrix in combination with a relatively high electron dose per dot; this leads to a partial overlap of deposited material, mainly due to the proximity effects described in Chapter 2.7, and therefore in a blurring of adjacent features in the pattern.

Fig. 4.6 (c) shows a micrograph of two carbon lines (template: each line 700 nm long), which were deposited with an electron dose of 432 $\mu\text{C}/\text{cm}$ (left) and 864 $\mu\text{C}/\text{cm}$ (right), respectively. Similar to the observations in Fig. 4.6 (a), the carbon lines exhibit a dark contrast in the SEM and are clearly distinguishable. The diameter of the left line could be estimated to ~ 70 nm, while the one of the right line is ~ 80 nm (values estimated via *ImageJ* (see Chapter 3.4)); this increase of the line width is attributed to differences in the applied electron dose and will be discussed in detail later in this chapter.

From the SEM images in Fig. 4.6 it is obvious that the lithographic attachment of the applied instrument can be used for the generation of arbitrarily shaped deposits via EBID. Caution has to be taken for the choice of the lithographic parameters, as the deposits resulting from each dot might overlap, leading to a blurring of certain features in the pattern (compare Fig. 4.6 (a)).

Influence of the primary beam energy

As it has been already described in Chapter 2.7, the size of the EBID structures is influenced by a manifold of parameters, e.g., the primary beam voltage U and hence the primary electron energy $E_{PE} = e \cdot U$. To study the corresponding effect on the carbon deposition process with C_2H_4 in more detail, two experiments were performed with different beam energies. The utilized template was identical in both cases and consisted of the following, vertically aligned letters:

FAU
Institut
fuer Physikalische
Chemie II

The size of the letters was decreased from the top row (height of letter “F” ~ 600 nm) to the bottom row (height of letter “C” ~ 100 nm) and therefore enables also to observe the resolution limit of the line deposition process in respect to the applied system and parameters. For both experiments a particular Si(111) sample was used, which had been already used for EBID before and was cleaned with parameters that differ from the standard procedure described in Chapter 3.4; the following data should therefore be considered as an explorative approach to the topic rather than a typical surface science experiment.

Fig. 4.7 shows two deposits that were both generated with a constant electron dose of $192 \mu\text{C}/\text{cm}$, a beam current of 400 pA and a background pressure of $1.0 \cdot 10^{-8} \text{ mbar}$, while the primary beam voltage was varied. Image acquisition of the resulting structures was performed with identical parameters ($U = 15 \text{ kV}$; $I = 400 \text{ pA}$; plane sample).

The deposits fabricated with a beam energy of 15 kV (Fig. 4.7 (a)) are laterally well defined and exhibit a line width of partly 67 nm (measured via *ImageJ* at letter “F” in the top row). Individual features of the template are clearly distinguishable, even in the second lowest row (height in the template $\sim 200 \text{ nm}$); in the bottom row the letters appear diffuse, which is attributed to the overlapping of deposited material due to the proximity effects described in Chapter 2.7.

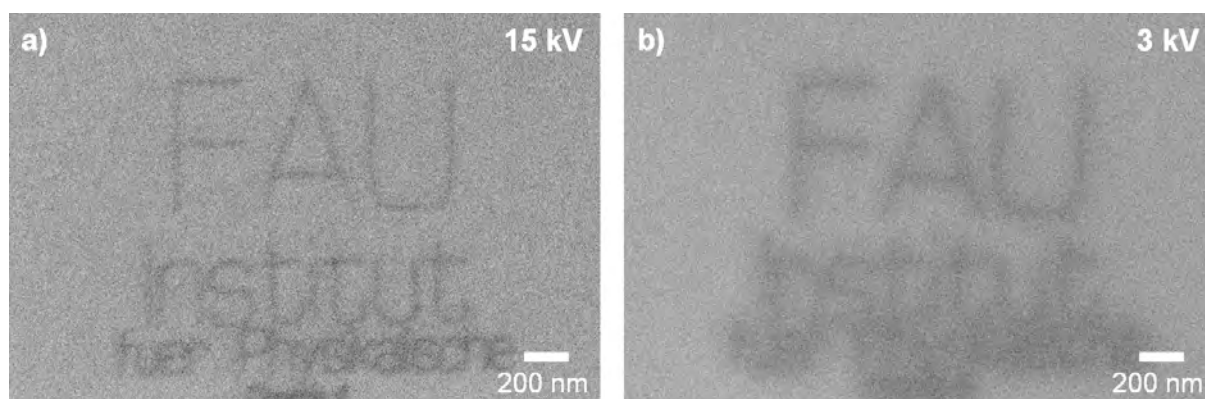


Fig. 4.7: Influence of the primary beam voltage on the deposition process. An identical pattern consisting of letters with a decreasing size from the top row to the bottom row was irradiated with the precursor ethene on $\text{Si}(111)$ with a) $U = 15 \text{ kV}$ and b) $U = 3 \text{ kV}$. In both cases a beam current of 400 pA , a background pressure of $1.0 \cdot 10^{-8} \text{ mbar}$ and an electron dose of $192 \mu\text{C}/\text{cm}$ was applied. Contrast and brightness of the SEM images were strongly varied to improve visibility. ($U = 15 \text{ kV}$; $I = 400 \text{ pA}$; plane sample)

On the other hand, the deposits generated with 3 kV (Fig. 4.7 (b)) appear significantly diffuser and less defined; a minimal line width of 105 nm could be determined (measured via *ImageJ* at letter “U” in the top row), while individual features of the pattern are only distinguishable in the two top rows (height in template $\sim 600 \text{ nm}$ and $\sim 400 \text{ nm}$, respectively). In the two bottom rows individual letters are not distinguishable.

From the two patterns depicted in Fig. 4.7 it is apparent that a lower beam energy (3 kV ; see Fig. 4.7 (b)) leads to broader and less defined structures compared to the utilization of higher energies (15 kV ; see Fig. 4.7 (a)). One explanation for this observation is an influence of the beam energy on the electron spot size; calibration measurements performed on a Au on

C sample showed that beam energies of 15 kV, 3 kV and 1.2 kV (beam current: 400 pA) resulted in beam diameters of 2.8 (3.0 nm for the simulation in Fig. 4.8), 4.8 and 5.2 nm, respectively (values measured according to the 20/80 criterion). Since these variations are rather small it can be supposed that this effect contributes only marginally to the observations in Fig. 4.7. Therefore, the primary electrons are not the determining factor for the dimensions of the resulting deposits.

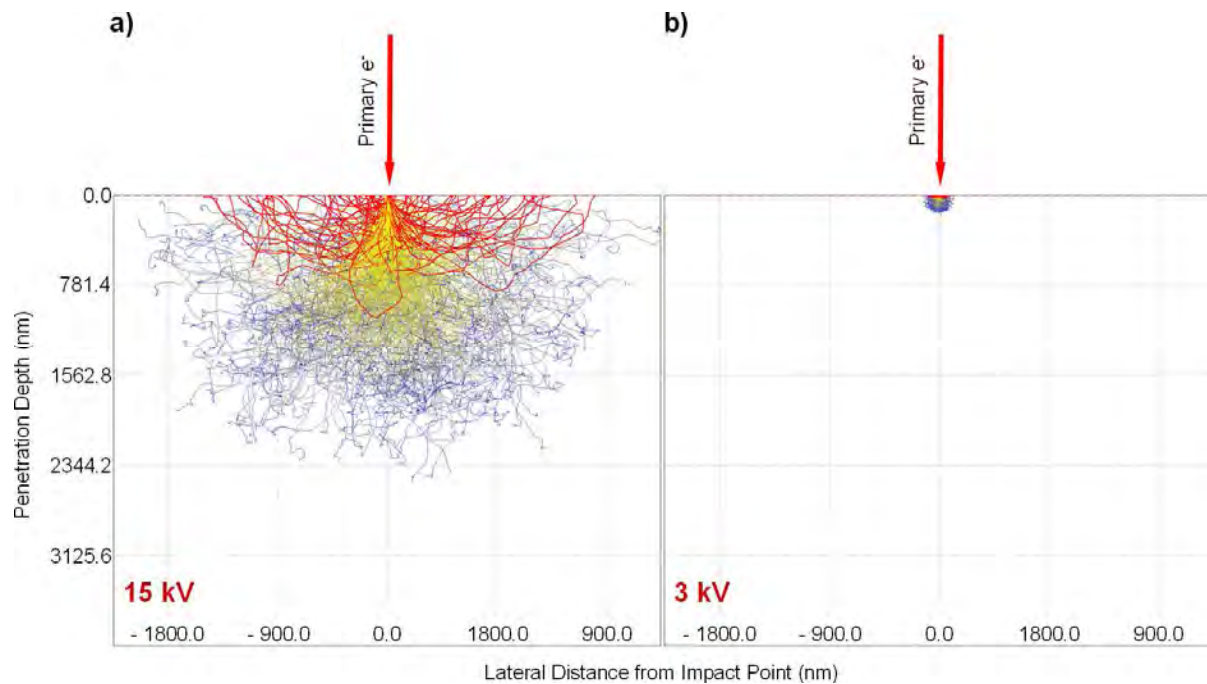


Fig. 4.8: Monte Carlo simulations of BSE trajectories in silicon with the software CASINO V2.42 [92]. Simulated were 200,000 backscattered electrons resulting from a) 15 kV and b) 3 kV primary electron-beam with a beam diameter of 3.0 nm and 4.8 nm, respectively; for better visualization only 500 BSEs are depicted in the images. The red trajectories correspond to BSEs that are able to reach the surface.

Another possible explanation is the influence of the size of the electron interaction area at the silicon surface, which is mainly defined by the BSE exit area. Fig. 4.8 shows simulations of BSE trajectories in silicon for primary electron-beams with a beam voltage of 15 kV ((a)) and 3 kV ((b)); they were calculated with a Monte Carlo simulation using the software CASINO V 2.42 [92]. Clearly visible is a completely different size of both interaction volumes: for the 15 kV primary beam ((a)) the BSE interaction volume appears rather large, while it is very small and compact in case of the 3 kV beam ((b)). Associated with the lower size of the interaction volume is a smaller BSE exit area at the surface for the 3 kV compared to the 15 kV electron-beam, as it is indicated by the BSE trajectories in Fig. 4.8 that are able

to reach the surface (red trajectories). From plots of the amount of emitted BSEs versus the radial position on the surface (with respect to the impact point of the primary electron-beam), which were extracted from the simulations in Fig. 4.8, the radius of the BSE exit areas could be estimated to be ~ 2300 and ~ 160 nm for the 15 and 3 kV electron-beam, respectively; this result is contrary to the observations in Fig. 4.7, where the deposit generated with the 15 kV beam (Fig. 4.7 (a)) is smaller than the one of the 3 kV beam (Fig. 4.7 (b)).

Yet, the significantly smaller interaction volume in case of the 3 kV beam leads to a higher local electron density in the BSE exit area compared to the 15 kV beam, as it is evident from the simulations in Fig. 4.8. This effect is further enhanced by the influence of the beam voltage on the total electron yield from the surface, which can be separated into a BSE and SE part; since SEs are also generated by backscattered electrons (SE II), their lateral extent on the surface is similar to the one of the BSE exit area. Reimer et al. determined the BSE coefficient η for the irradiation of silicon in a modified SEM with a 3 and 15 kV primary beam to be 0.212 and 0.197, respectively [133]; in the same work the secondary electron yield ϕ for a 3, 10 and 20 kV primary beam was determined to be 0.769, 0.3431 and 0.216, respectively. It has to be noted, that these values might vary significantly for different experimental setups and authors. However, a common tendency is a reduction of the backscattering coefficient and secondary electron yield with an increasing primary beam voltage between 1 and 30 kV. It is therefore obvious, that the total electron yield is higher for the irradiation with the 3 kV primary beam compared to the exposure with the 15 kV beam.

Concerning the observations in Fig. 4.7, it can be supposed that due to the higher electron density in the BSE exit area the amount of material deposited near the impact point of the primary electron-beam (BSE proximity effect; compare Chapter 2.7) is higher for 3 than for 15 kV; for the applied deposition parameters this effect leads to broader, less defined structures in SEM by the utilization of the lower beam energy. It has to be noted, that this observation depends strongly on the applied electron dose; at very high electron doses the ultimate range of material deposition due to scattered electrons is mainly defined by the size of the BSE exit area, which is larger for higher acceleration voltages (compare Fig. 4.8 and Chapter 6.3).

To summarize the experiments depicted in Fig. 4.7, it can be stated that at the applied electron dose ($192 \mu\text{C}/\text{cm}$) a lower primary beam energy causes a lateral deposit broadening. This effect is mainly attributed to a higher electron density in the direct surrounding of the irradiated area (BSE proximity effect), while minor contributions result from the simultaneous

broadening of the electron spot size; the primary electrons are therefore not the size determining factor for the resulting structures.

Influence of the electron dose on the width of carbonaceous line deposits

It is well-known from literature, that the applied electron dose has a significant influence on the lateral extent of the deposited structures [40, 134-136]. To confirm this effect and to study the potential to generate structures as small as possible for the system ethene on Si(111), an identical pattern was irradiated on the surface with different electron doses. The corresponding template is depicted in Fig. 4.9 (a). It consists of two horizontal and two vertical lines, which were irradiated with identical doses; within one pair of the line structures (horizontal and vertical) the electron dose was increased from the inside to the outside of the template. Additionally, it contains a (2x2) dot matrix with an increasing dose from the bottom left to the top right. The corresponding electron doses are indicated in Fig. 4.9 (a). The remaining parameters were kept constant for the experiment, with a beam energy of 15 kV, a beam current of 400 pA, and an ethene background pressure of $2.0 \cdot 10^{-8}$ mbar.

In Fig. 4.9 (b) to (f) SEM images of the resulting deposits are depicted. The applied electron doses can be extracted from the values given in Fig. 4.9 (a) by multiplication with a constant dose multiplier N . Compared to the structures in Fig. 4.9 (b), which were deposited with $N = 1$, this results in a two times (Fig. 4.9 (c)), four times (Fig. 4.9 (d)), eight times (Fig. 4.9 (e)) and sixteen times (Fig. 4.9 (f)) higher electron dose, respectively.

Clearly observable in the micrographs is an increasingly darker appearance of the deposits along with increasing electron dose; this observation is attributed to an increasing amount of deposited carbon, leading to a gradual decrease in the secondary electron yield at the corresponding area compared to the free silicon surface. Additionally, the size of the lines and dots is also increasing with the applied dose. To study this observation in more detail, a plot of the full width of the line deposits (measured via *ImageJ*) against the corresponding electron dose is depicted in Fig. 4.10; it shows separated data sets for the horizontal (blue rhombi) and vertical (green squares) lines as well as a plot of the mean values of all lines (red triangles).

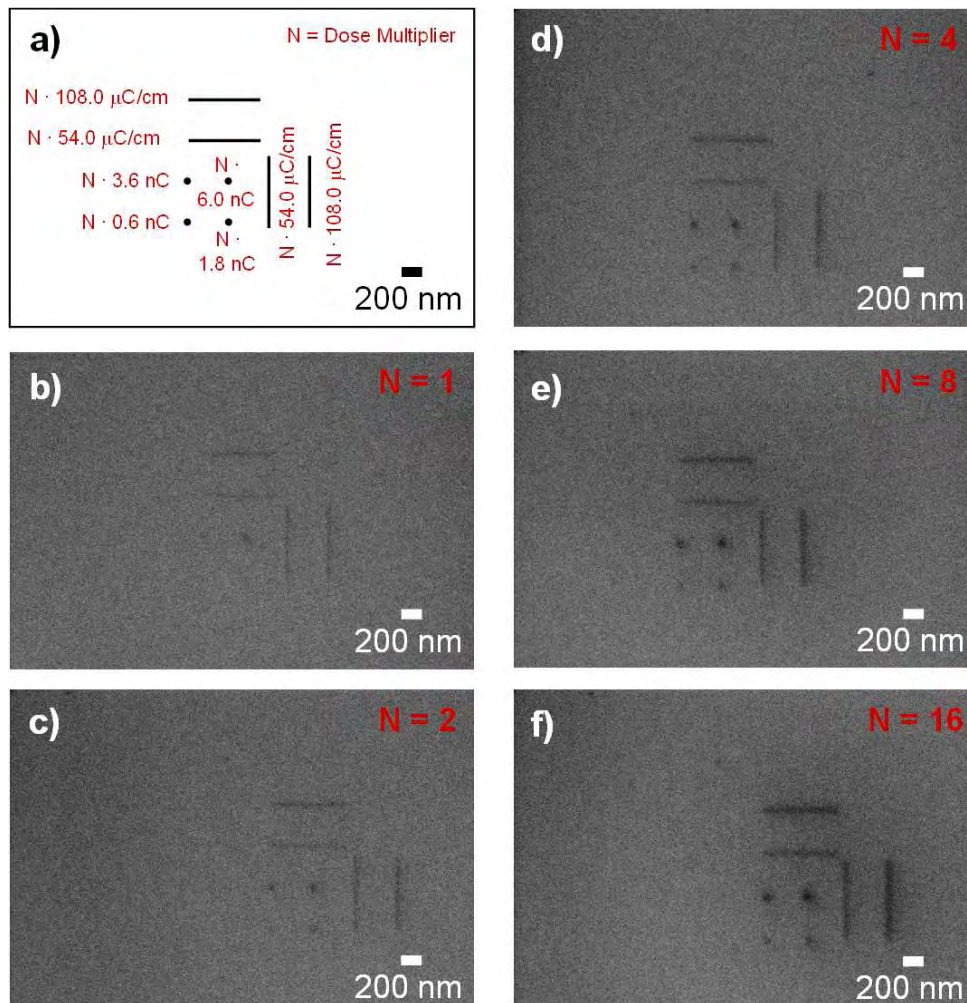


Fig. 4.9: Irradiation of an identical template with different electron doses on Si(111). a) Scheme of the utilized template. b) – f) SEM images of deposits generated via the irradiation with a dose multiplier of b) $N = 1$, c) $N = 2$, d) $N = 4$, e) $N = 8$ and f) $N = 16$. The actual electron dose for each structure can be calculated by multiplication of the dose multiplier with the nominal electron doses given in (a). Contrast and brightness of the SEM images in (b) – (f) were strongly varied to improve visualization. ($U = 15 \text{ kV}$; $I = 400 \text{ pA}$; plane sample)

Remarkable in Fig. 4.10 is that the line widths of the horizontal lines are partly larger than the corresponding vertical ones; a plausible explanation for this is a drift of the sample parallel to the direction of the image acquisition (i.e., from the top of the image to the bottom), leading to a false picture of a thicker line. Yet, the observed deviations are within the calculated margin of error (compare the error bars in Fig. 4.10).

All three data sets in Fig. 4.10 (in particular the one of the mean values (red triangles)) follow roughly a logarithmic trend, as indicated by the drawn lines. The initially steeper slope of the curve indicates therefore that at relatively low electron doses a small increase results in a comparably large broadening of the structure visible in SEM, while at higher doses the

increase of the line width is reduced. Similar results for the lateral broadening of EBI deposits have been reported in literature for the generation of tips with various precursors [134-137]; resulting plots of the deposit diameter versus the deposition time displayed also a logarithmic behavior [32].

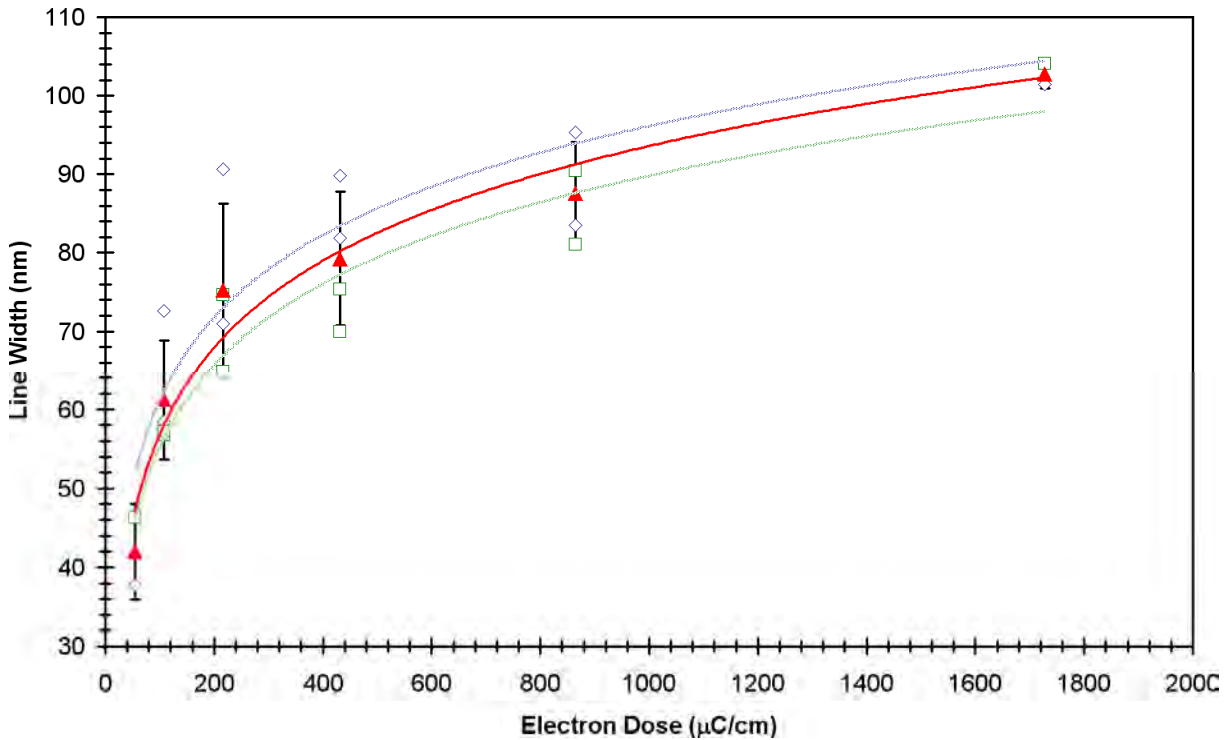


Fig. 4.10: Plot of the full width of the lines (measured via ImageJ) in Fig. 4.9 against the applied electron dose. \diamond = line widths taken from the horizontal lines together with a logarithmic trend line (blue). \square = line widths taken from the vertical lines together with a logarithmic trend line (green). \blacktriangle = mean values of the line widths from the combination of the values of the horizontal and vertical lines together with a logarithmic trend line (red). The error bars for the mean values were calculated by a root mean square deviation.

A model for the lateral broadening of tips, which describes the experimental observations in a qualitatively consistent way but considering only the dissociation by SEs generated via primary electrons (SE I), was suggested by Silvis-Cividjian et al. [87]. The process of the growth of a tip is described as follows: after a nucleation stage the deposit starts to grow. While SEs continue to be emitted from the substrate, emission from the deposit itself will also occur, leading to material deposition on the sidewalls of the tip and therefore outside the trajectories of the PEs. During this initial growth stage the diameter of the deposit increases rapidly. With an increasing size the growth rate is decreasing, as the escape length

of the secondary electrons limits the electron density on the sidewalls of the tip. Once the deposit diameter equals the beam diameter plus twice the maximum SE escape length, the lateral growth stops (saturation value).

Even though this model describes the relation between the applied electron dose and the deposit growth in a rather simplified way, a similar behavior can be assumed for the lateral extension of rather flat deposits (like the ones in Fig. 4.9) by taking the distribution of the backscattered and resulting secondary electron density (SE II) into account. Utke et al. calculated the corresponding distributions on silicon for a 3 and 25 kV electron-beam with the program *MOCASIM* [40]. The resulting plots displayed a high electron density (BSE and SE) near the area of the impinging primary beam, which is in case of the BSE curves decreasing with increasing distance according to an inverse power law (linearly in the double-log plot of reference [40]); for the plots of the SEs the radial density of electrons is decreasing roughly in a similar way, but with small modifications in the observed trend. The high density of electrons near the irradiated area results in an initial rapid growth rate of the deposit width visible in SEM, even at rather low electron doses (deposition due to BSE proximity effect; compare Chapter 2.7). In contrast, the electron density on the outside of the electron interaction area is significantly smaller, which reduces the amount of deposited material and therefore the lateral growth rate. Ultimately, the lateral structure growth stops if the size equals the beam diameter plus twice the radius of the BSE interaction area (radius ~ 2300 nm; compare the last subchapter).

These results clearly demonstrate that small deposits can only be generated via irradiation with rather low electron doses, at least in the system ethene / Si(111) and for the applied scan strategy. The smallest line width achieved with the given parameters in the experiment in Fig. 4.9 was estimated to be ~ 40 nm via irradiation with an electron dose of $54.0 \mu\text{C}/\text{cm}$ (lower horizontal and left vertical line in Fig. 4.9 (b)). It has to be noted, that a decrease of the applied electron dose is accompanied by a lower amount of deposited material. Yet, a certain amount of material is necessary to generate a deposit visible in SEM (due to changes in the SE yield; compare the increasing contrast in the SEM images in Fig. 4.9). It can therefore be supposed, that even though smaller, carbonaceous structures can be generated with lower electron doses, it might not be possible to observe them, at least with the applied system (ethene / Si(111)) or experimental setup.

Summarizing the results described in this subchapter, it can be confirmed that the applied electron dose has a significant influence on the line width of carbonaceous line structures deposited with ethene on Si(111). The observed variations in the size of the lines

follow roughly a logarithmic trend, which is attributed to the distribution of BSEs and SEs in the surrounding of the impinging electron-beam (deposition due to BSE proximity effect). Therefore, the utilization of very low electron doses is mandatory to reduce the BSE proximity effect and thus to enable the generation of deposits as small as possible.

4.4 Summary and conclusions

The main goals of the experiments described in this chapter were I) to test the lithographic attachment of the *Multiscan LAB* system, especially for the generation of arbitrarily shaped deposits, and II) to control the functionality of the gas dosage system in context with the EBID process in a rather simple system, namely the deposition of carbon with the precursor ethene on Si(111).

Concerning topic I) it was shown via electron-beam lithography (EBL) on a PMMA covered silicon surface that the instrument is capable of generating arbitrarily shaped structures at defined positions; hereby, line features and dots with a minimum size of ~ 0.3 and ~ 0.75 μm , respectively, were achieved. Furthermore, it was observed that variations of the applied electron dose have a significant influence on the morphology (crosslinking of PMMA at higher doses) and size of the resulting features (increasing proximity effects due to electron scattering), both well-known facts in literature [123, 126].

Subsequently, the lithographic attachment of the system was successfully combined with the self-constructed gas dosage system for the generation of carbonaceous deposits via EBID (topic II)). The resulting structures exhibited in the SEM a dark contrast on the applied silicon surface, which was attributed to the lower SE yield of carbon associated with the lower atomic number compared to silicon [48] (see Figs. 4.6, 4.7 and 4.9). Furthermore, some fundamental aspects for the generation of carbonaceous deposits on silicon and the EBID process itself were observed, which will be summarized in the following.

Of pivotal interest for the fabrication of well-defined structures in the system ethene / Si(111) is the choice of the lithographic parameters and the structuring of the applied template; relatively high electron doses in combination with too densely packed features in the template resulted in a blurring of individual features in the resulting pattern, mainly due to an overlapping of deposited material due to proximity effects (see Fig. 4.6 (a)). In this context a significant influence for the generation of rather small and defined deposits is also attributed to the primary electron energy. For an identical electron dose and template the utilization of a lower beam energy caused a lateral deposit broadening (see Fig. 4.7), an effect that is mainly

attributed to a higher electron density in the corresponding electron exit area, while minor contributions result from the simultaneous broadening of the electron spot size.

A significant influence on the width of line deposits is also attributed to the applied electron dose (see Fig. 4.9); a corresponding plot follows roughly a logarithmic trend line (see Fig. 4.10). This observation is mainly attributed to the distribution of BSEs and SEs in the surrounding of the area irradiated by the primary electron-beam, as it was calculated, e.g., in reference [40]. The smallest line width achieved with the electron doses in the experiment in Fig. 4.9 was estimated to be ~ 40 nm ($54.0 \mu\text{C}/\text{cm}$), while the largest value was ~ 100 nm ($1696.0 \mu\text{C}/\text{cm}$). Therefore, the utilization of very low electron doses is necessary for the generation of relatively small deposits, at least for the system ethene / Si(111). A major drawback in this case is a reduced amount of deposited material associated with a decrease of the applied electron-dose, leading to structures that are barely distinguishable on the silicon surface (e.g., see Fig. 4.9 (b)).

5 Iron pentacarbonyl on Rh(110)

5.1 Introduction

For the electron-beam induced deposition of metals mainly semiconductors [24, 30, 70, 83, 138] or inert metal substrates like, e.g., Au [34, 38] are used. The application of a catalytically active metal surface represents a novel aspect to this technique, which might lead to some additional information regarding the mechanisms of the deposition process and the influence of the surface.

Examples of such catalytically active metal substrates are single crystal surfaces of rhodium, which are in the field of surface science mainly used to study chemical reactions of gaseous compounds like, e.g., NO and H₂ [139] in an idealized way. For the experiments presented in this chapter, a Rh(110) surface was used. The combination of this surface with the precursor iron pentacarbonyl was chosen for several reasons: (1) the catalytic activity of Rh(110) is well studied in literature [115, 117, 140-142]; (2) for sample temperatures above 430 K dissociative adsorption of oxygen occurs on Rh(110) [115], which opens the possibility to oxidize unintended carbon contaminations with subsequent desorption as CO or CO₂; (3) chemisorbed oxygen on Rh(110) can be removed by dosing hydrogen [115, 117, 140] which might enable the selective oxidation of iron deposits and thus the generation of oxide nanostructures on a metallic substrate. Generally, adsorption and reaction properties of Fe(CO)₅ with metal substrates like Ag [143], Ni(100) [144] and Pt(111) [145, 146] vary strongly with substrate. The adsorption of Fe(CO)₅ on rhodium has not been studied so far, to the best of my knowledge.

Following this introduction, a detailed description of the applied Rh(110) substrate and the oxygen induced surface reconstruction is given (Chapter 5.2). The preparation state of the sample, which was improved in vacuum via sputtering and oxidation / reduction cycles (see Chapter 3.4), was periodically monitored using SEM, AES and LEED and will be discussed in Chapter 5.3. Thereby, an important indicator for the improvement of the specimen quality was the appearance of certain oxygen induced reconstructions. The dosage of H₂ onto the oxygen covered surface resulted in the appearance of propagating reduction fronts, which could be visualized via the SEM. Chapter 5.4 describes experiments which were performed to study these chemical waves in more detail and gives a perspective to predefine their starting position.

The first electron-beam induced depositions with iron pentacarbonyl on Rh(110) are reported in Chapter 5.5 and are mainly used to discuss the influence of an additionally applied

precursor gas dosage after the generation of the deposits. It is noteworthy that these results represent not only the first time that $\text{Fe}(\text{CO})_5$ was applied to a rhodium single crystal surface, but also that EBID was performed on a catalytically active metal substrate, to the best of my knowledge. An important finding was the influence of the surface quality (in terms of roughness, surface reconstruction and precoverage) of the Rh crystal for the EBID process; in Chapter 5.6 these parameters are mainly discussed in context with the selectivity of the process, the purity of the resulting structures and the possibility to generate spatially well defined deposits, taking the catalytic activity of the surface into account. The amount of deposited material may be determined by the applied electron dose; its influence on the thickness and morphology of the resulting structures is described in Chapter 5.7. Usually, structures deposited via EBID are contaminated by the co-deposition of other elements. A typical process used for the purification is post-deposition annealing; its influence on the iron structures deposited on rhodium and their thermal stability are discussed in Chapter 5.8. Finally, Chapter 5.9 describes the potential to selectively oxidize Fe deposits on Rh(110), in order to fabricate FeO_x structures.

5.2 The Rh(110) surface

Rhodium is a silvery-white metal with a density of 12.41 g/cm^3 and a melting point of 2230 K. It belongs to the group of the platinum metals and can be found naturally either as a sulfide or in its free state [99]. Pure rhodium crystallizes in a face centered cubic (fcc) Bravais lattice, as it is depicted in Fig. 5.1. The Rh(110) surface is obtained by a cut through the crystal parallel to the (110) plane (see turquoise area in Fig. 5.1), according to the nomenclature of Miller indices.

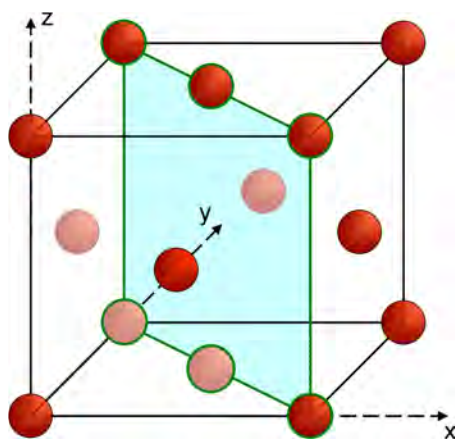


Fig. 5.1: Image of a fcc Bravais lattice with (110) area marked in turquoise.

A special characteristic of (110) surfaces from fcc crystals are troughs along the $[1\bar{1}0]$ direction (see top left image in Fig. 5.2). The resulting anisotropy leads to a high surface free energy, which makes the surface very sensitive towards reconstructions. This means, that during the adsorption of gas molecules (e.g., O_2) at an adequate crystal temperature a rearrangement of adsorbate and top most rhodium atoms takes place, with the lowering of the total surface energy of the adsorbed system being the thermodynamical driving force [140]. Depending on the nature of the applied adsorbate and its coverage on the surface a sequence of $(n \times 1)$ or $(1 \times n)$ *missing row* reconstructions is achieved, where a certain number of $[100]$ or $[1\bar{1}0]$ rows, respectively, are absent. This change in the surface geometry leads to the generation of new adsorption sites, which are energetically more favorable for the adsorbate atoms compared to the ones on the unreconstructed area. A detailed overview for adatom-induced reconstructions on (110) metal surfaces is given by Kiskinova [140].

Important for the work at hand is the oxygen induced reconstruction of the Rh(110) surface, which belongs, in contrast to the corresponding rearrangements on other metal substrates like Cu, Ni and Ag, to the group of the $(1 \times n)$ reconstructions. Due to its influence on certain catalytic reactions, e.g., the oxidation of CO, it was extensively studied in literature [140, 147-150].

Depending on the oxygen coverage and the applied surface temperature a sequence of complex *missing row* reconstructions takes place. Each of the resulting surface arrangements is accompanied by the periodic alignment of the adatoms. The dissociative adsorption of oxygen on Rh(110) is energetically favored at the positions of the threefold coordination sites at (111) microfacets in the missing rows. Repulsive interaction between the adsorbate atoms leads to an alignment in a “zick-zack” pattern along the rhodium rows in the $[1\bar{1}0]$ direction. The dominant surface reconstructions together with the corresponding oxygen superstructures at ~ 600 K are depicted in Fig. 5.2 [140, 151].

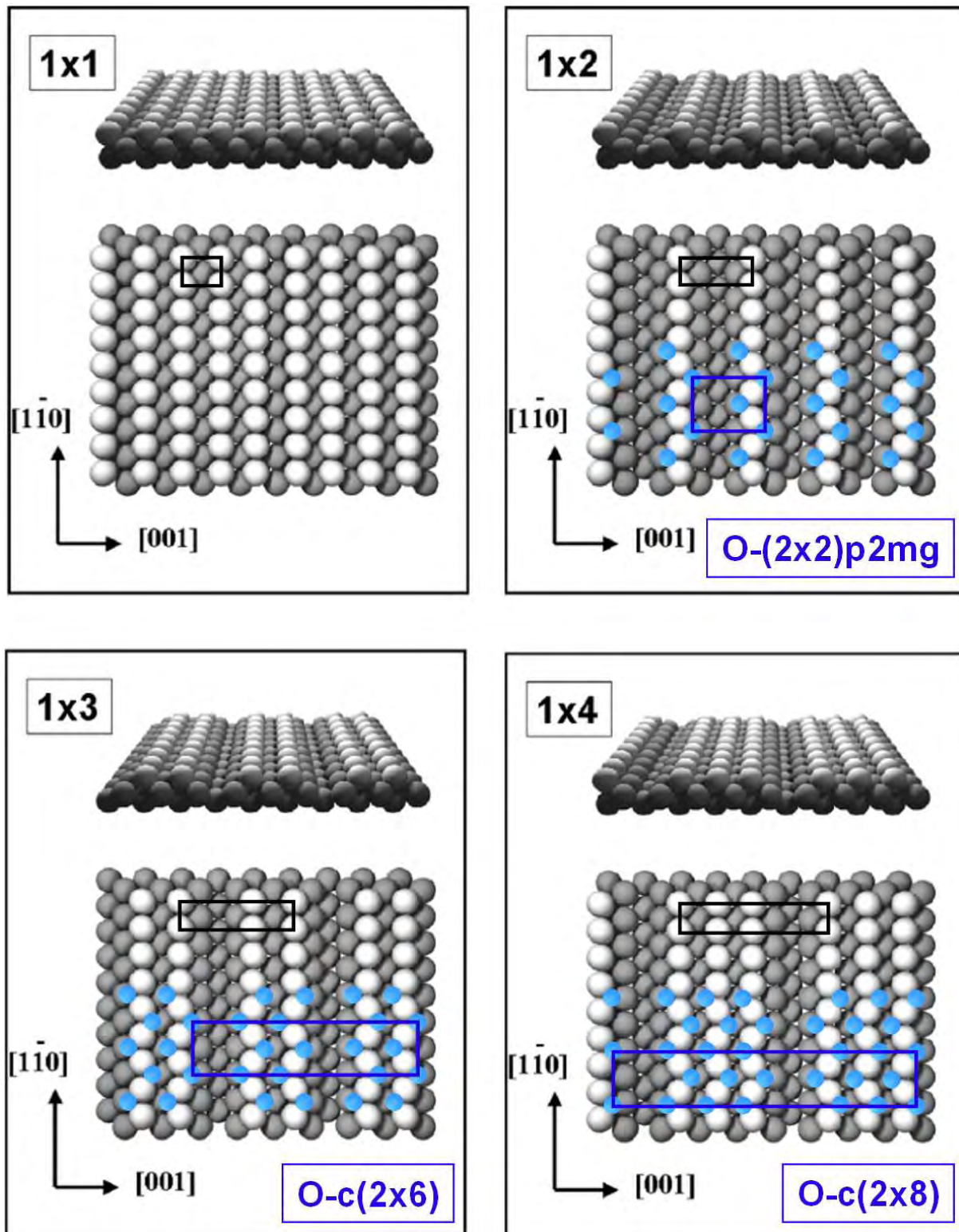


Fig. 5.2: Missing row reconstructions and oxygen superstructures induced by oxygen coverage. The black rectangulars mark the unit cell of the respective surface reconstruction, while the blue ones represent the oxygen superstructure. To display the surface reconstruction in the models precisely, only half of the area is covered with oxygen atoms. The images of the atom models of the surface are adapted from reference [151].

Due to a deeper embedment of the adatoms resulting from the structural rearrangements in the Rh outermost layer, adsorption on the fcc 3-fold sites along the (1x2) troughs is energetically more favored compared to the ones along the (1x1) troughs (see Fig. 5.3). For low oxygen coverages ($\theta_{\text{O}} \sim 0.5$ according to reference [151]) the lowest energy of the system can therefore be achieved by the removal of every second Rh row, i.e., a (1x2) surface reconstruction resulting in an O-(2x2)p2mg superstructure (see top right image in Fig. 5.2). Any further increase in oxygen coverage would lead in the case of the (1x2) reconstruction to the occupation of energetically unfavorable positions; the system's free energy at higher oxygen coverages is therefore lowered by a reduced number of missing rows, providing additional fcc 3-fold sites along the (1x1) troughs. The resulting (1x3) (with $\theta_{\text{O}} \sim 0.65$ according to literature [151]) and (1x4) (with $\theta_{\text{O}} \sim 0.75$ according to reference [151]) surface reconstructions, with every third respective fourth rhodium row removed, are depicted in the lower part of Fig. 5.2. Their corresponding oxygen superstructures are O-c(2x6) and O-c(2x8), respectively. According to literature, it is also possible to generate a (2x1)p2mg superstructure on an unreconstructed (1x1) surface at a temperature of 298 K, since the diffusion of the rhodium atoms is thermodynamically hindered under these conditions [140].

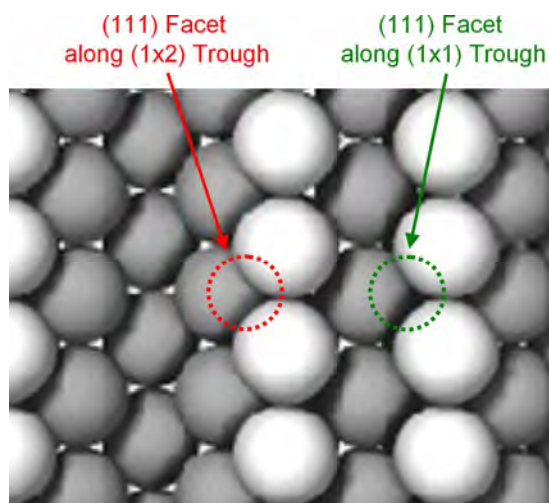


Fig. 5.3: Energetically favored 3-fold adsorption sites for oxygen at the (111) facets along the (1x2) and (1x1) troughs of a (1x3) surface reconstruction. The image of the atom model of the surface reconstruction is adapted from reference [151].

Removal of the adsorbed oxygen atoms and hence the retrieval of the (1x1)-reconstructed Rh(110) surface can be performed by the reaction with an additional adsorbate like, e.g., hydrogen. In this case, at reaction temperatures below 450 K the (1 x n) surface reconstruction is preserved ($n = 2, 3, 4, 5$), while at higher temperatures it reverts to the (1x1)

structure [140, 152]. According to the applied temperature and hydrogen pressure the reaction of surface adsorbed oxygen to water can either take place in a spatially homogeneous way or propagate on the surface via chemical reaction fronts [115] (see Chapter 5.4).

5.3 Preparation of Rh(110) in an UHV-SEM

Since the influence of the quality of the Rh(110) surface on the EBID process was studied, different conditions from the same crystal were prepared. The progressive improvement of the sample quality was periodically monitored using SEM, AES and LEED. The data presented in this chapter is one of the first examples where the preparation of a single crystal in UHV was studied with scanning electron microscopy in addition with typically used methods like AES and LEED.

Additional information on the quality of the surface was derived from the formation of oxygen-induced superstructures (see Chapter 5.2), which could be observed via LEED. For a well-prepared clean Rh(110) surface a sequence of ordered phases (reconstructions) was therefore expected to form upon increasing oxygen dosage at ~ 600 K: O-(2x2)_{p2mg}, O-c(2x6) and O-c(2x8) [141, 153], with the formation of the latter being very sensitive to the surface quality.

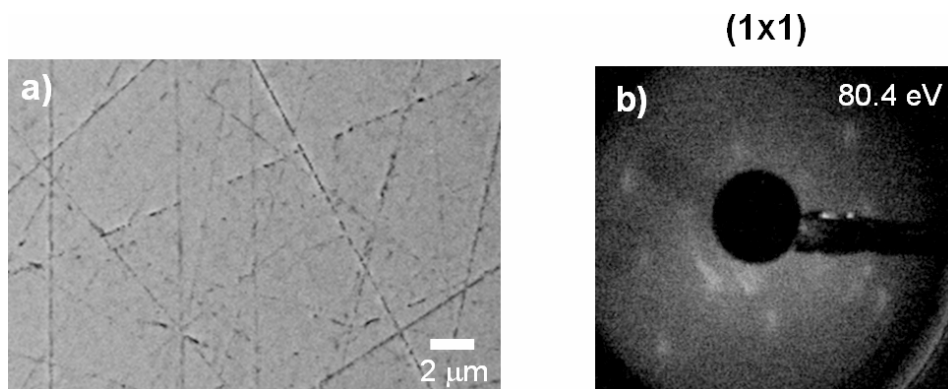


Fig. 5.4: a) SEM image of the untreated Rh(110) surface. ($U = 15$ kV; $I = 3$ nA; tilted sample) b) Image of LEED reflexes from the untreated sample, displaying a diffuse (1x1) surface reconstruction.

In Fig. 5.4 (a) an SEM image of the “fresh” sample is depicted, which means before any cleaning and preparation procedures were performed. The surface shows a lot of scratches in varying directions, most presumably from the polishing of the crystal. Residuals of the polishing procedure could also be found via Auger electron spectroscopy; a spectrum

acquired on the surface displays, beside the expected Rh MNN peaks, a minor amount of carbon and a small but significant sulphur LMM signal (see red spectrum in Fig. 5.5). The latter is attributed to the residuals of a sulphur containing polishing paste. LEED measurements on the fresh Rh(110) surface show very weak and diffuse spots of a (1x1) reconstruction (see Fig. 5.4 (b)). Upon oxygen dosage these reflexes quickly vanished, indicating the absence of any oxygen-induced superstructures and therefore the low quality of the untreated surface.

Originating from the untreated surface, other sample conditions were prepared by the application of cleaning procedures, as described in Chapter 3.4. The resulting sample states varied strongly in terms of surface quality and are discussed in the following:

Sample I was obtained after a minor preparation of the specimen, with a temperature of ~ 1000 K for the annealing steps (for the exact numbers of the performed cleaning procedures see the text in the arrows on the left side in Fig. 5.6). SEM images still show an inhomogeneous surface with a slightly reduced number of scratches (see Fig. 5.6 (a) and (b)). In the case of the image acquired with a higher beam current and a tilted sample (Fig. 5.6 (b)) these scratches are more clearly visible, which is mainly attributed to the well-known surface tilt and shadowing contrasts (compare Chapter 2.1) [48]; thereby, the amount of detected electrons exhibit local variations due to the dependence of the electron yield on the trajectory of the primary electron beam and the position of the electron detector with respect to the local surface normal. Remarkable in this micrograph is also a structuring of the surface into bright and dark areas, which appeared initially after an extensive oxidation / reduction cycle and is not visible in the image of the plane sample (see Fig. 5.6 (a)). The origin of this structuring is unclear. As local AES showed no differences in the surface areas, variations in the local chemical composition appear unlikely as an explanation. One possible explanation for this structuring is a difference in the local surface reconstruction and lattice planes, leading to an angular dependent crystal orientation contrast in the SEM [48]; since the backscattering coefficient and secondary electron yield of a single crystal are strongly anisotropic and depend sensitively on the direction of the electron incidence relative to the crystal lattice planes, these effects might lead to local variations in the electron yield and therefore to differences in the contrast in the SEM image, as observed for Fig. 5.6 (a). A representative AE spectrum of the surface is shown in Fig. 5.5 (blue spectrum); only a minor contamination of carbon is visible in this sample state, while the sulphur peak observed on the untreated surface has vanished. In some spectra acquired during the preparation of this condition, also minor indications for copper were observed (not shown here). The origin of this element on

the surface will be discussed later (see Chapter 5.6). LEED measurements displayed an improved (1x1) reconstruction compared to Fig. 5.4 (b). By dosing oxygen the formation of an O-(2x2)p2mg superstructure could be observed, which changed into a beginning O-c(2x6) superstructure at higher exposures.

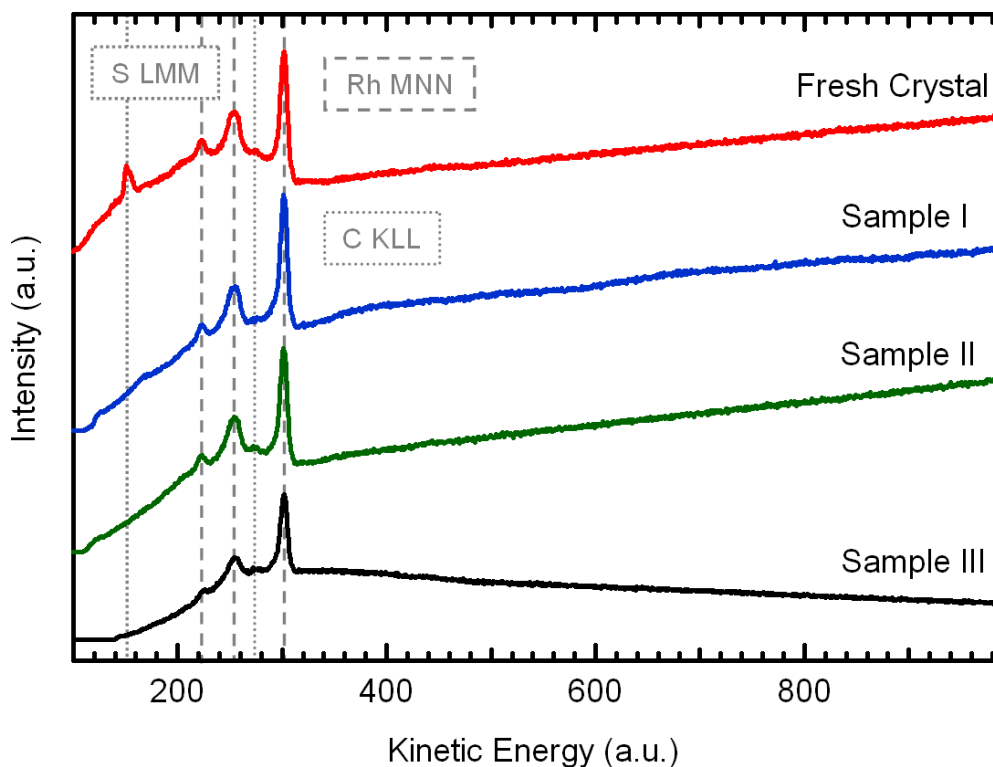


Fig. 5.5: AE spectra acquired from different surface states of the Rh(110) surface.

Sample II was prepared similarly to Sample I, but with a higher number of sputtering and oxidation / reduction cycles. The SEM images depicted in Fig. 5.6 (c) and (d) show a significantly reduced roughness of the surface, mainly resulting from a decreased number of polishing scratches. In the case of image acquisition from the tilted sample the previously reported structuring of the surface is still visible (see Fig. 5.6 (d)). AES shows a similar spectrum (green spectrum in Fig. 5.5) as the one of Sample I, also with a comparable amount of carbon. In LEED, no improvements of the surface reconstruction were observed; the spots of the (1x1) reconstruction were still rather diffuse and large oxygen exposures led only to a beginning O-c(2x6) superstructure.

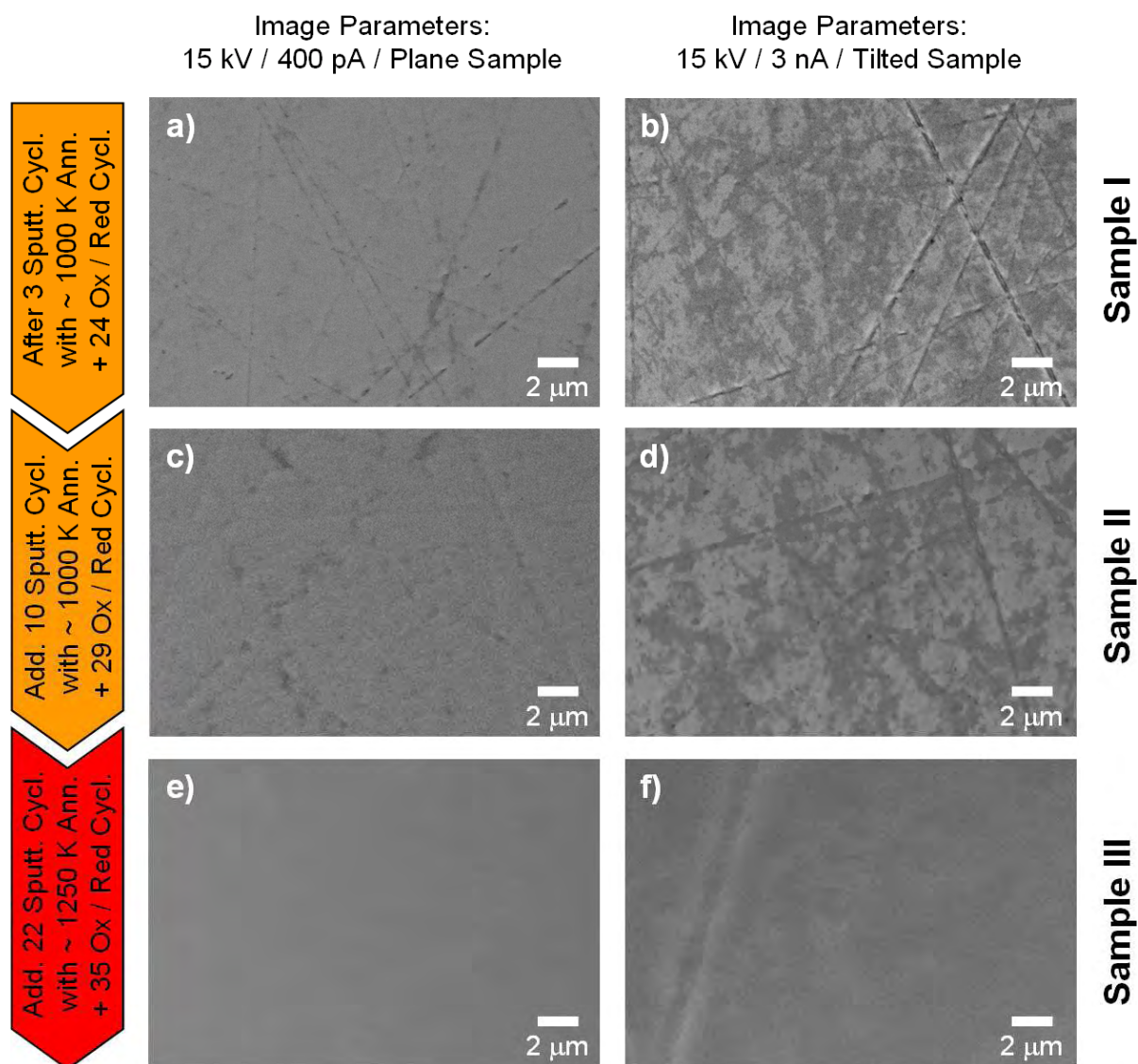


Fig. 5.6: SEM images of different surface conditions of the Rh(110) surface, acquired from the plane (left column) and tilted specimen (right column). The cleaning procedures necessary to achieve the corresponding conditions are indicated in the arrows on the left.

Sample III is a perfectly prepared Rh(110) surface; originating from Sample II it was obtained after additional sputtering and oxidation / reduction cycles, also with an increased annealing temperature of ~ 1250 K (see Chapter 3.4). This surface shows a structureless SEM image acquired from the plane sample (see Fig. 5.6 (e)) and only weak features from the remnants of larger scratches in the case of the tilted specimen (see Fig. 5.6 (f)). Additionally, the structuring observed for the tilted specimen of Sample I and Sample II has vanished. The respective AE spectrum depicted in Fig. 5.5 (black spectrum) displays again a minor amount of carbon, comparable to the spectra of the other two states. Differences in its overall shape are due to the different geometry of the applied sample holder, which was necessary to

achieve the higher annealing temperature (see Chapter 3.4); this influences the acceptance angle and the transmission of the electron analyzer. LEED measurements of the surface showed a very sharp (1x1) pattern. Upon oxygen dosage a sequence of O-(2x2)p2mg and O-c(2x6) superstructures followed that quickly changed into an O-c(2x8) superstructure at higher oxygen exposures. The appearance of the latter is an indicator for the high surface quality of Sample III.

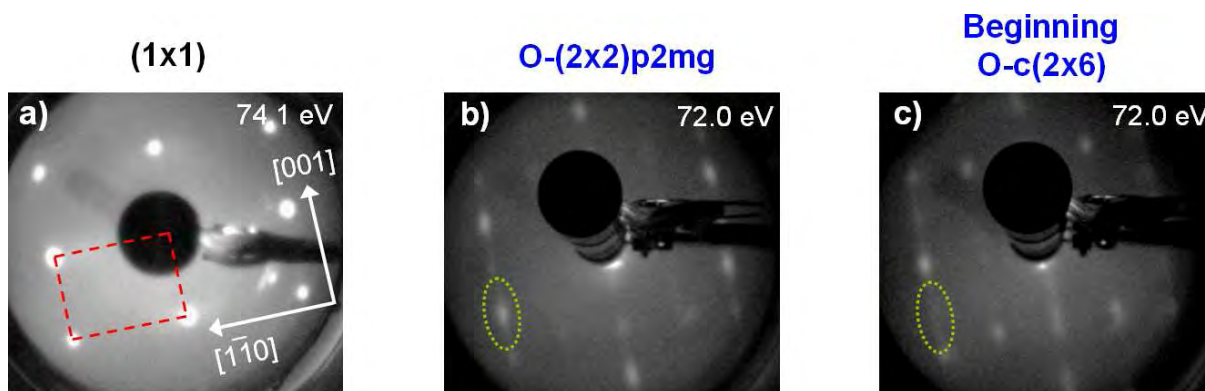


Fig. 5.7: Images of LEED patterns acquired from the Rh(110) surface in a state between Sample II and Sample III. a) (1x1) reconstruction with one of the unit cells denoted by a dashed rectangle. b) O-(2x2)p2mg superstructure obtained by oxygen dosage ($p(O_2) = 6.0 \cdot 10^{-8}$ mbar) while heating the sample to ~ 600 K. c) Beginning O-c(2x6) superstructure, realized by a higher oxygen exposure ($p(O_2) = 1.0 \cdot 10^{-7}$ mbar) at the same temperature (600 K).

To explain the observed changes in the LEED patterns caused by the different oxygen induced surface reconstructions, Fig. 5.7 shows images that were acquired after some additional preparation of Sample II. Originating from a clearly visible (1x1) reconstruction (see Fig. 5.7 (a); the dashed rectangle marks one unit cell), adsorption of oxygen leads to the development of additional spots along the [001] and $[1\bar{1}0]$ axis. A detailed description of the resulting LEED patterns is given in literature [154]. The assignment of the patterns to certain superstructures can be done according to the appearance of additional spots at the edges of the original unit cell parallel to the [001] axis: one, two or three additional spots for an O-(2x2)p2mg, O-c(2x6) or O-c(2x8) superstructure, respectively. Fig. 5.7 (b) shows the LEED pattern of an O-(2x2)p2mg superstructure, while the onset of a O-c(2x6) superstructure is depicted in Fig. 5.7 (c); the additional spot clearly observed for the O-(2x2)p2mg (marked area in Fig. 5.7 (b)) is very diffuse for the unfinished O-c(2x6) and starts to split into two separate reflexes (marked area in Fig. 5.7 (c)). The images of the LEED patterns depicted in

Fig. 5.7 are exemplary for the surface reconstructions and oxygen superstructures observed for Sample I and Sample II.

In summary, one can find that monitoring the state of the surface preparation of the rhodium crystal by the combination of a microscopic (SEM), spectroscopic (AES) and diffraction method (LEED) enables a more detailed description of the progress of the surface quality. Even though a high chemical purity is already achieved after a low number of cleaning cycles (see Sample I), an extensive preparation is necessary for a microscopically smooth and homogeneous surface that exhibits a defined surface reconstruction (see Sample III); in this context the performance of oxidation / reduction cycles by alternatively dosing O_2 and H_2 plays an important role for obtaining a highly ordered specimen surface. Three selected conditions, exhibiting different qualities, were described in detail in this chapter; these sample states, namely Sample I, Sample II and Sample III, were used for EBID experiments (see below). Important to remember is that the higher number indicates a higher quality of the surface (mainly in terms of surface roughness and reconstruction).

5.4 Visualizing reduction fronts on Rh(110)

An interesting topic concerning the system Rh(110) / $O_2 + H_2$ is the appearance of reaction fronts under certain conditions, which could typically be visualized via work function sensitive techniques like PEEM (photoemission electron microscopy) [115-117] or LEEM (low energy electron microscopy) [116, 151]. In this context the question arose, if it is also possible to see these chemical waves in an SEM. For these experiments Sample I was used; LEED measurements at this sample condition showed distinct but very diffuse spots for the (1x1) reconstruction, while during oxygen dosage an $O-(2 \times 2)_{p2mg}$ with indications for the transition to the $O-c(2 \times 6)$ superstructure was observed. A complete description of Sample I was given in Chapter 5.3.

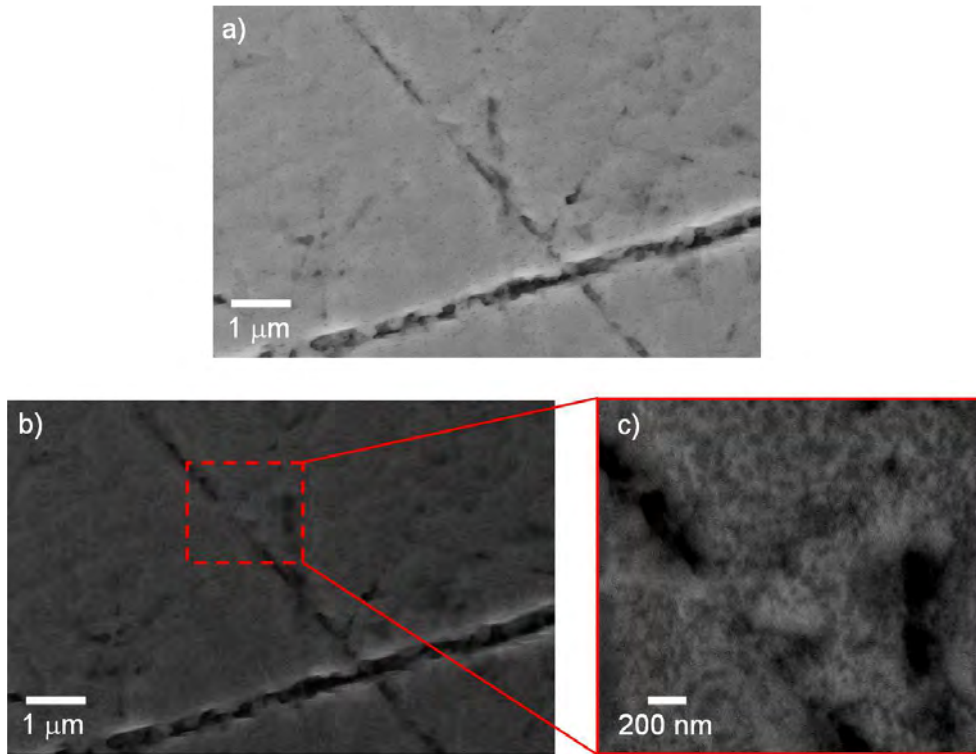


Fig. 5.8: SEM images of the same position on the Rh(110) surface a) before and b) during oxygen dosage ($p(\text{O}_2) = 1.0 \cdot 10^{-8}$ mbar). c) High magnification image of the area marked in (b) during oxygen dosage ($p(\text{O}_2) = 2.0 \cdot 10^{-7}$ mbar). Images (a) and (b) are shown with identical brightness and contrast values, while for image (c) the contrast and brightness were drastically enhanced to improve visualization. All images were acquired at a sample temperature of 610 K. ($U = 15$ kV; $I = 3$ nA; plane sample)

Fig. 5.8 (a) shows an image of a representative part of the specimen at a sample temperature of 610 K; as already described before (see Chapter 5.3), the surface in this sample state appears very rough, with a lot of scratches from the polishing of the crystal visible. Fig. 5.8 (b) displays an image of the same sample position immediately after the beginning of O_2 dosage ($p(\text{O}_2) = 1.0 \cdot 10^{-8}$ mbar) at 610 K; the micrograph was acquired with identical brightness and contrast values as Fig. 5.8 (a). Due to oxygen adsorption on the surface the image is appearing significantly darker compared to Fig. 5.8 (a). This is attributed to an increase in the work function to a maximum of up to 1.1 eV, resulting from a partial charge transfer from the substrate to the adsorbate [151]. In case of the photoelectrical effect the relation between an adsorbate induced change of the work function $\Delta\Phi$ and the resulting photoelectron current I is according to Fowler [151, 155]

$$I \propto (h\nu - (\Phi_e + \Delta\Phi))^2 \quad (5.1)$$

with the energy of the irradiated light $h\nu$ and the work function of the metal Φ_e . For the emission of secondary electrons in an SEM a similar relation is assumed, which would explain the observation in Fig. 5.8 (darker appearance of the surface due to oxygen adsorption). It has to be noted that the adsorbate might also have an influence on the backscattering coefficient and secondary electron yield of the sample and thereby on the local brightness observed in the micrograph. (compare Chapter 2.1) [48]. Equation 5.1 is therefore supposed to describe the observations in a rather qualitative way.

Additionally, the oxygen coverage leads to a structuring of the surface, which is more clearly visible in the high magnification image depicted in Fig. 5.8 (c) (image acquired during oxygen dosage at $p(\text{O}_2) = 2.0 \cdot 10^{-7}$ mbar; contrast and brightness of the image were strongly enhanced). It consists of an irregular alignment of dark and bright regions with different shapes and areas. The origin of this surface structuring is unclear at the moment. The most plausible explanation is that due to the oxygen induced *missing row* reconstruction a certain amount of material has to be redistributed, which might result in specific features on the surface; since Sample I showed a preference for the O-(2x2)p2mg oxygen superstructure (observed via LEED measurements; see Chapter 5.3), a redistribution of every second rhodium row is necessary for the corresponding (1x2) surface reconstruction. Another possibility would be that due to the roughly prepared sample only specific areas of the surface are capable of performing the described oxygen induced reconstructions; these regions would appear darker in the SEM (due to the adsorbed oxygen) compared to the remaining surface.

SEM images of the oxygen covered surface after electron irradiation revealed a significant influence of the electron exposure (see Fig. 5.9). Fig. 5.9 (a) shows an image of the surface with a rectangularly shaped area in the center that appears darker in SEM than the rest of the sample. Compared to Fig. 5.8 (a) and (b) the image was recorded with other contrast and brightness values. The central region corresponds to the area that was studied by SEM at a higher magnification level during oxygen dosage. A high magnification image (Fig. 5.9 (b)) shows in the non-irradiated area (left part) indications for a similar structuring as observed in Fig. 5.8 (c), i.e., an irregular alignment of dark and bright regions; in the irradiated area (right part in Fig. 5.9 (b)) this structuring appears to be vanished.

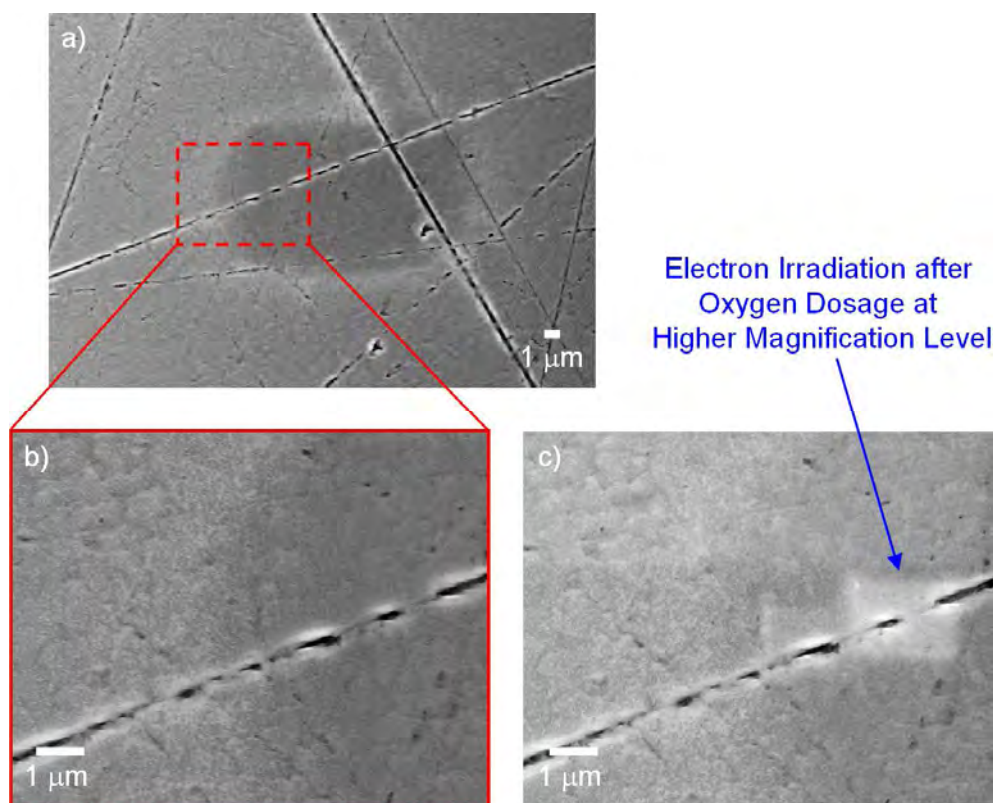


Fig. 5.9: Effect of electron irradiation on the oxygen covered surface. a) Image of an area previously irradiated at a higher magnification level during oxygen dosage ($p(O_2) = 1.0 \cdot 10^{-6}$ mbar). b) High magnification image of the area marked in (a). Images (a) and (b) were acquired during oxygen dosage ($p(O_2) = 1.0 \cdot 10^{-6}$ mbar). c) Image of the same area as in (b), acquired after oxygen dosage. The bright area on the right side results from electron irradiation at a higher magnification level. ($U = 15$ kV; $I = 3$ nA; plane sample)

The influence of the electron-beam during oxygen dosage is supposed to be either due to an electron induced desorption of oxygen or an additional electron stimulated adsorption of O_2 molecules, eventually combined with a reconstruction of the topmost rhodium layer. The former is well-known for the electron irradiation of metal oxides and chemisorbed oxygen layers on metals like, e.g., Fe and Ni, as it was shown by Niehus et al. via AES measurements [156]; depending on the respective metal – oxygen interaction (oxide or oxygen covered metal) different electron stimulated desorption (ESD) mechanisms were found to be responsible for the depletion of oxygen. However, in this case one would expect a brighter surface area (with respect to the rest of the oxygen covered surface) after electron exposure, resulting from a lower work function of the pure metal substrate (compare Equation 5.1). A brighter surface area is indeed observed after an additional irradiation of a certain region of the surface after the end of the oxygen dosage, as it can be seen in Fig. 5.9 (c). In the case of

electron stimulated dissociation of O₂ molecules, the resulting higher coverage of oxygen atoms would possibly result in the local rearrangement of the surface in the (1x3) or (1x4) reconstruction. The number of removed rhodium rows is significantly reduced under these conditions, which would explain the disappearance of the structuring in the irradiated area. The local electron assisted dissociation of oxygen has been already studied by Heras and Viscido on a Cu(100) surface [157]. Also a combination of both explanations account for the observed effects.

The interaction of the system Rh(110) / O₂ with hydrogen was extensively studied in literature [115, 117, 140, 151, 158]. As already mentioned before the resulting generation of water can either happen homogeneously on the whole surface or propagate by chemical waves in a reaction-diffusion system (with the H₂ adsorption starting at defects of the oxygen layer), depending on the applied temperature and H₂ pressure. In both cases, the basic reaction can be described by the Langmuir-Hinshelwood mechanism, which starts with the dissociative adsorption of O₂ and H₂ on the surface. Interaction of the adsorbed atoms leads to the formation of water via an intermediate OH compound [158].

Fig. 5.10 shows an example for hydrogen dosage ($p(\text{H}_2) = 6.0 \cdot 10^{-8}$ mbar) on an oxygen precovered surface with a temperature of ~ 610 K (without simultaneous O₂ dosage). The reaction was studied at the same position that was already depicted in Fig. 5.9. Clearly visible in the center of Fig. 5.10 (a) is the previously irradiated area (exposed to the electron-beam under oxygen dosage), which has now a slightly different shape due to some additionally performed SEM scans. Roughly 12 minutes after the start of hydrogen dosage two bright areas appear at the left and central part of the exposed area (Fig. 5.10 (b)). These regions grow and merge together (Fig. 5.10 (c)) until they elliptically surround the pre-irradiated part of the surface (Fig. 5.10 (d)). The reason for the observed bright areas is the removal of oxygen from the surface, which results in a lowering of the work function (compare Equation 5.1). Since these regions are growing steadily, it is obvious that for the heterogeneously catalyzed formation of water on Rh(110) the applied experimental parameters result in a reduction front mechanism, in which hydrogen is adsorbing at defect positions or irradiated areas and subsequently diffuses into the oxygen covered areas. The data depicted in Fig. 5.10 represents not only the first time that reaction fronts were visualized by an SEM, but also the possibility for the predefinition of a starting point via electron irradiation during oxygen dosage (presumably due to a different oxygen-induced surface reconstruction or an oxygen depletion). Similar results for the predefinition of starting positions and excitation of chemical waves have been reported for the oxidation of CO on Pt(100) [159] and Pt(110) [160] via

laser irradiation; in these studies the initiation of the fronts was attributed to the generation of “holes” in the CO adlayer due to local thermal desorption. A major advantage of an electron-beam with respect to a laser is the spatial limitation of the resulting starting position of the chemical wave, which is theoretically restricted by the spot size of the applied beam ($\sim 80 \mu\text{m}$ for one of the lasers in the references mentioned before compared to $\sim 3 \text{ nm}$ for the electron-beam in the applied system).

From the applied sample temperature the occurrence of reaction fronts in the observed system could have been already expected from PEEM measurements performed by Schaak et al. [115]; by varying the temperature and the partial pressures of oxygen and hydrogen they were able to determine the parameter region for a reduction or oxidation front propagation in the system Rh(110) / $\text{O}_2 + \text{H}_2$. A direct comparison to the pressure values given in this reference is not possible, due to differences in the experimental setup and performance.

The elliptical shape of the oxygen free area in Fig. 5.10 (d), with the longer diagonal aligned along the $[1\bar{1}0]$ crystallographic axis, reflects an anisotropic propagation of the front with a higher diffusion speed along the direction of the troughs (compare Fig. 5.3). A similar behavior was observed by Mertens et al. at temperatures below 630 K [117]. The shape of the front was found to vary from an elliptical deformation in the observed direction to one with the longer diagonal along the $[001]$ axis depending on $p(\text{H}_2)$ and the surface temperature [117, 158]. The authors attribute this behavior mainly to adsorbate-adsorbate interactions. Minor distortions of the elliptical shape can be observed at the positions of larger scratches, which lead to local extensions of the reduction front (see Fig. 5.10 (d)). Most presumably this behavior is due to a faster diffusion of hydrogen atoms along these scratches.

Fig. 5.10 (e) to (g) show images of the reduction front acquired at a lower magnification level. It propagates with an average speed of $\sim 204 \text{ nm/s}$ in the $[1\bar{1}0]$ direction and $\sim 138 \text{ nm/s}$ in the $[001]$ direction, respectively (speed values calculated from the change of the size of the oxygen free area in $[1\bar{1}0]$ and $[110]$ direction, as measured optically with the software *Analysis* (Soft Imaging Systems)). In the top left part of Fig. 5.10 (e) a second, smaller reduction front is visible. Most presumably, the starting position of this wave was a defect site. The two fronts are propagating towards each other (Fig. 5.10 (f)), until they collide (Fig. 5.10 (g)) and merge (Fig. 5.10 (h)).

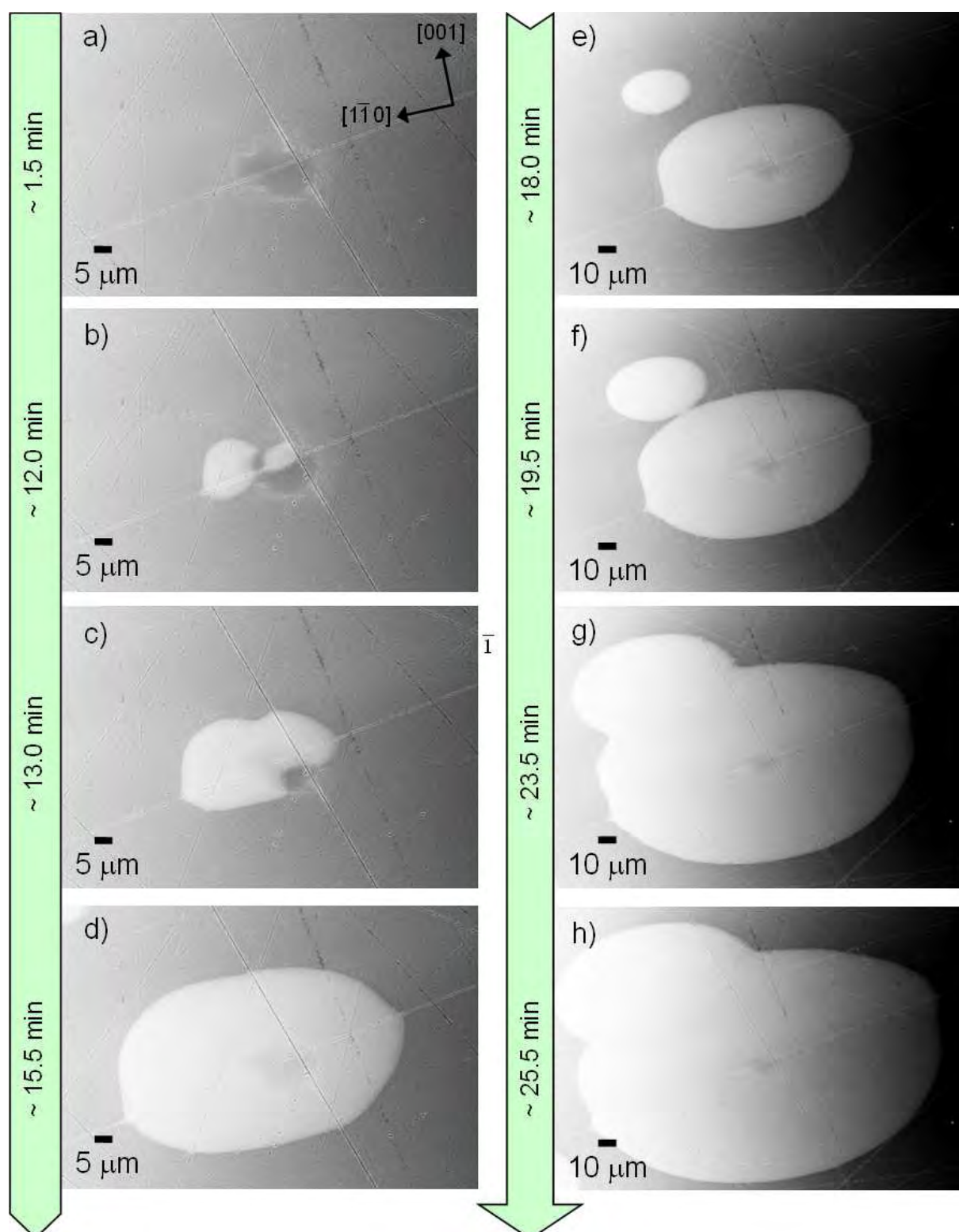


Fig. 5.10: SEM images of the reduction front formation and propagation on oxygen covered Rh(110) induced by hydrogen dosage ($p(\text{H}_2) = 6.0 \cdot 10^{-8}$ mbar). The times are given with respect to the start of H_2 dosage. Note that images (e) to (h) were acquired with a different magnification compared to images (a) to (d). The axis directions in (a) were acquired from LEED measurements (see Chapter 5.3). ($U = 15$ kV; $I = 3$ nA; plane sample)

The mechanism of reduction front formation and propagation is summarized in the scheme in Fig. 5.11. Oxygen dosage with a constant pressure leads to a surface covered with atomic oxygen after a certain time (see Fig. 5.11 (a)). In this situation, the adsorption of subsequently dosed hydrogen is inhibited, since all the adsorption sites are covered by oxygen. The dissociative adsorption of hydrogen can only take place on surface defects (strongly varied adsorption behavior of the surface) or areas formerly irradiated by the electron-beam (different oxygen-induced surface reconstruction or oxygen-free area due to electron induced desorption; see above) (Fig. 5.11 (b)). A certain amount of adsorbed hydrogen is necessary to start the reaction front, as it is obvious from the timescale of the images in Fig. 5.10. From these adsorption sites hydrogen is diffusing into the oxygen covered region, leading to the formation of water via an OH intermediate (Fig. 5.11 (c)), until the whole surface is oxygen free. Due to the nature of this reaction-diffusion mechanism, OH occurs at the front of the wave. The generated water molecules desorb quickly from the surface at the given sample temperature.

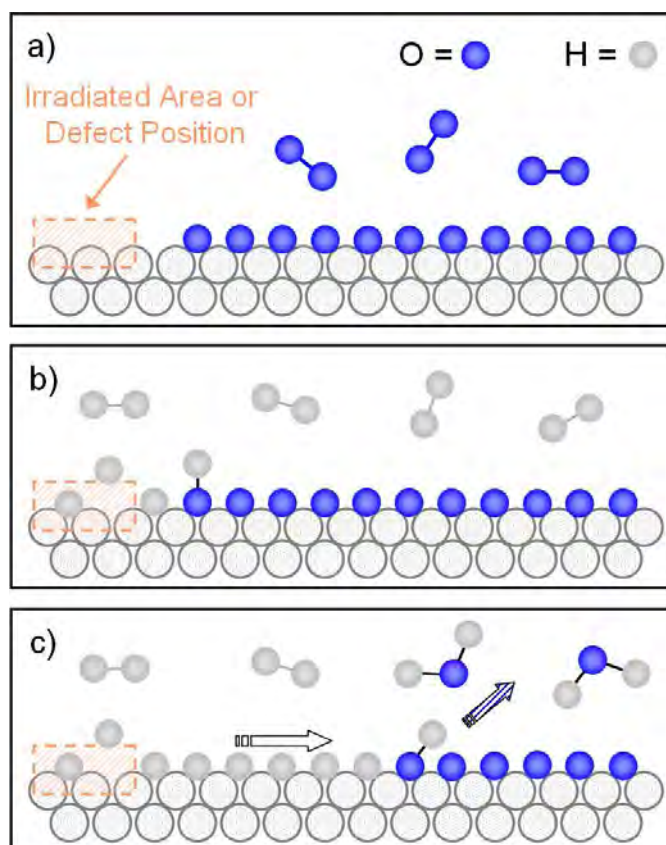


Fig. 5.11: Scheme, explaining the formation and propagation of a reaction front in the system Rh(110) / O₂ + H₂. a) Oxidation of the surface. b) Dissociative adsorption of hydrogen on surface defects or on previously irradiated areas. c) Front propagation.

Typically Rh(110) / O₂ + H₂ is a bistable system, with either reduction fronts propagating into the oxygen covered surface or oxidizing waves diffusing into the hydrogen covered area, depending on the actual partial pressures. Therefore, upon the simultaneous dosage of oxygen and hydrogen also a reverse direction of front propagation compared to Fig. 5.10 was expected.

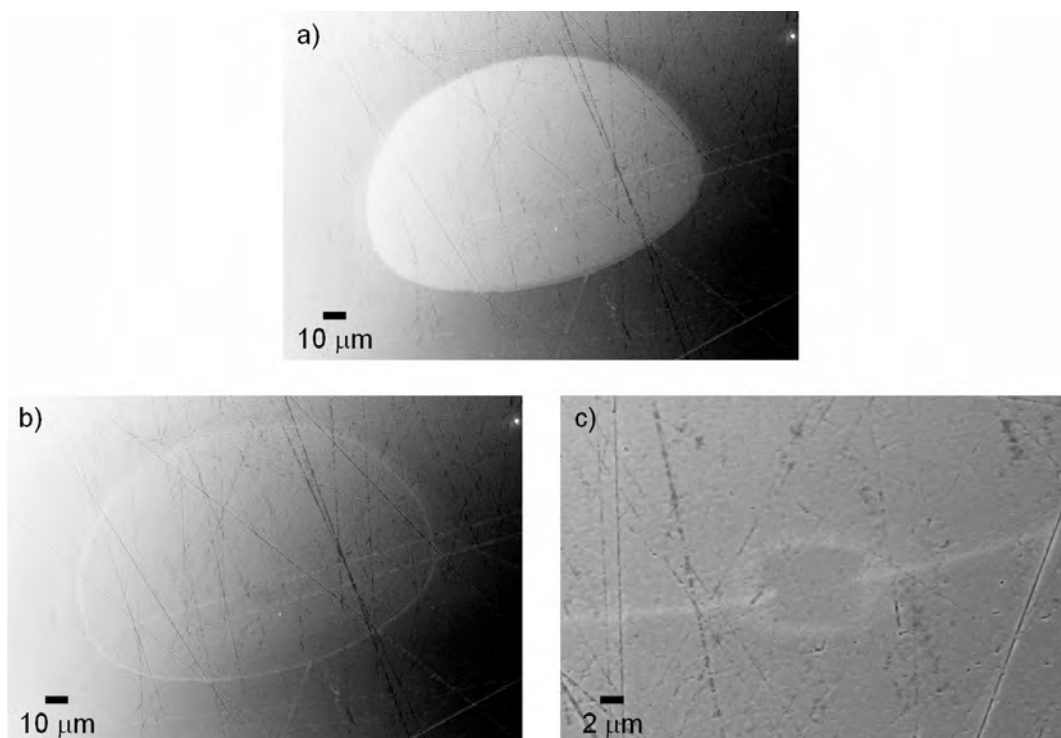


Fig. 5.12: SEM images of the oxidation of a hydrogen covered area. a) Image of a reduction front during hydrogen dosage ($p(\text{H}_2) = 2.0 \cdot 10^{-8}$ mbar). The image was acquired ~ 19.5 min after the start of the hydrogen dosage. b) Image of the same area as in (a) after the simultaneous dosage of oxygen ($p(\text{O}_2) = 2.5 \cdot 10^{-8}$ mbar) and hydrogen ($p(\text{H}_2) = 2.0 \cdot 10^{-8}$ mbar) for 7 min. c) High magnification image of the remaining structure after oxidation. The bright rectangular frame in the middle is the result of former electron irradiation. ($U = 15$ kV; $I = 3$ nA; plane sample)

Fig. 5.12 (a) shows a reaction wave induced by hydrogen dosage ($p(\text{H}_2) = 2.0 \cdot 10^{-8}$ mbar) at a surface temperature of ~ 610 K. The starting position of the front was again a previously, under oxygen dosage ($p(\text{O}_2) = 2.0 \cdot 10^{-7}$ mbar) irradiated area, similar to the one in Fig. 5.10 (a). Since the applied hydrogen pressure was lower compared to the experiment shown in Fig. 5.10, average front propagation was now estimated to be ~ 106 nm/s in the $[1\bar{1}0]$ direction and ~ 76 nm/s in the $[001]$ direction, respectively.

In Fig. 5.12 (b) an image of the same region is depicted after ~ 7 min of co-dosing oxygen ($p(\text{O}_2) = 2.5 \cdot 10^{-8}$ mbar) and hydrogen ($p(\text{H}_2) = 2.0 \cdot 10^{-8}$ mbar), with a total background pressure of $4.5 \cdot 10^{-8}$ mbar. The formerly oxygen free oval structure appears in the SEM not as bright as before the hydrogen dosage, indicating water formation and desorption and a subsequent oxygen adsorption in that region. No chemical wave propagation was observed. A possible explanation for the spatially homogeneous water formation in the reduced area is given by the literature: according to experiments performed by Schaak et al. the parameter region for the appearance of oxidation fronts in the system Rh(110) / $\text{O}_2 + \text{H}_2$ is very narrow [115]. Obviously, hydrogen bonding to the surface is much weaker than the oxygen one.

Still visible in Fig. 5.12 (b) is a bright line feature surrounding the former oxygen free oval structure. Fig. 5.12 (c) shows an image of a certain part of this residual after the end of the gas dosage. The bright rectangular frame in the center is the result of an additional scan at a higher magnification level, which was performed prior to the acquisition of the image in (c); this scan resulted also in a local vanishing of the bright line at the exposed position, which indicates that the residual can be locally modified via electron irradiation. The origin of this bright line is unclear. From literature it is well-known that a different surface reconstruction is observed directly in the front region compared to the ones in the reduced or oxidized areas [23]. It can therefore be assumed that the residual in Fig. 5.12 (b) is the result of a different surface reconstruction, which might be further modified by electron irradiation (compare Fig. 5.12 (c)), e.g., due to electron induced oxygen desorption.

Summarizing the data presented in this chapter the basic message is that for the system Rh(110) / $\text{O}_2 + \text{H}_2$ it is possible not only to visualize reaction fronts via an SEM but also to predefine their starting positions by electron irradiation of an area during oxygen dosage. The resulting reduction waves (upon hydrogen dosage) show propagation anisotropy with a higher speed along the $[1 \bar{1} 0]$ direction, at least for the applied parameters. The observed propagation speed depends strongly on the applied hydrogen pressure.

5.5 Influence of additional gas dosage

From literature it is well-known that the deposition of iron pentacarbonyl on metal surfaces like Pt(111) and Ni(100) at sample temperatures of 275 K and 300 K, respectively, results in a steady state growth of the resulting iron layer and therefore in an autocatalytic decomposition of $\text{Fe}(\text{CO})_5$ on the growing iron film [144-146]. The question is therefore, if a similar effect can also be observed for the iron deposits generated via EBID on Rh(110), which would result in an influence of the additionally applied precursor dosage time on the amount of deposited

material. Fig. 5.13 shows results of an experiment that was performed on Sample I. Based on the time of the start of the gas dosage, the same pattern was deposited after 15 and 233 min, which results in an additional precursor dosage time of 246 and 28 min, respectively, after the generation of the pattern. The applied template is depicted in Fig. 5.13 (a). It has to be noted, that during the whole experiment a loop number of two was adjusted in the *Elphy Quantum* software, which resulted in a double irradiation in direct succession at the same position. For the generated area (circles) and line deposits this resulted in a total electron dose that can be calculated by doubling the values given in Fig. 5.13 (a) and, in combination with thermal drift of the sample, in a partial, lateral enlargement of the structures. In case of the dot deposits the double irradiation and thermal drift lead to the generation of identical, separated dots in close vicinity. A summary of the generated structures in both patterns is given in the following:

- **Two circles** with a diameter of 400 and 800 nm, respectively, each one deposited with a total electron dose of 79.6 C/cm^2
- **Dot matrix** consisting of 20 dots; the electron dose is increasing from the bottom left (2.52 nC) to the top right (3.60 nC) by 0.12 nC per dot. Two dots each were deposited with the same electron dose and are in close proximity of each other.
- **Three lines** with a length of 600 nm, deposited with a total electron dose of 176.0, 208.0 and $240.0 \mu\text{C/cm}$.

An image of the structures irradiated shortly after the beginning of the gas dosage (15 min; additional gas dosage for 246 min) is depicted in Fig. 5.13 (b). The exposed surface area and the direct surrounding appear dark in the SEM; this can be interpreted as due to a decreased SE yield of the deposited iron associated with the lower atomic number compared to rhodium [48]. The observed deposits appear connected to each other; individual structures of the template in Fig. 5.13 (a) are hardly observed. Remarkable in Fig. 5.13 (b) are the centers of the circles (originally exposed area), which appear slightly brighter than the surrounding region. Upon close inspection (not shown here), these areas turn out to consist of small clusters aligned along the previous path of the electron-beam; their bright appearance can be attributed to height growth.

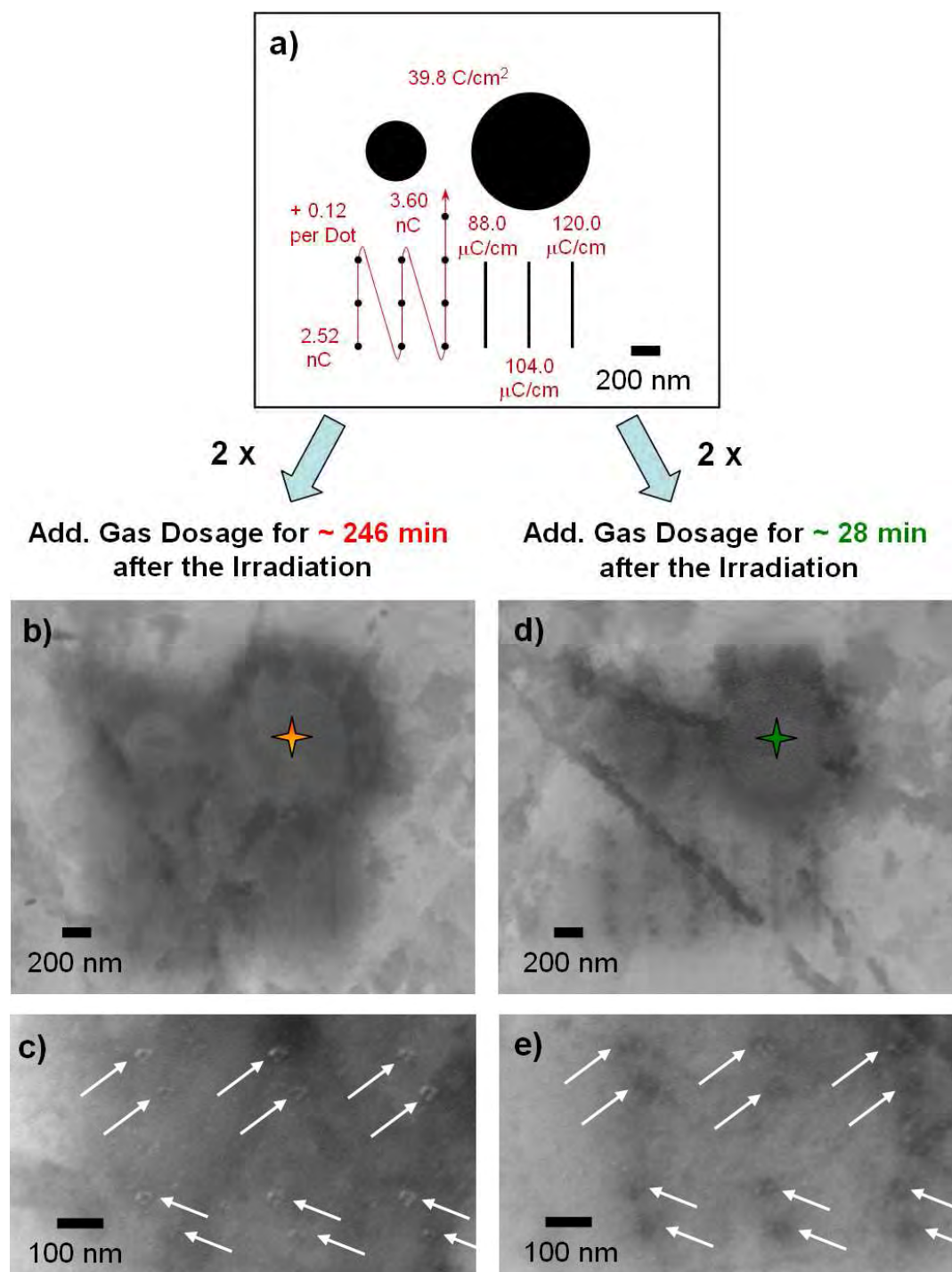


Fig. 5.13: Influence of the additional gas dosage time on the generated deposits. Sample I was irradiated two times according to the template in (a): b) roughly 15 min after the start of the gas dosage, resulting in an additional gas dosage of 246 min and d) roughly 233 min after the start of the gas dosage, with an additional dosage time of 28 min after the irradiation. Both patterns were irradiated twice at the same position (see text). c) and e) show high magnification images of the two bottom rows of the dot matrix in (b) and (d), respectively. Brightness and contrast were significantly changed in (c) and (e) to improve visualization. ($U = 15 \text{ kV}$; $I = 3 \text{ nA}$; tilted sample)

Fig. 5.13 (c) shows a high magnification image of one part of the dot matrix (two bottom rows); the dots appear as bright features ($\varnothing \approx 30$ nm; indicated by the bright arrows in (c)) with a dark center. Their nonuniform appearance is mainly attributed to a topographical contrast (bright areas for high deposits, dark areas for flat ones). Similar results have been reported by Reimer et al. [161] and Amman et al. [162] for EBID of carbonaceous deposits from residual gases. They interpreted this observation to result from deposition in the precursor limited regime, with surface diffusion being the prevalent supply mechanism of the precursor molecules (diffusion enhanced regime; see Chapter 2.7); a higher amount of material is therefore deposited on the edges of the electron-beam impact area, leading to an inhomogeneous appearance of the deposits. The dark regions surrounding the irradiated areas in Fig. 5.13 (b) and (c) are attributed to the deposition of material by electron exposure due to proximity effects, i.e., the scattering of electrons in the sample or on already deposited material (compare the BSE and FSE proximity effect described in Chapter 2.7). This “unintended” deposition is the main reason why individual structures are hardly observed in Fig. 5.13 (b), since the resulting deposits partly overlap.

Fig. 5.13 (d) shows a micrograph of the structures deposited ~ 233 min after the start of the gas dosage (additional gas dosage for 28 min after the irradiation). Compared to Fig. 5.13 (b) the unintended deposition in the surrounding of the structures is significantly reduced; e.g., each single line is clearly recognizable as a continuous, dark deposit. The centers of the circular structures consist again of small, bright clusters, even though they are not as dense as in Fig. 5.13 (b). In contrast to Fig. 5.13 (c) the point deposits in the dot matrix appear as dark features ($\varnothing = 45$ nm) with only minor indications for height growth (see Fig. 5.13 (e); indicated by the bright arrows).

The height growth and the stronger deposition due to proximity effects observed in Fig. 5.13 (b) and (c) indicate, that a higher amount of material was deposited in the pattern in (b)/(c) than in (d)/(e). Since both patterns were irradiated with the same template and electron dose, this observation is attributed to the additional gas dosage time after the irradiation (246 min for the pattern in (b)/(c) compared to 28 min for the pattern in (d)/(e)) and thereby to an autocatalytic dissociation of $\text{Fe}(\text{CO})_5$ on the iron deposits produced via EBID. A significant influence of the precursor dosage before the pattern generation in (b)/(c) (15 min) can be excluded, as the amount of material deposited during this time in the absence of the electron-beam is supposed to be rather low (compare the green spectrum in Fig. 5.16 (a), which displays the amount of material deposited in the non-irradiated area after the whole experiment).

Another possible explanation for the described differences might be a change in the precursor gas composition during the dosing process. This assumption is supported by recent results of QMS measurements for the dosage of iron pentacarbonyl onto SiO_x (300 nm) / Si (two spectra measured 10 min and 52 min after the start of the gas dosage; not shown here), in which all relevant signals decrease during the gas dosage, even though the background pressure in the chamber is kept constant (upon dosage of Fe(CO)₅ the leak dosage valve has to be closed stepwise, especially during the first 30 min, in order to keep the background pressure in the chamber constant); additionally, the ratio between the CO and iron pentacarbonyl signals were slightly increasing in favor for carbon monoxide. Possible explanations for the described effects are either the decomposition of the precursor on steel walls of the chamber and the gas dosage system or a change in the pumping behavior of the applied ion getter pump. The interaction of iron pentacarbonyl with steel walls has already been studied by Henderson et al. [163]. They reported a disproportionately large amount of CO upon the dosage of Fe(CO)₅, which was attributed to the partial decomposition of molecules on the steel walls of the doser assembly under UHV conditions. Similar to our QMS measurements they also observed an increase of the CO⁺ / Fe⁺ ratio with an increasing dosage time, indicating the autocatalytic dissociation of molecules on the Fe_x(CO)_y covered doser walls.

To obtain additional information on the chemical composition of the different deposits, local AES was performed in the center of the larger circles in Fig. 5.13 (b) (red/orange marker) and (d) (green marker). The resulting spectra are displayed in Fig. 5.14. The red spectrum acquired on the deposit in Fig. 5.14 (b) one day after the exposure shows three Fe LMM peaks between 570 and 710 eV, two O KLL signals at 492 and 512 eV and no rhodium peaks. A quantitative analysis via the damping of the Rh signal at 302 eV yields a layer thickness of more than 1.5 nm, assuming a continuous layer of pure iron (note that since no Rh substrate signal is detected any more, only a lower limit can be given for the thickness). Surprisingly, a spectrum acquired at the same position five days after the irradiation (orange spectrum in Fig. 5.14) displays a reduced intensity of the oxygen signals (only 72 %) and a 6 % increased intensity for the iron peaks (compared to the red spectrum in Fig. 5.14). Also a minor amount of carbon is now visible at ~ 273 eV. It is unclear, whether this obvious change in the deposit composition can solely be attributed to the waiting period between the two measurements (four days) or if the additionally applied electron dose during the acquisition of the images and spectra has a specific influence (e.g., electron induced desorption of oxygen).

The significant decrease of the oxygen peaks indicates at least partly a weakly bound oxygen containing species, which is covering the deposit and therefore damps the iron signals.

In contrast to that, the AE spectrum acquired on the larger circle in Fig. 5.13 (d) six days after the irradiation (green spectrum in Fig. 5.14) is dominated by the Fe LMM Auger transitions, while also a small O KLL peak and a minor amount of carbon (similar to the orange spectrum in Fig. 5.14) is observed. Again, no Rh substrate signals are visible, indicating an iron layer with a thickness of more than 1.5 nm (calculated from the damping of the Rh signal as described before). A spectrum measured on the same deposit one day after the irradiation (not shown here) appears similar, with nearly identical peak intensities. A change in the deposit composition, as discovered for the structures in Fig. 5.13 (b), is therefore not observed.

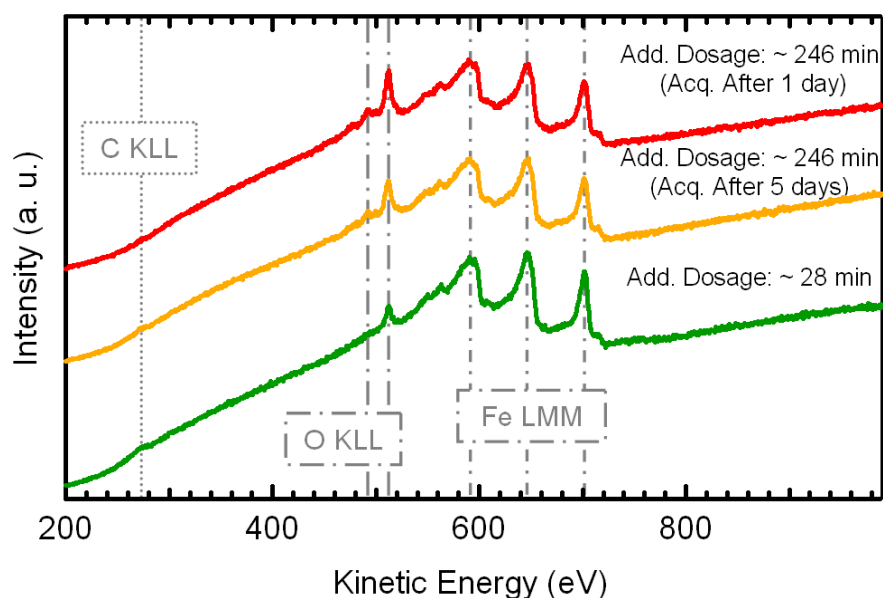


Fig. 5.14: Local Auger spectra acquired at the positions marked in 5.13 (b) (red and orange spectrum) and 5.13 (d) (green spectrum).

Compared to the spectra that were acquired on the deposits in Fig. 5.13 (b) (additional gas dosage time of 246 min; red and orange spectra in Fig. 5.14) the green spectrum exhibits some significant differences in the intensities of the observed elements: the oxygen peak amounts only to 44 % compared to one in the red spectrum and 61 % with respect to the orange one, while the iron signals are increased by 23 % and 15 %, respectively. Apparently, the structures that were generated shortly after the start of the gas dosage and thus experienced a much higher additional gas dosage after the irradiation (compare Fig. 5.13 (b)/(c)), showed a lower metal purity than the other deposit (compare Fig. 5.13 (d)/(e)).

The described variations in the chemical composition of the deposits are again attributed to an autocatalytic dissociation of $\text{Fe}(\text{CO})_5$ on already deposited iron; compared to the electron-induced deposition, this process might lead to an incomplete decomposition of the precursor molecules and therefore to an increased oxygen contamination in the structures, as it is observed for the red spectrum in Fig. 6.14. Additional electron irradiation might in this case result in further bond-breaking within the generated fragments and thus in a purification of the deposited material (compare the orange spectrum in Fig. 5.14). Yet, it has to be noted, that the observations in the AE spectra (see Fig. 5.14) could also be the result of variations in the precursor gas composition during the experiment (see above). Depositing while simultaneously monitoring the gas composition with a QMS would be necessary to address this topic. The occurrence of an additional precursor fragment at the beginning of the gas dosage procedure can be ruled out, since QMS measurements of other experiments showed no indications for that.

In summary, it can be stated that deposits generated via EBID on Rh(110) are influenced by the additionally applied precursor dosage time after the generation of the structures. Via SEM images it was shown, that an increasing amount of material was deposited with an increase of the additionally applied dosage time (compare Fig. 6.13). This effect is mainly attributed to an autocatalytic decomposition of $\text{Fe}(\text{CO})_5$ molecules on the generated structures, even though specific changes in the precursor gas composition during the experiment, e.g., due to reactions with the steel walls of the chamber, cannot be excluded. Additionally, variations in the chemical composition of the deposits could be observed via AES, i.e., that the structures, which experienced a longer additional precursor dosage, exhibited a higher oxygen contamination.

5.6 Surface quality determines the selectivity of EBID

A prerequisite for the local generation of nanostructures by EBID is the selectivity of the deposition process. In the framework of this thesis this means that deposits should only be generated in the region in which electron – precursor interactions occur. Due to the proximity effects described in Chapter 2.7 this also takes place in close vicinity of the area directly irradiated by the electron-beam. The size of the resulting interaction area varies with the electron-beam parameters (e.g., beam energy) and the applied material (e.g., density of the substrate). Therefore, the applied sample material can directly affect the shape and size of the deposits [32, 40, 162].

The influence of the substrate on the deposition process has been mainly investigated with respect to electron – substrate interaction or substrate – precursor interaction (e.g., adsorption, diffusion), as it has been already described in Chapter 2.7 [119]. In this context, the influence of the surface quality on the deposition process has not been studied in detail so far. In this chapter, it will be demonstrated how important this parameter is for the whole deposition process and how it might be exploited for pattern generation applications.

5.6.1 Iron deposition on different sample states

Three different states of the rhodium crystal, varying mainly in their roughness and the quality of their surface reconstructions, were used for the experiments. These samples, namely Sample I, Sample II and Sample III, have already been described in detail in Chapter 5.3.

EBID on a low quality Rh(110) surface (Sample I):

In Fig. 5.15 (a) an SEM image of Sample I after EBID of the pattern shown in Fig. 5.13 (a) with a lower electron dose is depicted² (total electron dose for the circles 26.6 C/cm^2 and for the lines $16.0 \mu\text{C/cm}$, $48.0 \mu\text{C/cm}$ and $80.0 \mu\text{C/cm}$; electron dose for the dots: 0.12 nC (bottom left) to 1.2 nC (top right)). Clearly visible are the two circles, which appear darker as the rest of the surface; as described before, this is interpreted as due to a lower SE yield from the deposited iron compared to the clean rhodium surface (again associated with the higher atomic number of Rh compared to Fe [48]). The size of the deposits fit quite well to the originally exposed areas (400 nm and 800 nm diameter; marked by white dotted line); a slight darkening in the direct surrounding indicates some deposition due to proximity effects (compare Chapter 2.7).

² Note, that on Sample I the experiment was performed by a double irradiation of each pattern at the same position (compare Chapter 5.5). In combination with thermal drift this resulted in the generation of two separated dots in close vicinity at each position of the dot matrix.

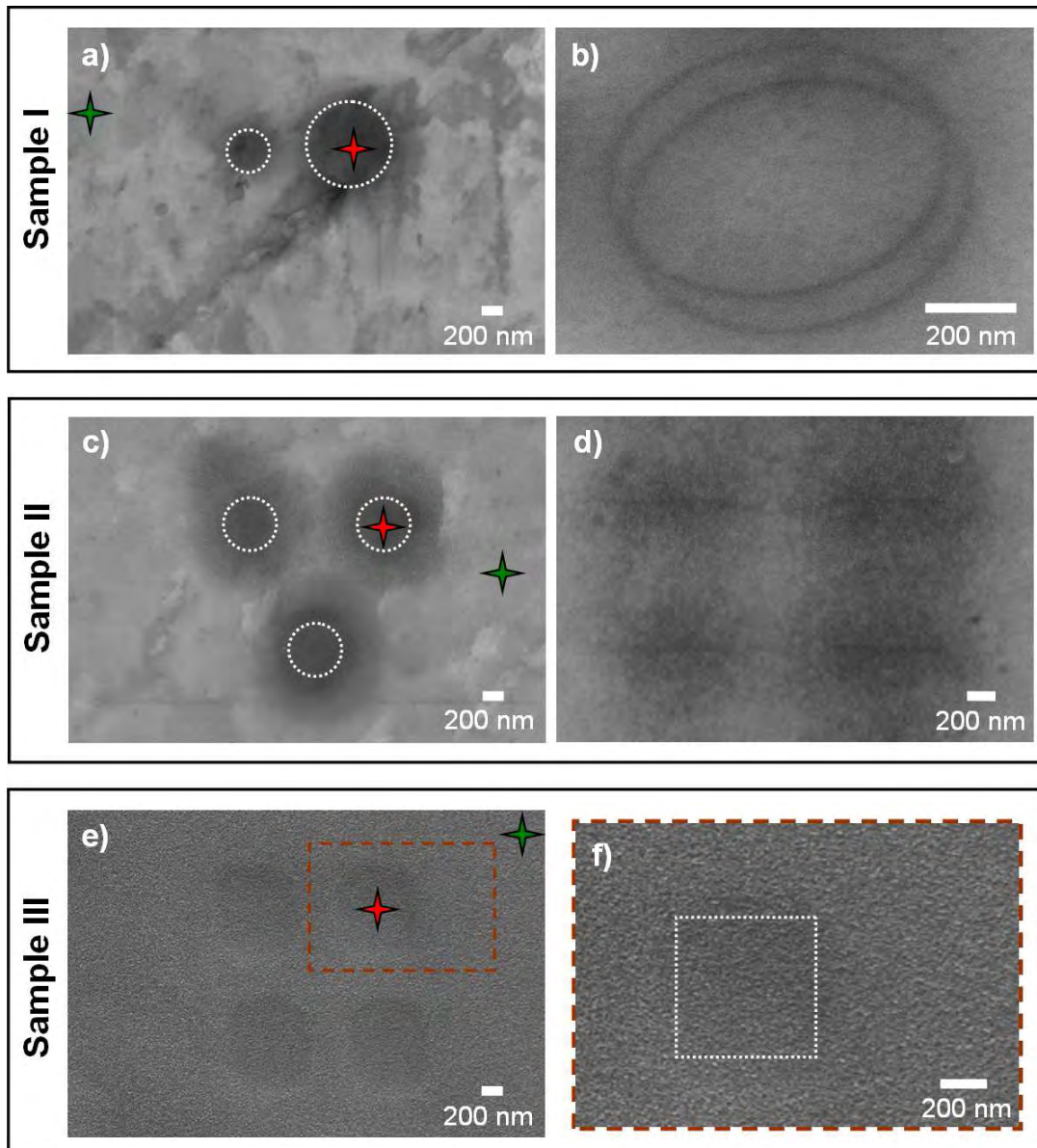


Fig. 5.15: SEM images of EBID structures deposited on different surface states of the Rh(110) crystal. The markers in (a), (c) and (e) correspond to the positions where the Auger spectra in Fig. 5.16 were acquired. The white dotted lines in (a), (c) and (e) mark the positions of the irradiated areas. **Sample I:** a) Same pattern as in Fig. 5.13 (a), deposited with a lower electron dose. b) Two ellipses deposited with an electron dose of $80 \mu\text{C}/\text{cm}$ each. **Sample II:** c) Three circles were deposited with an electron dose of $13.3 \text{ C}/\text{cm}^2$ (upper left), $26.6 \text{ C}/\text{cm}^2$ (upper right) and $39.8 \text{ C}/\text{cm}^2$ (bottom). d) Four lines deposited with an electron dose of $8 \mu\text{C}/\text{cm}$ (bottom left), $12 \mu\text{C}/\text{cm}$ (top left), $24 \mu\text{C}/\text{cm}$ (bottom right) and $28 \mu\text{C}/\text{cm}$ (top right). **Sample III:** e) The dark squares correspond to areas irradiated with an increasing electron dose from $22.6 \text{ C}/\text{cm}^2$ (lower left) to $26.6 \text{ C}/\text{cm}^2$ (upper right). f) Blow-up of the upper right square in (e). (Images (a), (c), (d), (e), (f): $U = 15 \text{ kV}$; $I = 3 \text{ nA}$; tilted sample / Image (b): $U = 15 \text{ kV}$; $I = 400 \text{ pA}$; plane sample)

To obtain additional chemical information local AE spectra were acquired after the EBID process at exposed and non-exposed regions of the surface, as indicated by the color-coded markers in Fig. 5.15 (a). Fig. 5.16 (a) shows the corresponding spectra as well as a spectrum of the free Rh surface before the experiment (blue). The red spectrum was recorded after the EBID process in the larger circular area exposed to the electron-beam (red marker in Fig. 5.15 (a)). It is dominated by the Fe LMM Auger peaks at 593, 647 and 702 eV; the Rh substrate signals are visible with a very low intensity, indicating a considerable amount of iron deposited on top of the rhodium. A quantitative analysis of the layer thickness via the damping of the Rh signal yields a value of ~ 1.4 nm assuming a continuous layer of pure iron. Additionally, small peaks for carbon (~ 273 eV) and oxygen (~ 493 eV and 513 eV) KLL transitions are observed, which are attributed to the unintended decomposition of CO ligands from the precursor. The total amount of these contaminations was estimated to be below 8 % (2 % carbon contamination, as derived from a comparison to the spectrum of a thick carbon layer under consideration of deposit thickness (see Chapter 3.4); the oxygen contamination was roughly estimated to be lower than 6 % (see Chapter 3.4)), which indicates a high purity of > 92 % of the deposited iron. The green spectrum in Fig. 5.16 (a) was acquired on the area not exposed to the electron-beam (see Fig. 5.15 (a)); it shows large Rh peaks, but also small signals due to deposited Fe. Furthermore, small but significant signals for Cu LMM transitions are visible at 770, 843 and 918 eV. The origin of the latter is unclear. The fact that the signals are not observed in the spectrum of the irradiated region implies that the copper is situated directly on the surface and covered by the deposited iron. Some spectra acquired before the EBID process showed minor indications for a copper contamination, but to a smaller extent as observed for the unexposed region in Fig. 5.16 (a). A possible explanation might be that the Cu originates from the Cu electrodes used for spot welding during the mounting of the crystal. Another explanation to be considered could be a contamination in the precursor flow, resulting from a copper plate at the bottom of the storage device used for the first experiments. This explanation is rather unlikely, since a similar contamination was not observed in other experiments, e.g., on silicon samples or at other rhodium sample states; additionally, the red AE spectrum in Fig. 5.15 (a) exhibit no indications for copper in the irradiated area.

The observed Fe peaks in the green spectrum in Fig. 5.16 (a) are considerably smaller (only 21 %) than those in the surface region exposed to the electron-beam (red spectrum). The Rh signals are significantly damped in comparison to the surface before the EBID process (blue spectrum) but still more intense than for the exposed surface (red spectrum). From these

data it is obvious, that in the irradiated area a higher amount of material is deposited compared to the non-irradiated region. A determination of the layer thickness is difficult in the case of the unexposed area, since it is also covered by a significant amount of copper; assuming a continuous layer of pure iron, a value of 0.4 nm could be calculated from the damping of the Rh peak at ~ 302 eV. The fact that a higher amount of iron is deposited in the exposed region implies that the EBID process on Sample I, i.e., the low quality Rh(110) surface, is moderately selective. The selectivity is, however, lower than observed for EBID with $\text{Fe}(\text{CO})_5$ on Si(100), where no iron was detected in the unexposed area (see Chapter 6.4).

Additionally, the potential to write line structures on Sample I was studied. In Fig. 5.15 (b) the SEM image of two spatially well-defined ellipses is depicted, each deposited with an electron dose of $80 \mu\text{C}/\text{cm}$ (template ellipse with a size of ~ 700 nm for the longer diagonal and ~ 465 nm for the shorter diagonal). Both structures comprise continuous lines with a diameter below 25 nm. Only minor indications for iron deposition due to proximity effects are visible in the direct surrounding of the ellipses, even though a relatively high electron dose (compared to the line structures deposited on Sample II (see Fig. 5.15 (d)) was applied. This absence of unintended deposits is mainly attributed to the roughness of the surface; thereby the trajectories of the backscattered electrons are strongly disturbed (e.g., due to shadowing effects near the surface), leading to a reduction of the effective electron interaction area and therefore to the generation of relatively defined deposits on Sample I. A significant influence of the copper contamination can be ruled out, since the adlayer is supposed to be too thin to exhibit a relevant effect on the lateral extent of the backscattered electrons.

EBID on an improved Rh(110) surface (Sample II):

Fig. 5.15 (c) shows an SEM image of Sample II after the deposition of three circular structures (template circles: $\varnothing = 500$ nm), fabricated with electron doses of $13.3 \text{ C}/\text{cm}^2$ (upper left), $26.6 \text{ C}/\text{cm}^2$ (upper right; identical electron dose as used for the two circles in Fig. 5.15 (a)) and $39.8 \text{ C}/\text{cm}^2$ (bottom). Again, the structures appear darker in comparison to the free surface, due to a reduced SE yield of the iron compared to rhodium. In contrast to Sample I, the deposits are now clearly enlarged as compared to the directly exposed area (marked by white dotted line); this is attributed to proximity effects (mainly the BSE proximity effect), which were described in Chapter 2.7. The actual broadening due to these effects can be roughly estimated by the diameter of the BSE exit area. A Monte Carlo simulation of the BSE area on Rh(110) with the software *CASINO V2.42* [92] for a 3 nm wide 15 kV electron-beam

(as used in the experiment; compare Fig. 2.13 (b) in Chapter 2.7) yields a radius of ~ 450 nm, which is in good agreement with the observed broadening in the experiment. The outer region of the structures shows also a reduced contrast compared to the center (appears not as dark in the SEM), indicating a lower amount of deposited iron in that area. This observation will be discussed in detail in Chapter 5.7.

The AE spectra acquired for Sample II are shown in Fig. 5.16 (b), with the blue spectrum again displaying the surface before the experiment. The red spectrum was acquired after the EBID process in the upper right circular area (compare Fig. 5.15 (c)). It is dominated by the Fe LMM Auger transitions, whereas the Rh substrate signals are strongly damped, indicating again a high amount of deposited iron. A quantitative analysis of the layer thickness via the damping of the Rh signal yields a value higher than 1.5 nm, assuming a homogeneous, pure iron deposit (note that since the Rh substrate signal is too small to determine the signal intensity properly, only a lower limit can be given for the thickness). Also, small peaks for carbon and oxygen are observed, again presumably resulting from the unintended decomposition of CO ligands of the precursor; compared to the corresponding spectrum on Sample I the C peak is increased, while the O signal shows a similar intensity. In this case, the total amount of the contamination is below 13 % (8 % carbon contamination, as derived by a comparison to the spectrum of a thick carbon layer (compare Chapter 3.4); oxygen contamination roughly estimated to be lower than 5 % (compare Chapter 3.4)), which indicates again a high metal purity of > 87 % for the deposit. The green spectrum in Fig. 5.16 (b) was measured on the non-irradiated area (see Fig. 5.15 (c)). Similar to Sample I it is dominated by the Rh peaks, but also shows Fe and C signals. The Fe peaks are again considerably smaller (only 16 %) than those in the irradiated region (red spectrum), while the Rh signals are slightly damped in comparison to the surface before the EBID process. From the data in Fig. 5.16 (b), the following picture can be established for the deposition on Sample II: a high amount of almost pure iron was deposited in the irradiated area via the EBID process (thickness > 1.5 nm; iron content > 87 %) with only small contaminations of carbon and oxygen due to the unintended dissociation of carbon monoxide ligands. In the unexposed region a significantly smaller amount of iron was found (estimated thickness: 0.2 nm). The observed results indicate therefore a similar selectivity of the deposition process as described for Sample I, i.e., a moderately selective deposition process.

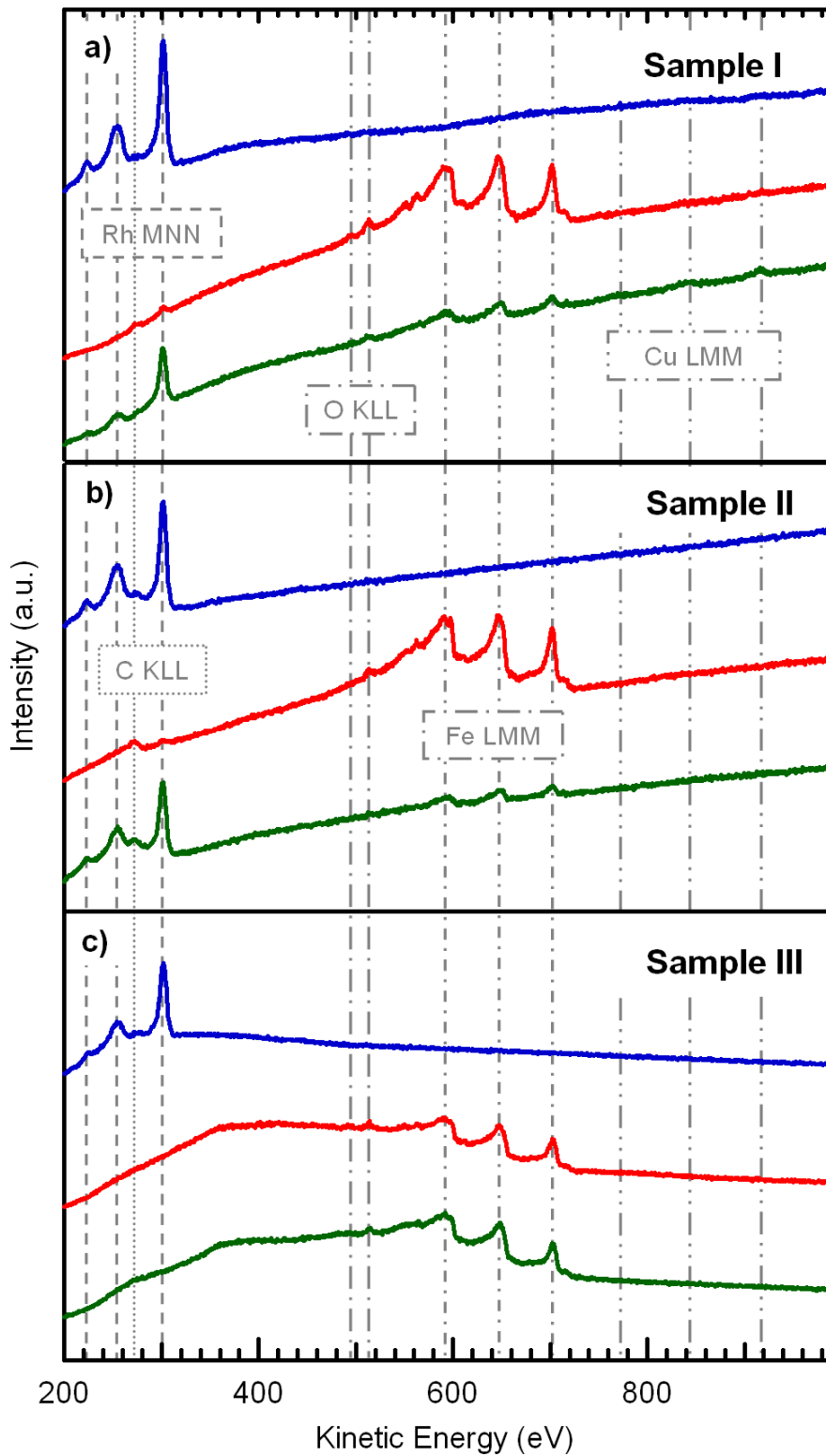


Fig. 5.16: Local AE spectra acquired on a) Sample I, b) Sample II and c) Sample III. The blue spectra were measured before EBID and are identical to the respective spectra in Fig. 5.5. The red and green ones were acquired on the irradiated and non-irradiated areas, respectively, as displayed by the corresponding markers in Fig. 5.15 (a), (c) and (e).

Fig. 5.15 (d) displays an SEM image of four lines (length: 400 nm) deposited on Sample II with an electron dose of 8 $\mu\text{C}/\text{cm}$ (bottom left), 12 $\mu\text{C}/\text{cm}$ (top left), 24 $\mu\text{C}/\text{cm}$ (bottom right) and 28 $\mu\text{C}/\text{cm}$ (top right). The structures appear rather diffuse, with a defined feature in the center (originally irradiated area) and a lot of material deposited in the direct surrounding. This unintended deposition close to the region exposed to the electron-beam is again attributed to proximity effects, similar as it was observed for the circles in Fig. 5.15 (c). Compared to the ellipses deposited on Sample I (see Fig. 5.15 (b)), the deposition due to proximity effects in the surrounding of the irradiated lines is enhanced, even though a much lower electron dose was applied (factor 1/10 to $\sim 1/3$). This phenomenon is mainly assigned to the reduction of the surface roughness in Sample II, which leads to a reduced disturbance of the backscattered electron trajectories (compared to Sample I) and thus to a higher amount of unintended deposition. An influence resulting from an autocatalytic dissociation of $\text{Fe}(\text{CO})_5$ due to an additional gas dosage after the irradiation of the pattern in (d) (compare Chapter 5.5) can be excluded, as the additional dosage time (~ 70 min for the structures in (d)) was even shorter than the one applied for the ellipses in (b) (Sample I; ~ 155 min).

EBID on a perfectly ordered Rh(110) surface (Sample III):

In Fig. 5.15 (e) an SEM micrograph of four quadratic structures (template squares: 600 nm x 600 nm) deposited on Sample III with an increasing electron dose from the lower left (22.6 C/cm^2) to the upper right (26.6 C/cm^2) is depicted. The resulting EBID deposits are hardly distinguishable from the rest of the surface; only a slight darkening of the exposed areas indicates their position upon close inspection. Overall, the substrate appears more or less homogeneously structured with small protrusions (size: 9 - 23 nm; see blow-up of Fig. 5.15 (e) in Fig. 5.15 (f)), in contrast to the almost featureless, smooth appearance of the clean, unexposed surface in Fig. 5.6 (e) and (f); note, that an image acquired before the deposition procedure at a magnification level similar to the one in Fig. 5.15 (e) and (f) showed the same result), i.e., a structureless surface.

Local AE spectra were again acquired after the EBID process at irradiated (marked by a white dotted line in Fig. 5.15 (f)) and non-irradiated regions of the surface (see color-coded markers in Fig. 5.15 (e)). The corresponding spectra together with a spectrum of the free Rh surface before the experiment (blue; identical to the black spectrum in Fig. 5.5) are depicted in Fig. 5.16 (c). As already described in Chapter 5.3, the differences in their overall shape compared to the spectra in Fig. 5.16 (a) and (b) are due to the different geometry of the applied standard sample plate. The red spectrum in Fig. 5.16 (c) was recorded after the

experiment in the upper right quadratic area exposed to the electron-beam (red marker in Fig. 5.15 (e)). Similar to Sample I and Sample II it is dominated by the Fe LMM Auger peaks between 570 and 710 eV; the Rh substrate signals are completely suppressed, indicating a considerable amount of deposited iron on the rhodium surface. A quantitative analysis via the damping of the Rh signal yields a layer thickness of more than 1.5 nm, assuming a continuous layer of pure iron (note that since no Rh substrate signal is detected any more, only a lower limit can be given for the thickness). No C KLL signal and only a small oxygen KLL peak are observed, indicating a high purity of the Fe deposit; the O concentration can only be roughly estimated to be lower than 4 % (compare Chapter 3.4). When comparing the spectrum of the irradiated area (red) in Fig. 5.16 (c) with that of the unexposed region (green) it becomes evident that both appear very similar. In the unexposed region again only Fe and O signals are observed. The O signal exhibits a slightly lower intensity than for the irradiated area. Since for both, the exposed and unexposed surface, no signals of the rhodium substrate are detected, the deposited iron layers in both regions are thicker than 1.5 nm.

The almost identical Fe peak intensities of the spectra in Fig. 5.16 (c) and the absence of a pronounced topographical contrast in SEM (Fig. 5.15 (e) and (f)) indicate that for Sample III the amount of deposited Fe is very similar for the regions exposed and not exposed to the electron-beam. Thus, for the well defined Rh(110) surface the decomposition of the precursor $\text{Fe}(\text{CO})_5$ and consequently the deposition of Fe does not rely on the electron induced process. The observed effect can be attributed to the catalytic dissociation of $\text{Fe}(\text{CO})_5$ molecules on the well prepared Rh(110) surface and thereafter as an autocatalytic decomposition on the deposited iron; both processes already occur at 300 K, i.e., room temperature (RT). Similar results were reported by Zaera et al. for the decomposition of $\text{Fe}(\text{CO})_5$ on Pt(111) and Ni(100) at sample temperatures of 275 K or 300 K, respectively [144-146].

This sequence of catalytic and autocatalytic behavior means that EBID in the corresponding system is completely unselective. The only difference comparing the area not exposed with the one exposed to the electron-beam is a slightly higher O Auger signal for the latter, most presumably due to electron induced dissociation of carbon monoxide originating from the precursor itself. This additional oxygen results in a small damping of the Fe peaks compared to the spectrum of non irradiated surface regions and a somewhat darker appearance of the irradiated areas in the SEM image in Fig. 5.15 (e).

Similar to the experiments at the other sample states, also lines were irradiated on Sample III. Due to the catalytic decomposition of the precursor on the well prepared Rh(110) sample and the resulting structuring of the surface these features were not observable.

Summarizing the observations for the experiments at the different surface states, it is evident that the surface quality has a high influence on the selectivity of the EBID process. While independent of surface quality the deposits contain almost pure iron, the deposition of material in surface regions where no electron-precursor interaction takes place depends on the actual condition of the Rh sample. This phenomenon is mainly attributed to the surface roughness in combination with the quality of the surface reconstruction.

Furthermore, the generation of spatially well defined deposits is also directly influenced by the surface quality. Unintended deposition due to proximity effects is significantly suppressed on rough surfaces, as it was observed on Sample I; it is assumed to result from the disturbance of the BSE trajectories, leading to a reduction of the effective electron-precursor interaction area.

5.6.2 Reduction of the autocatalytic behavior via a thin titanium layer

In the course of the characterization of Sample III, some scattered regions were detected that differ significantly from the rest of the surface, as it is evident from the SEM image in Fig. 5.17 (a). This image shows an elliptically shaped halo of $\sim 160 \mu\text{m}$ diameter around a central particle of 5-10 μm size. The high magnification images of the halo in Fig. 5.17 (b) and (c) reveal that it consists of bright and dark regions. To determine the chemical composition, local Auger spectroscopy was performed at the positions of the color coded markers in Fig. 5.17 (b). The corresponding spectrum in the bright region (red) in Fig. 5.17 (d) shows the Rh MNN Auger peaks between 200 and 320 eV, as expected for the clean Rh(110) surface, with no indications for other elements. The spectrum in the dark region (dark green) shows the Rh peaks, albeit with lower intensity, and additional peaks at 384 and 418 eV, which are assigned to Ti LMM transitions. With this spectroscopic information, one can now assign the brighter areas observed in SEM (Fig. 5.17) as clean Rh(110) surface and the dark regions as areas covered with Ti; from the damping of the Rh signal, the average thickness of the Ti layer is estimated to be $\sim 0.14 \text{ nm}$, i.e., less than a monolayer.

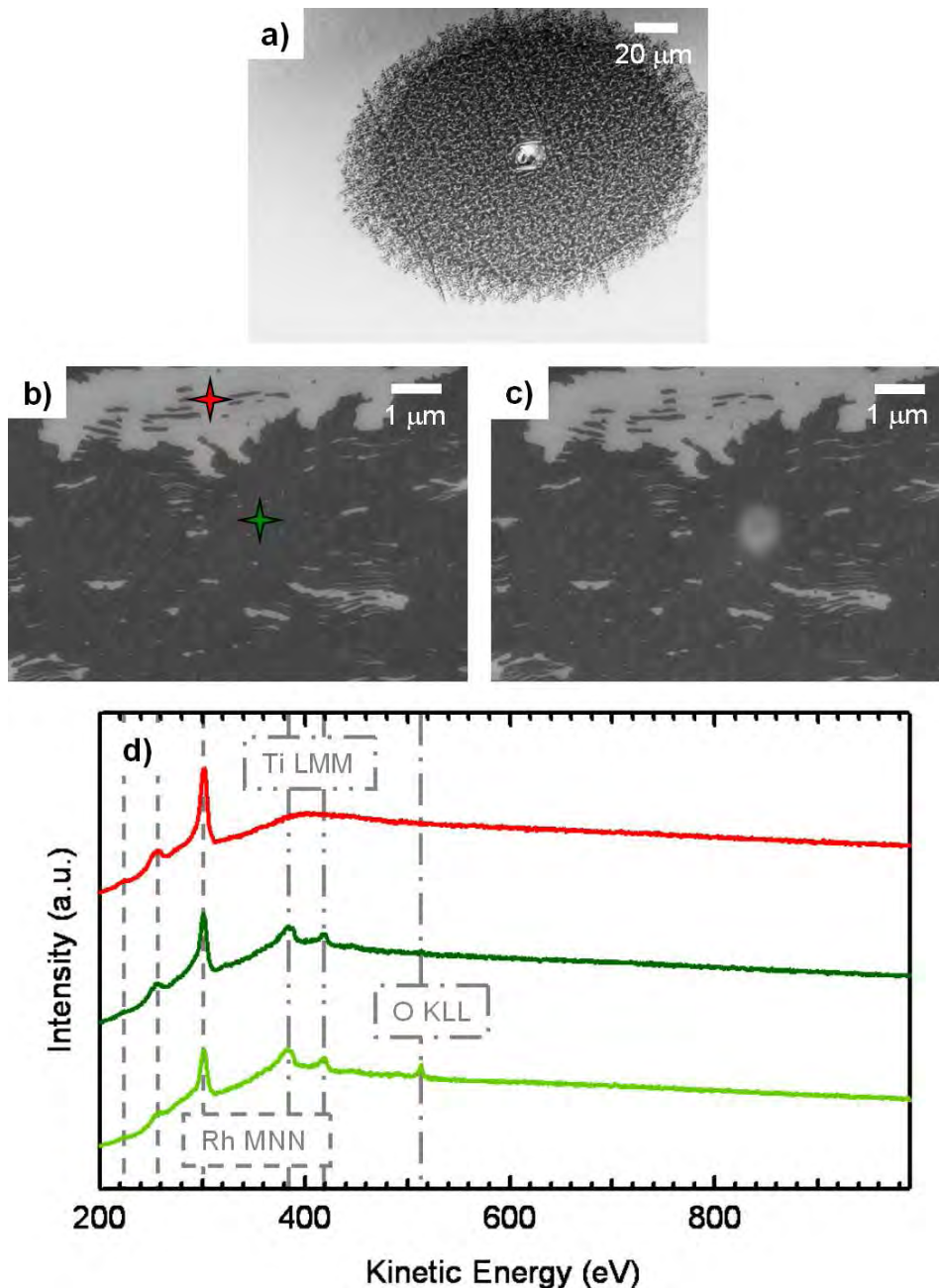


Fig. 5.17: Characterization of Sample III-Ti: a) SEM image showing a dark halo with a centered particle. b) High magnification image of the halo region. The red and green markers correspond to the positions where the Auger spectra in (d) were measured. c) SEM image of the same position as depicted in b, after AES was performed. d) Local AE spectra taken on the different areas of the halo. The red and dark green spectra were measured at the positions marked in (b). For the light green spectrum an “area scan” was applied to the dark surface area, as described in Chapter 3.4. ($U = 15$ kV; $I = 3$ nA; tilted sample)

Interestingly, the SEM image in Fig. 5.17 (c), taken after the measurement of the AE spectrum on the dark area shows a bright spot at the corresponding position. Obviously, the local electron exposure during the acquisition modified the surface. To study this effect in

more detail, we performed an “area scan”, according to the description in Chapter 3.4. In the corresponding AE spectrum (light green in Fig. 5.17 (d)) an additional oxygen peak is observed, which is an indication that the surface species yielding the dark area in SEM is TiO_x . The missing O signal in the normal spectrum (dark green) is attributed to electron stimulated desorption, a well known effect for TiO_2 [164] and SiO_x [165, 166]. The bright spot after the Auger scan in Fig. 5.17 (c) thus indicates an oxygen depleted region. This finding clearly demonstrates that the focused electron-beam locally modifies the ultra thin TiO_x film implying the potential to exploit this effect to nanostructure the corresponding area.

The observed Ti contamination is most likely due to a pair of Ti tweezers used when mounting the sample; the formation of the structured halo is mainly attributed to diffusion from the centered particle during heating of the crystal. This TiO_x -containing region is used as a fourth sample, denoted as Sample III-Ti, on which EBID and in particular the influence of the substrate on the selectivity can be investigated. For that purpose, experiments were performed on both surface regions, i.e., clean and titanium covered. These deposition processes were realized with a lower partial pressure of the precursor; the respective values of the background pressure are given in the corresponding figure captions.

First, EBID was performed on clean Rh(110) areas. Fig. 5.18 (a) shows an SEM image of the surface before EBID with $\text{Fe}(\text{CO})_5$, with the clean Rh(110) region in the center brighter than the titanium covered region at the top and at the bottom. Similar to the observations of oxygen on rhodium (compare Chapter 5.4) this is mainly interpreted as due to an increase of the work function upon adsorption of oxygen (see Fig. 5.8). In Fig. 5.18 (b) the SEM image after EBID of four squares (template squares: 600 nm x 600 nm) onto the clean Rh(110) region is shown. The former clean rhodium area appears significantly darkened and four square shaped structures can be identified, which appears even darker. The local AE spectra taken on (red) and beside (green) the irradiated area are very similar (see Fig. 5.18 (c)); they are dominated by the Fe signals with no Rh substrate signals visible, confirming the lack of selectivity of the EBID process on clean and well prepared Rh(110) (see also results for Sample III in Chapter 5.6.1). Since no Rh signals are observed the deposited iron layer must be again thicker than 1.5 nm. The darker appearance of the irradiated area is again attributed to a slightly higher amount of oxygen (see red and green spectra in Fig. 5.18 (c)), resulting from the decomposition of carbon monoxide ligands.

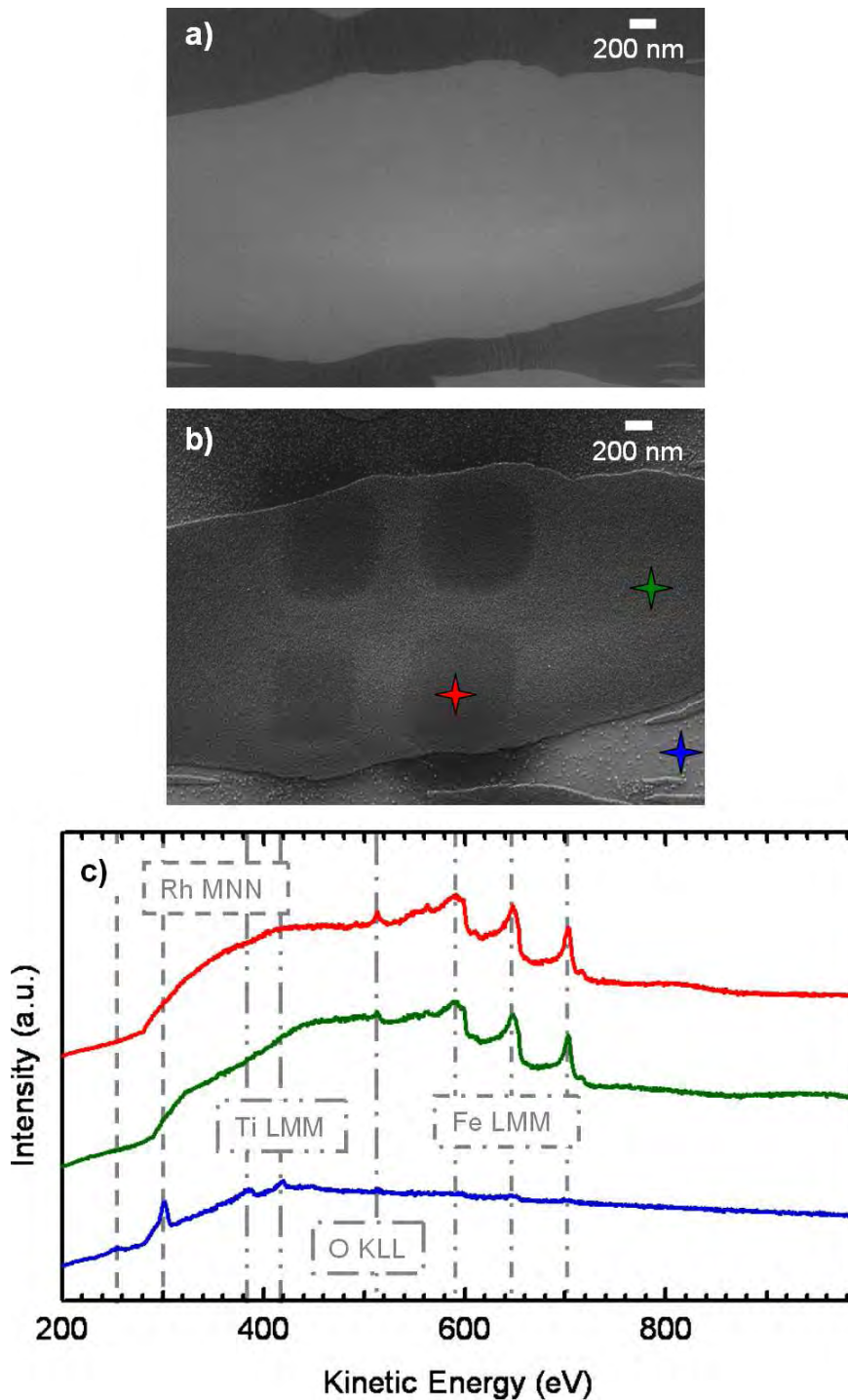


Fig. 5.18: EBID on a clean Rh area on Sample III-Ti. a) SEM image before $\text{Fe}(\text{CO})_5$ dosage. ($U = 15$ kV; $I = 400$ pA; plane sample) b) SEM image of the same region after EBID of four quadratic areas with an increasing electron dose from 13.3 C/cm^2 (lower left) to 53.1 C/cm^2 (top right). During the $\text{Fe}(\text{CO})_5$ dosage the background pressure in the chamber was $4.3 \cdot 10^{-8}$ – $8.0 \cdot 10^{-8}$ mbar. ($U = 15$ kV; $I = 3$ nA; tilted sample) c) Local Auger spectra acquired at the positions marked in (b).

The AE spectrum (blue) measured on the titanium containing region shows the expected Rh and Ti peaks, but only minor Fe signals, indicating that $\text{Fe}(\text{CO})_5$ is not decomposed catalytically in this region. In other words, the catalytic effect of the clean Rh(110) surface can be effectively inhibited via a surface modification, i.e., an ultra thin TiO_x layer. The Auger spectra also explain the contrast inversion in the SEM images after the $\text{Fe}(\text{CO})_5$ dosage: the titanium covered regions (upper and lower part of the image) in Fig. 5.17 (b) appear brighter than the central region, since iron, now completely covering the previously clean Rh areas, has a lower SE yield than rhodium covered with a thin Ti layer (again associated with the higher atomic number of Rh compared to Fe [48]). Small portions of the titanium covered region close to the exposed areas remain dark after the dosage (e.g., in the middle of the lower part of Fig. 5.18 (b)), which is attributed to EBID via scattered primary electrons.

To further investigate selectivity, EBID was also performed on titanium covered regions. The SEM image in Fig. 5.19 (a) shows a section of a titanium covered region, with a dark area on the left. This feature was generated via EBID of a square template (size: 600 nm x 600 nm), as indicated by the dotted white line, with the same electron dose as for the top right square in Fig. 5.18 (b). A significant amount of material was also deposited outside the irradiated region (see Fig. 5.19 (a)); this unintended deposition is again attributed to proximity effects (BSE proximity effect), since the observed broadening of 400 – 450 nm fits quite well to the radius of the BSE exit area, calculated from a Monte Carlo simulation (see Fig. 2.13 (b) in Chapter 2.7). Peculiar features in Fig. 5.19 (a) are the bright clusters that appear in and around the exposed area. Their origin will be discussed in detail below.

Local AES was performed on the EBID deposit (red marker in Fig. 5.19 (a)). The corresponding red spectrum in Fig. 5.19 (b) is dominated by the Fe signals with a minor O peak, indicating that the EBID deposit mainly consists of iron, similar to the results obtained on the clean rhodium surface. No Rh substrate signal is observed, indicating that the deposit is again thicker than 1.5 nm. The green spectrum in Fig. 5.19 (b) was measured on the nearby unexposed area (green marker in Fig. 5.19 (a)). Apart from the damped Rh substrate peaks and signals from the TiO_x layer, no other elements are observed. It is therefore concluded that the EBID process on the titanium covered surface is strictly selective, in contrast to the observations on the clean Rh surface.

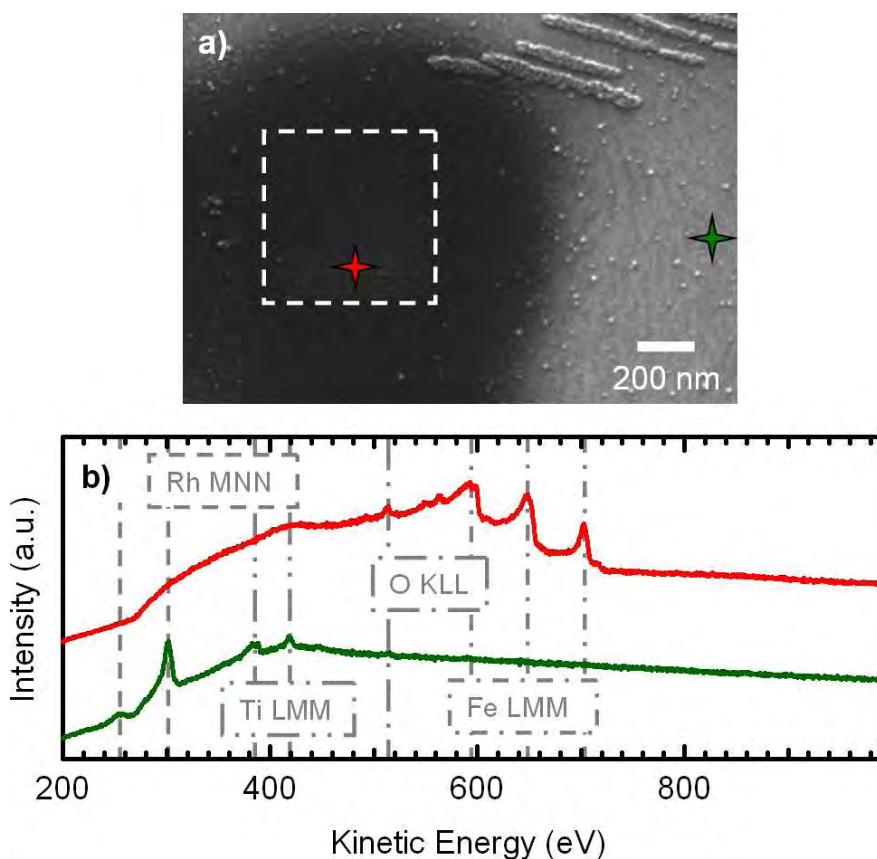


Fig. 5.19: EBID deposit with $\text{Fe}(\text{CO})_5$ on a Ti covered area on Sample III-Ti. a) SEM image of an iron structure, which was generated by the irradiation of a quadratic area (white dotted line) with an electron dose of 53.1 C/cm^2 and an $\text{Fe}(\text{CO})_5$ background pressure in the chamber of $8.0 \cdot 10^{-8} - 1.3 \cdot 10^{-7} \text{ mbar}$. b) Local Auger spectra acquired at the positions marked in (a). ($U = 15 \text{ kV}$; $I = 3 \text{ nA}$; tilted sample)

In the following the origin of the bright features on the titanium covered surface after $\text{Fe}(\text{CO})_5$ dosage will be investigated. These features are visible mostly as small protrusions with a diameter of roughly 10 nm (e.g., compare Fig. 5.19 (a)) or, for example, as longish features with a granular structure in the top right corner in Fig. 5.19 (a). In Fig. 5.20 an SEM image (Fig. 5.20 (a)) of an unexposed area is shown along with two images of the same surface acquired via scanning Auger microscopy (SAM), revealing the distribution of iron (Fig. 5.20 (b)) and titanium (Fig. 5.20 (c)); to obtain these images, the electron analyzer was set to the Fe LMM peak at 702 eV and Ti LMM peak at 382 eV, respectively. Red regions in Fig. 5.20 (b) indicate a high amount of iron, while blue regions in Fig. 5.20 (c) correspond to a high amount of titanium.

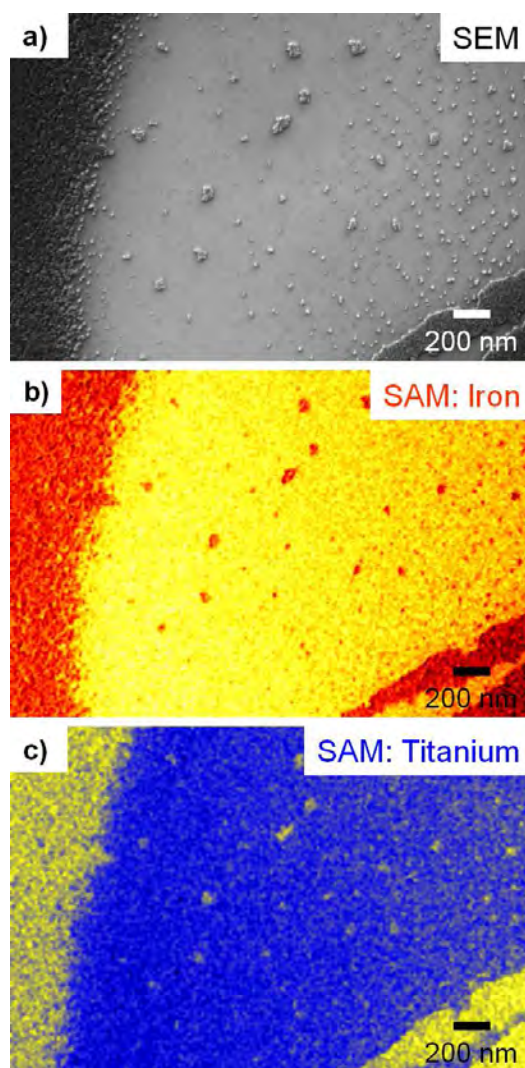


Fig. 5.20: Measurements on an unexposed area of Sample III-Ti after $\text{Fe}(\text{CO})_5$ dosage. a) SEM image of the corresponding region, displaying areas of the Ti free (dark) and Ti covered (bright) surface. ($U = 15 \text{ kV}$; $I = 3 \text{ nA}$; tilted sample) b) SAM image for the element iron; red areas correspond to a high iron coverage. ($E_{\text{Peak}} = 702 \text{ eV}$; $E_{\text{Bkg}} = 730 \text{ eV}$; $t_{\text{Dwell}} = 6.55 \text{ ms}$) c) SAM image for the element titanium; blue areas correspond to a high titanium coverage. ($E_{\text{Peak}} = 382 \text{ eV}$; $E_{\text{Bkg}} = 400.2 \text{ eV}$; $t_{\text{Dwell}} = 6.55 \text{ ms}$) Yellow areas in (b) and (c) correspond to a low amount of the respective element.

A comparison between Fig. 5.20 (b) and (c) evidences that a high local amount of Ti coincides with basically no Fe and vice versa. Based on the SAM images the bright features in the SEM image are identified as iron. Interestingly, these Fe features appear bright in SEM, whereas the more or less continuous iron film (e.g., in the left part and lower right corner of Fig. 5.20 (a)) appears darker than the rest of the surface. This observation is attributed to the well known tilt and edge effects in SEM [167], indicating the three-dimensional nature of these bright features: apparently they are higher than the titanium covered surface areas and

they are therefore assigned as small iron clusters. The origin of these iron clusters on the titanium covered regions is interpreted as due to local defects (holes) in the titanium film, locally exposing the clean rhodium and thus catalytically decomposing the $\text{Fe}(\text{CO})_5$ precursor, resulting in iron deposits.

5.6.3. Summary

The interaction between $\text{Fe}(\text{CO})_5$ with the Rh(110) surface is summarized in the scheme in Fig. 5.21. On the perfectly ordered Rh(110) surface (Sample III and titanium free regions of Sample III-Ti) the precursor molecules dissociate even without any electron assistance (Fig. 5.21 (a)) already at room temperature. This catalytic decomposition leads to the deposition of iron, while the CO ligands mainly desorb (Fig. 5.21 (b)). Additional precursor molecules impinging onto these regions are also dissociated via an autocatalytic effect of the pre-deposited iron (Fig. 5.21 (c)). Therefore, the formerly clean Rh(110) surface area is covered with a thick Fe layer at the end of the $\text{Fe}(\text{CO})_5$ dosage (Fig. 5.21 (d)). In regard to the EBID process this catalytic behavior means a complete loss of selectivity, as the electron interaction is not necessary to induce the dissociation of the precursor molecules. The only difference is a slightly higher amount of oxygen in the irradiated areas, accompanied by a darker appearance in the SEM images, presumably due to electron induced dissociation of small amounts of carbon monoxide (see Fig. 5.15 (e), 5.15 (f), 5.16 (c) and 5.18).

For the TiO_x -modified Rh(110) surface (Sample III-Ti) the situation is different (left part of the scheme in Fig. 5.21). Here, the catalytic activity of the rhodium surface is inhibited by the thin overlayer and $\text{Fe}(\text{CO})_5$ adsorbs and desorbs intact in the area unexposed to electrons. In the irradiated areas, the precursor molecules are dissociated, resulting in the deposition of iron with minor contaminations (see Fig. 5.19). This implies that the EBID process is selective on the titanium covered region, as iron is only observed on areas that were irradiated by electrons. The described elemental distribution on Sample III and Sample III-Ti after an EBID experiment was also confirmed via Auger line scans (see appendix to Chapter 5).

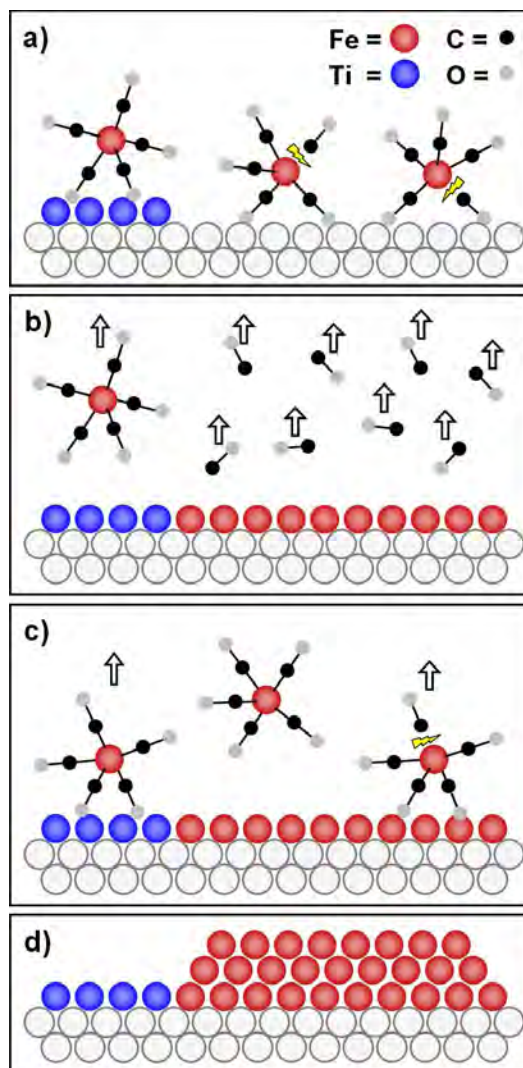


Fig. 5.21: Scheme summarizing the behavior of $\text{Fe}(\text{CO})_5$ on clean and Ti covered Rh(110). a) Adsorption of $\text{Fe}(\text{CO})_5$ molecules on the clean and Ti covered surface. b) Catalytic dissociation of $\text{Fe}(\text{CO})_5$ on the clean and well ordered Rh surface: Fe atoms stick to the surface while the CO ligands are mainly removed from the system. On the Ti covered region $\text{Fe}(\text{CO})_5$ desorbs molecularly without decomposition. c) Additional $\text{Fe}(\text{CO})_5$ molecules adsorb on the Fe-covered Rh surface and are dissociated autocatalytically. On the Ti covered surface the molecules again desorb molecularly. d) After the $\text{Fe}(\text{CO})_5$ dosage the free Rh surface is covered with a thick Fe layer, while no Fe was deposited on the Ti covered area.

In the case of the rough surfaces exhibiting a limited long range order (Sample I and Sample II) the observed selectivity lies between the two cases described before, with a small amount of iron deposited on the non-irradiated area (see Fig. 5.16 (a) and (b)). Obviously, the catalytic activity of the rhodium sample is significantly lowered under these surface conditions. The origin of the moderate selectivity in these cases is not clear at the moment.

The copper precoverage observed for Sample I cannot be the only explanation for the observed selectivity, since Sample II showed a similar result without any metal contaminations on the surface before the experiment. The same applies for the small carbon contamination visible before the EBID process on Sample I and Sample II (see blue spectra in Fig. 5.16 (a) and (b)) as a similar amount was observed during the characterization of Sample III (see blue spectrum in Fig. 5.16 (c)). Possibly, the surface reconstruction plays a vital role for the catalytic activity of the Rh(110) surface, which was lower for Sample I and Sample II compared to Sample III. Further investigations are necessary to clarify this observation.

Moreover, it was shown, that the quality of the surface has also a significant influence on the lateral distribution of the deposited material. Deposition in the direct surrounding of the irradiated area due to proximity effects is strongly suppressed on a rough surface (Sample I), enabling the generation of spatially well defined structures in close vicinity (see Fig. 5.15 (b)). Further preparation and smoothing of the surface leads to an increase of unintended deposition around the exposed area and thus to diffuser deposits (Sample II; see Fig. 5.15 (d)). In the case of the perfectly ordered Rh(110) surface (Sample III) the generation of laterally defined structures is impossible, since the whole surface is covered with a similar amount of iron after the EBID process. The precoverage with a thin titanium overlayer (Sample III-Ti) inhibits the catalytic decomposition of the precursor, but still unintended deposition due to proximity effects takes place in the surrounding of the irradiated area (see Fig. 5.19); the structures appear therefore diffuse, similar to the observations on Sample II.

The described experiments, especially the ones on Sample III, were only possible under ultra clean, i.e., UHV, conditions, which are a prerequisite for the preparation of a well-defined single crystal surface. It would therefore be impossible to study the relation between the surface quality and the selectivity of the EBID process in a high vacuum environment, in which most of the commercially available SEMs operate.

5.7 Effect of the electron dose on the EBID process

One important lithographic parameter with an impact on the EBID process is the applied electron dose. To study its influence on the system $\text{Fe}(\text{CO})_5 / \text{Rh}(110)$ in more detail, circular structures with an identical template (template circles: $\varnothing = 500 \text{ nm}$) were deposited with varying electron doses. This experiment was conducted on Sample II (improved specimen), since the selective deposition of iron on this surface was demonstrated (see Chapter 5.6.1). The three resulting structures, namely Deposit I, Deposit II, and Deposit III, which were

irradiated with an electron dose of 13.3, 26.6, and 53.1 C/cm², respectively, are depicted in Fig. 5.22. The originally exposed areas are marked in the SEM images by white dotted lines.

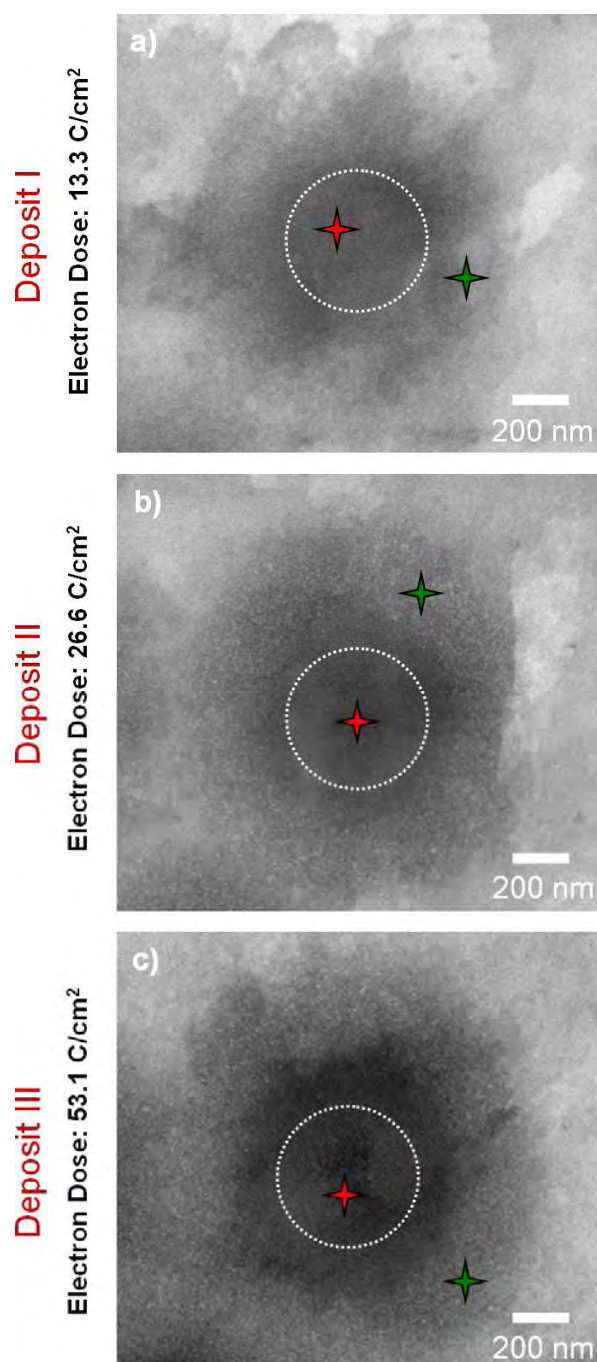


Fig. 5.22: Three circular iron structures, deposited with an increasing electron dose from a) to c). The white dotted lines mark the positions of the originally exposed areas ($\varnothing = 500$ nm). The markers correspond to the positions where the Auger spectra in Fig. 5.24 were acquired. ($U = 15$ kV; $I = 3$ nA; tilted sample)

As already described in Chapter 5.6.1 the deposits on Sample II exhibit an inhomogeneous contrast in SEM: Deposit I (Fig. 5.22 (a)) consists of a dark circular area in the center with a diameter of 550 – 600 nm, which is somewhat larger than the size of the originally exposed area. It is surrounded by a 250 – 325 nm wide area exhibiting a lower contrast compared to the center, indicating that a lower amount of iron was deposited in this region. An increase of the applied electron dose leads to a significant influence on the generated deposits: upon irradiation with a two times (Deposit II; Fig. 5.22 (b)) and four times (Deposit III; Fig. 5.22 (c)) higher dose, the diameter of the dark central region is increasing to 650 – 700 and 770 – 850 nm, respectively, while the width of the surrounding area is rather constant (~ 300 nm). For Deposit II and Deposit III the central dark region of the structure is also significantly larger than the originally exposed area. Additionally, the whole deposit (central region and surrounding area) appears darker at higher electron doses.

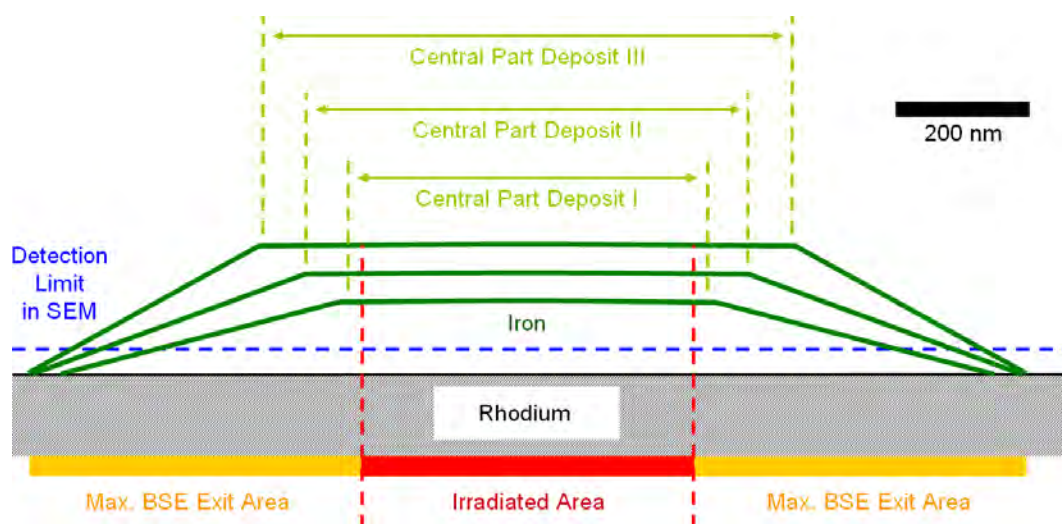


Fig. 5.23: Schematic profiles of the EBID deposits from Fig. 5.22. The horizontal dimension was chosen according to the scale bar on the top right, while the vertical dimension contains no concrete size information. The red dashed lines mark the position of the originally exposed area, while the orange bars indicate the maximal distance of the BSE exit area; the detection limit of iron in the SEM is marked blue. The dark green lines represent the schematic profiles of the deposits (from bottom to top: Deposit I, Deposit II, Deposit III); for simplification, the size of the observed dark areas are denoted as horizontal lines.

The observed deposition in the region surrounding the irradiated area is attributed to proximity effects, mainly the BSE proximity effect (see Chapter 2.7) [119]. For Deposit III a

total size of 1350 – 1450 nm is observed, which fits quite well to the size of the irradiated region and the BSE exit area, as calculated from a Monte-Carlo simulation with the program *CASINO V 2.42* [92] (500 nm for the irradiated region plus twice the radius of ~ 450 nm for the BSE exit area). A reduction of the applied electron dose, i.e., half of the electron dose for Deposit II and one third for Deposit I, leads to structures with a total size of 1150 – 1300 nm and 1100 – 1150 nm, respectively. This observation is mainly attributed to the electron density in the surrounding of the irradiated area: as it is well-known from literature (e.g., [40, 119]) and performed Monte-Carlo simulations (compare Fig. 2.13 in Chapter 2.7) is the number of BSEs leaving the surface and therefore the local electron density decreasing with an increasing distance from the primary electron impact position. The resulting influence on the deposited material is sketched in Fig. 5.23. In the area directly exposed to the electron beam a high amount of iron is deposited, while it is decreasing gradually from the edge of the structure to the limit of the outermost BSE exit area (via irradiation at the edges of the structure; orange bars in Fig. 5.23). Since a certain thickness of the deposit is necessary for detection in SEM (blue dashed line in Fig. 5.23), the total size of the observed structure is at lower electron doses (Deposit I and Deposit II) smaller than the expected size from the calculation of the BSE exit area, as the electron density and thus the amount of deposited material in the corresponding region is also depending on the applied primary electron dose. A similar result for an increasing size of the deposited structure associated with an increase of the applied electron dose has been already reported in Chapter 4.3.2 for the generation of carbonaceous structures on Si(100) with the precursor ethene. The observed increase of the size of the dark central area (increasing from Deposit I to Deposit III; schematically depicted by the horizontal lines in Fig. 5.23) is also attributed to the electron distribution in the BSE exit area. An increasing primary electron dose, results in a growing region in the surrounding area, in which the deposited material exhibits a similar contrast in the SEM as observed for the irradiated area.

In order to characterize the chemical composition of the deposits and to determine their thickness, local AES was performed in all three cases on the exposed area and in the region surrounding the dark central area (see color coded markers in Fig. 5.22; the spectra in the surrounding (green markers) were acquired with a similar distance from the dark central region). The corresponding spectra acquired on the irradiated area (red spectra in Fig. 5.24) are dominated by Fe signals between 570 and 710 eV. In all measured spectra only a small C signal (~ 272 eV) and a minor O peak (~ 513 eV) is visible, indicating that the deposits are again very pure (similar purity as described in Chapter 5.6.1 for the deposits on Sample II);

the ratios of the intensities of these signals (O, C) and the iron peaks appear to be roughly constant, which indicates that the purity of the deposits is independent of the applied electron dose.

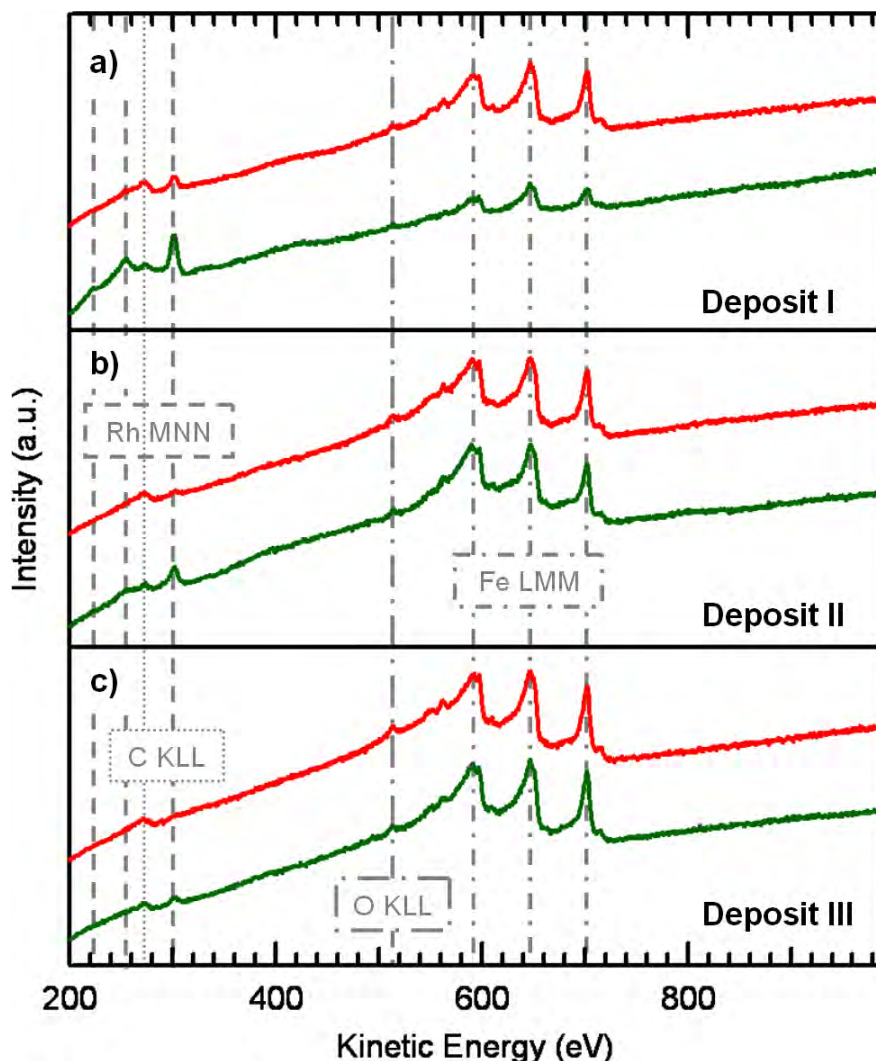


Fig. 5.24: Local Auger spectra acquired on the irradiated area (red) and on the iron layer deposited in the direct surrounding via proximity effects (green), as marked in Fig. 5.22.

Additionally, a small Rh peak is observed on Deposit I (red spectrum in Fig. 5.24 (a)), which is decreasing in intensity with an increase of the applied electron dose (i.e., from Deposit I to Deposit III). In contrast to this, the intensities of the Fe peaks show a contrary behavior: compared to Deposit I (Fig. 5.24 (a)) a two times higher electron dose (Deposit II; Fig. 5.24 (b)) leads to an increase by 20 %, while 31 % higher signals are observed for a four times higher electron dose (Deposit III; Fig. 5.24 (c)). This rise in the signal intensities indicates an increasing amount of deposited iron associated with an increase of the applied electron dose. It is confirmed by a quantitative analysis of the layer thicknesses via the

damping of the Rh signals in the spectra, assuming a continuous layer of pure iron: a value of ~ 1.1 nm was calculated for Deposit I, while for Deposit II and Deposit III the layer thickness is higher than 1.5 nm (compared to the spectrum of the sample before the deposition process (see green spectrum in Fig. 5.5; note that since the Rh substrate signal is too small to determine the signal intensity properly, only a lower limit can be given for the thickness in Deposit II and Deposit III). Similar results for an increasing height of the deposit with an increasing electron dose were also reported in literature for the deposition of tips with various precursor molecules [11, 19, 119, 134, 136].

The spectra acquired in the area, where deposition due to proximity effects appeared, display the same signals as in the irradiated regions (see green spectra in Fig. 5.24); again large Fe peaks accompanied by small C and O signals are visible. The latter exhibit a similar intensity compared to the red spectra in Fig. 5.24 (acquired on the irradiated area), while the intensity of the C peak is difficult to determine due to an overlap with the Rh substrate signals. The low amount of contaminations observed indicates again a high purity of the deposits in these areas. The intensity of the Rh peaks is decreasing with an increasing electron dose, but exhibit in all three cases a higher intensity compared to the corresponding signals of the exposed area. This behavior is contrary to that of the Fe peak intensities, i.e., they are increasing with an increasing electron dose and are always less intense compared to the spectra of the exposed region.

These observations indicate that at the measurement positions marked green in Fig. 5.23 the amount of deposited iron is lower compared to the ones in the respective irradiated regions (red). A quantitative analysis of the layer thicknesses via the damping of the Rh signals assuming a continuous layer of pure iron yield values of ~ 0.6 nm for Deposit I, ~ 0.9 nm for Deposit II and ~ 1.4 nm for Deposit III. This effect could be expected, as the electron density in the surrounding of the irradiated region is gradually decreasing from the edge of the irradiated area to the maximal radius of the BSE exit area (see above). Since the amount of deposited material in the irradiated area is always higher, it can be supposed that the deposit growth in the surrounding region takes place in the electron limited regime (see Chapter 2.7). An increase of the applied electron dose leads also to an increase of the electron density in the BSE exit area, which is accompanied by a higher amount of deposited material, as observed for the respective measurement positions in Deposit I to Deposit III.

Summarizing the data presented in this chapter, two main influences of an increasing electron dose on the deposition process in the system $\text{Fe}(\text{CO})_5 / \text{Rh}(110)$ can be determined: I) the amount of deposited material is increasing, which is evidenced by the growing thickness

of the iron layer and II) the lateral size of the structures is also increasing, which is attributed to an increasing electron density in the surrounding of the exposed area due to proximity effects. The amount of iron deposited via proximity effects is lower compared to the one in the directly irradiated region, at least for the applied electron doses; this effect results from the distribution of the BSEs in the surrounding of the irradiated area, which leads to a steady decrease of the electron density with an increasing distance from the exposed region.

5.8 Thermal stability of iron structures

Annealing is a typical post-deposition technique for EBID, e.g., for the purification of the structures. To study its effect on the iron structures deposited on rhodium and to determine their thermal stability for further applications, the deposits generated on Sample I (low quality Rh(110) surface; see Chapter 5.3) were heated in 100 K steps in the analysis chamber. Fig. 5.25 (a) shows an image of a deposited pattern prior to the heating procedure; the pattern consists of area and line structures, which are described in detail in the following³:

- **Three ovals** (area deposits), with the longer diagonal parallel to the $[1\bar{1}0]$ direction of the surface. The size of the ovals is increasing from left to right: longer diagonal ~ 355 nm, ~ 525 nm, ~ 700 nm / shorter diagonal ~ 230 nm, ~ 355 nm, ~ 465 nm. Each was irradiated with a total electron dose of 79.6 C/cm².
- **Six ellipses** (line structures); their sizes correspond to the ones of the respective oval deposits, i.e., they are increasing from left to right. Two ellipses each exhibited the same size and were irradiated in close proximity of each other. Each line deposit was irradiated with an identical electron dose of 120 μ C/cm.

In the case of the ovals, separated structures are not distinguishable in Fig. 5.25 (a), mainly due to the unintended deposition of iron in the direct surrounding of the irradiated areas due to proximity effects (see Chapter 2.7); in contrast to that, separated and laterally well defined ellipses were generated (see bottom part of Fig. 5.25 (a))

³ Note, that on Sample I the experiment was performed by a double irradiation of each pattern at the same position (compare Chapter 5.5). In combination with thermal drift this resulted in a certain enlargement of the oval deposits and the generation of two separated ellipses in close proximity (the original template contained three ellipses).

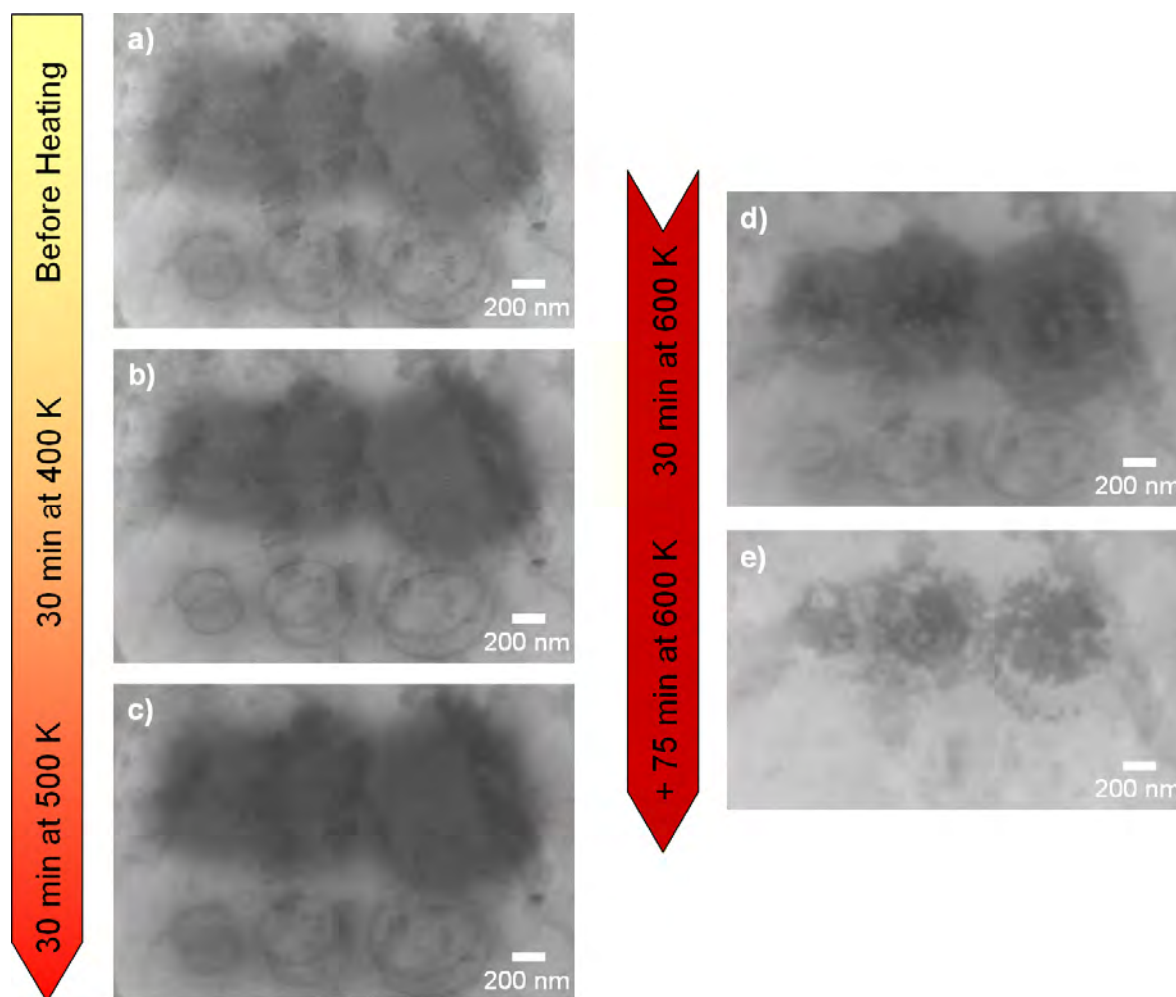


Fig. 5.25: Annealing of iron structures deposited on Sample I. SEM images b) to d) were acquired after the corresponding heating process with the sample at the respective elevated temperature, while e) was taken after cooling the sample to room temperature. ($U = 15$ kV; $I = 3$ nA; tilted sample)

The structures were observed in situ during the annealing of the sample in order to observe changes in morphology or contrast in the SEM. Fig. 5.25 (b) and (c) show the same deposits as in Fig. 5.25 (a) after heating for 30 min at 400 K and 500 K, respectively (image acquisition with the sample at the respective elevated temperature (image acquisition time: ~ 160 s)). Clearly visible in the images is an increasing contrast between the deposited iron and the free surface (i.e., the deposit appears darker with respect to the surface) associated with an increase of the temperature. Explanations for this behavior are highly speculative with the data at hand. Local AE spectra acquired after the heating steps on an irradiated area (not shown here) exhibit an increased O signal compared to a spectrum measured before the annealing procedure. One assumption is therefore that due to the heating process contaminations like oxygen or carbon are segregating from the bulk of the deposit to the free

surface region, leading to an effective increase of the work function and thus to a darker appearance in the SEM. Another possible explanation is the adsorption of additional oxygen (e.g., originating from co-heated components of the manipulator) from the gas phase on the iron deposits. Significant differences in the morphology of the structures cannot be observed in Fig. 5.25 (b) and (c).

In situ observation upon heating to 600 K turned out to be difficult due to an increased thermal drift of the sample setup. An image of the pattern acquired after heating for 30 min at 600 K is depicted in Fig. 5.25 (d) (image acquisition with sample at elevated temperature). Upon close inspection, it can be observed that the formerly continuous lines structures (ellipses) are partly vanished and are difficult to distinguish. The iron deposits at the positions of the ovals exhibit a significantly lower contrast compared to Fig. 5.25 (c) (i.e., the deposits appear less dark with respect to the free surface); additionally, the deposited material appears inhomogeneously structured with brighter protrusions, while the edges of the structures are clearly more defined compared to Fig. 5.25 (a) to (c).

Additional heating at 600 K results in a further change of the morphology of the EBID deposits. Fig. 5.25 (e) shows an image, which was acquired after an additional heating time of 75 min (image acquired after cooling the sample to room temperature); the ellipses have completely vanished, while the deposits at the positions of the ovals are rather discontinuous and consist of regions that appear dark and regions which are bright in the SEM. Similar results for the deformation of Pt-containing deposits upon heating have been reported in reference [119].

To study the chemical composition of these regions to obtain additional information on the influence of the temperature on deposited iron structures on Rh, local AES was performed. The spectra were acquired on a different pattern as depicted in Fig. 5.25 in order to exclude any influence of the electron-beam on the chemical composition that might have occurred during the in situ observation with the SEM. An image of the corresponding structures (template: compare Fig. 5.13 (a)) before the heating procedure is depicted in Fig. 5.26 (a). It is identical to the image shown in Fig. 5.13 (c) and was discussed in detail in Chapter 5.5. Similar to the results obtained for other EBI deposits on Sample I (see Chapter 5.6) the Auger spectrum measured on the irradiated area (red spectrum in Fig. 5.26 (c); acquired on the large circle) is dominated by Fe signals with a small oxygen contamination and a minor C peak, while on the non-exposed region (orange spectrum) a strong Rh signal at 302 eV and small Fe peaks are observed, indicating again the moderate selectivity obtained on this sample state. The copper contamination observed for the non-irradiated area (between

740 and 960 eV) is also visible in this case (contamination from the assembly of the crystal on the sample holder; compare Chapter 5.3).

Fig. 5.26 (b) shows the same pattern after the complete heating procedure (image acquired after cooling the sample to room temperature), which results in a similar change of the deposit morphology as observed for the pattern in Fig. 5.25: the line structures, which were clearly visible before the heating procedure, have completely vanished, while the two circles at the top of the pattern exhibit an inhomogeneous structuring with bright and dark areas. The dot matrix at the bottom left has partly vanished, i.e., that some dots, especially those irradiated with a higher electron dose, are still visible in the SEM image. Local Auger spectra were acquired after the heating procedure on the dark and bright regions of the irradiated area and on the non-irradiated area. Since these spectra show a different shape compared to the ones acquired before the heating procedure, they will not be compared in a quantitative way.

In the case of the dark region in the irradiated area (dark green spectrum in Fig. 5.26 (c)) the spectrum is again dominated by the Fe peaks; small Rh signals can also be observed, indicating that the iron layer is thinner than before the heating procedure. Surprisingly, the Cu peaks are clearly visible in this spectrum, even though they are not visible in the red spectrum acquired before the annealing (compare Fig. 5.26 (c)). The blue spectrum in Fig. 5.26 (c) was measured on one of the bright areas in the irradiated region (see blue marker in Fig. 5.26 (b)). Compared to the spectrum of the dark area the Fe peaks are significantly smaller, while the Rh substrate signals exhibit a higher intensity, indicating that the iron deposit is thinner in these areas. Again the Cu peaks can be clearly observed and exhibit a similar intensity compared to the dark green spectrum (dark area). In both cases (dark and bright areas) no carbon peak is visible, but it has to be noted that it might be partly overlapping with the increasing substrate peaks.

The spectrum acquired on the non-irradiated area (light green spectrum in Fig. 5.26 (c)) after the annealing procedure is again dominated by the Rh substrate peaks, but also shows signals for iron and copper; similar to the observations for the unheated sample surface (orange spectrum in Fig. 5.26 (d)) the amount of iron is significantly smaller compared to the exposed region.

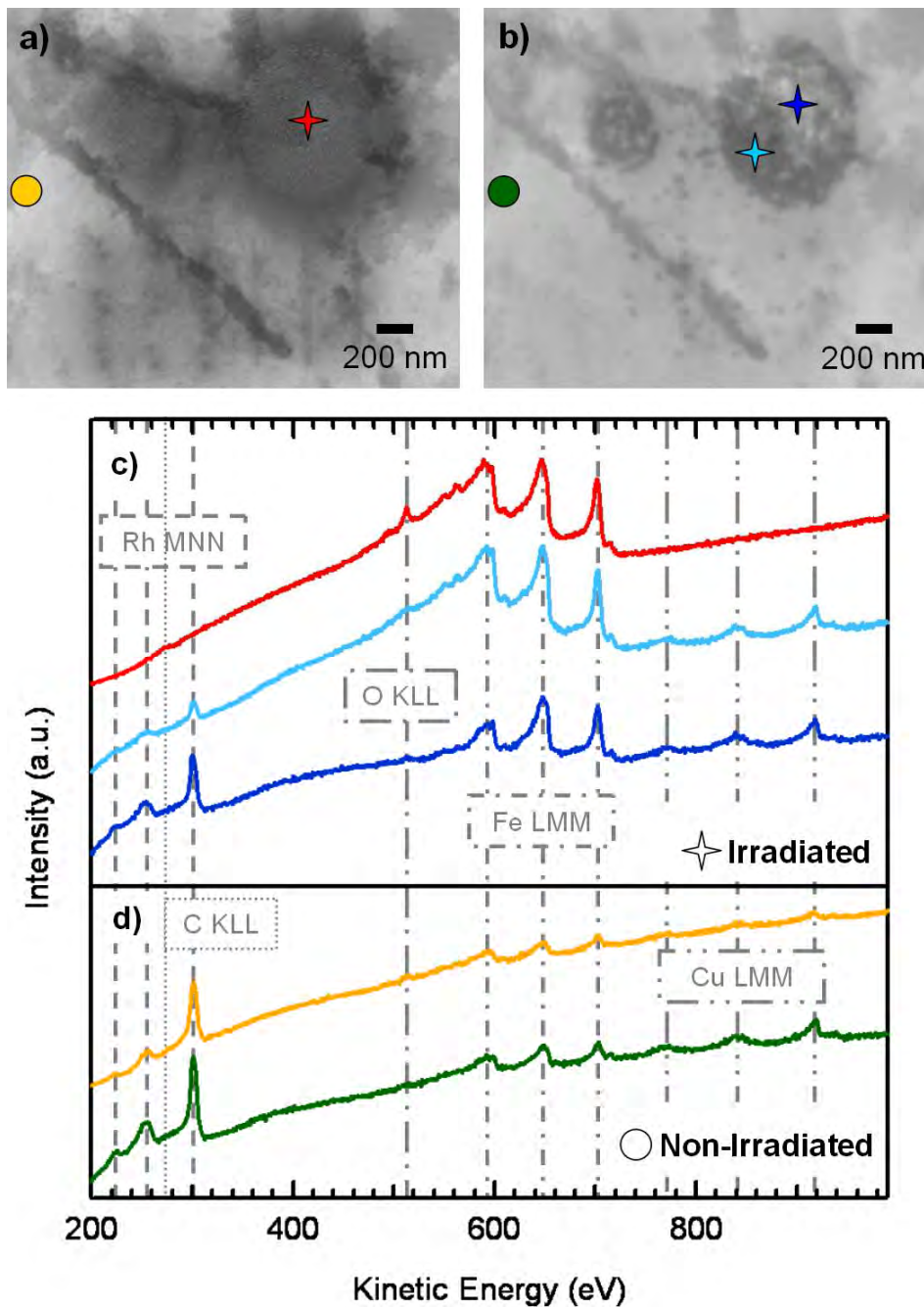


Fig. 5.26: SEM images of a deposit a) before and b) after the described heating procedure. The color coded markers assign the positions where the spectra in (c) and (d) were acquired. ($U = 15$ kV; $I = 3$ nA; tilted sample) c) Local Auger spectra acquired on the irradiated area before (red) and after the heating procedure (dark green on the dark area, blue on the bright area). d) Local Auger spectra acquired on the non irradiated area before (orange) and after the heating procedure (light green).

From the described SEM images (Figs. 5.25 and 5.26) and local Auger spectra (Fig. 5.26 (c)) it is obvious that the deposited iron structures are unstable at temperatures ≥ 600 K; for line deposits fabricated with the given electron doses extended heating (105 min) at 600 K

results in a complete disappearance of the structures, while the area deposits are decomposing into regions with different iron layer thicknesses. The most plausible explanation for these observations is diffusion of Fe on the surface or into the bulk of the rhodium substrate. The latter appears unlikely, since the spectrum measured on the non-exposed surface after the annealing procedure (light green) still shows significant Fe signals; if diffusion into the bulk would be mainly responsible for the change in the morphology and composition of the deposits, one would assume that the iron signal intensities in this region are strongly reduced as well. The appearance of the Cu peaks in the spectra of the irradiated area after the heating procedure is attributed to segregation to the free deposit surface. Before the heating procedure the corresponding signals were completely damped by the overlaying iron (see red spectrum in Fig. 5.26 (c)), while the spectra acquired on the dark (dark green) and bright (blue) areas exhibit a similar amount of copper, regardless of the thickness of the iron layer. It is therefore obvious that the copper is no longer damped by the iron, which clearly indicates a material transport through the deposit.

Surprisingly, the oxygen contamination observed before the annealing process on the irradiated area (red spectrum in Fig. 5.26 (c)) has almost disappeared afterwards, since both spectra (dark green and blue) exhibit only a minor O peak. It is therefore assumed, that the observed oxygen is mainly weakly bound in the deposited material; heating at temperatures around 400 K leads to an increase of oxygen at the top of the structures, indicated by the darkening of the deposits in Fig. 5.25 (b) (after 30 min heating at 400 K) compared to Fig. 5.25 (a) (before the heating procedure), while at 600 K it desorbs. Auger spectra acquired on irradiated areas of the patterns in Figs. 5.25 and 5.26 after 30 min of heating at 600 K (not shown here) exhibit also only a minor O signal, i.e., the structures consist of clean iron. It is concluded that the heating time is not the limiting factor for the removal of oxygen; thus it is proposed to clean the deposits from oxygen by a short annealing to 600 K and therefore probably to reduce the effect on the morphology of the deposits, i.e., the diffusion of iron and the resulting inhomogeneous structuring in Fig. 5.26 (b). Similar results for the purification of iron deposits by post-deposition annealing were reported by Takeguchi et al. for free standing iron rods generated via EBID with iron pentacarbonyl on a silicon film [106]; the as-formed structures exhibited an amorphous phase containing iron, carbon and oxygen, which was transformed into pure, crystalline α -Fe upon heating. In a different work heating of iron nano-dots and free standing iron rods on a carbon film resulted in the formation of iron carbide and the separation into α -Fe and Fe_7C_3 , respectively, while small amounts of oxygen visible before the annealing have disappeared [37].

Summarizing the discussion in this chapter, it can be concluded that the iron structures deposited via EBID on the low quality Rh(110) surface (Sample I) are stable up to 500 K. Extended heating at 600 K results in a significant change of their appearance accompanied by a partial removal of the deposited iron from the irradiated area, which is mainly attributed to diffusion on the surface. Heating at lower temperatures (400 - 500 K) leads to an increase of oxygen on the deposits, which subsequently desorbs at 600 K. With this information one might envision to purify the EBID deposits by a short annealing at 600 K, which would probably minimize the diffusion of iron and therefore have only a minor influence on the morphology of the deposits.

5.9 Selective oxidation of the iron structures

To further explore the potential of our approach to generate tailored nanostructures, we performed an experiment with the goal to oxidize iron nanostructures, produced by EBID. For that purpose, we used Sample II (improved Rh(110) surface; see Chapter 5.6.1); Fig. 5.27 shows the corresponding data. The starting point was the structure, which corresponds to the bottom EBI deposit shown in Fig. 5.15 (c) (template circle: $\varnothing = 500$ nm; deposited with an electron dose of 39.9 C/cm²). Fig. 5.27 (a) and (b) show the corresponding SEM images and AE spectra after the deposit was heated for 30 min at ~ 525 K (performed in the preparation chamber). The SEM micrograph (Fig. 5.27 (a)) displays again a dark circular area; similar to the results described in Chapter 5.8 the structure appears significantly darker than before the post-deposition annealing (see Fig. 5.15 (c)).

The AE spectrum of the irradiated area (dark blue) shows intense Fe peaks, with only a minor O peak and a small C signal visible. From the damping of the Rh signal the thickness of the iron layer is estimated to be ~ 1.5 nm (note that the Rh substrate signal is too small to determine the signal intensity properly). The spectrum on the unexposed surface area (dark green) exhibits small Fe signals and a minor carbon peak, similar to the results observed for the other deposits on Sample II (see Chapter 5.6.1).

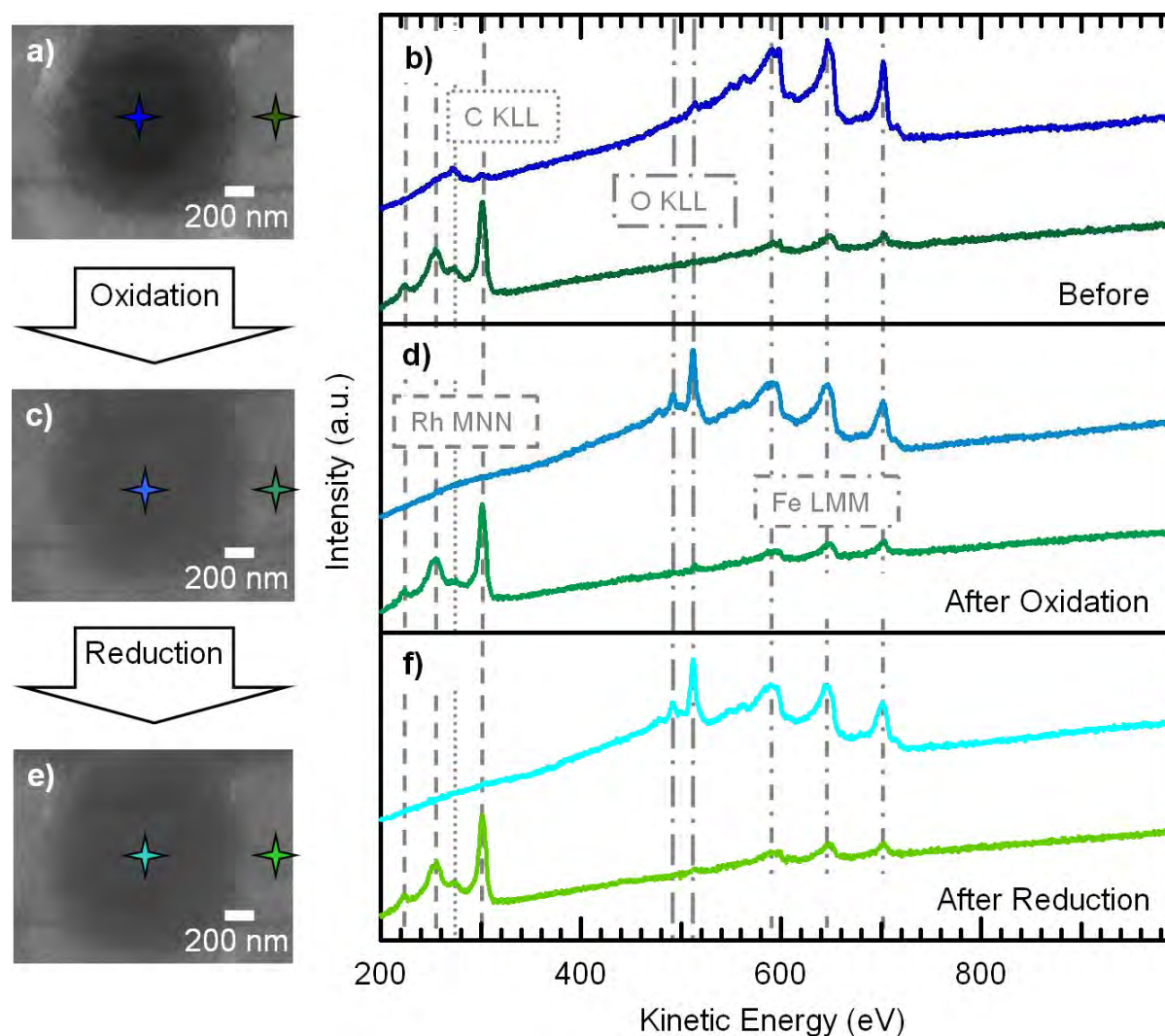


Fig. 5.27: Selective oxidation of iron EBID deposits to iron oxide structures. The markers in the SEM images correspond to the positions where the spectra were taken. a) SEM: Blow-up of the bottom EBID deposit from Fig. 5.15 (c). b) Auger spectra taken in and beside the circular EBID structure in (a). c) SEM image of the circular EBID structure in (a) after the oxidation procedure. d) Auger spectra taken in and beside the deposit in (c) after the oxidation procedure. e) SEM image of the circular EBID structure in (c) after the subsequent reduction procedure. f) Auger spectra acquired in and beside the deposit in (e) after the reduction procedure. ($U = 15$ kV; $I = 3$ nA; tilted sample)

To oxidize the iron structure in Fig. 5.27 (a) a sequence of alternatively dosing oxygen (three times) and hydrogen (two times) was performed with the background pressure set to $1.0 \cdot 10^{-6}$ mbar and the sample at ~ 525 K (~ 10 min for each step; performed in the preparation chamber). The SEM image in Fig. 5.27 (c) acquired after this procedure shows the circular deposit with no observable changes in size and shape. The contrast of the structure is weaker than in Fig. 5.27 (a) (i.e., the deposit appears not as dark compared to the rest of the surface),

which is most probably due to changes of the SE yield in the exposed and unexposed area, induced by adsorbed oxygen and the conversion of iron into iron oxide. The corresponding AE spectra are shown in Fig. 5.27 (d). The spectrum of the irradiated area (light blue) exhibits intense oxygen and smaller Fe peaks compared to before the oxygen dosage (Fig. 5.27 (b)). The small C and Rh signals prior to the oxidation procedure have disappeared. This indicates that the deposited iron is indeed oxidized by the given procedure, resulting in a thicker layer (Fe_xO_y vs. Fe), which leads to a complete damping of the Rh substrate signal. For carbon, a reaction with oxygen to CO or CO_2 is likely, which subsequently desorb, leading to a purification of the EBI deposit.

A clear indication for the formation of iron oxide, i.e., a chemical shift of the signals or a significant change in the lineshape, could not be observed; according to literature the formation and assignment of different Fe_xO_y species is primarily observed in AES in the kinetic energy region between 20 eV and 60 eV [168-170], which is not accessible in our case due to instrumental limitations. From experiments performed on iron single crystal surfaces [168, 169] and rods [170] it is well known that oxidation at the applied temperature results mainly in the formation of Fe_3O_4 , covered with a thin layer of Fe_2O_3 .

The spectrum on the non-irradiated area (light green) displays only a minor oxygen peak, due to the oxidation of the small amounts of iron present in this region and the adsorption of oxygen on the Rh(110) sample, leading to specific surface reconstructions (see Chapter 5.2). Otherwise, the spectrum remains unchanged as compared to before the oxidation. These results clearly demonstrate that the oxidation procedure is selective, as only the iron covered areas exhibit oxygen signals. One should also note here that oxygen is sensitive to radiation damage, as AE spectra taken not at one spot but while performing an “area scan” (see Chapter 3.4) of the unexposed surface show a higher oxygen peak (not shown here).

In order to check the chemical stability of the oxidized iron structures, hydrogen was dosed into the chamber once more ($1.0 \cdot 10^{-6}$ mbar; ~ 525 K; ~ 10 min). The SEM image and the AE spectra in Fig. 5.27 (e) and (f), respectively, are almost identical with the ones prior to the hydrogen treatment (Fig. 5.27 (c) and 5.27 (d), respectively), with only a small decrease of the O signal visible. This is a strong indication that the deposited iron was indeed transformed into iron oxide by the applied procedure and that it is stable against molecular hydrogen at ~ 525 K.

From the data presented in this chapter it can be derived, that iron structures deposited via EBID on Rh(110) can be selectively oxidized into iron oxide species. The applied method

comprises of an alternating dosage of oxygen and hydrogen at ~ 525 K. The resulting Fe_xO_y structures are stable against molecular hydrogen, which gives a clear indication for the transformation into iron oxide. Additionally, a purification of the deposits by the applied procedure in terms of oxidizing carbon contaminations to CO and CO_2 is indicated.

5.10 Summary and conclusions

The application of a catalytically active metal substrate, namely Rh(110), for EBID with the precursor iron pentacarbonyl opens up new possibilities for the nanostructuring of surfaces. In this context, our UHV experiments yield a novel aspect for the technique of EBID, since a well-prepared single crystal surface with a high long range order cannot be maintained under the typically applied high vacuum conditions.

Starting with an untreated Rh(110) sample, the stepwise improvement of the surface quality was monitored using SEM, AES and LEED, which resulted in a more detailed picture of the preparation of a single crystal surface in UHV (Chapter 5.3). A high chemical purity of the sample was already achieved after few cleaning procedures (combination of Ar-sputtering, oxygen treatment and annealing). However, extensive preparation was necessary to acquire a homogeneous surface that appears smooth in the SEM. Three specific sample conditions were selected during the course of the sample preparation and were applied for EBID experiments; these sample states, referred to as Sample I, Sample II and Sample III, differed mainly in terms of surface roughness and reconstruction (the higher the number, the better the surface quality).

Another preparation procedure for obtaining a highly ordered Rh(110) surface was to conduct oxidation / reduction cycles by alternately dosing O_2 and H_2 . Under certain conditions (pressure and temperature) the dosage of hydrogen onto an oxygen covered Rh(110) surface results in propagating reaction fronts. With our SEM setup it was not only possible to visualize such reactions fronts but also to induce their starting positions on the surface by electron irradiation during oxygen dosage (Chapter 5.4).

The first EBID deposits generated with iron pentacarbonyl on Rh(110) (Sample I) were presented in Chapter 5.5. Compared to the non-irradiated part of the sample they appeared dark in the SEM, which was attributed to a decreased SE yield of the deposited iron associated with the lower atomic number compared to rhodium [48]. It was also observed, that an increasing amount of material was deposited with an increase of the additionally applied precursor dosage time after the generation of the structures and that the resulting

deposits exhibit a higher oxygen contamination. This effect results from an autocatalytic dissociation of $\text{Fe}(\text{CO})_5$ molecules on the deposited iron.

Also the influence of the condition of the Rh(110) surface on the EBID procedure was studied (Chapter 5.6). Thereby, a specific influence was observed on the selectivity of the process, i.e., the deposition only in irradiated regions. On a perfectly ordered and clean Rh(110) (Sample III) the deposition with $\text{Fe}(\text{CO})_5$ was not selective, i.e., Fe deposits were formed on the whole surface by a catalytic decomposition of $\text{Fe}(\text{CO})_5$ at room temperature, irrespective of electron irradiation. This process was then followed by an autocatalytic decomposition of iron pentacarbonyl on already Fe-covered regions. In contrast, on a structurally non-perfect Rh(110) surface (Sample I and Sample II; exhibiting mainly a limited long-range order compared to Sample III) EBID was moderate selective, i.e., only a small amount of iron was deposited on the non-irradiated areas. In the case of a Rh(110) surface precovered with TiO_x , EBID was highly selective, which means that Fe deposits were only observed in the area simultaneously irradiated by the electron-beam. Regardless of the surface condition, the purity of the Fe deposits was always very high ($\geq 87\%$) compared to the values of $< 60\%$ typically achieved in literature (compare Chapter 2.7).

In particular from the results of the TiO_x -precovered surface one might envision to utilize local surface modifications, which inhibit the catalytic growth of iron upon dosage of $\text{Fe}(\text{CO})_5$ as a tool to produce a negative pattern on a catalytically active surface for the generation of catalytically grown structures. This would be an interesting concept to simultaneously generate thick, e.g., iron structures via the described catalytic effect at the predefined positions. Since in the usual EBID process the amount of deposited material scales with the electron exposure time this approach could reduce the time needed for the generation. In this way one would address one of the main weaknesses of EBID, which is the comparably low writing speed.

An additional influence of the quality of the surface was observed in respect to the lateral size of the generated structures. In the case of a rough Rh(110) surface (Sample I) the generation of spatially well defined line structures with a diameter < 25 nm was achieved, while an improvement of the surface quality resulted in broader and thus diffuser deposits (Sample II). This observation was attributed to a disturbance of the scattered electron trajectories (compare the proximity effects described in Chapter 2.7) on the rough surface, leading to a lower amount of unintended deposits in the surrounding of the primary electron impact point. In the case of the perfectly ordered Rh(110) surface (Sample III) the generation

of laterally defined structures could not be achieved, since $\text{Fe}(\text{CO})_5$ is catalytically and autocatalytically decomposed on the whole surface.

The influence of the primary electron dose on selectively deposited iron structures (Sample II) was studied in Chapter 5.7. Via AES measurements it was shown that the thickness of the deposit and thereby the amount of deposited material was increasing with an increasing electron dose. Furthermore, the lateral size of the structures was also increasing, which was attributed to a higher electron density in the surrounding of the exposed area due to the scattering of backscattered electrons in the sample material (BSE proximity effect; compare Chapter 2.7).

The iron structures deposited on Rh(110) (Sample I) were thermally stable at least up to 500 K (Chapter 5.8). Extended heating at 600 K resulted in a significant change of their appearance, which was mainly attributed to the diffusion of iron on the surface. Via AES measurements it could be shown that heating at temperatures between 400 and 500 K resulted in an increase of oxygen on top of the deposits, which subsequently desorbed at 600 K. One might therefore envision to purify the EBID deposits from oxygen contaminations by a short annealing at 600 K.

Finally, it was demonstrated that the deposited Fe structures could be selectively oxidized to iron oxide via an alternating exposure to oxygen and hydrogen at ~ 525 K (Chapter 5.9). The resulting iron oxide structures were stable against molecular hydrogen. AE spectra acquired before and after the oxidation procedure indicated also a purification of the deposits in terms of carbon contaminations, which were supposed to be oxidized to CO and CO_2 . Thus, the applied post-deposition procedure expands our potential to generate tailored nanostructures via EBID.

6 Iron pentacarbonyl on silicon single crystal surfaces

6.1 Introduction

After discussing the possibilities to generate clean iron nanostructures on the catalytically active metal surface Rh(110), this chapter describes EBID with the precursor iron pentacarbonyl on silicon single crystals with the surface orientation (100) and (111). Silicon is often used as sample material for electron-beam induced deposition processes [11, 22, 24, 33, 72], also in combination with $\text{Fe}(\text{CO})_5$ [33, 34, 36, 39, 104, 106, 171]. Advantages of Si are that it is I) cheap, II) easy to handle and III) rather simple to clean and prepare. Even more importantly, the generation of metal containing nanostructures on a semiconductor surface is interesting for industrial applications, like, e.g., the rewiring of integrated circuits [77]. Up to now, most of the EBID experiments for the generation of nanostructures on silicon samples were performed in an HV environment (e.g., compare references [22, 33, 34, 36, 39]). Under these conditions the surface purity and reconstruction cannot be maintained due to residual gases in the chamber (mainly hydrocarbons and water). Under UHV conditions, such contaminations are avoided and a well-defined, clean silicon surface can be ensured during the EBID process. This approach might therefore lead to some new aspects for the electron induced generation of iron deposits on silicon as well as for the whole EBID process.

A detailed description of the applied silicon single crystal surfaces, namely Si(100) and Si(111), is given in Chapter 6.2. In Chapter 6.3 the influence of the primary beam energy on the range of unintended deposition in the surrounding of the electron impact point will be discussed. The corresponding experiments are presented in context with Monte-Carlo simulations from the program *CASINO V 2.42* [92].

In Chapter 6.4, different experiments to study the influence of the sample temperature and precursor gas composition on the electron-beam induced deposition of iron structures on silicon samples with $\text{Fe}(\text{CO})_5$ are presented. Surprisingly, the iron deposits generated at room temperature on a clean and well-prepared silicon sample exhibit a discontinuous morphology and consist of small iron clusters with a size of partly below 10 nm. The local density of these iron clusters is depending on the applied electron dose and pattern geometry, as it will be presented in Chapter 6.5. Important for any further applications is the thermal stability of the clusters, which is discussed in Chapter 6.6.

A potential application for the generated iron deposits on silicon is the utilization as seeds for the growth of carbon nanotubes in arbitrary arrangements. First test experiments for

this, which were performed in cooperation with the “Lehrstuhl für Chemische Reaktionstechnik” (FAU Erlangen-Nürnberg), are presented in Chapter 6.7.

6.2 The substrates: Si(111) and Si(100)

Silicon (Latin: silicium, silex, silicis), which belongs to the fourth main group in the periodic table of elements, is after oxygen the second most abundant element on earth. Due to its high affinity towards oxygen, it never occurs elementarily in nature; a typical source is therefore silicon dioxide (SiO_2 ; “silica”) in the form of, e.g., sea sand, quartz, rock crystal or amethyst. Other widespread compounds in the mineral kingdom are the silicates, like, e.g., granite, feldspar and hornblende [99].

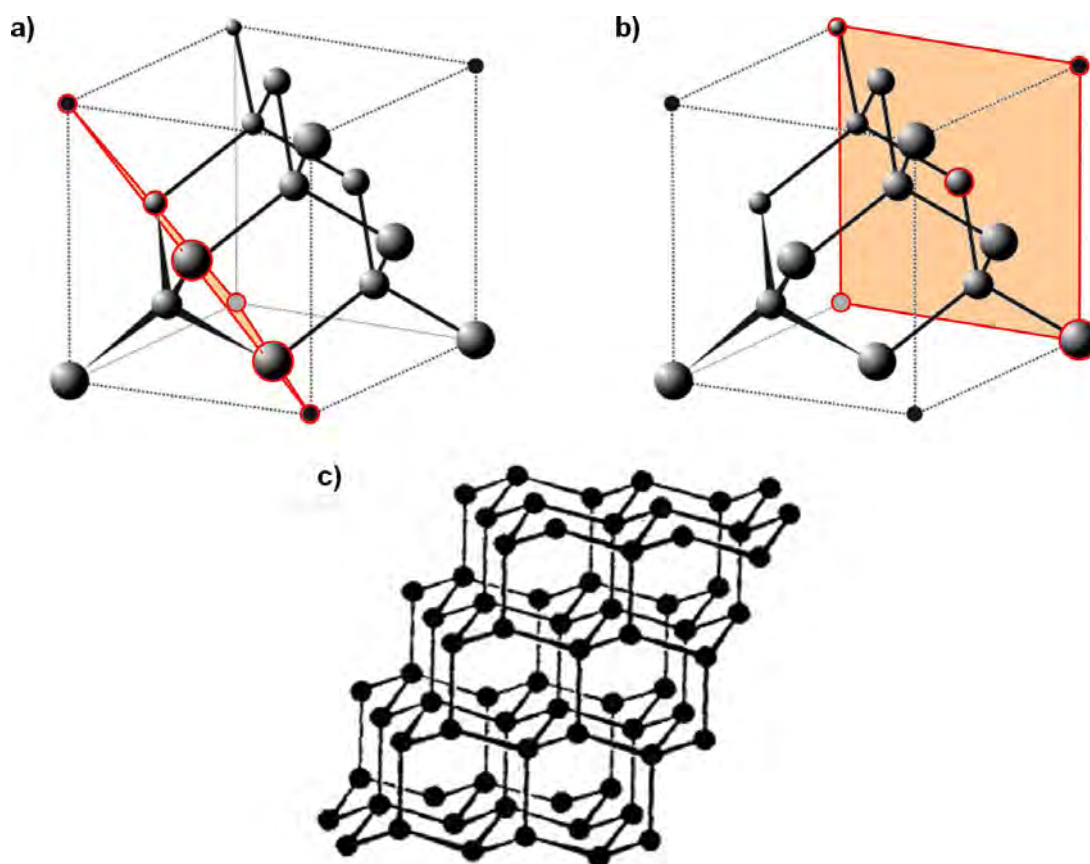


Fig. 6.1: The unit cell of silicon with the cutting planes for a) Si(111) and b) Si(100). The images of the unit cell are adapted from reference [172]. c) Crystal structure of silicon, as adapted from reference [173].

The high importance of elementary silicon for modern technical applications derives from its excellent semiconductor properties (band gap: 1.09 eV [99]), which makes it the

primary component of most electronic and photovoltaic devices. Pure silicon is commercially prepared via the reduction of high-purity silicon dioxide in a redox reaction by means of wood, charcoal or coal; the resulting product has a purity of at least 99 % (“metallurgical grade silicon”). Elemental silicon is a dark gray solid with a bluish tinge and a metallic luster; it has a density of 2.33 g/cm^3 and a melting point of 1680 K [99].

The crystal structure of Si is very similar to diamond: each silicon atom is tetrahedrally bonded to four neighboring atoms. This results in a unit cell with two face-centered cubic lattices, which are displaced to each other along the space diagonal by $1/4$ of the length of a unit cell. Fig. 6.1 displays the silicon unit cell ((a) and (b)) and the resulting crystal structure ((c)).

In the work at hand, silicon single crystal samples with two different surface orientations were applied, namely Si(111) and Si(100). The respective cutting planes in the silicon unit cell are marked in Fig. 6.1 (a) and (b), respectively. Both surfaces will be discussed in the following.

The Si(111) single crystal surface

A Si(111) surface is created by cutting a silicon single crystal along a defined plane, as depicted in Fig. 6.1 (a). The truncation of the chemical bonds generates an unreconstructed surface with “unsaturated” topmost atoms. Therefore, the preparation, i.e., heating, of the crystal in UHV leads to a new lateral periodicity in order to minimize the Gibbs free energy of the surface.

The structure of the resulting (7x7) reconstruction can be described by the “Dimer Adatom Stacking fault” (DAS) model of Takayanagi et al. [174]; evidence for its validation has been given by extensive scanning tunneling microscopy (STM) and transmission electron diffraction (TED) measurements. Images of the (7x7) reconstruction of Si(111) according to the DAS model are displayed in Fig. 6.2. Since the exact description of the reconstructed surface and the underlying theory are very complex, only the most important results and its implications for the surface are discussed in the following. For further information the reader is referred to reference [174].

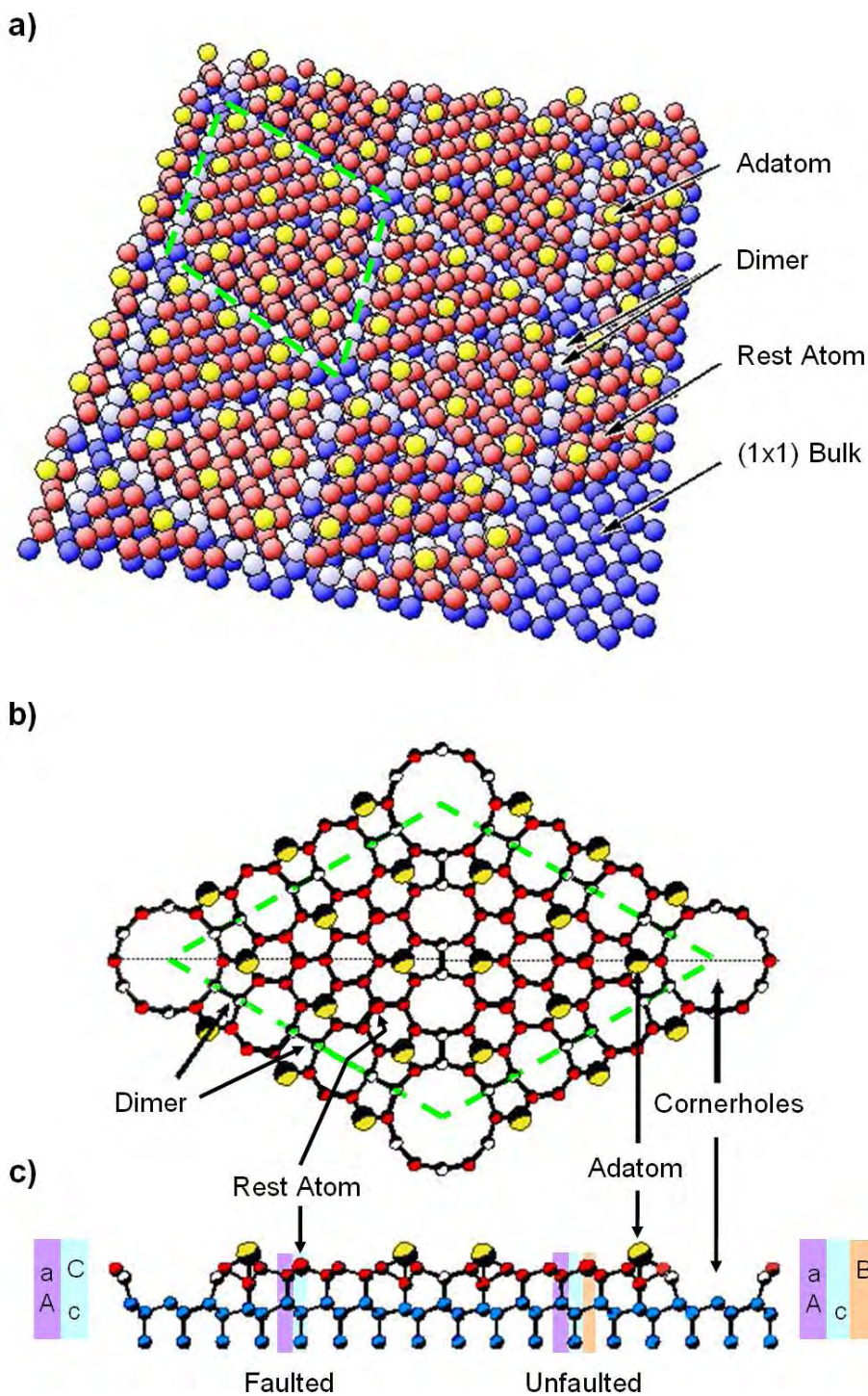


Fig. 6.2: Images of the “Dimer Adatom Stacking fault” (DAS) model of $\text{Si}(111)-(7 \times 7)$. a) Atom model from a birds-eye view. The image is adapted from reference [122]. b) Top view of a (7×7) surface unit cell. The black, dotted line marks the position of the side view in c). Images (b) and (c) are adapted from reference [175]. Depicted on the left and right side of (c) are the stacking sequences in the corresponding subcells. The green dashed line in (a) and (b) marks the position of a (7×7) unit cell.

The surface unit cell of the (7x7) reconstructed surface (marked by the green dashed line in Fig. 6.2 (a) and (b)) consists of 49 original Si(111) unit cells and exhibits a threefold symmetry. Each reconstructed surface cell comprises 12 adatoms (yellow atoms in Fig. 6.2), which are locally arranged in a (2x2) structure, and is divided into two triangular subcells; the latter differ in their stacking sequence, leading to a faulted (left part in Fig. 6.2 (c); stacking sequence cAaC) and unfaulted part (right part in Fig. 6.3 (c); stacking sequence cAaB) of the unit cell. Furthermore, each subcell is confined by 9 dimers on the sides (white atoms in Fig. 6.2) and a vacancy at each of the three corners (“cornerhole”) [174]. Due to the described (7x7) reconstruction the number of dangling bonds of each unit cell is reduced from 49 to 19 [174].

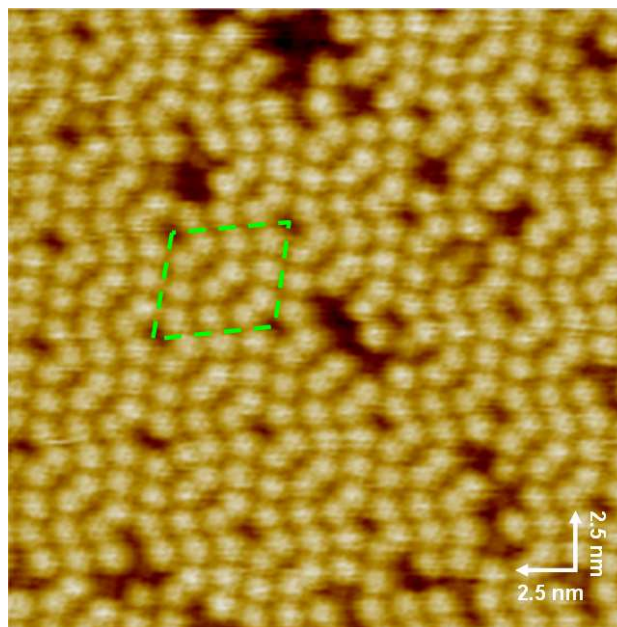


Fig. 6.3: STM image of an atomically resolved Si(111)-(7x7) surface, acquired via our instrument. The green, dashed line marks the position of a surface unit cell. (Image parameters: size = 25 nm x 25 nm; $U_{Gap} = -0.5$ V; $I_{Gap} = 1$ pA)

In STM measurements (compare the image in Fig. 6.3, which was acquired via our instrument) the cornerholes are characteristic for the Si(111)-(7x7) reconstructed surface, as they are clearly visible in the micrographs (vacancies in Fig. 6.3); the bright protrusions in Fig. 6.3 are attributed to adatoms. It is noteworthy, that the image in Fig. 6.3 was acquired with a rather low tunneling current I_{Gap} (1 pA), which represents a special characteristic of the applied STM electronics.

The Si(100) single crystal surface

A cut through a different plane of the silicon single crystal (see Fig. 6.1 (b)) results in the fabrication of a Si(100) surface. As depicted in Fig. 6.4 (a), this cut leads to a topmost layer of silicon atoms that are only bonded to two neighboring silicon atoms (orange atoms in Fig. 6.4 (a)). In order to minimize the Gibbs energy of this (1x1) surface, the “unsaturated” atoms form bonds with each other in a specific pattern. This results in the thermodynamically more stable (2x1) reconstructed Si(100) surface (see Fig. 6.4 (b)), in which each atom in the topmost layer builds one covalent bond to a neighboring atom, thus forming the so-called “symmetric dimers”. Still, each of the dimer atoms has one single dangling bond left.

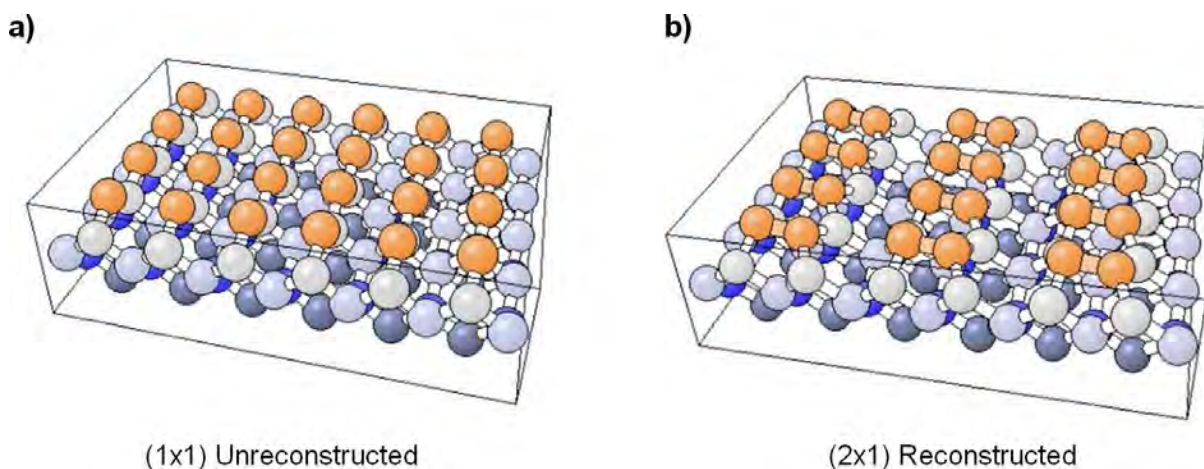


Fig. 6.4: a) Unreconstructed Si(100)-(1x1) surface and b) reconstructed Si(100)-(2x1) surface. Both images were adapted from reference [176].

The symmetry of the Si(100)-(2x1) reconstructed surface is very different compared to the (7x7) reconstructed Si(111) surface: while the latter shows a threefold symmetry after reconstruction, Si(100) exhibits a twofold one.

6.3 Influence of the beam energy on the electron exit area

As described in Chapter 2.7, the lateral extent of deposited material strongly depends on electron scattering processes; backscattered electrons (BSEs) and secondary electrons caused by those BSEs (SE II) determine the electron exit area and therefore have a significant influence on the region in which electron – precursor interactions take place. The resulting deposition of material in areas that were not directly exposed to the primary electron-beam results in a specific influence on the structures close by (compare the proximity effects discussed in Chapter 2.7).

One way to reduce this effect is the application of primary electrons with a lower kinetic energy and thus to limit the maximum range of the BSEs in the sample material. Fig. 6.5 shows two SEM images of deposits that were generated with the precursor iron pentacarbonyl on Si(111) with different primary beam energies, namely 15 and 8 kV; otherwise the structures were both irradiated with an identical beam current, total area electron dose and lithographic parameters. The electron irradiation in the specific experiments was realized via repeatedly scanning the same rectangular area in the image acquisition mode of the SEM. Thereby, the electron-beam scans over the surface in horizontal lines from the left to the right; in order to stabilize the beam at the start of each line, a constant waiting time of 102.4 μs is applied. Additionally, at the start of each frame the beam is irradiating the top left corner of the rectangular scan area for 24 ms. These waiting times result in an increased electron dose at the left boundary of the scanned region. Additionally, the repeated irradiation of an identical region provides a constant replenishment time for the precursor molecules between each frame, which might influence the amount and composition of the deposited material. The identical parameters applied for the irradiation of the structures in Fig. 6.5 are listed below:

- **Frame size:** 1.00 μm · 1.33 μm
- **Number of irradiated points per frame (image resolution):** 1024 · 768
- **Irradiation time per point (pixel time):** 1.6 μs
- **Scan speed:** 5
- **Total exposure time:** 12 min
- **Number of frames:** 529
- **Beam current:** 400 pA
- **Total electron dose:** 20.0 C/cm^2

It has to be noted, that the Si(111) sample used for the experiments in Fig. 6.5 had already been used for EBID before and was cleaned with parameters that differ from the standard procedure described in Chapter 3.4; additionally, it displayed some peculiar surface defects in SEM (e.g., a large scratch over the central part of the sample). The following data should therefore be considered as an explorative survey to the topic.

Fig. 6.5 (a) displays an SEM image of a bright, oval area that was generated via the described irradiation procedure with a primary beam energy of 15 kV; contrast and brightness of the image were enhanced to visualize the entire area of deposited material. In distinction to

the observations on Rh(110) (compare Chapter 5) the deposit appears brighter than the substrate in the SEM; this can be interpreted as due to an increased SE yield of the deposited iron associated with the higher atomic number compared to silicon [48]. Additionally, the irradiated area (marked by the dashed rectangle) appears slightly brighter than the surrounding region, indicating a higher amount of deposited material in this area.

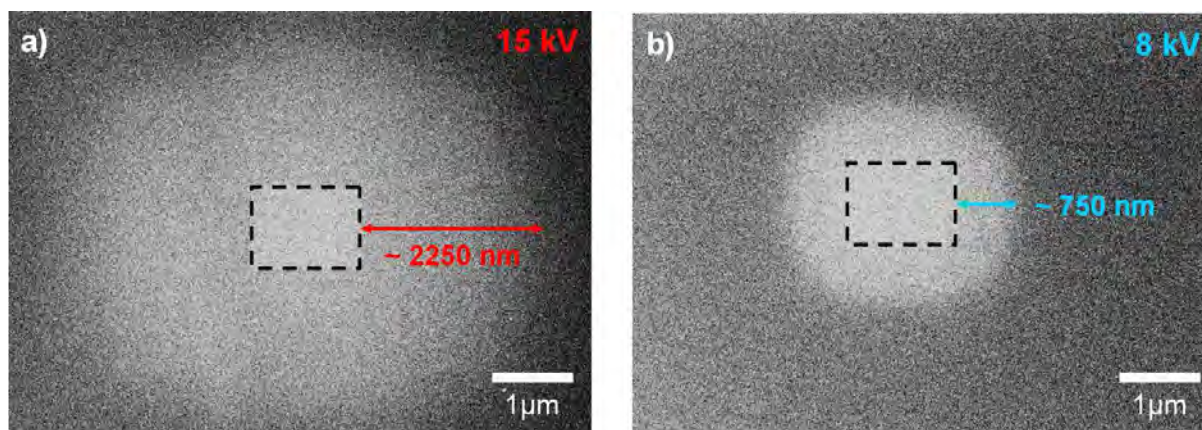


Fig. 6.5: SEM images of deposits that were generated via irradiation of a rectangular area with a primary beam energy of a) 15 and b) 8 kV on Si(111). In both cases a beam current of 400 pA and an electron dose of 20.0 C/cm² was applied. The irradiation was performed via the image acquisition mode of the SEM as described in detail in the text. Contrast and brightness of the images were drastically enhanced to improve visibility. (U = 15 kV; I = 400 pA; plane sample)

The deposition of material in the region surrounding the exposed area is attributed to the interaction of precursor molecules with scattered electrons (BSEs and SEs). This assumption is confirmed by a Monte-Carlo simulation of the BSE exit area on silicon with the program *CASINO V 2.42* [92]; the corresponding plot of the amount of BSEs versus the radial position on the silicon surface with respect to the impact point of the primary electron-beam is depicted in Fig. 6.6 (red spectrum). The maximum range of the backscattered electrons could be extracted from this plot to be ~ 2300 nm, which fits quite well to the distance between the boundaries of the irradiated area and the surrounding halo in Fig. 6.5 (a) (~ 2250 nm).

Fig. 6.5 (b) shows an image of a deposit that was generated with a primary beam energy of 8 kV. Again, irradiation of a rectangular area resulted in a structure with an oval shape, appearing bright in the SEM. In this case, there is no significant difference between the brightness in the exposed area (dashed rectangle) and the surrounding halo; this observation is mainly attributed to an increasing electron density in the BSE exit area associated with a

reduction of the primary beam energy, as it has been already discussed in Chapter 4.3.2 for the deposition of carbon with ethene at 3 and 15 kV. The size of the oval in Fig. 6.5 (b) is smaller compared to the one in (a); the distance between the boundaries of the irradiated region and the surrounding halo was in this case estimated to be ~ 750 nm, which is again in good agreement with the radius of the simulated BSE exit area extracted from the blue plot in Fig. 6.6 (~ 775 nm). This observation confirms that a reduction of the applied primary beam energy reduces the range of “unintended” deposition in the surrounding of the exposed area.

A different effect associated with the reduction of the primary beam energy is a change in the electron spot size. Calibration measurements performed on a Au on C sample showed that beam energies of 15, 3 and 1.2 kV (beam current: 400 pA) resulted in beam diameters of 2.8, 4.9 and 5.2 nm, respectively (values measured according to the 20/80 criterion). Since these variations are rather small compared to the radius of BSE exit area (compare Fig. 6.6) it can be supposed that this effect has only a minor influence.

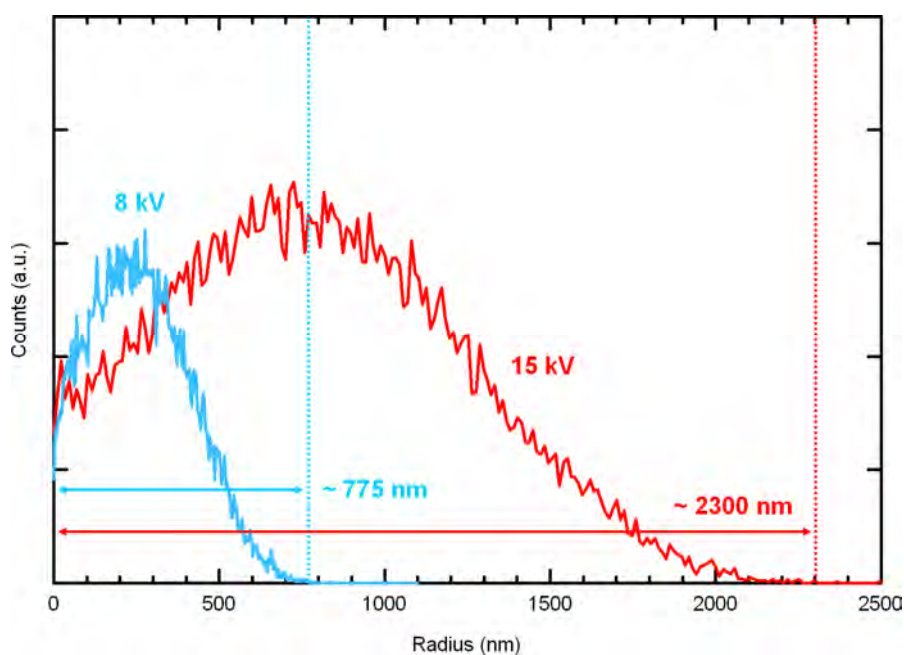


Fig. 6.6: Plots of the amount of BSEs released from silicon versus the radial position on the surface with respect to the impact position of the primary electron-beam (at radius = 0) for 15 (red) and 8 kV (blue). They were calculated with a Monte-Carlo simulation via the software CASINO V 2.42 [92].

From the experiments described in this chapter, it can be stated that the range of “unintended” deposition in the surrounding of the irradiated area due to the BSE proximity effect can be effectively reduced via a reduction of the applied primary beam energy. This

was shown in Fig. 6.5 for the application of a 15 and 8 kV electron-beam; the resulting distances between the boundaries of the irradiated region and the surrounding halo were in good agreement with Monte-Carlo simulations of the respective radii of the BSE exit areas (see Fig. 6.6). A simultaneous enlargement of the beam diameter with a decreasing primary beam energy is supposed to have only a minor influence on the lateral size of the generated deposits. It has to be noted, that the ultimate sizes of the deposits reported in this chapter were only achieved at very high electron doses. At lower electron doses the unintended deposition in the surrounding of the electron impact point is also determined by the statistics of the scattering processes. However, for the generation of small EBID structures the application of lower acceleration voltages was found to be disadvantageous, i.e., the structures fabricated with 15 kV in the framework of the thesis at hand were smaller (compare Chapter 4.3.2). One explanation is the influence of the primary beam energy on the distribution and density of the scattered electrons in the surrounding of the impact point. Another reason is certainly that the larger beam diameter for smaller primary beam energies starts to account for the generation of very small deposits. Directly related to the latter is the more difficult optimization of the beam size for lower acceleration voltages, especially for substrates with weak contrast in SEM. Therefore and to ensure comparability of the results the primary beam energy was usually fixed at 15 kV.

6.4 Material parameters in EBID with $\text{Fe}(\text{CO})_5$ on silicon

In Chapter 5.6 the influence of the surface quality on the selectivity (i.e., selective deposition in areas, where electron – precursor interaction takes place) of the electron-beam induced deposition of iron with $\text{Fe}(\text{CO})_5$ on Rh(110) was discussed. These results already demonstrated that the condition of the applied EBID components may exhibit a specific influence on the deposition procedure.

To further address this topic and to study the potential to generate iron structures with iron pentacarbonyl on silicon single crystal surfaces under varying conditions, different experiments were performed, which are presented in the following subchapters. Thereby, the main focus lies on the influence of the surface temperature and the precursor gas composition. Most of the experiments were performed on Si(100) samples; some explorative experiments on Si(111) are also presented.

6.4.1 Deposition of iron on Si(100) at room temperature

First of all, the EBID process with $\text{Fe}(\text{CO})_5$ on Si(100) was studied at room temperature. The experiments were performed on new and freshly cleaned samples that exhibited in LEED a sharp and well-defined (2x1) reconstruction. SEM images of resulting deposits are depicted in Fig. 6.7. From these micrographs it is apparent that all structures are discontinuous, i.e., they consist of small clusters with a size below 10 nm. Fig. 6.7 (a) shows a matrix consisting of ten point structures (three in the left and middle column, four in the right column), which were generated by irradiation with an increasing electron dose from the bottom left (1.32 nC) to the top right (2.40 nC). The point deposits do not continuously increase in size with an increasing electron exposure, as to be expected from literature [32, 40, 177]. Instead, the number of clusters within one exposed point increases. With an electron dose of 1.32 nC a single and very defined cluster was generated (Fig. 6.7 (b)), while an electron dose of 2.40 nC results in a conglomerate of 15 to 17 clusters (Fig. 6.7 (c)), which are randomly scattered in a small area around the impact point of the primary beam. The specific placement of the iron clusters is due to the statistical nature of the deposition process on the nanometer length scale [12]. At electron doses higher than 2.40 nC this effect is further proceeding, leading to a high number of clusters aligned in a densely packed conglomerate (not shown here). Below the electron dose of 1.32 nC, no clusters are visible on the surface, which indicates that a minimum electron dose is necessary to create the clusters observed in Fig. 6.7 (a) to (c). A detailed description of the correlation between the applied electron dose and the number of resulting clusters is given in Chapter 6.5.

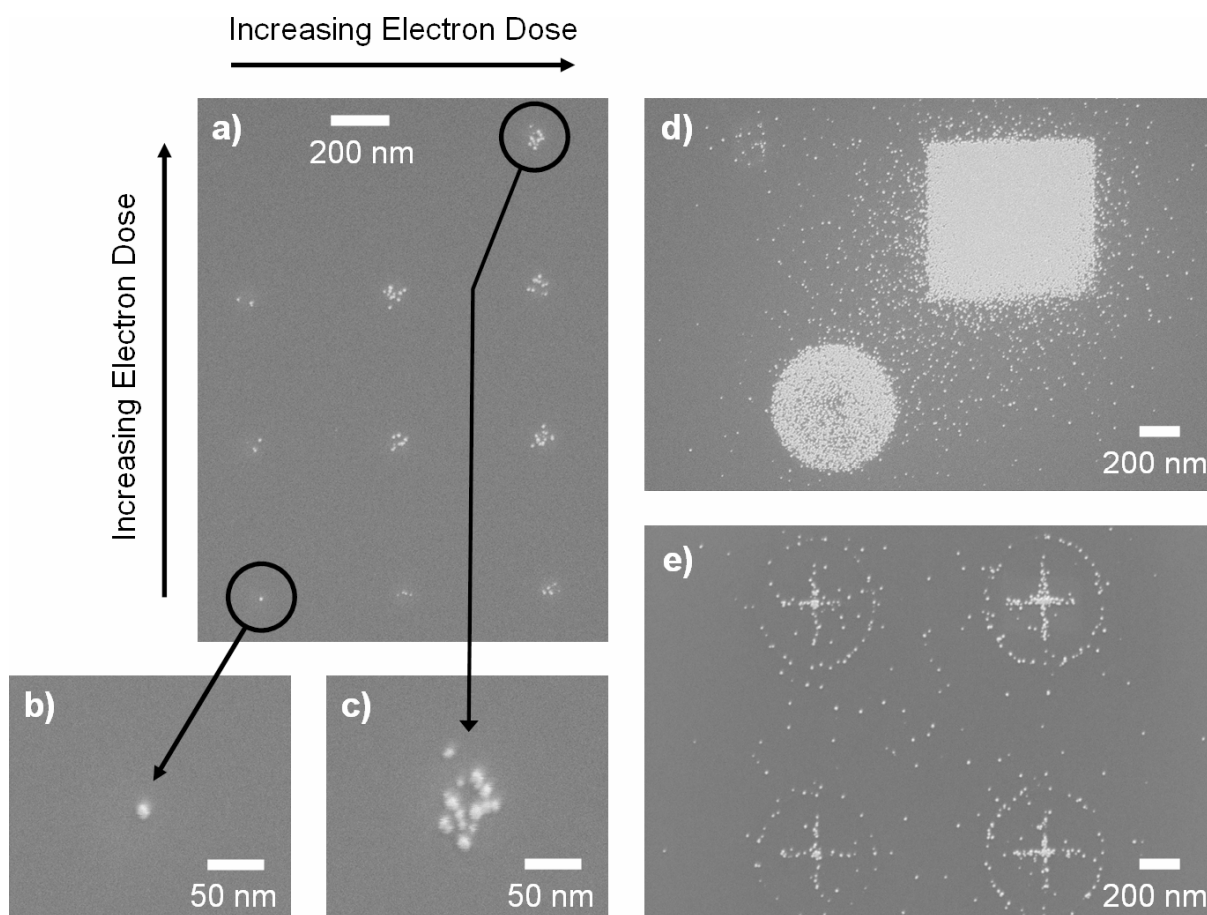


Fig. 6.7: SEM images of various deposits generated via EBID with $\text{Fe}(\text{CO})_5$ on a $\text{Si}(100)\text{-(}2\times 1\text{)}$ at room temperature. a) Pattern of ten point structures, which were generated by irradiation with an increasing electron exposure from 1.32 (lower left) to 2.40 nC (upper right). b) Image of the point deposit generated with the lowest exposure time in (a). c) Image of the point deposit generated with the highest exposure time in (a). d) Area deposits (template square and circle), which were generated with an electron dose of 13.3 C/cm^2 . e) Line deposits (template: circle with centered cross), which were generated with an electron dose of 72 (lower left), 80 (upper left), 88 (lower right) and $96 \mu\text{C/cm}$ (upper right). ((a), (b), (c), (d): $U = 15 \text{ kV}$; $I = 400 \text{ pA}$; plane sample / (e): $U = 15 \text{ kV}$; $I = 3 \text{ nA}$; tilted sample)

As examples for structures of different shape, area and line deposits are depicted in Fig. 6.7 (d) and (e), respectively. Similar to the dots, these structures are composed of small clusters. The area deposits in Fig. 6.7 (d) with the shape of a square (template size: $800 \text{ nm} \cdot 800 \text{ nm}$) and a circle (template diameter: 600 nm) were both generated by irradiation with an electron dose of 13.3 C/cm^2 . In the exposed area the clusters are closely packed such that the surface appears to be almost completely covered. In addition, a small but significant number of clusters is randomly distributed around the desired structures, i.e., in a surface region,

which was not directly exposed to the primary beam. This observation is mainly attributed to the exposure of non-irradiated areas in the surrounding of the primary electron impact point due to backscattered electrons and their resulting secondary electrons (“BSE proximity effect”, compare Chapter 2.7) or primary electrons scattered by the three dimensional deposits (“FSE proximity effect”; compare Chapter 2.7). Alternatively, diffusion of iron atoms on the surface cannot be completely ruled out; the diffusion of entire clusters can be excluded as the SEM images show no changes over extended periods of time.

The line deposits in Fig. 6.7 (e) consist each of a circle (template diameter: 600 nm) with a centered cross (template length: 400 nm) and were irradiated with an increasing electron dose from the bottom left ($72 \mu\text{C}/\text{cm}$) to the top right ($96 \mu\text{C}/\text{cm}$). Similar to the point deposits (compare Fig. 6.7 (a)), the cluster density in the irradiated area is increasing with an increase of the applied electron dose; yet, a complete coverage of the exposed region could not be achieved with the applied parameters. A certain amount of clusters is also randomly distributed between the line structures; similar as for the area deposits (compare Fig. 6.7 (d)), this is attributed to electron exposure due to the BSE proximity effect.

To determine the chemical composition of the deposits local Auger electron spectroscopy was performed. Fig. 6.8 (a) and (b) show SEM images of quadratic area structures (template square: $600 \text{ nm} \cdot 600 \text{ nm}$); the deposits in (a) were generated with an electron dose below the onset of the cluster growth (lower left: $1.3 \text{ C}/\text{cm}^2$; upper left: $2.7 \text{ C}/\text{cm}^2$; lower right: $4.0 \text{ C}/\text{cm}^2$; upper right: $5.3 \text{ C}/\text{cm}^2$), while for the structures in (b) a significantly higher electron dose was applied (lower left: $17.3 \text{ C}/\text{cm}^2$; upper left: $18.6 \text{ C}/\text{cm}^2$; lower right: $20.0 \text{ C}/\text{cm}^2$; upper right: $21.3 \text{ C}/\text{cm}^2$). The SEM micrograph in Fig. 6.8 (a) reveals continuous square deposits, which appear darker than the unexposed surface. On the other hand, the image in Fig. 6.8 (b) shows an enhanced contrast and displays in the irradiated region an arrangement of closely packed clusters, similar as it was observed for the area deposits in Fig. 6.7 (d). Again, a certain amount of clusters is randomly distributed in the direct surrounding due to electron scattering processes (see above). The markers in Fig. 6.8 (a) and (b) indicate the positions where the Auger spectra, shown in Fig. 6.9, were acquired.

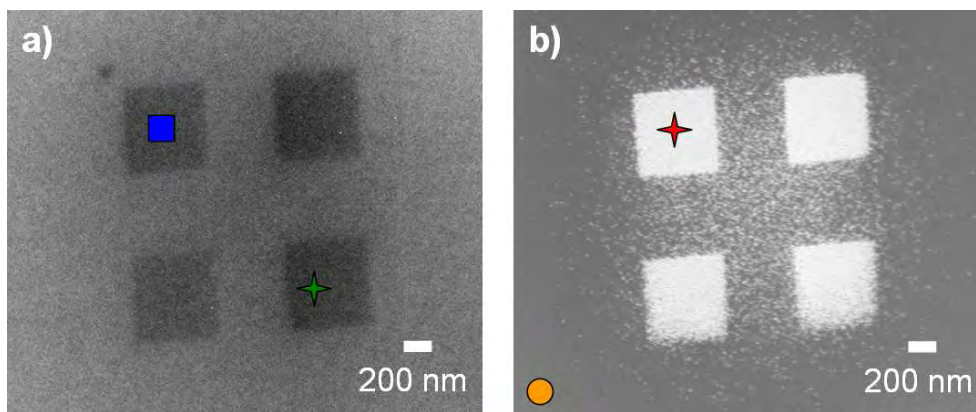


Fig. 6.8: SEM images of square nanostructures on Si(100) that were generated by EBID using $\text{Fe}(\text{CO})_5$. a) Pattern of four squares, which were generated by irradiation with an electron dose of 1.3 (lower left), 2.7 (upper left), 4.0 (lower right) and 5.3 C/cm^2 (upper right). b) Pattern of four squares, which were generated by irradiation with an electron dose of 17.3 (lower left), 18.6 (upper left), 20.0 (lower right) and 21.3 C/cm^2 (upper right). The markers in (a) and (b) indicate the positions where the spectra in Fig. 6.9 were acquired. Contrast and brightness of the image in (a) was drastically enhanced to improve visibility. ($U = 15 \text{ kV}$; $I = 3 \text{ nA}$; tilted sample)

The local Auger spectra acquired in the center of the upper left square in Fig. 6.8 (b) (red spectra in Fig. 6.9 (a) and (b)) are dominated by Fe LMM transitions at 593, 648 and 702 eV, while only small peaks for carbon (274 eV) and oxygen (512 eV) can be observed. From this data it is apparent, that the cluster deposit contains a high amount of iron. A determination of the intensity ratio between the iron signal at 648 eV and the carbon peak yields a value of ~ 37.6 , indicating the very low carbon contamination level of the deposit. An estimation of the total amount of contaminations results in a value of $\sim 4\%$ ($\sim 1\%$ carbon contamination, as derived from a comparison to the spectrum of a thick carbon layer (see Chapter 3.4); the oxygen contamination was roughly estimated to be lower than 3% (see Chapter 3.4)). The resulting metal purity of 96% represents one of the highest values achieved via EBID with metal containing precursors so far. Since the Auger spectra were acquired more than 16 hours after the structures were produced, we assume that the initial purity of the iron deposits must be even higher; therefore, we conclude that the generated clusters consist of pure iron.

In the spectrum acquired at the higher kinetic energies (Fig. 6.9 (b)) a small but significant signal from the silicon substrate is visible (1616 eV); the strong damping of the peak indicates that a high amount of iron was deposited in the corresponding irradiated

region. A quantitative analysis of the layer thickness yields a value of ~ 1.9 nm assuming a homogeneously closed layer of pure iron (note, that the silicon peak in the spectrum acquired on the non-irradiated area (orange in Fig. 6.9 (b)) was taken as reference for the undamped signal).

The local Auger spectra acquired on the lower right square in Fig. 6.8 (a) (green spectra in Fig. 6.9 (a) and (b)) reveal that the deposit consists only of an ultra thin layer, as the silicon signal shows almost no damping compared to the non-irradiated surface. A quantitative analysis of the layer thickness yields a value of ~ 0.10 nm assuming a homogeneously closed layer of pure iron and ~ 0.13 nm for the calculation with a pure carbon layer (note, that the silicon peak in the spectrum acquired on the non-irradiated area (orange in Fig. 6.9 (b)) was taken as reference for the undamped signal). Small iron and carbon peaks with an Fe / C ratio of 2.3 are observed, indicating the relatively low purity of this layer compared to the deposits in Fig. 6.8 (b) (note, that the intensity of the green spectrum in Fig. 6.9 (a) was tripled in order to improve visualization). To minimize the influence of the electron-beam during AES measurements on the structures in Fig. 6.8 (a), the chemical composition of the upper left square was determined using an “area scan”, according to the description given in Chapter 3.4. In the corresponding spectrum (blue in Fig. 6.9 (a) and (b)) an additional, small oxygen peak is observed; the missing O signal in the normal, i.e., point, spectrum (green) is attributed to electron stimulated desorption (ESD) of oxygen, as it was described in Chapter 5.6.2 for a thin titanium oxide layer on Rh(110). Apart from that, both spectra appear almost identical, with a similar intensity of the iron, carbon and silicon signals.

Since this type of deposit is observed before the onset of the cluster substructure, it is therefore regarded as a prerequisite for the formation of the latter. On the other hand, as this initial layer also partly contributes to the contamination signal in the spectra of the cluster deposits obtained at higher exposures (which is concluded from the fact that some signal from the Si substrate is also observed; compare red spectrum in Fig. 6.9 (b)), the true contamination level of the clusters could be even lower. This observation confirms the assumption that the cluster substructure consists of pure iron.

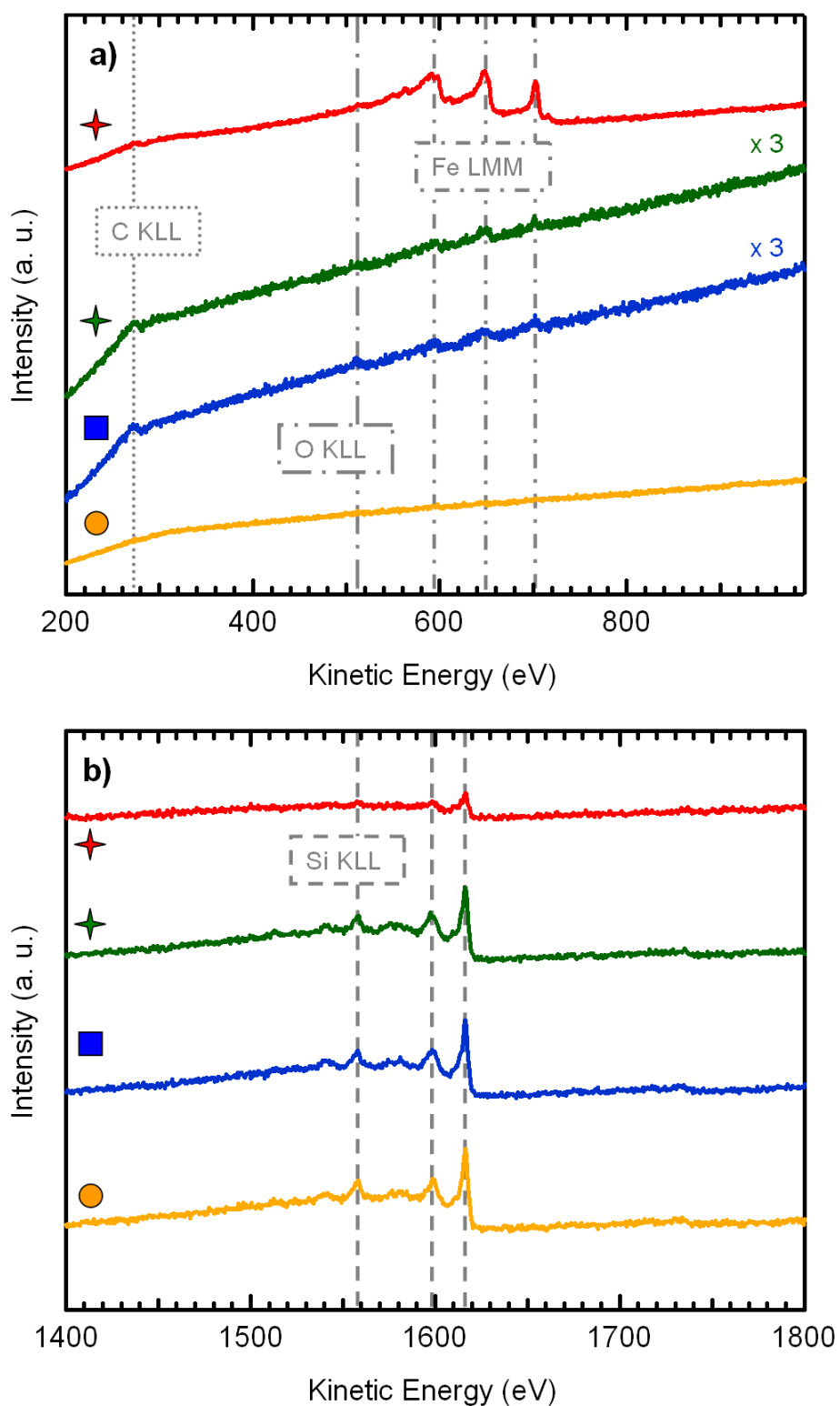


Fig. 6.9: Local Auger spectra of the kinetic energy region a) of the C KLL, O KLL and Fe LMM transitions and b) of the Si KLL transitions, which were acquired on the positions marked in Fig. 6.8. The red, green and orange spectra were acquired via a “normal” point scan, while the blue spectra were acquired via an “area scan” (see Chapter 3.4). Note, that the intensity of the green and blue spectra in (a) were tripled in order to improve visualization.

The selectivity of the EBID process in the system $\text{Fe}(\text{CO})_5$ on $\text{Si}(100)$ is verified by the Auger spectra of the surface region close to the EBID structures (orange spectra in Fig. 6.9), which show no indications for iron and oxygen and only a minor amount of carbon. The selectivity is therefore higher compared to the one achieved for the deposition of iron with $\text{Fe}(\text{CO})_5$ on $\text{Rh}(110)$ (compare Chapter 5.6). The absence of deposited iron in the non-irradiated area on $\text{Si}(100)$ is consistent with Auger electron spectroscopy measurements performed by Foord and Jackman [178]; they reported that virtually no iron was found on the silicon surface following exposure to $\text{Fe}(\text{CO})_5$ at 300 K.

A possible explanation for the formation of the iron clusters (compare Fig. 6.7 and Fig. 6.8 (b)) is a high tensile stress relative to the initial layer (probably due to lattice mismatch), which leads to a preference for the formation of small clusters due to an overall energy minimization [179], with some analogy to the Stranski-Krastanov growth mode [180]. Considering the high purity of the clusters the proposed tensile stress should be determined by lattice mismatch of pure iron and the prerequisite layer. Since iron grows on $\text{Si}(100)$ in a layer by layer fashion [181, 182], it is concluded that the prerequisite layer is indeed necessary to induce the tensile stress resulting in the observed cluster growth. At this point, we can just speculate about the exact nature of this layer. Considering the estimated thickness and composition observed in the AE spectra (compare Fig. 6.9) we suggest an atomically well ordered submonolayer structure consisting of iron, carbon and oxygen, which enhances / enables the complete decomposition of iron pentacarbonyl and the subsequent desorption of the remaining carbon monoxide. The agglomeration into the observed iron clusters also requires the mobility of the involved atoms or molecules, i.e., the clustering process relies on diffusion. A summary of this process is given by the scheme in Fig. 6.10. An additional effect resulting from this diffusion mechanism is to overcome the size limitation from the “classical” EBID process, which is mainly induced by the scattering of electrons in the sample material; even though the electron interaction area on silicon is rather large (compare Chapter 2.7), the resulting iron clusters have a size of a few nanometers.

For the deposition of iron with $\text{Fe}(\text{CO})_5$ on $\text{Rh}(110)$ an autocatalytic dissociation of the precursor molecules was observed (compare Chapters 5.5 and 5.6). It has to be noted, that this effect might also have an influence on the generation of the iron clusters in Fig. 6.7 and Fig. 6.8 (b). Additional experiments would be necessary to further address this topic.

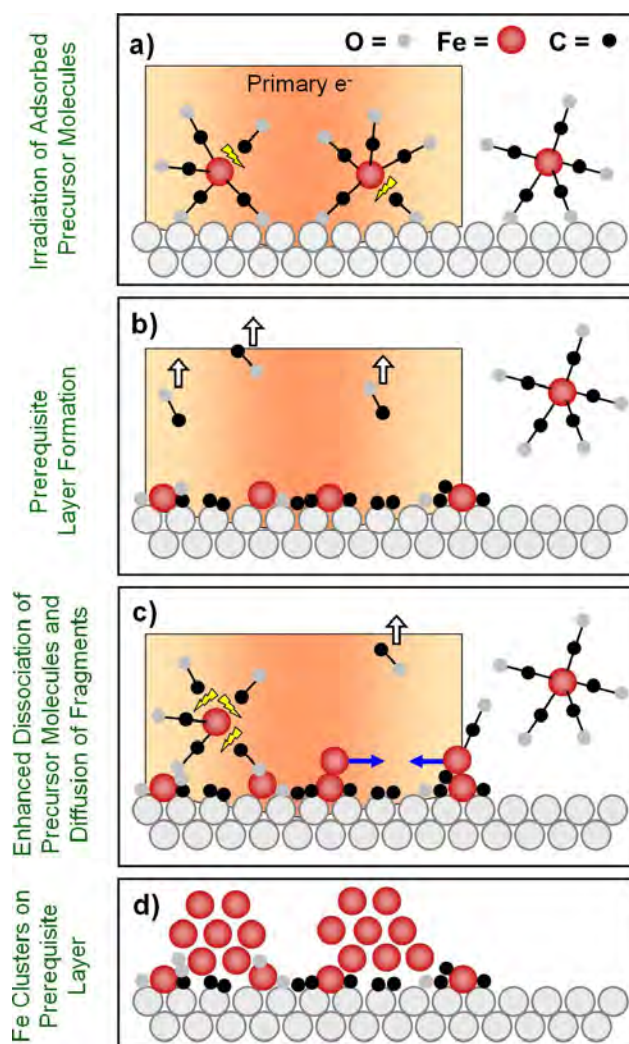


Fig. 6.10: Scheme summarizing the proposed mechanism for the growth of iron clusters on Si(100). a) Irradiation of Fe(CO)₅ molecules adsorbed on the surface. b) Resulting initial layer. The purity of this initial layer is supposed to be rather low, with carbon and oxygen contaminations being present. c) Further irradiation leads to an enhanced dissociation of precursor molecules and a tensile stress induced diffusion of the resulting fragments on the prerequisite layer. d) Resulting Fe clusters on the prerequisite layer. From the non-irradiated surface the precursor molecules were desorbing intact.

In summary it can be stated, that performing EBID with iron pentacarbonyl on Si(100)-(2x1) at room temperature results in a discontinuous structure morphology (compare Fig. 6.7 and 6.9 (b)). The generated deposits consist of pure iron clusters (purity at least 96 %) with a diameter < 10 nm. The formation of these clusters during EBID is interpreted as due to a tensile stress between the deposited iron clusters and an underlying prerequisite layer, which formed in the initial deposition process before the onset of the

cluster growth; also a specific influence by an autocatalytic dissociation of precursor molecules cannot be completely ruled out.

6.4.2 Influence of the precursor gas purity

In the previous chapter it was reported, that EBID with $\text{Fe}(\text{CO})_5$ on Si(100) under UHV conditions results in the generation of pure iron clusters. An important question is, if the quality of the precursor gas has a specific influence on this process, which is studied in detail in this section by a combination of QMS measurements and EBID experiments.

Fig. 6.11 shows QM spectra of two different precursor gas compositions, namely A and B. In gas composition A the precursor was only marginally purified by an initial cleaning. The corresponding QM spectrum (compare Fig. 6.11 (a)) exhibits numerous, large peaks in the region of $m/z = 2 - 44$, while in the region of $m/z = 50 - 200$ only some minor signals are observed. A summary of the most likely fragments and their corresponding peaks in the spectrum is given in Table 6.1; additionally, the intensity ratios between the respective signals and the Fe^+ -peak at $m/z = 56$ are listed. The most dominant signals in gas composition A are assigned as H_2^+ -peak ($m/z = 2$), N^+ -peak (14), Ar^{++} -peak (20), $\text{CO}^+ / \text{N}_2^+$ -peak (28), Ar^+ -peak (40) and CO_2^+ -peak (44). The Ar related signals are attributed to a contamination, resulting from previous cleaning procedures of the Rh(110) single crystal (sputtering with Ar^+ ; compare Chapter 3.4). The relatively high intensity of the N^+ -peak at $m/z = 14$ indicates that the gas originating from the iron pentacarbonyl storage device contains a considerable amount of nitrogen (the precursor is filled into the storage device under nitrogen atmosphere; compare Chapter 3.4); furthermore, a certain fraction of the signal at $m/z = 28$ can be attributed to CO^+ , resulting from decomposed $\text{Fe}(\text{CO})_5$ molecules. At $m/z = 56$ and 84 two additional signals occur (compare inset in Fig. 6.11 (a)), which are assigned as peaks from Fe^+ and $\text{Fe}(\text{CO})^+$, respectively, and are therefore directly related to the precursor molecule. Due to their low intensity, it is supposed that gas composition A contains only a minor amount of iron pentacarbonyl.

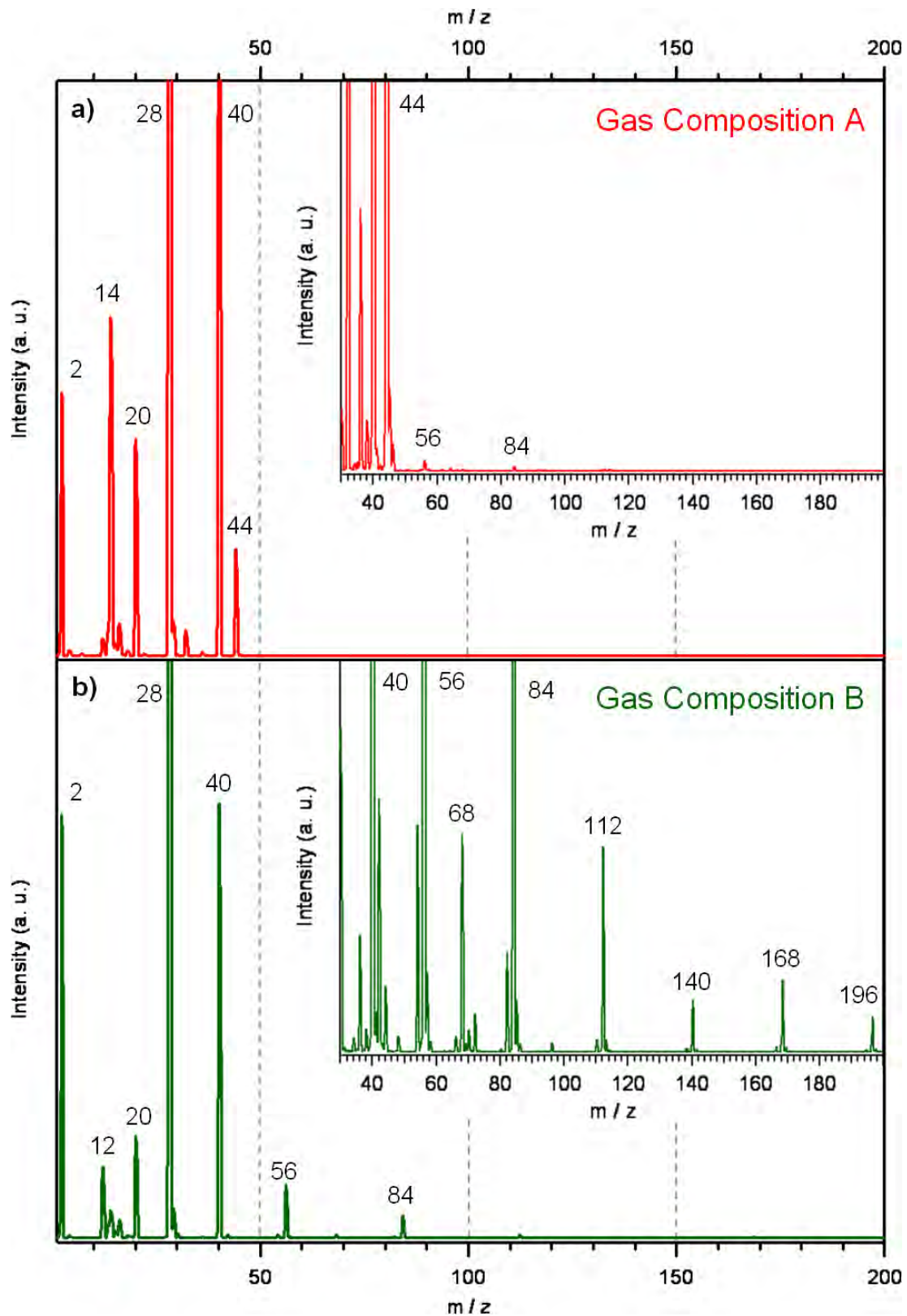


Fig. 6.11: QM spectra of different precursor gas compositions. a) Spectrum of an almost unpurified gas, contaminated with argon (gas composition A). Only minor iron containing signals were detected. b) Spectrum of the purified precursor gas, contaminated with argon (gas composition B).

		Intensity ratio with respect to Fe ⁺ (m/z = 56)	
m/z	Possible Fragments	Gas Composition A	Gas Composition B
Precursor Fragments			
12	C ⁺	104.23	7.80
16	O ⁺	187.18	0.34
28	C ₂ H ₄ ⁺ , CO ⁺ , Fe ⁺⁺ , N ₂ ⁺	n.a.	n.a.
56	Fe ⁺	1	1
68	FeC ⁺	0.12	0.06
84	Fe(CO) ⁺	0.39	0.42
112	Fe(CO) ₂ ⁺	0.14	0.06
140	Fe(CO) ₃ ⁺	0.025	0.014
168	Fe(CO) ₄ ⁺	0.027	0.020
196	Fe(CO) ₅ ⁺	---	0.004
Other Fragments			
2	H ₂ ⁺	1605.63	1.81
14	N ⁺	2049.30	0.52
18	H ₂ O ⁺	33.94	0.05
20	Ar ⁺⁺	1309.86	1.98
32	O ₂ ⁺	154.93	---
36	?	23.31	0.03
40	Ar ⁺	5654.93	7.98
44	CO ₂ ⁺	647.89	0.02
64	?	0.21	0.0001

Table 6.1: Possible fragments from the QM spectra in Fig. 6.11 with their respective mass to charge ratios. Additionally, the respective intensity ratio with respect to the Fe⁺-peak (m/z = 56) is given. The signals with the highest intensities are marked bold. n.a. is given in the table to indicate that the intensity of the corresponding m/z-ratio was out of measurement range.

Fig. 6.11 (b) shows a QM spectrum of gas composition B; it was achieved via extensive cleaning of the precursor compound. Still the argon contamination is visible in the spectrum, even though the intensities of the respective signals (Ar^{++} -peak ($m/z = 20$) and Ar^+ -peak ($m/z = 40$)) are reduced compared to gas composition A. Also a drastic decrease of the N^+ -peak ($m/z = 14$) is observed, indicating that the nitrogen content of the precursor gas was significantly reduced by the purification procedure. Due to the low intensity of the N^+ -peak ($m/z = 14$) the high signal at $m/z = 28$ is in this case mainly attributed to CO^+ , resulting primarily from the decomposition of $\text{Fe}(\text{CO})_5$ during the QMS measurement or in the storage device and the gas dosage system. In addition, the number and intensity of fragments resulting from $\text{Fe}(\text{CO})_5$ have increased. The signals at $m/z = 56$ (Fe^+), 84 ($\text{Fe}(\text{CO})^+$), 112 ($\text{Fe}(\text{CO})_2^+$), 140 ($\text{Fe}(\text{CO})_3^+$), 168 ($\text{Fe}(\text{CO})_4^+$) and 196 ($\text{Fe}(\text{CO})_5^+$) are now clearly visible. Smaller signals in the direct surrounding of these peaks are mainly attributed to the isotopic pattern of iron (i.e., ^{54}Fe (natural abundance = 5.8 %), ^{56}Fe (91.7 %), ^{57}Fe (2.2 %) and ^{58}Fe (0.3 %)) [99]. A comparison with the spectrum in Fig. 6.11 (a) shows that gas composition B has a much higher quality in terms of precursor purity compared to gas composition A (compare also the intensity ratios in Table 6.1).

With respect to the described precursor gas compositions, two EBID experiments were performed on new and freshly cleaned Si(100) samples. Fig. 6.12 displays SEM images of two area patterns from each experiment (template square (upper right; size: 800 nm · 800 nm) and circle (lower left; diameter: 600 nm)), which were irradiated with an electron dose of 13.3 C/cm² and 39.8 C/cm², respectively. The deposits displayed in the upper row (Fig. 6.12 (a) and (b)) were generated with a gas composition similar to the one in Fig. 6.11 (a) (gas composition A). In contrast to that, the structures in Fig. 6.12 (c) and (d) were deposited shortly after the spectrum in Fig. 6.11 (b) was acquired (gas composition B).

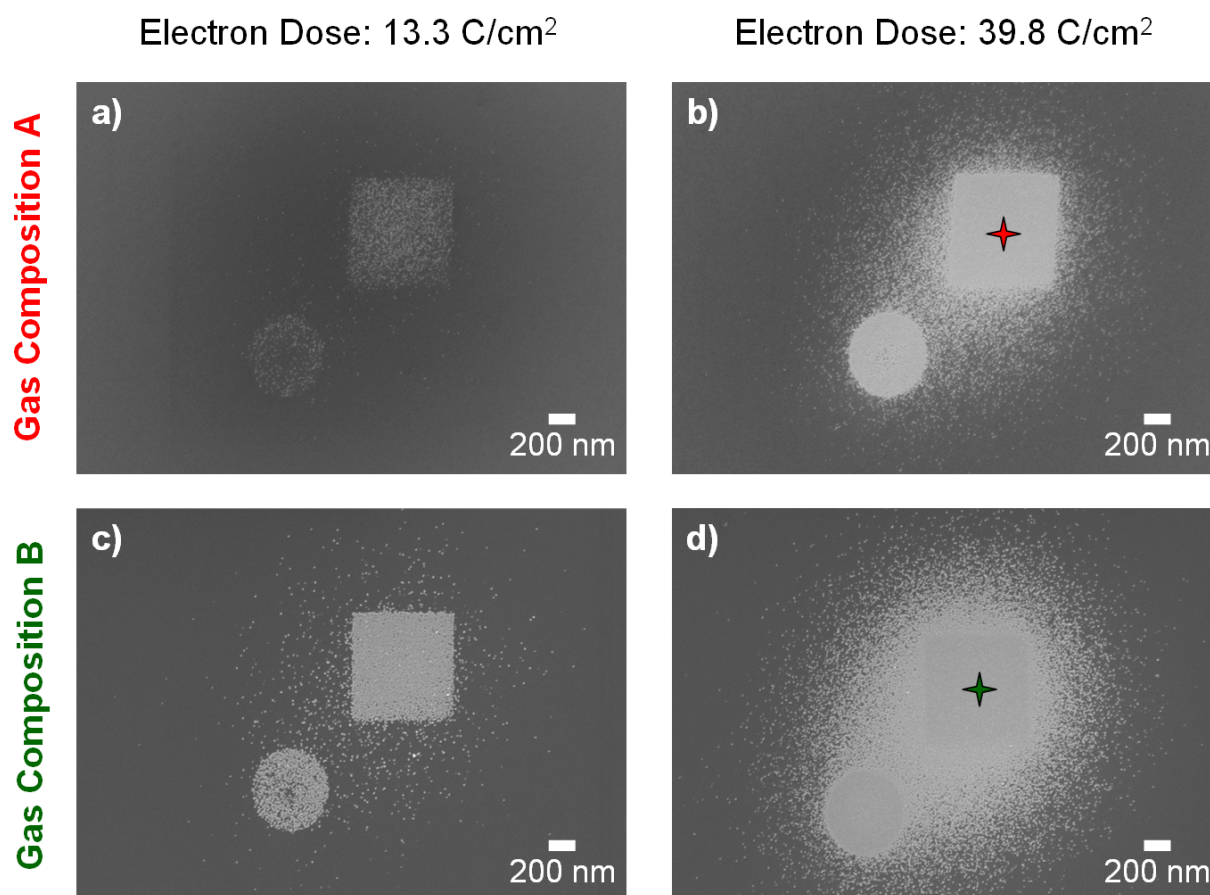


Fig. 6.12: SEM images of square and circle deposits, generated with the two gas compositions from Fig. 6.11 and different electron doses. a), b) Deposits generated with gas composition A (low quality gas) and an electron dose of 13.3 C/cm² and 39.8 C/cm², respectively. c), d) Deposits generated with gas composition B (purified gas) and an electron dose of 13.3 C/cm² and 39.8 C/cm², respectively. The markers in (b) and (d) indicate the positions where the spectra in Fig. 6.13 were acquired. ($U = 15$ kV; $I = 3$ nA; tilted sample)

For both experiments depicted in Fig. 6.12 the structures exhibit the discontinuous growth, which is typical for the deposition on a new and well-defined cleaned Si(100) sample (compare Chapter 6.4.1). Yet, it is clearly observed that the amount and density of the iron clusters generated with gas composition A is lower compared to the ones resulting from gas composition B. In case of the square generated with an electron dose of 13.3 C/cm², gas composition A leads to an irradiated area, which is incompletely covered by a random distribution of small iron clusters (Fig. 6.12 (a)), while for gas composition B the corresponding structure appears to be homogeneously covered (Fig. 6.12 (b)); additionally, the amount of clusters in the direct surrounding due to electron exposure via the BSE proximity effect (compare Chapter 2.7) is significantly higher for the deposit in (c) compared to (a). The structures in Fig. 6.12 (a) exhibit also a lower contrast compared to the ones in Fig.

6.12 (b). An increase of the applied electron dose leads in the case of gas composition A to a homogeneously covered, irradiated area (Fig. 6.12 (b)). However, the amount and density of the clusters in the direct surrounding are still lower compared to the corresponding deposit that was generated with gas composition B. One might suspect that the higher number of clusters in the case of gas composition B might be the result of an autocatalytic effect due to additional gas dosage after the generation of the patterns (compare Chapters 5.5 and 5.6). Yet, such an effect can be ruled out, since the additional precursor dosage time for the structures in Fig. 6.12 (a) and (b) was higher (~ 65 min) than the one applied to the deposits in (c) and (d).

In order to compare the chemical composition of the structures, which were generated with the different precursor gas compositions, local AES measurements were performed on the positions marked in Fig. 6.12 (b) and (d). The corresponding spectra are depicted in Fig. 6.13. They are both dominated by relatively large iron peaks at 593, 647 and 702 eV, accompanied by signals for carbon and oxygen at 272 and 513 eV, respectively. The composition of the deposit in Fig. 6.12 (d) (green spectrum in Fig. 6.13) is similar to that of the top left square in Fig. 6.8 (b) (compare the red spectrum in Fig. 6.9), i.e., the iron purity of the deposit is estimated to be higher than 96 %. At the higher kinetic energy (Fig. 6.13 (b)) a small signal from the silicon substrate is visible (1616 eV); compared to a spectrum acquired on the non-irradiated area (not shown here) it appears strongly damped, which indicates that a high amount of iron was deposited in the irradiated region.

The spectrum acquired on the deposit in Fig. 6.12 (b) (red spectrum in Fig. 6.13) displays some significant differences in the intensities of the signals. Comparing the iron peaks in both spectra, the ones in the red spectrum amount only to 66 % of the ones in the green spectrum. For carbon the situation is reversed, with the signal in the red spectrum being roughly ten times more intense than the one in the green spectrum, while the oxygen peak exhibits a similar intensity in both spectra. From these observations it is apparent, that the deposits in Fig. 6.12 (b), which were generated with gas composition A, i.e., the almost unpurified gas, exhibit a much lower purity compared to the structures resulting from gas composition B (Fig. 6.12 (d)). A determination of the intensity ratio between the iron signal at 647 eV and the carbon peak yields a value of ~ 1.74 for the red spectrum compared to 27.21 for the green one. In case of the red spectrum the total amount of contaminations could be estimated to be ~ 17 % (~ 14 % carbon contamination, as derived from a comparison to the spectrum of a thick carbon layer (see Chapter 3.4); the oxygen contamination was roughly estimated to be lower 3 % (see Chapter 3.4)).

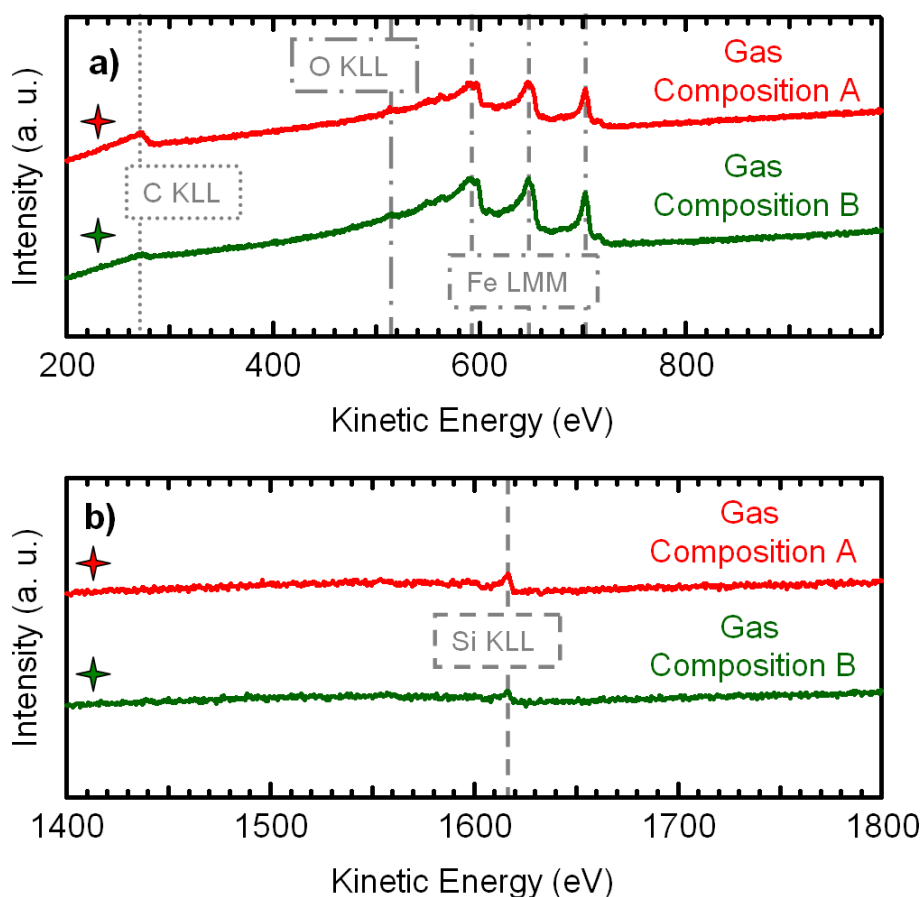


Fig. 6.13: Local Auger spectra of the kinetic energy region a) of the C KLL, O KLL and Fe LMM transitions and b) of the Si KLL transitions, which were acquired on the positions marked in Fig. 6.12.

Furthermore, at a higher kinetic energy it is also observed that the silicon signal is larger in the red spectrum compared to the green spectrum ($\sim 31\%$ / Fig. 6.13 (b)). This indicates, that the amount of material deposited in the irradiated area with gas composition A is lower than the one resulting from gas composition B. Thus, it is concluded that the deposition rate must be higher in the case of the purified precursor gas (B). This observation is attributed to the higher partial pressure of the iron containing precursor fragments, as it is evident from the signal intensities in the QM spectrum in Fig. 6.11 (b) (compare Table 6.1); in combination with the precursor limited deposition regime typically observed in our EBID experiments (compare Chapter 2.7), this results in the higher deposition rate visible in Fig. 6.13. In a similar way, the lower purity of the deposits generated with gas composition A might be attributed to the higher partial pressures of the contaminations relatively to the iron pentacarbonyl fragments.

To summarize it can be said that in the system $\text{Fe}(\text{CO})_5 / \text{Si}(100)$ the condition of the used precursor gas has a major influence on the generated structures. While independent from the precursor quality the deposits on a new and freshly cleaned surface exhibit the discontinuous morphology already discussed in Chapter 6.4.1, the local density and purity of the resulting iron clusters depend strongly on the $\text{Fe}(\text{CO})_5$ content of the applied gas. The application of an almost unpurified gas (A), which contains large amounts of nitrogen and argon and only a minor amount of $\text{Fe}(\text{CO})_5$, results in deposits with an iron purity of $\sim 83\%$, while with a highly purified gas (B) a value higher than 96% was achieved. Additionally, the amount of material deposited from the low quality gas is lower, which is attributed to a lower EBID deposition rate during the irradiation of the pattern. From these results it is evident, that the precursor quality plays an important role for EBID, especially for the fabrication of pure deposits. Monitoring of the precursor composition is therefore a crucial topic for understanding the process.

6.4.3 Deposition under clean conditions at 200 K

In Chapter 6.4.1 it was assumed that the formation of the pure iron clusters on a well-ordered $\text{Si}(100)$ sample is the result of tensile stress relative to a deposited initial layer and that it relies strongly on the diffusion of molecules and atoms on this layer. To test this hypothesis, additional experiments were performed at lower temperatures, to hinder the diffusion of the adsorbates.

Fig. 6.14 shows SEM images of deposits that were generated at 200 K. In contrast to the room temperature experiments (compare Fig. 6.7 and Fig. 6.8) they all exhibit a continuous morphology, without any iron clusters visible. Furthermore, since the images in Fig. 6.14 were acquired at room temperature, it can be stated that the structures are stable at least up to this temperature. These findings further support the hypothesis that the formation of the observed sub 10 nm iron dots at room temperature relies on diffusion and is strain induced.

A point matrix consisting of 25 point deposits, which were all irradiated with an identical electron dose of 1.2 nC, is depicted in Fig. 6.14 (a). Each of the point structures is visible as a well defined, bright deposit with a size of ~ 35 nm. A high magnification image of these deposits (Fig. 6.14 (b)) shows that they actually consist of a small, dark spot directly in the center, which is surrounded by a bright ring. Similar results were obtained for the generation of iron deposits on $\text{Rh}(110)$ (compare Fig. 5.13 (c)). This observation is mainly attributed to a deposition mechanism in the precursor limited regime, with surface diffusion

being the prevalent supply mechanism for the molecules in the irradiated region (diffusion enhanced regime; compare Chapter 2.7). Thereby, the precursor molecules will be “pinned down” before they reach the center of the irradiated area, which results in the observed ring structure of the deposit. This effect has been studied by different groups for the generation of point [161, 183], line [162] and area deposits [184] using AFM, TEM, HR-TEM, EELS, Raman spectroscopy and secondary ion mass spectrometry; Utke et al. developed also a continuum model, which can be used to describe this observation [183].

Fig. 6.14 (c) and (d) show images of line deposits, which were generated with the same template as used for the deposits in Fig. 6.7 (e) (template circle with centered cross). For the structures in (c) the electron dose was increased from 8 $\mu\text{C}/\text{cm}$ (lower left) to 32 $\mu\text{C}/\text{cm}$ (top right), while the deposits in (d) were generated with an electron dose of 40 $\mu\text{C}/\text{cm}$ (lower left) to 64 $\mu\text{C}/\text{cm}$ (top right). Again, all of the structures are continuous with a partial line width of approximately 30 nm (lower left deposit in (d)). Yet, the contrast of the structures in the SEM varies with the applied electron dose: at low electron doses (compare the two structures on the left side in Fig. 6.14 (c)) the deposits are darker than the free silicon surface, while an increase of the applied dose is associated with a steady contrast inversion of the structures, i.e., their appearance is getting increasingly brighter compared to the non-irradiated surface. Due to the observations described in Chapter 6.4.1, the dark structures generated with low electron doses are attributed as prerequisite layer, which was observed before the onset of the cluster growth and contained a relatively high amount of carbon. The bright deposits observed for higher electron doses are therefore attributed as a layer with a relatively high iron content on top of this initial layer.

Two area deposits, generated at 200 K, are displayed in Fig. 6.14 (e) and (f). For the pattern in (e) the template of a square (upper right; size: 800 nm · 800 nm) and a circle (lower left; diameter: 600 nm) was irradiated with an electron dose of 26.6 C/cm^2 . Both structures are clearly visible in the SEM image as bright areas, which are surrounded by an oval shaped halo of somewhat darker appearance. Surrounding this halo is a ring, which again appears darker than the free Si surface; it is again indicative for the occurrence of a prerequisite layer before the onset of the observed bright deposits. This observation is confirmed by area deposits that were generated with rather low electron doses (not shown here); the resulting structures exhibit a dark contrast in the SEM and local AES measurements displayed a chemical composition of iron, oxygen and carbon (similar to the one observed for the deposits in Fig. 6.8 (a) (compare Fig. 6.9)). The deposition of material in the direct surrounding of the

irradiated area in Fig. 6.14 (e), i.e., the bright halo and the surrounding dark ring, is attributed to the BSE proximity effect (compare Chapter 2.7).

The area deposit in Fig. 6.14 (f) exhibits a similar structure, i.e., the bright irradiated area in the center is surrounded by a lesser bright, oval shaped halo and a dark ring at a higher distance. It was generated via repeatedly scanning the same rectangular area with the image acquisition mode of the SEM; the same technique has already been applied for the generation of the structures in Fig. 6.5. The shape of the originally exposed region in Fig. 6.14 (f) is difficult to recognize, which is mainly attributed to drift effects during the irradiation. In this case, a specific waiting time was applied at the start of each horizontal line (11 ms plus a certain time for the net frequency synchronization), while at the start of each frame the beam stopped for additional 24 ms in the top left corner of the scan area (stabilization of the beam). Additionally, an image of the surface was saved after each frame. The remaining parameters applied for the irradiation of the structure in Fig. 6.14 (f) are listed in the following:

- **Frame size:** 4.57 μm · 3.43 μm
- **Number of irradiated points per frame (image resolution):** 1024 · 768
- **Irradiation time per point (pixel time):** 204.8 μs
- **Scan speed:** 12
- **Total exposure time:** ~ 56.5 min
- **Number of frames:** 20
- **Beam current:** 400 pA
- **Total electron dose:** 8.22 C/cm²

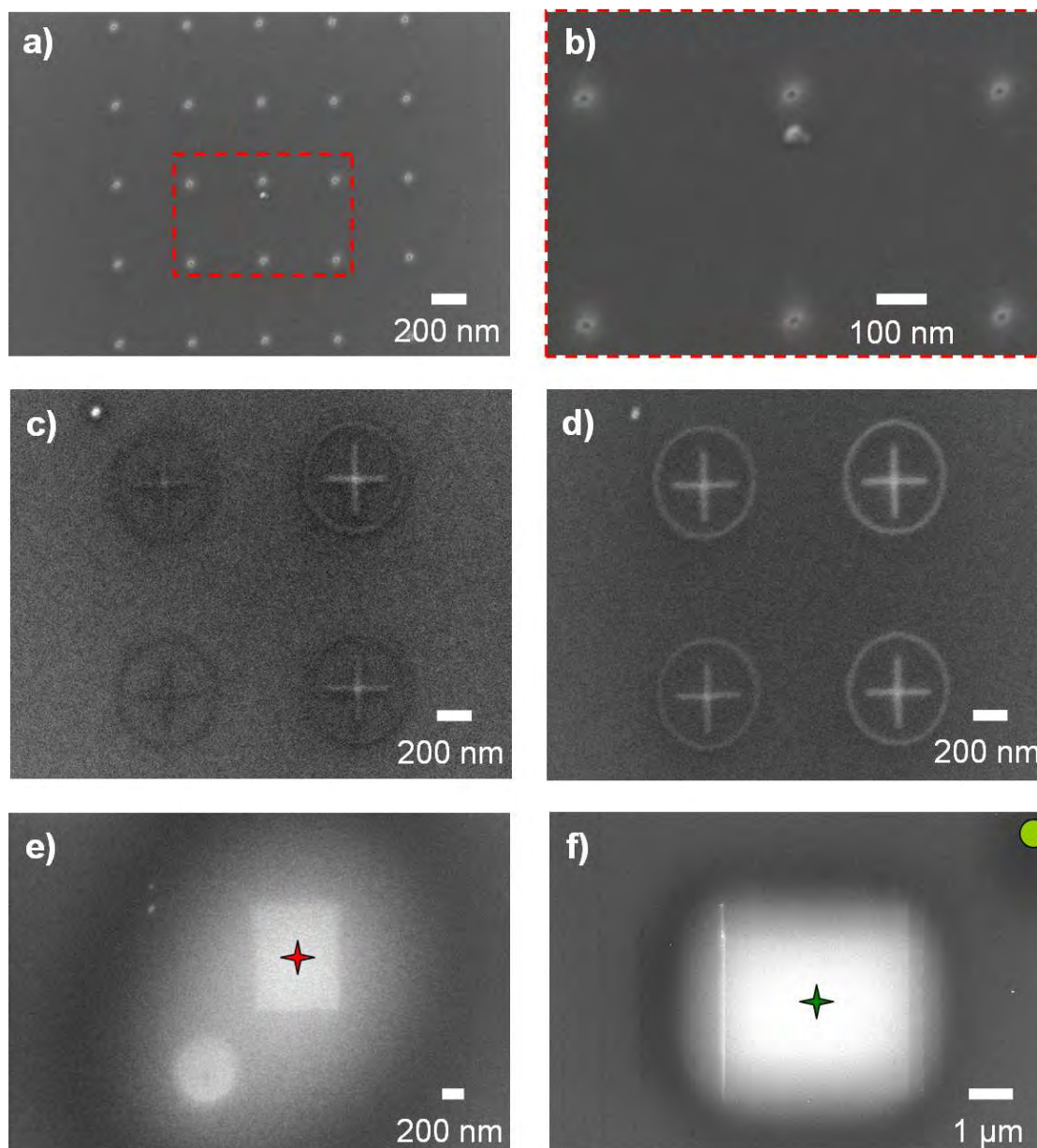


Fig. 6.14: SEM images of deposits generated on Si(100) at 200 K. Note, that the images were acquired at room temperature. a) Pattern of 25 points irradiated with an identical electron dose of 1.20 nC. b) High magnification image of the area marked by a red, dashed line in (a). c) Line deposits (template square with centered cross), which were irradiated with an electron dose of 8 (lower left), 16 (upper left), 24 (lower right) and 32 $\mu\text{C}/\text{cm}$ (upper right). d) Line deposits, which were irradiated with an electron dose of 40 (lower left), 48 (upper left), 56 (lower right) and 64 $\mu\text{C}/\text{cm}$ (upper right). e) Area deposits (template square and circle), which were irradiated with an electron dose of 26.6 C/cm^2 . f) Area deposit, generated by the repeated irradiation of a rectangular area via the image acquisition mode of the SEM; a total electron dose of 8.22 C/cm^2 was applied. The markers in (e) and (f) indicate the positions where the spectra in Fig. 6.15 were acquired. ($U = 15 \text{ kV}$; $I = 3 \text{ nA}$; tilted sample)

In order to determine the chemical composition of the deposits generated at 200 K, local Auger electron spectroscopy was performed on the structures in Fig. 6.14 (e) and (f), as indicated by the color coded markers. The corresponding spectra are displayed in Fig. 6.15 (red and dark green spectrum). They both exhibit large peaks for iron, as well as signals for oxygen and carbon (Fig. 6.15 (a)). While the intensities of the O peaks are almost identical, the intensities of the Fe and C signals strongly differ. The iron peaks in the red spectrum (acquired on the square in Fig. 6.14 (e)) amount only to 71 % of the ones in the spectrum acquired on the deposit in Fig. 6.14 (f) (dark green); for carbon the situation is reversed, with the signal in the red spectrum showing roughly a three times higher intensity than the carbon peak in the green spectrum. The total amount of contaminations was estimated to be ~ 21 % for the deposit in (e) (~ 18 % carbon contamination, as derived from a comparison to the spectrum of a thick carbon layer (see Chapter 3.4); the oxygen contamination was roughly estimated to be 3 % (see Chapter 3.4)) and ~ 8.0 % for the structure in (f) (~ 5 % carbon contamination and 3 % oxygen contamination). From this data it is obvious, that the deposit in (f) has a significantly higher metal purity than the structures in (e).

Even though the metal content of the structures in Fig. 6.14 (e) (~ 79 %) is still higher than typical values reported in literature (compare references [11, 15-18, 22, 24-31]), it is lower compared to the room temperature deposits (compare Chapter 6.4.1). This is most probably due to an increased residence time of CO molecules or CO containing fragments, which are resulting from the dissociation of $\text{Fe}(\text{CO})_5$ molecules; these components may be incorporated into the deposit or cracked by electrons, which results in an additional contaminant of the resulting structure. In case of the deposit in Fig. 6.14 (f) the observed metal content is only slightly lower compared to the one of the room temperature experiments. Possible explanations for this observation will be given below.

In Fig. 6.15 (b) it is observed that the damping of the silicon substrate signal is higher for the dark green compared to the red spectrum; this clearly shows that a higher amount of material is deposited in case of the structure in Fig. 6.14 (f), even though the applied electron dose amounts only to ~ 31 % of the one used for the generation of the deposits in (e). The light green spectra in Fig. 6.15 were acquired on the non-irradiated area near the deposit in Fig. 6.14 (f) (as indicated by the light green marker). It proves again the selectivity of the EBID process in the system $\text{Fe}(\text{CO})_5 / \text{Si}(100)$ also at low temperatures (200 K), since no iron signals are observed.

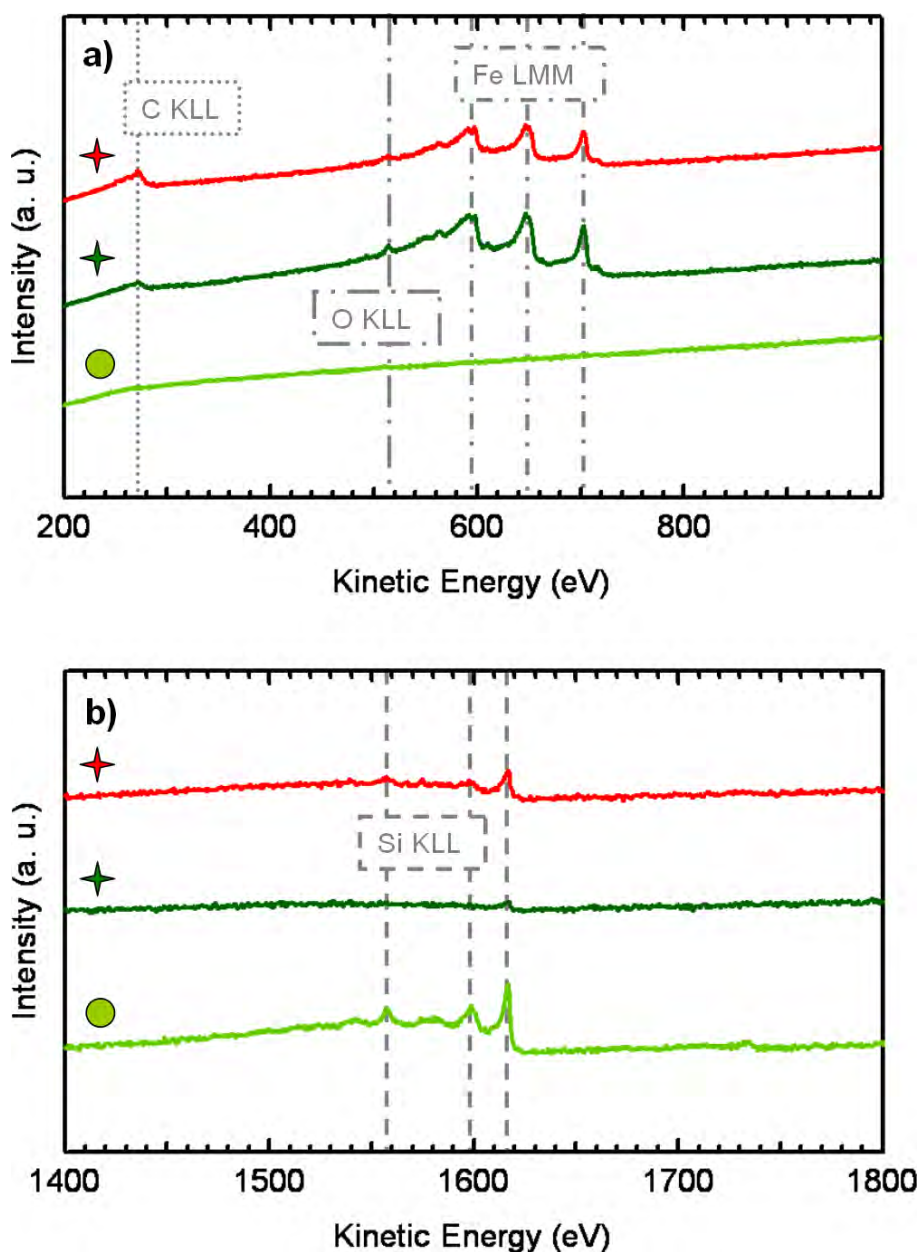


Fig. 6.15: Local Auger spectra of the kinetic energy region a) of the C KLL, O KLL and Fe LMM transitions and b) of the Si KLL transitions, which were acquired on the positions marked in Fig. 6.14.

In the following, the observed variations in amount and composition of the deposits in Fig. 6.14 (e) and (f) (i.e., the higher purity and higher amount of deposited material in (f)) are discussed. These observations are mainly attributed to differences in the applied scan strategies; the pattern in (e) was irradiated via the “lithographic attachment” in a typical single sweep (continuous irradiation), while the “image acquisition mode” of the SEM resulted in a repeated irradiation of the area for (f). Associated with the repeated irradiation is a certain replenishing time for the precursor molecules in the irradiated region and therefore a higher

amount of adsorbed molecules during the exposure; from literature it is well-known that this effect results in a higher deposition yield compared to a continuous exposure with the same accumulated charge [32]. Kohlmann-von Platen et al. studied the influence of the time between individual exposures of the same point deposit (specified as “loop time”) on the deposition yield [185]; it was reported that the normalized deposition yield (normalized to a continuous exposure with the same accumulated charge) increases from 1 to 2 by an increase of the loop time from 0 to 150 μs . Concerning the higher purity of the deposit in Fig. 6.14 (f), one might speculate that the repeated irradiation leads to a completion of the (initially) partial decomposition of already deposited $\text{Fe}(\text{CO})_5$ -fragments and therefore to a purification of the previously deposited material. Similar results have been obtained for the post-deposition irradiation of metal containing deposits with relatively high beam currents [77, 186], which resulted in a considerable increase of the conductivity of the structures. Another possibility is, that the signals from the carbon containing prerequisite layer are damped stronger by the higher amount of deposited material in (f) compared to (e).

Additional EBID experiments were also performed at a sample temperature between 125 K – 145 K. The resulting structures appeared very diffuse in the SEM, with a large amount of material deposited in the irradiated regions as well as in their direct surrounding due to proximity effects (compare Chapter 2.7). The obvious increase of the amount of deposited material compared to the experiment at 200 K is attributed to a higher residence time of the precursor molecules and fragments on the surface.

In summary, it can be stated that performing EBID in the system $\text{Fe}(\text{CO})_5 / \text{Si}(100)$ at low temperatures (200 K) results in the generation of continuous deposits, which are stable at least up to room temperature; this result is a clear indication that the cluster growth observed at room temperature (compare Chapter 6.4.1) relies on a diffusion mediated process. At rather low electron doses a dark deposit could be observed in the SEM (compare Fig. 6.14 (c)), which is attributed to a carbon and oxygen containing prerequisite layer, similar to the one observed at room temperature. In contrast to that, deposits generated with a higher electron dose appear bright in the SEM. Local AE spectra acquired on these structures display an iron purity of $\sim 79\%$ for a deposit generated via the typically applied single sweep method (lithographic attachment). By applying a different scan strategy, i.e., by repeatedly scanning the irradiated area (acquisition mode of the SEM), the amount and the iron purity of the deposit can be significantly increased; this is attributed to a certain replenishing time between each scan and a further decomposition of already deposited $\text{Fe}(\text{CO})_5$ -fragments. With this

information, one might envision to generate continuous iron structures with a high iron purity by the repeated irradiation of a pattern with large loop numbers at low sample temperatures.

6.4.4 EBID with $\text{Fe}(\text{CO})_5$ on Si(111)

EBID experiments with the precursor iron pentacarbonyl were also performed on new and freshly cleaned Si(111) samples, which exhibited a well-defined (7x7) reconstruction (compare Chapters 3.4 and 6.2) in LEED. In contrast to the experiments performed on Si(100) only a few experiments had been performed on Si(111). The following data should therefore mainly be considered as an explorative survey.

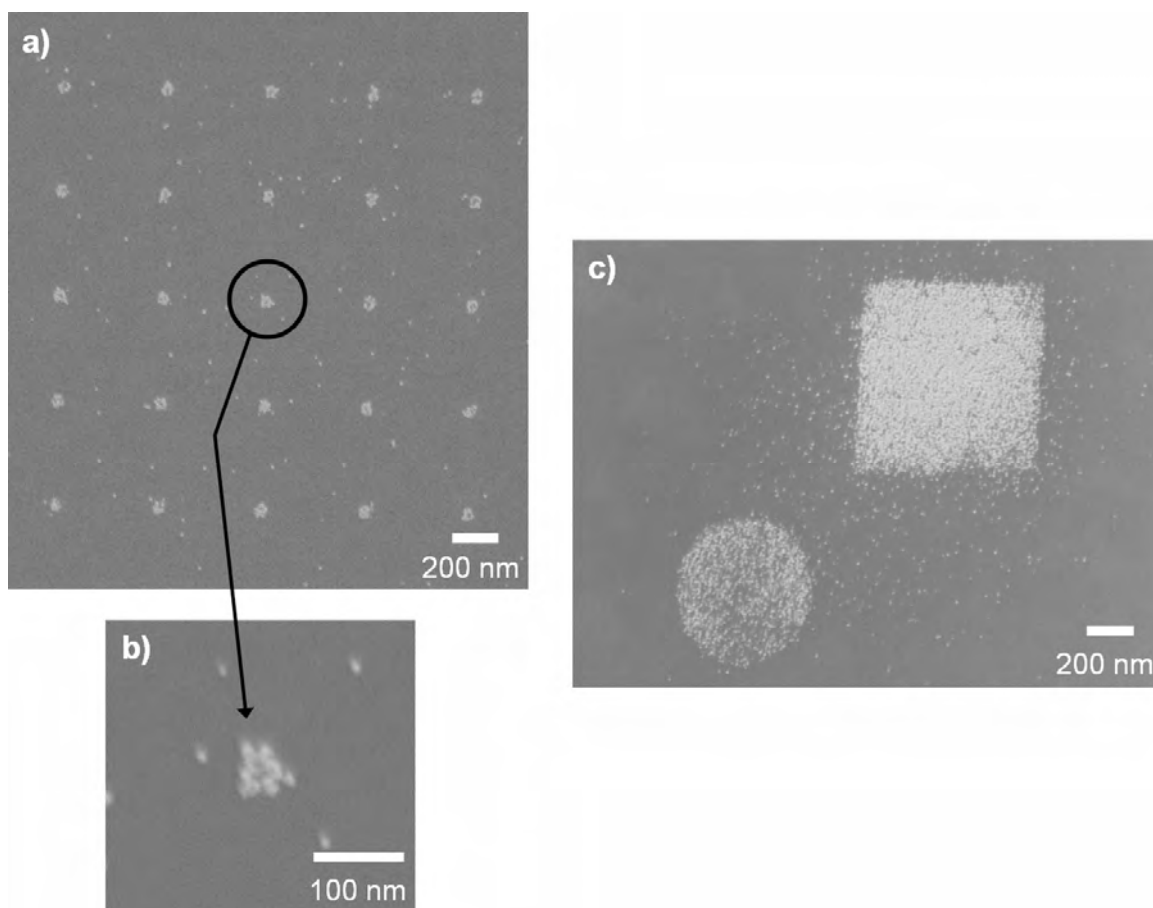


Fig. 6.16: SEM images of various deposits generated via EBID with $\text{Fe}(\text{CO})_5$ on a fresh Si(111) sample. a) Pattern of 25 points irradiated with an identical electron dose of 1.44 nC. b) High magnification image of one of the point deposits in (a). c) Area deposits (template square and circle), which were irradiated with an electron dose of 13.3 C/cm^2 . ((a), (b): $U = 15 \text{ kV}$; $I = 400 \text{ pA}$; plane sample / (c): $U = 15 \text{ kV}$; $I = 3 \text{ nA}$; tilted sample)

Fig. 6.16 shows a series of EBID deposits with different shape, which were generated on Si(111) at room temperature. Each one of these structures consists of a conglomerate of small iron clusters, similar as it was observed for Si(100) (compare Chapter 6.4.1). From this observation it is obvious that the discontinuous growth of the iron deposits and the diffusion of precursor fragments is independent from the applied crystal surface orientation. In addition, the existence of a prerequisite layer could be confirmed. A pattern consisting of 25 point deposits, which were irradiated with an identical electron dose of 1.44 nC, is depicted in Fig. 6.16 (a). Each of the point structures consists of an average number of ~ 12 iron clusters with a size of partly below 10 nm (compare the high magnification image of the central point in Fig. 6.16 (b)). A certain amount of iron clusters is also randomly distributed between the irradiated areas. These features are attributed to the exposure with scattered primary electrons in the sample material or on already deposited iron clusters (BSE and FSE proximity effect; compare Chapter 2.7) and their resulting secondary electrons (SE II); also the diffusion of iron atoms from the irradiated areas cannot be excluded.

Fig. 6.16 (c) shows area deposits (template square and circle with a size of 800 nm · 800 nm and a diameter of 600 nm, respectively), which were generated with an electron dose of 13.3 C/cm². Similar to the observations on Si(100) (compare Fig. 6.7 (d)) the irradiated areas are covered with densely packed iron clusters, while a significantly lower amount is again distributed in close proximity.

One of the advantages of the applied UHV system is the combination of the SEM with an STM scanner of flat design, which enables the controlled positioning of the STM tip (compare Chapter 3.3). In case of the deposition of iron on Si(111) this possibility was used to confirm the size of the resulting clusters via STM measurements. Fig. 6.17 (a) shows an SEM image of a deposit that was generated via the irradiation of four squares (marked by black dashed lines; template square: 600 nm · 600 nm) with an increasing electron dose from the lower left (22.6 C/cm²) to the upper right (26.6 C/cm²). A scanning tunneling micrograph, which was acquired at a position of the deposit in (a), is depicted in Fig. 6.17 (b). It is dominated by densely packed protrusions with varying size and shape, which are identified as iron clusters. From a line profile (Fig. 6.17 (c)), taken at the position marked by the blue line, the size of one of these protrusions was estimated to be ~ 10 nm (measurement position marked by the green and red triangle in (b) and (c)). By considering the shape of the applied STM tip the size of this iron cluster is assumed to be even smaller than 10 nm, which confirms the observations from SEM.

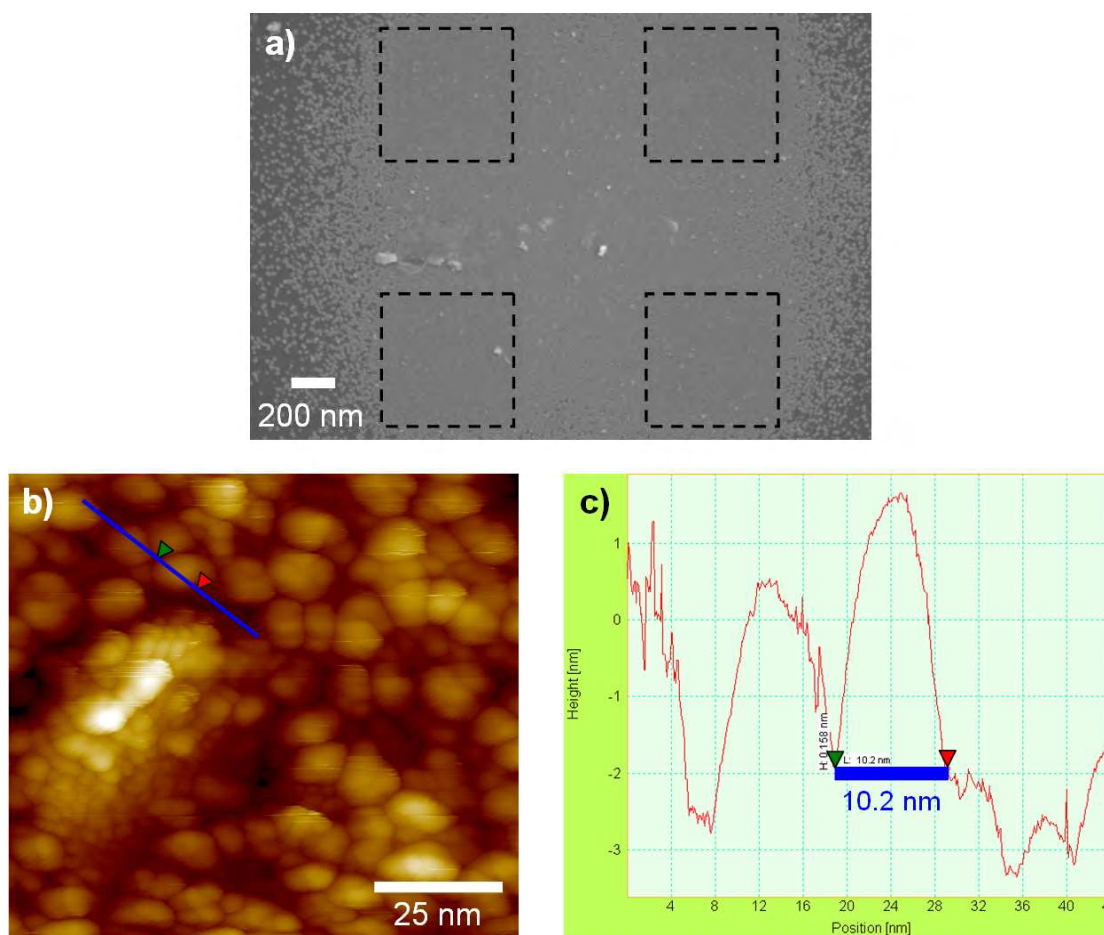


Fig. 6.17: STM measurement on an iron deposit. a) Deposit, generated by the irradiation of four squares with an electron dose of 22.6 C/cm^2 (lower left; irradiated area marked by the dashed line), 23.9 C/cm^2 (upper left), 25.2 C/cm^2 (lower right) and 26.6 C/cm^2 (upper right). ($U = 15 \text{ kV}$; $I = 400 \text{ pA}$; plane sample) b) STM image acquired on the deposit in (a). Clearly visible are the generated iron clusters. The blue line marks the position where the line profile in (c) was acquired. (Image parameters: size = $100 \text{ nm} \times 100 \text{ nm}$; $U_{\text{Gap}} = 0.9 \text{ V}$; $I_{\text{Gap}} = 50 \text{ pA}$) c) Line profile acquired at the position marked in (b). The green and red triangles mark the distance between the corresponding markers in (b), i.e., the size of one distinct iron cluster.

Similar to Si(100), the amount of deposited material strongly depends on the precursor gas composition, i.e., the utilization of a low quality gas results in a lower number and density of the resulting iron clusters than achieved for a gas containing a significantly higher amount of $\text{Fe}(\text{CO})_5$ (compare Chapter 6.4.2). Local AES measurements performed on iron structures that were generated on Si(111) displayed always a higher carbon contamination than observed for deposits on Si(100) ($\sim 8\% - 16\%$, as derived from a comparison to the spectrum of a thick carbon layer (see Chapter 3.4)). It is assumed that this observation is a result of the

specified surface orientation. However, additional experiments are necessary to confirm this assumption.

In summary, it can be stated that the deposition of iron with $\text{Fe}(\text{CO})_5$ on fresh Si(111) samples at room temperature results in a discontinuous structure morphology, similar as it was observed for Si(100). The resulting deposits consist again of small iron clusters on top of a continuous prerequisite layer. The growth mechanism for this prerequisite layer and the observed iron clusters is therefore supposed to be independent from the applied crystal surface orientation. STM measurements performed on one of these deposits confirm the size of the iron clusters to be lower than 10 nm (compare Fig. 6.17). Similar as for Si(100) the amount and density of the generated iron clusters is influenced by the precursor gas purity.

6.5 Influence of the electron dose on the iron cluster density

In Chapter 6.4 it was reported that the electron-beam induced deposition of iron with $\text{Fe}(\text{CO})_5$ on new and freshly cleaned silicon single crystals results in the generation of clean iron clusters on top of a prerequisite layer. In Fig. 6.8 and Fig. 6.12 it could be observed that the number of generated clusters depends strongly on the applied electron dose. To further address this topic, additional experiments were performed in order to find a relation between the electron dose and the number of resulting clusters.

Fig. 6.18 shows a series of three patterns, each containing a matrix of 10 point irradiations with varying electron doses, which were generated on Si(100). The electron dose within each pattern was increased from the lower left to the upper right, as it is schematically depicted in Fig. 6.18 (d). Furthermore, the dose for each pattern was adjusted such that it is increasing from the pattern in (a) to the pattern in (c) with a steady increase of 0.12 nC per point (compare the electron doses for the lower left (blue) and upper right point (green) of each pattern depicted in Fig. 6.18 (d)). In total, this means that 30 point deposits were generated with electron doses between 0.12 nC (lower left point in (a)) and 3.60 nC (upper right point in (c)).

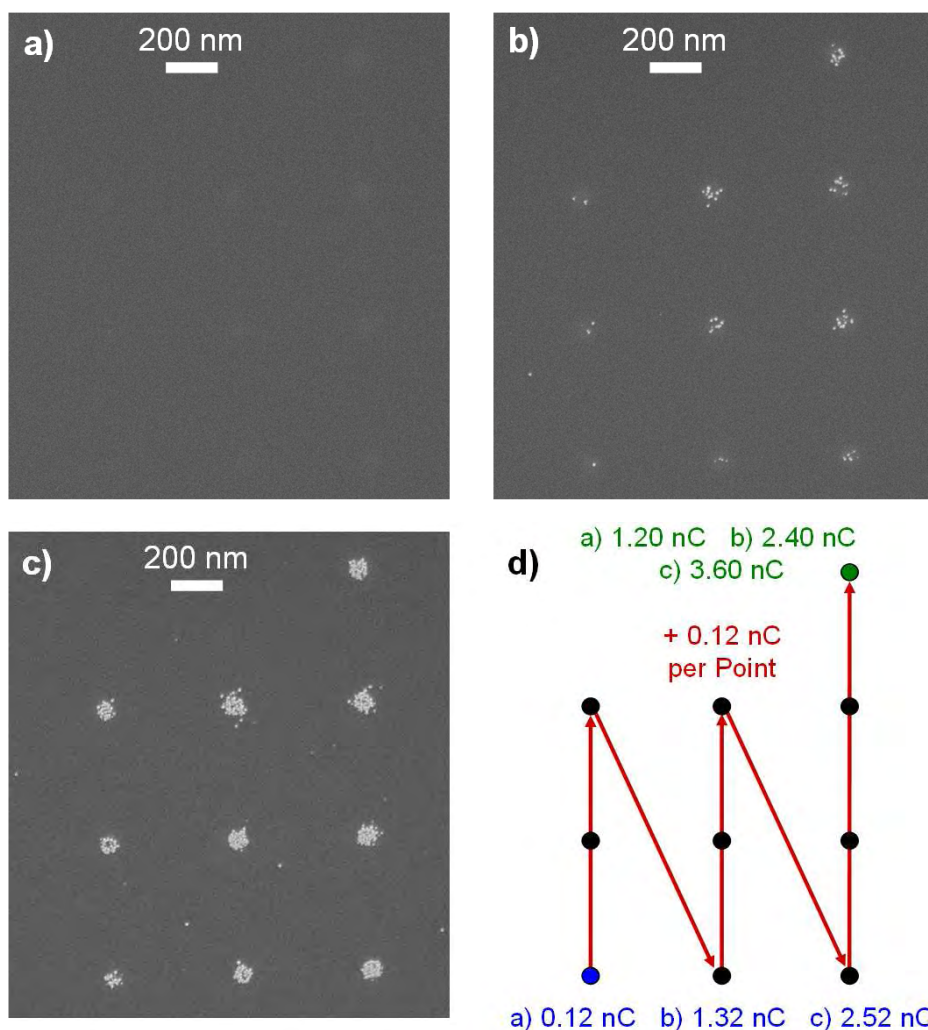


Fig. 6.18: Influence of the applied electron dose on the number of resulting clusters. a), b), c) SEM images of patterns containing ten point deposits, which were generated on Si(100) with an increasing electron dose from the lower left to the upper right. The applied electron doses were also increased from (a) to (c), as it is schematically depicted in (d). The number of generated clusters vs. the applied electron dose is displayed in Fig. 6.19 (blue data set). ($U = 15$ kV; $I = 400$ pA; plane sample) d) Scheme, displaying the individual electron doses used for the irradiation of the patterns in (a) to (c).

In the SEM images in Fig. 6.18 (a) to (c) it can be observed that clusters are only generated with an electron dose of at least 1.32 nC (lower left point deposit in Fig. 6.18 (b)). Below this “onset” electron dose, no clusters are visible on the surface, which indicates that a minimum electron dose is necessary to fabricate the point deposits. In Chapter 6.4.1 it was reported that below this onset electron dose an initial layer is formed, which is supposed to be a prerequisite to induce the tensile stress resulting in the cluster growth. Additionally, it can be clearly recognized in Fig. 6.18 (b) and (c) that the number and density of the resulting iron

clusters is increasing with an increase of the applied electron dose. At higher electron doses (compare Fig. 6.18 (c)) a small amount of clusters is also randomly distributed between the irradiated points. Similar as it was described for the pattern in Fig. 6.16 (a), these features are attributed to result from the BSE and FSE proximity effect (compare Chapter 2.7), i.e., the exposure with primary electrons scattered in the sample material or on already deposited iron clusters and their resulting secondary electrons (SE II); such “unintended” deposits are significantly reduced in the pattern in Fig. 6.18 (b), since the applied primary electron doses and therefore the amount of scattered electrons are too low.

In Fig. 6.19 the number of iron clusters for each point deposit is plotted versus the respective applied electron dose (blue data set); only the clusters which could be directly associated to one of the irradiated areas were counted, while the features generated due to the exposure with scattered electrons were ignored. For each value an error of 15 % was assumed, which is indicated by the error bars in Fig. 6.19; this means that with an increase of the amount of generated clusters also the error is increasing, which is in line with the observation that at a higher density of the iron clusters individual features in the irradiated area cannot be distinguished properly, since they are partly overlapping. The blue data set in Fig. 6.19 shows beyond the already mentioned “offset” electron dose of 1.32 nC a linear growth of the number of clusters with the electron dose (indicated by the blue trend line), with a slope of approximately 1 cluster / 0.084 nC. At electron doses higher than 2.40 nC the corresponding values indicate also a linear growth, but with a steeper slope. The origin of this change in the cluster growth rate is unclear; yet, it has to be noted, that the determined values at electron doses higher than 2.40 nC comprise a large error, as the clusters are densely packed in this case (see Fig. 6.18 (c)). Also imaginable is an exponential behavior of the cluster growth rate over the whole range of the applied electron dose.

To further address the observations from the experiment in Fig. 6.18 and to verify the roughly linear relation between the numbers of generated iron clusters and the applied electron dose, three additional data sets, resulting from other point irradiation experiments on Si(100) and Si(111) samples, are plotted in Fig. 6.19. Important parameters for the experiments (applied surface orientation, pattern geometry) as well as the results extracted from the respective plots in Fig. 6.19 (offset electron dose for cluster growth and slope of linear trend line) are summarized in Table 6.2. Furthermore, in order to discuss any possible influence of an autocatalytic dissociation of $\text{Fe}(\text{CO})_5$, the additional gas dosage time after pattern irradiation is listed. The error bars for the red data set in Fig. 6.19 (P3) were determined in the same way as for the blue data set (P4; compare Fig. 6.18), i.e., a constant

error of 15 % was assumed for each value. The error bars of the purple (P1) and green (P2) data sets were determined via root mean square deviation.

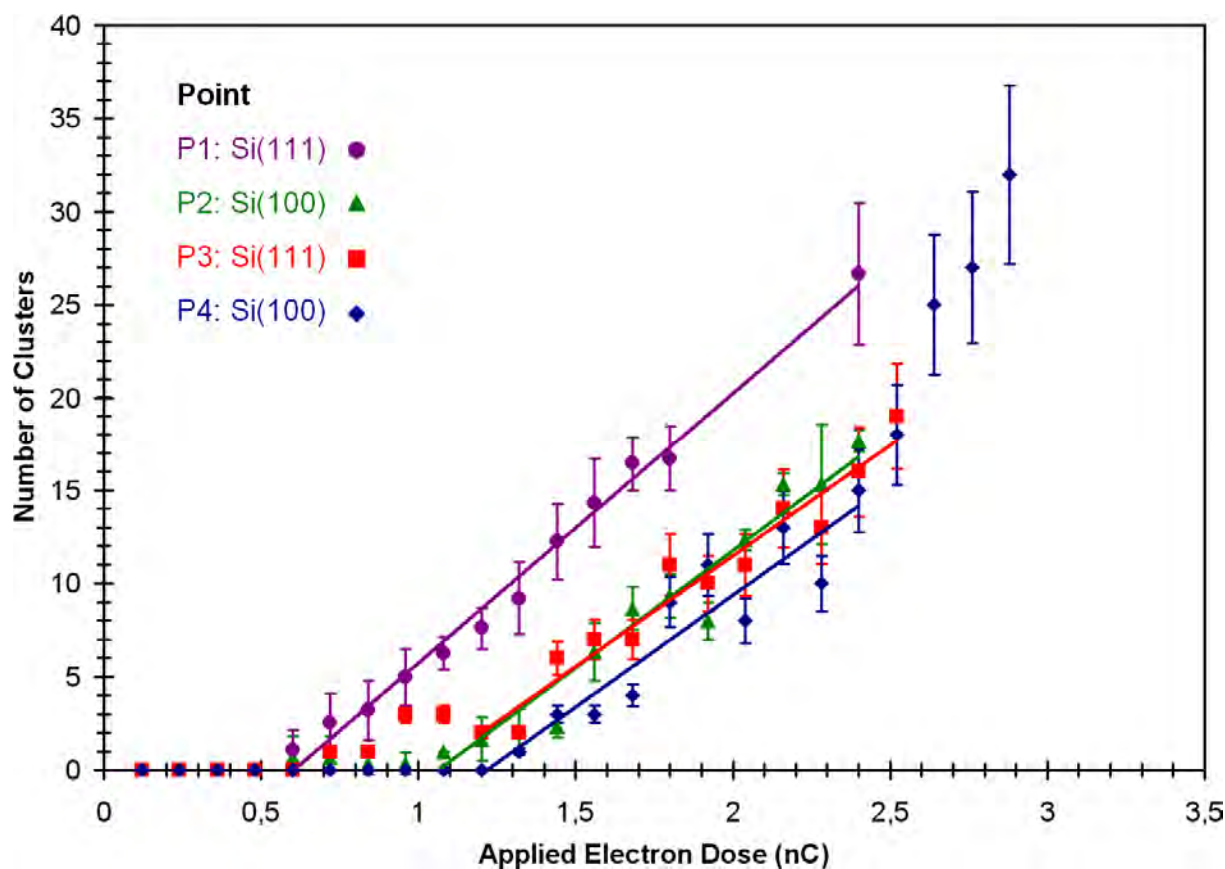


Fig. 6.19: Number of clusters generated via point irradiations vs. the applied electron dose from four different experiments on Si(100) and Si(111). Additional information of the corresponding experiments are listed in Table 6.2. The blue data set results from the experiment depicted in Fig. 6.18. For certain parts of each data set, a linear trend line was added; the resulting slopes are listed in Table 6.2. The values of the purple and green data sets were averaged from a group of point deposits, which were irradiated with an identical electron dose; the error bars in both cases were therefore determined via their root mean square deviation, while for the red and blue data sets a constant error of 15 % was assumed for each value.

From the plots in Fig. 6.19 it is obvious, that the relation between the numbers of generated clusters and the applied electron dose follows in each case at least partly a linear trend, which confirms the observation from the experiment in Fig. 6.18 (blue data set in Fig. 6.19). Additionally, the slopes of the respective trend lines vary only marginally, from 1 cluster / 0.069 nC (purple) to 1 cluster / 0.084 nC (red and blue). However, a significant

difference is observed for the offset electron dose of the cluster growth. For P4 (blue) and P3 (green) values of 1.32 nC and 1.08 nC, respectively, were determined, while in the case of P1 (purple) clusters were observed over the whole range of the applied electron dose (from 0.60 nC to 2.40 nC); for the latter the offset electron dose is therefore supposed to be ≤ 0.6 nC. For P1 (red) also a certain discrepancy between the offset of the cluster growth (0.72 nC) and the beginning of the linear growth relation (1.20 nC) is observed.

The observed differences in the offset electron dose of the cluster growth are mainly attributed to a variation of the structure density in the applied templates. For P1 (purple) each pattern consisted of 25 point deposits with a pitch (i.e., the lattice constant within the template) of 450 nm, which were irradiated with an identical electron dose. In contrast, for P2 the template consisted of 12-point (four rows, each with three point deposits with identical electron doses) and for P3 and P4 of 10-point deposits (compare Fig. 6.18 (d)), in both cases with a pitch of 500 nm. Since the pitches in the templates are significantly lower than the size of the BSE exit area (compare Fig. 2.13 (a)), it is evident that the electron interaction areas of the irradiated positions are partly overlapping. For P1, the higher number of point deposits in combination with the smaller pitch compared to the other data sets results in a significantly higher structure density and therefore in a higher electron density in the pattern due to scattered electrons. This effect increases the total electron dose for each single deposit and thus explains the relatively low offset electron dose observed for P1; it might also explain the minor variations in the slope of the linear trend lines (compare Table 6.2.). The increased scattering effect in the patterns of P1 is confirmed by the fact that a higher number of clusters is observed between the irradiated points for P1 (see Fig. 6.16 (a)) compared, e.g., to P4 (blue; see Fig. 6.18).

The observed difference in the offset electron dose between P2 (green data set) and P4 can be attributed to the same effect, as for P2 a 12-point and for P4 a 10-point template was used. The red data set (P3; 10-point template) shows an unexpected behavior at the beginning, although the increase at higher electron-doses is as it is expected, i.e., a linear trend is observed. Therefore, the offset electron dose can in this case not be determined accurately. However, the difference between the trend lines in P3 (red) and P4 (blue), which are resulting from experiments with an identical template (compare Fig. 6.18 (d)), is rather small and is supposed to be within the expected margin of error.

Data Set	Surface	Pattern Geometry	Offset of Cluster Growth	Slope of Linear Trend Line	Additional Gas Dosage Time
Point Deposits (Fig. 6.19)					
P1	Si(111)	(5 x 5)-Point Matrix with an Identical Dose (comp. Fig. 6.16 (a))	≤ 0.60 nC	~ 1 Cluster / 0.069 nC	~ 75 – 145 min
P2	Si(100)	(3 x 4)-Point Matrix with an Identical Dose in each Line	1.08 nC	~ 1 Cluster / 0.079 nC	~ 60 – 70 min
P3	Si(111)	10-Point Matrix with Increasing Dose (comp. Fig. 6.18 (d))	(0.72 nC)	~ 1 Cluster / 0.084 nC	~ 45 – 55 min
P4	Si(100)	10-Point Matrix with Increasing Dose (comp. Fig. 6.18 (d))	1.32 nC	~ 1 Cluster / 0.084 nC	~ 115 – 120 min
Area Deposits (Fig. 6.21 (a))					
A1	Si(100)	Pattern Consisting of Four Squares (600 nm · 600 nm) with Different Doses	5.31 C/cm ²	~ 1 Cluster / 0.066 C/cm ²	~ 12 – 15 min
Line Deposits (Fig. 6.21 (b))					
L1	Si(100)	Pattern Consisting of Ten Lines (Length: 400 nm)	96.0 μ C/cm	~ 1 Cluster / 2.435 μ C/cm	~ 105 – 113 min

Table 6.2: Important parameters from the plots in Fig. 6.19 and Fig. 6.21 and their corresponding experiments: applied crystal surface orientation, pattern geometry, offset electron dose for a visible cluster growth, slope of the linear trend line and additional gas dosage time after the irradiation.

Another possible explanation for the described observations are minor variations in the quality of the precursor gas, which was used for the different experiments. In Chapter 6.4.2 it was reported, that the precursor gas composition has a significant influence on the amount and density of the generated clusters; a similar effect might also be anticipated for the data

sets presented in Fig. 6.19. A possible autocatalytic dissociation of iron pentacarbonyl is assumed to exhibit, at least, no significant influence, since Table 6.2 shows no clear relation between the parameters extracted from the plots in Fig. 6.19 (offset electron dose for the cluster growth and slope of the linear trend line) and the additional gas dosage time after the irradiation of the patterns. Yet, a specific influence of this effect cannot be completely ruled out. Also possible is a combination of the previously described explanations.

From the data presented so far, one might envision to generate a pattern of point irradiations with a specific electron dose to deposit single iron clusters at defined positions. In this context, Fig. 6.20 shows an SEM image of a specific part of one of the patterns from the green data set (P2). It displays a row of three individual clusters at a defined distance from each other, which were generated by the irradiation of the respective positions with a constant electron dose of 1.08 nC. This observation demonstrates the possibility to generate individual, pure iron nanoclusters at defined positions on silicon single crystal surfaces with a size below 10 nm.



Fig. 6.20: SEM image of three point deposits, which were generated on a fresh Si(100) sample with an identical electron dose of 1.08 nC (taken from the green data set (P2) in Fig. 6.19 and Table 6.2). Each deposit consists of a single, individual iron cluster. ($U = 15$ kV; $I = 400$ pA; plane sample)

Up to now the relation between the number of generated iron clusters and the applied electron dose was discussed according to the irradiation of point deposits. The question is, if the observed linear relation applies also to structures with a different shape, since this might enable to fabricate large arrays of iron clusters with a defined density. In order to address this topic, Fig. 6.21 shows plots resulting from an area ((a)) and a line deposition experiment ((b)), which were both performed on a new and freshly cleaned Si(100) surface (no images shown here). Additional information about the applied experiments and the resulting plots are

summarized in Table 6.2. For both experiments an error of 15 % was assumed for each value, which is indicated by the error bars in Fig. 6.21.

From the information in Fig. 6.21 (a) (area deposition; applied patterns consisted of four squares with varying electron dose; compare Fig. 6.8), again a specific offset electron dose for the cluster growth (5.31 C/cm^2) can be deduced. Afterwards, the values follow roughly a linear trend with a slope of 0.066 C/cm^2 (blue trend line), even though it has to be noted, that the variations from the applied trend line are rather large in this case.

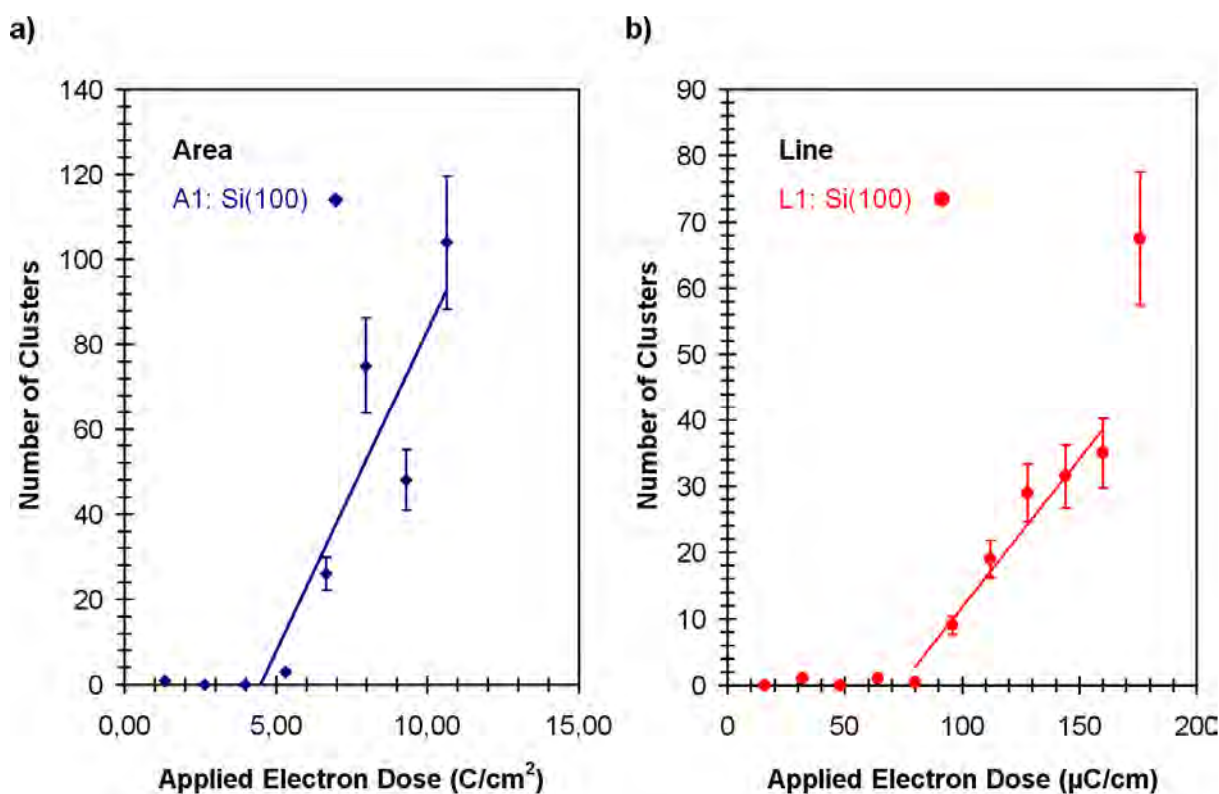


Fig. 6.21: Number of clusters generated via irradiations of a) areas and b) lines vs. the applied electron dose on Si(100). Additional information about the corresponding experiments are listed in Table 6.2. For certain parts of each data set, a linear trend line was added; the resulting slopes are listed in Table 6.2. For all data sets a constant error of 15 % was assumed for each value.

Concerning the generation of line structures, a corresponding plot is depicted in Fig. 6.21 (b). The applied template consisted of ten lines (five horizontal and five vertical) each with a length of 400 nm. The plot shows an offset electron dose for the cluster growth of $96 \mu\text{C/cm}$, followed by a linear increase (indicated by the red trend line) of the cluster number with the applied electron dose up to a value of $160 \mu\text{C/cm}$; the linear trend line yields a slope

of 1 cluster / 2.435 $\mu\text{C}/\text{cm}$. At higher electron doses ($> 160 \mu\text{C}/\text{cm}$), the amount of clusters differs significantly from this linear trend, similar as it was observed for point deposits in Fig. 6.19 (compare the blue data set (P4)). Yet, due to the partial overlapping of the clusters, no reliable values could be determined in the corresponding region, which makes a prediction of the development of the cluster number at higher electron doses difficult.

In summary, it was demonstrated that the relation between the number of iron clusters, generated via point, area and line irradiations on new and freshly cleaned Si(100) and Si(111) samples, and the applied electron dose follows at least partly a linear trend. The linear increase of the point irradiations show roughly a constant slope with an average value of 1 cluster / $0.079 \pm 0.007 \text{ nC}$ (error according to root mean square deviation). In contrast, the offset electron dose necessary for the generation of the iron clusters differs significantly between the different data sets; this observation is mainly attributed to different structure densities in the applied templates and therefore to variations in the local electron density due to scattered electrons. At higher electron doses ($> 2.40 - 2.52 \text{ nC}$) the slope of cluster growth rate for point deposits appears to increase (compare blue data set in Fig. 6.19). For area and line structures a linear trend with a slope of 1 cluster / $0.066 \text{ C}/\text{cm}^2$ and 1 cluster / $2.435 \mu\text{C}/\text{cm}$, respectively, was observed beyond a specific offset electron dose (compare Fig. 6.21). However, it has to be noted, that the number of experiments performed with these structure shapes were significantly lower compared to the point irradiations. The findings presented in this chapter represent a new route towards the lithographic fabrication of pure iron clusters at defined positions, whose density can be controlled from individual clusters (compare Fig. 6.20) to densely packed cluster fields with a narrow size distribution, by tuning the applied electron dose and pattern geometry.

6.6 Thermal stability of iron clusters on silicon

Concerning the envisioned application of the iron structures as seeds for the catalytical growth of, e.g., carbon nanotubes (compare Chapter 6.7) an important parameter is the thermal stability of the deposits, as catalytical growth processes typically require higher sample temperatures. In order to address this topic, a pattern that was generated on a new and freshly prepared Si(100) sample was subsequently annealed during in situ observation in the SEM.

Fig. 6.22 a) shows an image of the structures prior to the post-deposition heating procedure; the corresponding template consists of a square (top right corner; size: $800 \text{ nm} \cdot 800 \text{ nm}$) and a circle (bottom left corner; diameter: 600 nm), which were both irradiated with

an electron dose of 13.3 C/cm^2 . As already described in Chapter 6.4.1 (compare Fig. 6.8 (d)), the pattern contains a high amount of bright iron clusters, which are densely packed in case of the irradiated area and randomly scattered in close proximity due to electron exposure via proximity effects. An AE spectrum acquired on the square in Fig. 6.22 (a) indicates again the high purity of the iron structures, generated at room temperature ($> 96 \%$; compare Chapter 6.4.1).

Subsequent heating, with a steadily increasing sample temperature up to 680 K (heating time at each temperature: 10 min), exhibited no visible changes in the shape and morphology of the deposits. Various AE spectra acquired on the square in Fig. 6.22 (a) up to a sample temperature of 470 K (spectra acquired while cooling the sample to room temperature) indicate a minor increase of the carbon content compared to a spectrum measured before the annealing procedure (not shown); the corresponding area appears after the AES measurement also slightly darker than the rest of the iron structure. The most plausible explanation for this observation is the adsorption of carbon containing species on the iron structures, which are locally dissociated by electron irradiation during the Auger measurements; the observed contrast of the resulting C covered deposit can be interpreted as due to a decreased SE yield associated with the lower atomic number compared to pure iron [48]. Between 470 and 680 K no studies of the chemical composition of the structures via AES were performed.

Heating for 10 min at 780 K results in a significant change of the appearance of the deposits (Fig. 6.22 (b)). In case of the irradiated circle (compare the high magnification image in Fig. 6.22 (c)) the formerly densely packed, small iron clusters have changed into a lower number of bright features with varying sizes and shapes on top of a bright, continuous layer. Similar applies for the square, except that the features are concentrated on the right part of the irradiated region while the rest of the area is mainly covered by a continuous layer with minor protrusions. In contrast to this observation, the individual, less densely packed iron clusters in the surrounding of the irradiated area (generated due to the BSE proximity effect) remain unchanged by the annealing procedure, as it is visible in the high magnification image in Fig. 6.22 (d). It is therefore obvious that a specific cluster density is necessary for the changes observed in Fig. 6.22 (b) and (c) and that single, separated clusters are stable at the applied sample temperature. Similar results were obtained for line and dot deposits (not shown here), i.e., upon reaching a certain density of iron clusters, annealing to 780 K results in a closed layer covered by larger features, while individual clusters remain unchanged.

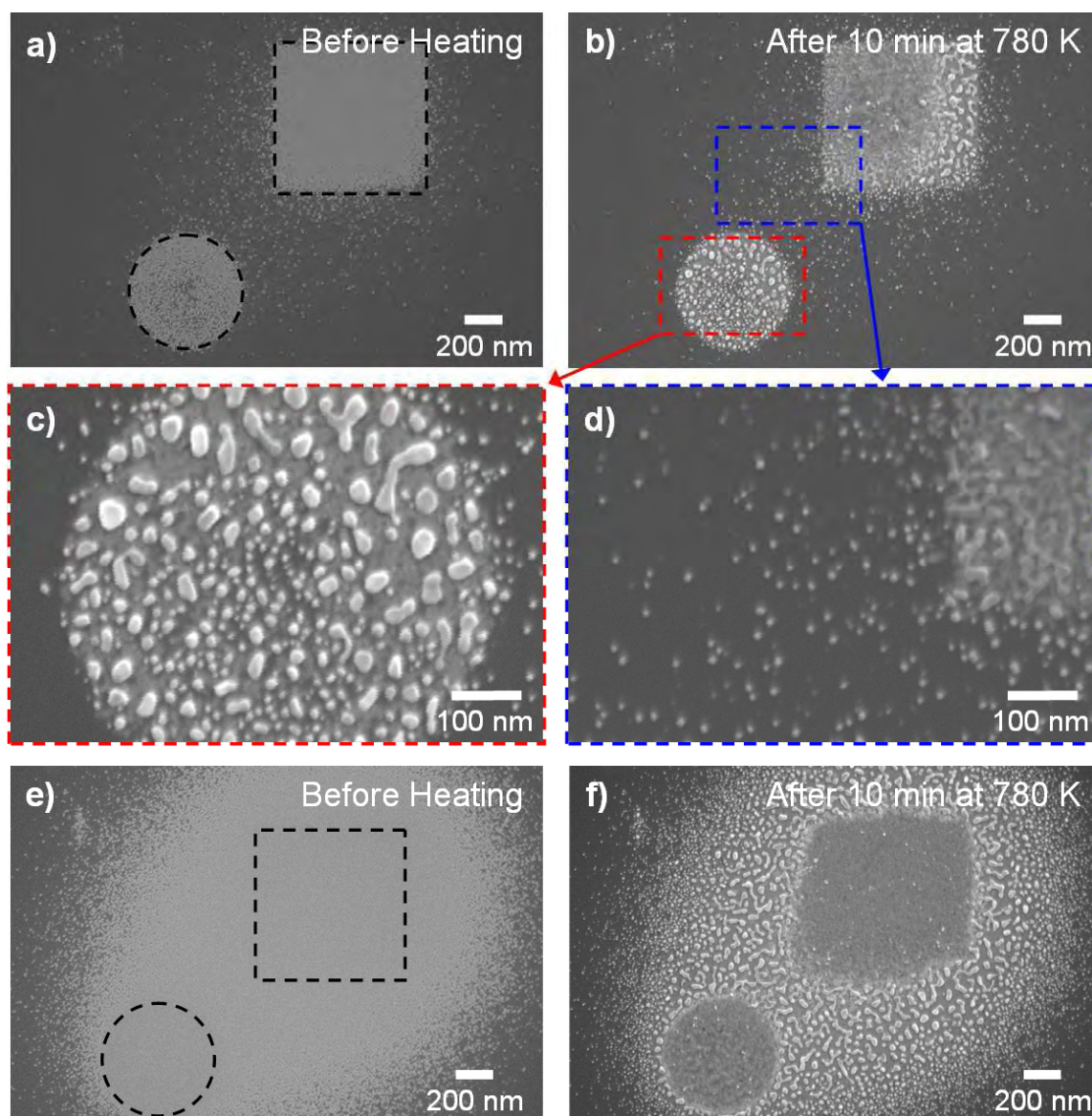


Fig. 6.22: SEM images of iron structures on Si(100) before and after 10 min heating at 780 K. a) Deposits generated with an electron dose of 13.3 C/cm^2 before and b) after the annealing procedure. c) High magnification image of the circle in (b) after the annealing procedure. d) High magnification image of the area marked with a blue rectangle in (b). e) Deposits generated with an electron dose of 39.8 C/cm^2 before and f) after the annealing procedure. ($U = 15 \text{ kV}$; $I = 400 \text{ pA}$; plane sample)

A significant influence on the appearance of the structures following the annealing procedure is therefore attributed to the amount of the deposited material. Fig. 6.22 (e) shows an image of a deposit that was generated with the same template but a three times higher electron dose (39.8 C/cm^2) compared to the deposit in Fig. 6.22 (a), resulting in a much higher amount of iron clusters, especially in the surrounding of the irradiated areas (marked by black dashed lines); due to the high density of the iron clusters, individual structures of the pattern

are not visible. Annealing at the given parameters, i.e., heating for 10 min at 780 K, results in a homogeneously closed layer at the whole irradiated areas, similar to the observations on the top left part of the square in Fig. 6.22 (b). The larger features (compare circle and right part of the square in Fig. 6.22 (b)) are in this case observed in the surrounding regions that were previously covered with a high density of iron clusters; single, individual clusters at a higher distance from the exposed area remain unchanged again.

In order to specify the reason of the morphological changes observed in Fig. 6.22 and to determine the chemical composition of the structures after the annealing procedure, scanning Auger microscopy (SAM) was performed. Fig. 6.23 shows elementarily resolved images of the structures in Fig. 6.22 (a) and (b) before (left column) and after (middle column) the heating process. They directly reveal the distribution of iron, oxygen, carbon and silicon in and beside the irradiated area; regions with a higher amount of the respective element appear bright in the SAM images, while a low amount appears dark (compare the color bar in Fig. 6.23).

A comparison of the SAM images acquired before the annealing procedure (left column in Fig. 6.23) gives a similar result for the chemical composition of the deposits as described by the AES measurements in Fig. 6.9 (red and orange spectra): the structures contain a high amount of iron with a minor oxygen contamination, leading to a significant damping of the signal of the underlying silicon substrate in the corresponding region. In the carbon image the exposed area displays a slightly lower amount of carbon compared to the rest of the surface. This observation is attributed to a minor carbon coverage of the free silicon substrate in this experiment, as it was observed via AES; it is unclear, if this surface contamination was induced by the EBID process or if it was already present on the surface prior to the experiment.

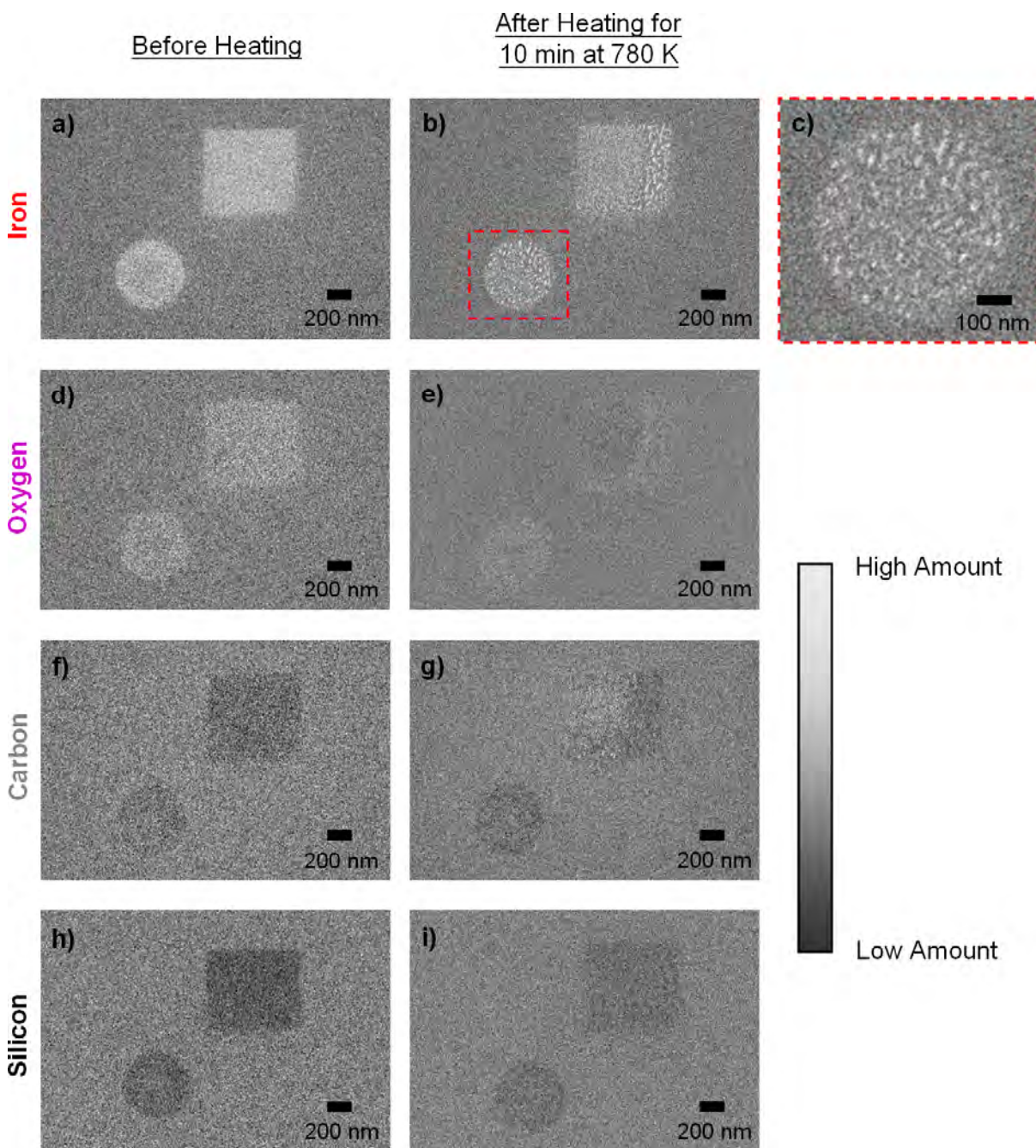


Fig. 6.23: SAM images of the pattern in Fig. 6.22 before (left column; compare Fig. 6.22 (a)) and after (middle column; compare Fig. 6.22 (b)) the annealing procedure. Bright areas indicate a high amount of the respective element, while a low amount appears dark. a), b), c) Iron SAM images. The image in (c) is a blow-up of the area marked by the red, dashed line in (b). ($E_{Peak} = 702.5$ eV; $E_{Bkg} = 727.5$ eV; $t_{Dwell} = 6.55$ ms) d), e) Oxygen SAM images. ($E_{Peak} = 512$ eV; $E_{Bkg} = 522.5$ eV; $t_{Dwell} = 6.55$ ms) f), g) Carbon SAM images. ($E_{Peak} = 271.5$ eV; $E_{Bkg} = 284.5$ eV; $t_{Dwell} = 6.55$ ms) h), i) Silicon SAM images. ($E_{Peak} = 1616.5$ eV; $E_{Bkg} = 1634$ eV; $t_{Dwell} = 6.55$ ms)

Compared to that, the images acquired after the heating procedure (middle column in Fig. 6.23) display some differences in the elemental distribution. While in the iron SAM image in Fig. 6.23 (a) the exposed area appears mostly as a homogeneously closed layer, a clear structuring is visible after the annealing process (compare Fig. 6.23 (b) and the high magnification image of the circle in Fig. 6.23 (c)). The latter consists of iron features with varying size and shape, which are mainly observed in the circle and on the right side of the square; the remaining part of the square exhibits also a certain amount of iron, which appears to be smaller compared to before the heating procedure (indicated by the lower brightness in the SAM image). A comparison between the iron SAM image in Fig. 6.23 (c) (blow-up of the circle) and the SEM image in Fig. 6.22 (c) shows that the position and the shape of the bright features in the SEM image matches the one of the iron features in the SAM image; the bright features with a varying shape visible in the SEM can therefore be identified as iron structures.

Oxygen appears to be significantly reduced after the annealing procedure, which is indicated by the lower brightness of the exposed area in Fig. 6.23 (e) compared to (d); similar to the results observed for iron deposits on Rh(110) (compare Chapter 5.8) this effect is mainly supposed to result from thermally induced oxygen desorption. The minor amount of remaining oxygen is concentrated in the area of the iron features, i.e., in the circle and right part of the square, while the left part of the square appears to be oxygen free. For the carbon SAM image after the annealing process (Fig. 6.23 (g)) the situation is reversed: compared to the free silicon surface the regions covered by the iron features exhibit a lower amount of carbon, while in the top left part of the square a similar amount is observed. The silicon substrate signal is less damped in the complete exposed area (Fig. 6.23 (i)) compared to the SAM image that was acquired before the heating (Fig. 6.23 (h)). A common observation in the SAM images of the different elements after the annealing procedure is a lower contrast compared to the SAM micrographs acquired before the heating process. This effect strongly indicates that annealing at the applied parameters (780 K for 10 min) results in material transport processes for the deposited material, like, e.g., diffusion and segregation. SAM measurements performed on the deposit in Fig. 6.22 (f) show similar results for the elemental distribution after the annealing procedure.

According to the SAM images depicted in Fig. 6.23 the morphological changes of the deposits observed in the SEM images in Fig. 6.22 can be at least partly explained. Heating at 780 K for 10 min results for the areas with a high iron cluster density in the growth of larger iron features, whereas the small iron clusters observed prior to the annealing procedure diminish. In the field of surface science this effect is known as Ostwald ripening, according to

a process discovered by Wilhelm Ostwald [187] around 1900, which was later taken over for the decomposition of islands on surfaces by Chakraverty and Peterson [188-190]; the driving force behind this process is the lowering of the surface free energy. The resulting larger features contain a high amount of iron with a minor oxygen contamination visible in the corresponding SAM image (compare Fig. 6.23 (e)). Conclusions concerning a potential carbon contamination can not be given for these structures with the data at hand; yet, the observed amount of carbon in the large iron features is lower compared to the one on the free silicon surface (compare Fig. 6.23 (g)). The chemical composition of the continuous layer situated below the features (e.g., compare Fig. 6.22 (c)) cannot be determined from the SAM images in Fig. 6.23, as the elemental distributions in the corresponding areas are dominated by the iron features.

The appearance of the homogeneously closed layer on the left side of the square in Fig. 6.22 (b) and in the irradiated areas of Fig. 6.22 (f) is mainly attributed to a local variation in the chemical composition of the structures prior to the annealing procedure. In the case of the square in Fig. 6.22 (b) this difference might be the result of the unintended electron induced deposition of, e.g., carbon during multiple SAM measurements performed in the corresponding area. For the structures in Fig. 6.22 (f), the higher applied electron dose during the EBID process may influence the chemical composition in the irradiated regions, e.g., via additional bond breaking reactions during the formation of the deposits. The SAM measurements depicted in Fig. 6.23 indicate that this layer contains a certain amount iron and carbon, while no oxygen is visible. Furthermore, the silicon signal is less damped in the corresponding region compared to before the annealing procedure, indicating again a partial removal of the covering layer via diffusion or segregation. Similar results were obtained via AES measurements in the corresponding areas before and after the heating process. A possible explanation for the formation of this layer is a reaction of the deposited material with silicon, resulting, e.g., in iron silicide (FeSi) and / or silicon carbide (SiC); this process would highly rely on the segregation of the components. AES measurements performed in the corresponding regions showed no clear indications for the formation of such species (no chemical shift or change in the lineshape visible), even though it cannot be completely ruled out.

Summarizing the data presented in this chapter, it can be stated that the iron clusters deposited with iron pentacarbonyl on Si(100) are thermally stable at least up to 680 K. Heating for 10 min at 780 K results in a significant change of the deposit morphology: depending on the amount and composition of the deposited material certain parts of the

irradiated area and the surrounding are dominated by large iron features with a minor oxygen contamination on top of a continuous layer. In contrast, other specific parts are covered with a homogeneously closed layer consisting of iron and carbon (compare Fig. 6.22 (b) and (f)); this layer is supposed to originate from a local variation in the chemical composition of the deposits. The large iron features are interpreted as a result from an Ostwald ripening, which depends also strongly on the density of the iron clusters. An important finding was that individual, separated clusters are stable at the applied conditions, i.e., heating for 10 min at 780 K (compare Fig. 6.22 (d)). These features might therefore be ideally suited as seeds for catalytic growth processes.

6.7 Application: carbon nanotube growth on iron deposits

A possible application of the generated iron deposits on silicon is the utilization as catalytically active sites for the growth of carbon nanotubes (CNTs) via a chemical vapor deposition (CVD) process. The CNTs, which are a specific allotrope modification of carbon, are known since 1991 [191] and exhibit a local hexagonal structure of sp^2 -hybridized carbon atoms with the shape of a cylinder [192, 193]. Generally, two types of carbon nanotubes exist: single walled (SWCNT) and multi walled carbon nanotubes (MWCNT), which differ in their respective tube diameters.

Carbon nanotubes exhibit very interesting properties in the field of materials science, which are further enhanced by the possibility to functionalize them via wet chemical processes. For example, SWCNT show a high flexibility [194], a high thermal conductivity along the cylinder axis [195] and either a semiconductor or metallic conductivity (depending on the structure of the tubes) [196, 197]. Therefore, potential application fields for CNTs are in the focus of research efforts in industry as well as academic institutes. Coatings with densely grown CNTs result in a superhydrophobic surface, similar as it is observed for the lotus effect [198]. Other possible applications are, e.g., the utilization in transistors [199, 200] or the deployment in so called field emission monitors [201]. Beside the described technical applications, additional research work has been performed in the field of bio science in order to use CNTs, e.g., as carriers for bio sensors [202, 203] or as stable matrices for growing tissue (tissue engineering) [204, 205]. Recently, it was also demonstrated that functionalized CNTs can be applied to transport siRNA into isolated rat cardiomyocytes (gene silencing) [206].

With respect to the generation of CNTs, mainly three different manufacturing methods are used: arc discharge at two graphite electrodes [207], laser ablation of graphite rods in a

heated reaction chamber [208] and the already mentioned chemical vapor deposition at specific catalyst particles with gases like carbon monoxide, methane, ethane, ethene and ethine [193]. Especially the so called HiPco[®] process, in which the tubes grow in the gas phase from CO on catalytic clusters of iron (generated via the thermal decomposition of Fe(CO)₅), has developed to an industrial relevant technique for the mass production of SWCNTs [209].

By combining a CVD process for the growth of the CNTs with the EBID process, it should be possible to generate carbon nanotubes at defined positions and thus to functionalize the specimen surface. This technique would therefore represent a further step towards nanostructuring of surfaces.

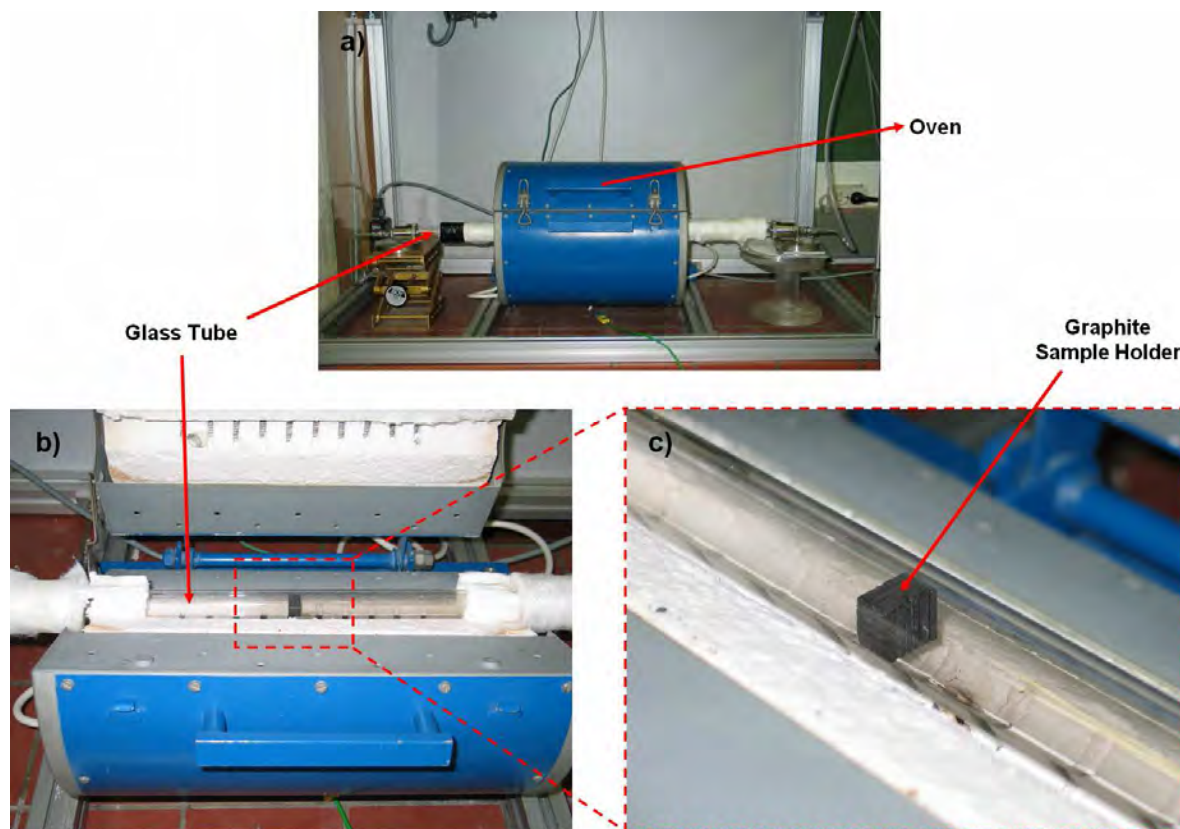


Fig. 6.24: Images of the CVD setup that has been used for the growth of carbon nanotubes on silicon samples, which have been previously used for EBID of iron with iron pentacarbonyl.

The CVD experiments for the CNT growth described in this chapter were performed by Katia Danova from the working group of Prof. Nadejda Popovska (“Lehrstuhl für Chemische Reaktionstechnik”, FAU Erlangen-Nürnberg) in the framework of collaboration. Some images of the used continuous flow reactor are depicted in Fig. 6.24. The setup consists of an oven with a glass tube inside as the main part (compare Fig. 6.24 (a) and (b)); the latter

acts as the reaction vessel and is connected to a removable gas inlet system on one side and an outlet system on the other one. Sample mounting within the tube is realized via a graphite block, which exhibits some slits on one of the sides (see Fig. 6.24 (c)). The irradiated silicon wafers are inserted into these slits and thereby clamped to the graphite sample holder, with the longer sides of the samples being aligned perpendicular to the respective side of the graphite block, i.e., that the exposed sides are also aligned perpendicular. The tube diameter and the size of the graphite block was chosen in such way, that the samples can be inserted with the irradiated side either in a parallel arrangement with respect to the tube axis and thus parallel to the gas flow (compare Fig. 6.24 (c)) or in a perpendicular alignment, which might have an influence on the CNT growth. Other parameters that could be varied in this setup are the temperature of the oven, the gas flux, the gas composition and the applied pressure. After the CVD process the samples were reinserted into the *Multiscan LAB* system for microscopic characterization.

In order to demonstrate the possibility to grow carbon nanotubes on iron deposits that were generated via EBID, Fig. 6.25 shows SEM images of two patterns containing area structures before and after the CVD process. Both patterns were irradiated with an identical template (square (upper right) and circle (lower left) with a size of $800\text{ nm} \cdot 800\text{ nm}$ and a diameter of 600 nm , respectively) on a fresh Si(100) sample at 200 K (see Fig. 6.25 (a) and (b)). For the pattern in Fig. 6.25 (a) an electron dose of 13.3 C/cm^2 was applied, while the pattern in (b) was exposed to a dose of 26.6 C/cm^2 . Similar as it was described for the results in Chapter 6.4.3, the structures appear in the SEM as continuous, bright deposits. The bright appearance of the regions surrounding the irradiated areas indicate also that a certain amount of material was deposited due to the exposure with scattered electrons (proximity effects; compare Chapter 2.7); this effect is much stronger for the deposits in (b), which is attributed to the higher applied electron dose compared to (a). Furthermore, local AE spectra acquired on both patterns (not shown here) showed that in the case of (b) a significantly higher amount of material was deposited in the irradiated area than in (a). The iron purity of both deposits was estimated to be roughly similar, i.e., a contamination value of roughly 21% was extracted from the AE spectra (under consideration of the respective thicknesses of the deposits).

The images in Fig. 6.25 (c) to (g) show the same patterns as in (a) and (b) after the CVD process was performed. The parameters applied for this procedure are listed in the following:

- **Gas composition:**
 $C_2H_2 / H_2 / N_2 = 2:1:10$
- **Total pressure:** 973 mbar
- **Gas flux:** 5 cm/s
- **Temperature:** 970 K
- **Process time:** 30 min
- **Alignment of the exposed area (with respect to the gas flow):** perpendicular
- **Post treatment:** flushing with pure N_2 until sample at 410 K

After the CVD process both patterns exhibit some peculiar features. In case of the pattern, which was irradiated with the lower electron dose ($13.3 C/cm^2$), individual nanotubes are visible in the exposed quadratic area (compare Fig. 6.25 (c) and the high magnification image in Fig. 6.25 (e)). They are accompanied by small particles with varying size and shape; the origin of these particles is not clear at the moment; it can be supposed that they represent a prequel for further CNT growth. In case of the irradiated circular area (lower left in Fig. 6.25 (c)), only a minor amount of particles is visible in the SEM. Yet, two bright, rectangular structures can be observed (compare Fig. 6.25 (g)). The origin of these features is again unclear; it might be speculated that it is some type of graphene layer prior to the rolling-up process in order to build the CNTs. On the other hand, the pattern generated with a higher electron dose ($26.6 C/cm^2$) is covered by a large amount of carbon nanotubes with varying size and a non-uniform arrangement after the CVD process (compare Fig. 6.25 (d)). In contrast to the deposit in (c), individual structures of the original pattern are not distinguishable anymore. The diameters of the resulting CNTs vary from ~ 6.5 nm to values higher than 55 nm (compare Fig. 6.25 (f)). It can therefore be assumed that the generated CNTs are built from differing numbers of carbon layers. It has to be noted that the observed features are designated as carbon nanotubes, even though their specific structure was not determined. A certain amount of particles, similar to the ones observed in Fig. 6.25 (c), is also visible in the image in (d). From the results presented in Fig. 6.25 it is obvious, that the applied electron dose for the generation of iron containing structures via EBID and therefore the amount of the deposited material has a significant influence on the amount of the subsequently generated carbon nanotubes (higher amount of CNTs for higher electron dose).

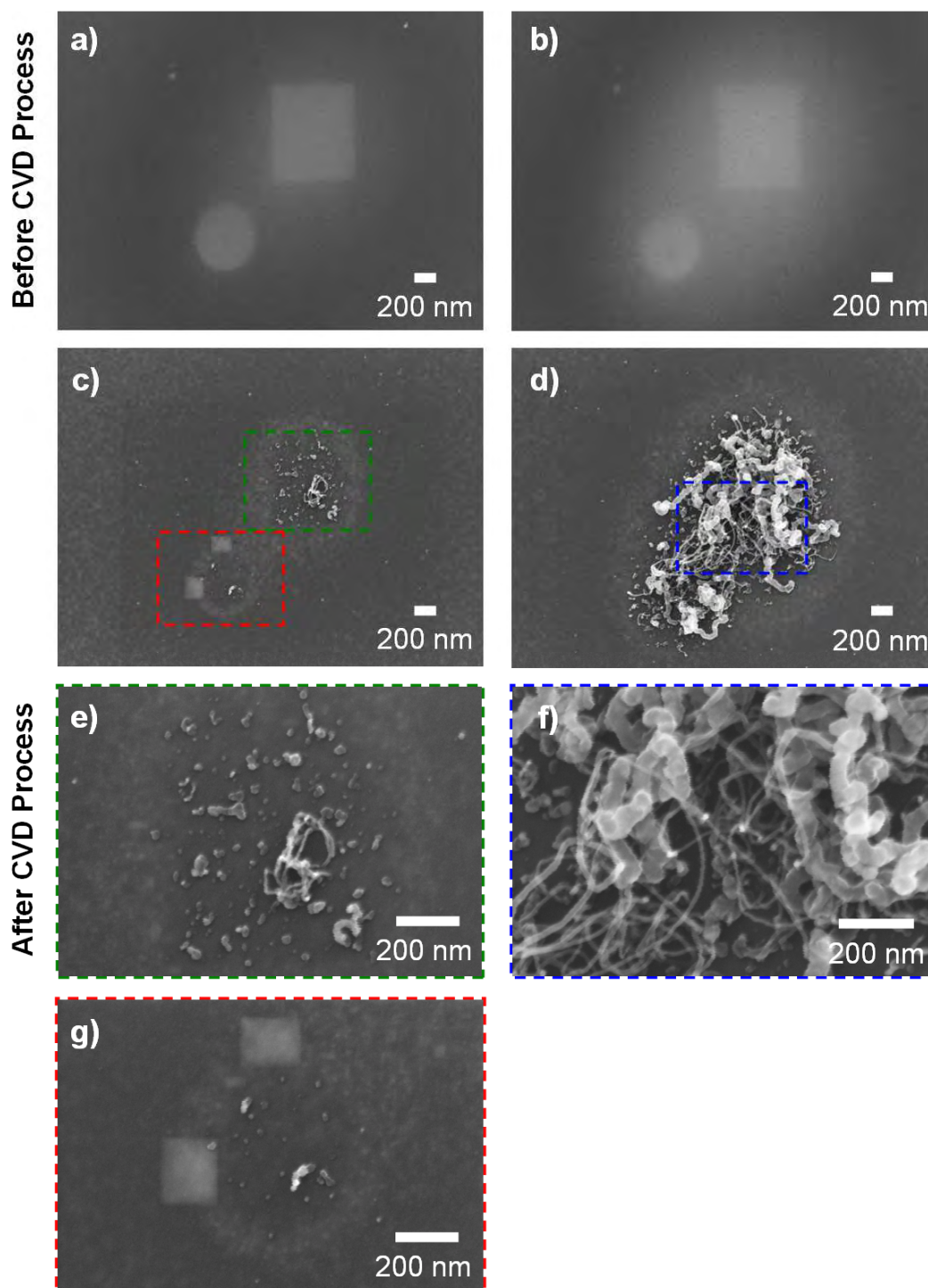


Fig. 6.25: SEM images of iron containing EBID deposits, which were generated on Si(100) at 200 K, before and after the CVD process. a), b) Images of the patterns (template: square and circle) before the growth process. They were generated with an electron dose of a) 13.3 C/cm^2 and b) 26.6 C/cm^2 . c), d) Images of the patterns in (a) and (b), respectively, after the growth process. e), g) High magnification images of the areas marked by the colored, dashed lines in (c). f) High magnification image of the area marked by a blue, dashed line in (d). ((a), (b): $U = 15 \text{ kV}$; $I = 3 \text{ nA}$; tilted sample / (c), (d), (e), (f), (g): $U = 15 \text{ kV}$; $I = 400 \text{ pA}$; tilted sample)

From the previously described observations one might envision to generate individual, separated CNTs by the deposition of preferably small, i.e., point, structures. To address this topic, Fig. 6.26 (a) shows an SEM image of a pattern of 25 point irradiations, which were generated on Si(100) at 200 K with an electron dose of 1.68 nC each. Every single point deposit is visible as a separated, bright structure, similar as it was reported in Chapter 6.4.3 (compare Fig. 6.14 (a)).

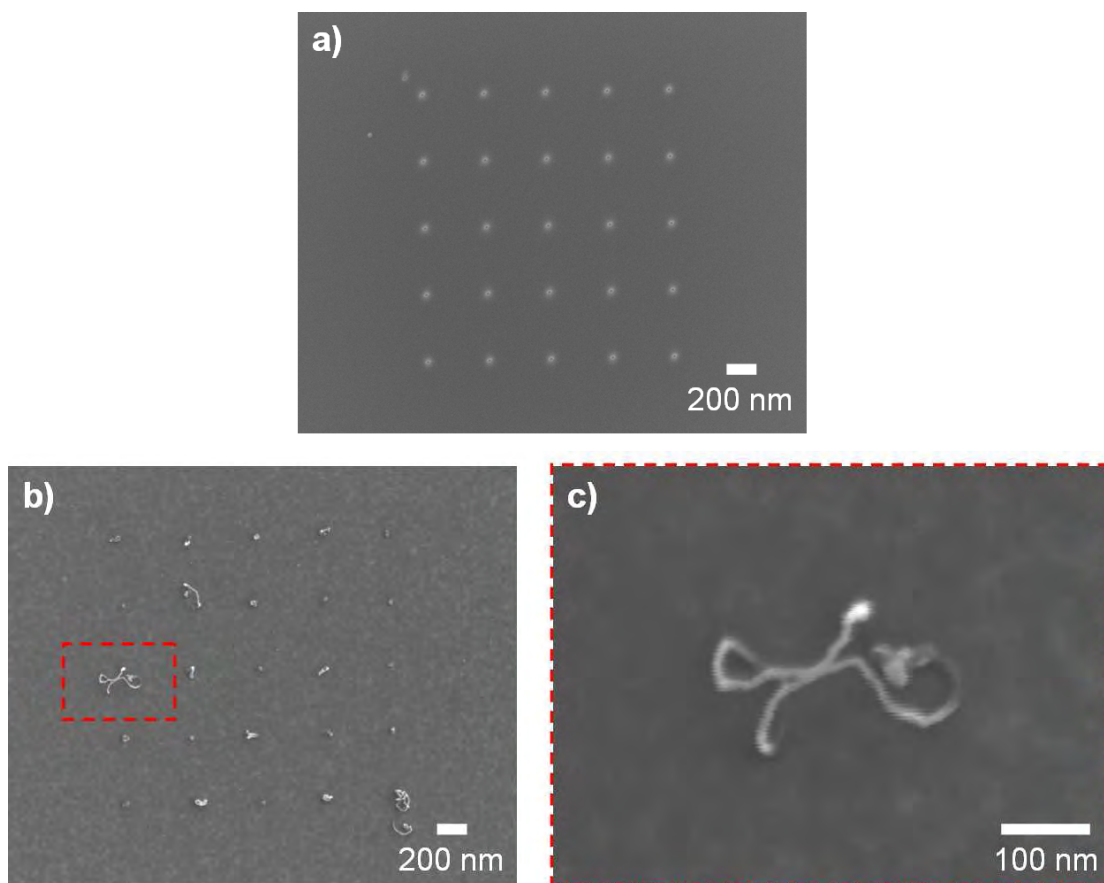


Fig. 6.26: SEM images of iron containing point deposits, which were generated on Si(100) at 200 K, a) before and b) after the CVD process. The point matrix in (a) was generated by the irradiation with an electron dose of 1.68 nC for each point. c) High magnification image of the area marked by a red, dashed line in (b). ((a): $U = 15$ kV; $I = 3$ nA; tilted sample / (b), (c): $U = 15$ kV; $I = 400$ pA; plane sample)

An image of the same deposit after the subsequently performed CVD process (identical parameters as used for the patterns in Fig. 6.25; see above) is depicted in Fig. 6.26 (b). Due to the applied procedure, individual carbon nanotubes with a varying length were grown at some of the irradiated positions. Fig. 6.26 (c) shows an image of one of these tubes at a higher magnification level. It has a diameter of ~ 10 nm and exhibits at one end a bright,

circular shaped slub. The origin of this slub is unclear at the moment; its position fits quite well to the one of the originally exposed point (compare the matrix of structures in Fig. 6.26 (b)), whereby it can be supposed that it is some type of iron containing feature, from which the CNT growth started. The remaining irradiated positions in Fig. 6.26 (b) exhibit bright features with a varying size and shape; similar to the observations in Fig. 6.25 (c) and (d) these features are attributed as a prequel for the growth of CNTs. The non-uniform effect of the applied CVD process on the individual structures of the point matrix in Fig. 6.26, which is expressed by the rather sporadic growth of CNTs, is attributed either to minor variations in the composition or amount of the material deposited via EBID or to the parameters chosen for the chemical vapor deposition process. In order to improve the amount and reproducibility of the generated CNTs, the parameters applied for both techniques have to be optimized.

From the results presented in Figs. 6.25 and 6.26 it is evident that the iron containing deposits generated via EBID can in principal be applied as catalysts for the local generation of CNTs via the described CVD process. Disadvantages of this method are, at least for area deposits that were generated at 200 K, that the resulting CNTs exhibit a large variety of the tube diameters (compare Fig. 6.25 (f)) and that the tubes are not aligned in a specific direction (compare Figs. 6.25 (d) and 6.26 (b)). For the latter it could be suggested, that a specific prestructuring of the iron containing deposits might induce a preferential growth direction of the CNTs. Concerning the variety of the tube diameters, a possible solution would be to generate deposits with a constant size via EBID, as the diameters of the CNTs grown by a CVD process are defined by the size of the applied catalyst particles [210-212]. In this context, one might envision to utilize the iron clusters generated on new Si(100) and Si(111) at room temperature as catalyst particles (compare Chapters 6.4.1 and 6.4.4), as they exhibit a rather narrow size distribution. Furthermore, their size of partly below 10 nm could also result in the aimed fabrication of SWCNTs at defined positions on the surface. It has to be noted, that densely packed iron clusters are thermally unstable at a sample temperature of 780 K, which leads, e.g., to the formation of larger iron islands on the surface (compare Chapter 6.6). This temperature is significantly lower than the temperature applied for the CVD process (~970 K). For individual, separated iron clusters the situation is different, as they are stable at least up to 780 K. These features might therefore be more adequate for the fabrication of CNTs with a rather small diameter by the applied procedure. Another possibility would be to change the parameters of the CVD process (e.g., by the utilization of higher pressures) in order to reduce the necessary sample temperature. For the deposits in Figs. 6.25 and 6.26, which were generated via EBID at 200 K, the thermal stability of the structures was not

determined prior to the CNT growth procedure. From the image in Fig. 6.25 (c), in which the outlines of both structures are still visible after the CVD process, it can be assumed that at least the overall shape of the deposits remain intact.

An additional problem of the applied CVD procedure is the unintended growth of carbon nanotubes at certain positions on the silicon single crystal surface. Fig. 6.27 shows SEM images of such areas and high magnification images of individual CNTs from the same sample as the structures in Figs. 6.25 and 6.26. The origin of this unintended growth is attributed to contamination particles, which were either present on the surface prior to the EBID procedure and thereby covered with iron due to the dosage of $\text{Fe}(\text{CO})_5$ or accidentally deposited during the assembly of the specimen on the graphite sample holder. These particles led in some cases to the growth of carbon nanotubes in a very high density, as it is visible in Fig. 6.27 (a) and (b). Furthermore, some of the resulting CNTs exhibit a high length (compare Fig. 6.27 (a)) or a strange appearance, as it is observed, e.g., for the helical structure of the CNTs in Fig. 6.27 (c).

A remarkable arrangement of carbon nanotubes can also be observed in the image in Fig. 6.27 (d). Clearly visible is a single, long tube, accompanied by a number of shorter and smaller CNTs. Yet, a high magnification image of this long tube shows a completely different morphology compared to the other CNTs observed so far: it appears like a group of smaller CNTs, which are “plaited” around each other homogeneously to generate some type of “rope”-like structure. Fig. 6.27 (f) shows a different part of this conglomerate (position marked by the blue, dashed line in Fig. 6.27 (d)). It displays a disturbance in the arrangement of the tubes, which allows to better distinguish the individual CNTs. Before and after this perturbation the “rope”-structure is visible again, which indicates the high stability of this structure. This type of carbon nanotube arrangement observed in Fig. 6.27 (d) to (f) has not been reported so far, to the best of the knowledge of the author. It can be supposed that the observed alignment of the carbon nanotubes is induced by the shape of the catalytically active structure, from which they grow. Even though this could not be confirmed via the SEM, one might envision to generate such “rope”-structures in a directed way by tuning the shape of the generated EBID deposits (maybe also in a three-dimensional way).

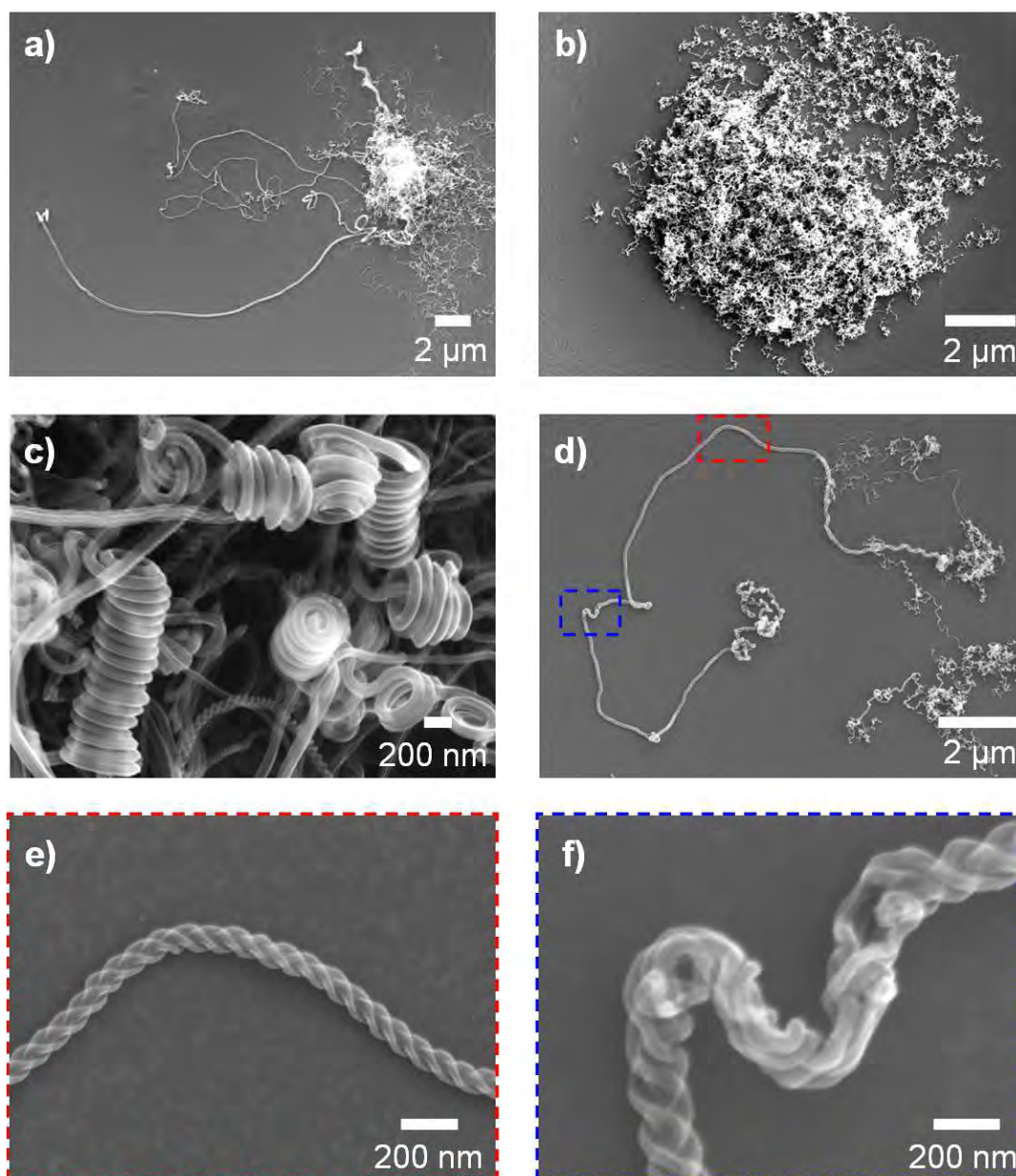


Fig. 6.27: SEM images of carbon nanotubes that were unintendedly grown on Si(100) due to the applied CVD process. The images in (e) and (f) are high magnification images of the positions marked by the red, dashed lines and blue, dashed lines, respectively, in (d). ((a), (b), (d), (e), (f): $U = 15$ kV; $I = 400$ pA; plane sample / (c): $U = 15$ kV; $I = 400$ pA; tilted sample)

In summary, it could be shown that the iron containing deposits generated via EBID can act as seeds for the catalytic growth of carbon nanotubes by a chemical vapor deposition process with a gas mixture of C_2H_2 , H_2 and N_2 . Experiments performed with deposits that were generated on Si(100) at 200 K showed in the case of area structures a large variety of tube diameters and a non-uniform arrangement, while in the case of point deposits only a sporadic growth of the CNTs could be observed; the latter is mainly attributed to the non-

optimized parameters of the EBID as well as the CVD process. Factors that could be rather disadvantageous for the applied procedure are the thermal stability of the iron structures (especially for iron clusters generated at room temperature in a high density) and the unintended growth of CNTs at certain contamination particles on the surface. Some of the unintendedly fabricated CNTs exhibit also a strange alignment, resulting in a conglomerate of tubes with a homogeneously, “rope”-like structure, which is supposed to be influenced by the shape of the catalytically active center.

6.8 Summary and conclusions

Performing EBID under UHV conditions with the precursor iron pentacarbonyl on silicon single crystal surfaces yielded novel findings, with the possibility for interesting applications. The results also demonstrate the importance of the applied ultra-high vacuum conditions to gain a deeper understanding of the EBID process.

It was shown that the range of “unintended” deposition in the surrounding of the irradiated area, which is mainly defined by the range of backscattered electrons in the sample material, can be reduced via a reduction of the applied electron acceleration voltage (Chapter 6.3). A decrease from 15 to 8 kV resulted in a reduction of the size of the halo surrounding the irradiated region from 2250 to 750 nm, which is in line with the size of the BSE exit areas, determined via Monte-Carlo simulations for the corresponding voltages. It has to be noted that this ultimate size of the deposits is only achieved at very high electron doses. At lower electron doses the unintended deposition in the surrounding of the electron impact point is also determined by the statistics of the scattering processes.

In Chapter 6.4 different experiments to study the influence of the sample condition and precursor gas composition on the EBID process were discussed. The deposition with iron pentacarbonyl on Si(100)-(2x1) at room temperature resulted in the generation of discontinuous structures, consisting of iron clusters with a typical size of < 10 nm (Chapter 6.4.1). Via AES measurements it was shown, that these clusters have an iron purity of at least 96 %, which represents one of the highest metal contents achieved via EBID up to now. The formation of these clusters was attributed to a tensile stress between the deposited iron and a carbon, oxygen and iron containing prerequisite layer, which is formed in the initial stage of the deposition process. A key factor for the observed high purity and discontinuous morphology of the generated deposits is attributed to the cleanliness of the deposition process, i.e., UHV conditions plus a well defined surface and gas composition.

EBID with $\text{Fe}(\text{CO})_5$ on fresh $\text{Si}(111)-(7\times 7)$ samples at room temperature was performed in a rather explorative way, i.e., only few experiments were performed. The generated deposits exhibited an identical morphology compared to the structures on $\text{Si}(100)$, i.e., the deposits consisted of small iron clusters on top of an initial layer (Chapter 6.4.4). The growth mechanism for the iron clusters is therefore supposed to be independent from the applied crystal surface orientation. On $\text{Si}(111)$ the iron clusters were also studied via STM measurements; thereby, the cluster size was confirmed to be lower than 10 nm. The carbon contamination of the deposits on $\text{Si}(111)$ was always higher than on $\text{Si}(100)$.

It was also demonstrated that the purity of the applied precursor gas, i.e., $\text{Fe}(\text{CO})_5$, has a major influence on the iron deposits generated at room temperature on $\text{Si}(100)$ (Chapter 6.4.2). A highly purified gas lead to the generation of iron clusters with a purity of at least 96 %, while iron clusters generated from a less purified $\text{Fe}(\text{CO})_5$, which contained large amounts of nitrogen and argon and only a minor amount of the precursor, had a purity of ~ 83 %. Additionally, the amount and density of the generated clusters was significantly higher for the high quality gas compared to the low quality one. Similar results were also obtained for the generation of iron deposits on $\text{Si}(111)$. These findings demonstrate the significance of the precursor quality for the EBID process.

The tensile stress induced mechanism that was suggested for the growth of the iron clusters at room temperature relies on the diffusion of molecules. This hypothesis was verified by performing EBID on $\text{Si}(100)$ at a sample temperature of 200 K (Chapter 6.4.3). The resulting structures appeared continuous and were stable at least up to room temperature. At rather low electron doses, indications for the prerequisite layer were observed. The iron content of these deposits was estimated via local AES measurements to be ~ 79 %, which is lower compared to the structures generated at room temperature; this observation is attributed to the higher residence time of the carbon containing precursor fragments, i.e., CO, on the surface at 200 K. Deposits with a higher iron content (~ 92 %) were in this case generated via a different scan strategy, comprising the repeated irradiation of an identical area.

In Chapter 6.5 it was shown that the local density of the iron clusters generated at room temperature on $\text{Si}(100)$ and $\text{Si}(111)$ is strongly depending on the applied electron dose. For point, area and line irradiations the number of clusters followed roughly a linear trend after a specific offset electron dose. A similar slope (average: 1 cluster / 0.079 ± 0.007 nC) was observed for the linear trends of multiple point irradiation experiments. In contrast, the offset electron dose varied for the different experiments (from < 0.6 nC to 1.32 nC), which is mainly attributed to different structure densities in the applied templates and therefore to

variations in the local electron density due to scattered electrons. The linear trend of the amount of generated clusters for point irradiations could be observed up to an electron dose of 2.40 – 2.52 nC; at higher electron doses the slope of the cluster growth appears to increase. For area and line structures the linear trend shows a slope of 1 cluster / 0.066 C/cm² and 1 cluster / 2.435 μC/cm, respectively, after an offset electron dose. The finding that the amount of the generated iron clusters is directly related to the applied electron dose and the pattern geometry indicates a new route for the fabrication of pure iron nanostructures with a defined density and a narrow size distribution on surfaces.

The iron clusters generated in a high density were thermally stable at least up to 680 K, while heating for 10 min at 780 K resulted in a significant change of their morphology (Chapter 6.6). Due to this heating procedure, specific parts of the deposit were either dominated by large iron features on top of a continuous layer or covered by a closed layer containing iron and carbon. The large iron features are interpreted as a result of Ostwald ripening, while the origin of the homogeneously closed layer is attributed to local variations in the chemical composition of the deposited material. It is important to mention that individual, separated clusters exhibited no change in their appearance and are therefore thermally stable at least up to 780 K.

In Chapter 6.7 it was shown, that the iron containing EBI deposits on silicon samples can be applied as catalysts for the local fabrication of carbon nanotubes by a CVD process. Experiments performed with area deposits that were generated on Si(100) at 200 K resulted in the generation of tubes with a large variety of tube diameters and a non-uniform arrangement. In the case of point deposits only a sporadic tube growth was observed, which is attributed to the non-optimized deposition and CVD parameters. A drawback of this procedure is the unintended growth of CNTs at certain contamination particles on the surface. Some of the carbon nanotubes generated thereby exhibited peculiar arrangements, e.g., a homogeneous, “rope”-like structure.

7 Summary

In this thesis the potential for the generation of clean iron nanostructures via the technique of electron-beam induced deposition (EBID) in ultra-high vacuum (UHV) was explored. The central part of the corresponding experimental setup was an SEM column, which was used for imaging of the specimen, as an electron source for chemical analysis via Auger electron spectroscopy and, in combination with a commercial lithography package, for EBID of arbitrarily shaped deposits. This system enabled the study of the EBID process under clean and well-defined conditions and therefore to overcome the adsorption and co-deposition of residual gases (e.g., hydrocarbons and water) typically observed in high vacuum (HV) environments. The UHV system was installed shortly before the start of the thesis at hand; therefore one of the main tasks was to test the functionalities of the setup, especially the lithographic attachment via electron-beam lithography on a PMMA sample, and to modify the systems to the specific demands of EBID. The principal scientific theme of this thesis is the generation of iron structures from the precursor iron pentacarbonyl on different single crystalline samples, namely Rh(110) as a catalytically active metal substrate and on silicon (100) and (111) surfaces as prototypes for semiconductor samples. The application of a catalytically active metal substrate represented one of the novel aspects for the EBID process. In the following, a summary of the most important results will be given.

Test measurements: generation of carbonaceous deposits with ethene on Si(111)

In the system C_2H_4 / Si(111) the capabilities of the instrument to fabricate arbitrarily shaped deposits via EBID were successfully tested. Via the attached lithography package the successful generation of patterns with virtually any desired shape (e.g., logo of the FAU Erlangen-Nuremberg) was demonstrated.

Another topic was to study the influence of specific electron-beam parameters, namely electron-beam voltage and applied electron dose. It was found that a smaller structure size can be realized by the application of lower electron doses and higher primary electron voltages.

EBID with $Fe(CO)_5$ on Rh(110)

The application of a catalytically active metal substrate for the electron induced deposition of iron structures resulted in some novel and unexpected observations, especially with respect to the selectivity of the process, i.e., the deposition in regions of precursor – electron interaction. On a well-ordered and clean Rh(110) surface the deposition process with the precursor

$\text{Fe}(\text{CO})_5$ was found to be not selective, since Fe was deposited on the whole surface due to a catalytic and autocatalytic dissociation of the precursor without electron irradiation already at room temperature. In contrast to that, for structurally “non-perfect” Rh(110) substrates, which exhibited a rough surface and an inferior long-range order, the deposition process was moderately selective, i.e., a small amount of iron was deposited in the non-irradiated area. A high selectivity was achieved by covering the perfectly ordered Rh(110) surface with an ultra thin layer of titanium oxide and thereby suppressing the catalytic decomposition of $\text{Fe}(\text{CO})_5$. Regardless of the specific surface condition, the purity of the generated iron deposits was always very high ($\geq 87\%$). In addition it was observed that the surface quality is influencing the lateral size of the deposited structures. In this respect it was found that smaller and better defined structures (lateral size < 25 nm) could be fabricated on a “rougher” surface.

The spatially well defined structures deposited on the rough surface were thermally stable at least up to 500 K. Extended heating at 600 K resulted in a loss of their structure, which was attributed to diffusion of iron on the surface. Furthermore, it was demonstrated that the Fe structures can be selectively oxidized to iron oxide via dosage of O_2 at elevated temperatures. A noteworthy finding, although not directly related to EBID, was the possibility to observe and induce hydrogen reduction fronts on an oxygen covered Rh(110) surface with SEM.

EBID with $\text{Fe}(\text{CO})_5$ on silicon single crystal surfaces

The electron induced deposition with iron pentacarbonyl on Si(100) at room temperature resulted in the generation of discontinuous structures consisting of pure iron clusters (iron purity $> 96\%$). An identical structure morphology was also observed on Si(111), even though the purity of the deposits was not confirmed on that surface. The typical size of these clusters was < 10 nm, which is significantly lower than the minimum size of deposits achievable via our instrument with the “classical” EBID process (~ 20 nm). The formation of the Fe clusters was attributed to a tensile stress between the deposited iron and an initial layer, which is formed before the onset of the cluster growth; this clustering process was also supposed to rely on diffusion of the involved molecules. The hypothesis was verified by performing EBID on Si(100) at a sample temperature of 200 K, which resulted in the generation of continuous structures that were stable at least up to room temperature. In this case the purity of the deposits was estimated to be $\sim 79\%$. Continuous deposits with a higher iron content ($\sim 92\%$) were generated at a sample temperature of 200 K by applying a different scan strategy, comprising the repeated irradiation of an identical area. The density of the iron clusters

generated at room temperature was found to be depending on the applied electron dose. For point, area and line structures an at least partially linear trend between the number of generated clusters and the electron dose was observed beyond a specific offset electron dose. Different experiments performed with point deposits exhibited a similar slope of the linear trend, while the offset electron dose strongly varied; the latter was attributed to local variations in the electron density due to the density of the structures in the applied templates. Another important parameter influencing the iron cluster growth at room temperature was the precursor gas composition. The application of a purified gas resulted in the generation of a high density of pure iron clusters (~ 96 %), while with a marginally cleaned $\text{Fe}(\text{CO})_5$ both the amount and the purity (~ 83 %) of the generated clusters were reduced. These findings demonstrate the importance of the precursor gas quality for the EBID process and the necessity to monitor its composition.

The iron clusters generated at room temperature in a high density were thermally stable at least up to 680 K. Annealing to 780 K resulted either in the formation of larger iron features as a result of an Ostwald ripening or in a continuous carbon and iron containing layer, depending on the local composition of the deposits. In contrast, individual, separated iron clusters were thermally stable up to at least 780 K. As a possible application for the iron deposits on silicon, the local catalytic growth of carbon nanotubes via a CVD process was demonstrated, with the Fe structures acting as catalytic seeds.

From the results presented, it is obvious that EBID performed under UHV conditions yielded novel aspects, in particular for the precursor $\text{Fe}(\text{CO})_5$. Typical iron purities achieved on Rh(110) and Si(100) at room temperature were $\geq 87\%$ and $> 96\%$, respectively, which represents one of the highest metal contents realized via EBID up to now. The cleanliness of the whole process, i.e., an environment free of residual gases and the application of pure and well defined surfaces and precursor compounds, was identified as the key feature for the achieved metal purities. Expanding EBID to a catalytic active surface opens up new possibilities for the field of electron-beam induced processes, since the catalytic activity of the surface may be locally modified via deposition of a thin overlayer. In this regard, the presented approach to perform EBID under UHV conditions considerably expands the possibilities to engineer nanostructures.

8 Zusammenfassung

Das wesentliche Ziel dieser Arbeit war die Erzeugung reiner Eisen-Nanostrukturen mittels elektronenstrahlinduzierter Abscheidung („electron-beam induced deposition“; EBID) im Ultrahochvakuum (UHV). Die Hauptkomponente des verwendeten experimentellen Aufbaus war ein Rasterelektronenmikroskop („scanning electron microscope“; SEM), das für die Abbildung der Probe, als Elektronenquelle für die chemische Analyse mittels Augerelektronenspektroskopie und, mit einer Lithographie-Erweiterung, für die Erzeugung von Abscheidungen mit definierter Form genutzt wurde. Mit diesem Aufbau konnte der EBID-Prozess unter saubereren und wohl definierten Bedingungen untersucht werden. Ein wichtiger Aspekt dabei war die Vermeidung von Abscheidungen aus Restgasmolekülen (z.B. Kohlenwasserstoffe und Wasser), wie sie typischerweise im Hochvakuum beobachtet wird. Das UHV-System wurde kurz vor Beginn dieser Arbeit installiert und musste zunächst getestet und an die spezifischen Anforderungen des EBID Prozesses angepasst werden. Hierbei lag ein besonderes Augenmerk auf der Funktionalität der Lithographie-Erweiterung, welche mittels Elektronenstrahl-Lithographie auf einer PMMA-Probe verifiziert wurde. Der wissenschaftliche Fokus dieser Arbeit lag auf der elektronenstrahlinduzierten Erzeugung von Eisenstrukturen unter Verwendung des Präkursors Eisenpentacarbonyl auf verschiedenen einkristallinen Proben. Dabei wurde insbesondere der Einfluss der Eigenschaften der Probe auf den EBID Prozess studiert. Als Beispiel für ein katalytisch aktives Metallsubstrat wurde Rh(110) eingesetzt und als Prototypen für Halbleiteroberflächen kamen Si(111) und Si(100) zum Einsatz. Die Verwendung eines katalytisch aktiven Metallsubstrats stellte dabei einen neuartigen Aspekt für den EBID-Prozess dar. Es folgt ein Überblick über die wichtigsten Ergebnisse der Arbeit.

Test-Messungen: Erzeugung von kohlenstoffhaltigen Abscheidungen mit Ethen auf Si(111)

Am System C_2H_4 / Si(111) wurde die lithographische Herstellung von EBID Abscheidungen mit definierter Form erfolgreich getestet (z.B. Logo der Universität Erlangen-Nürnberg). Ein weiteres Thema war die Untersuchung des Einflusses der Beschleunigungsspannung des Elektronenstrahls und der Elektronendosis. Es wurde gezeigt, dass eine kleinere Strukturgröße durch die Verwendung von kleineren Elektronendosen und höheren Beschleunigungsspannungen der Primärelektronen erzeugt werden kann.

EBID mit $Fe(CO)_5$ auf Rh(110)

Die Verwendung eines katalytisch aktiven Metallsubstrats für die elektronenstrahlinduzierte Erzeugung von Eisenstrukturen führte zu einigen unerwarteten Beobachtungen, speziell in Bezug auf die Selektivität des Prozesses, d. h. die selektive Abscheidung ausschließlich in Bereichen der Wechselwirkung zwischen Elektronen und dem Präkursor. Auf einer geordneten und sauberen Rh(110) Oberfläche erwies sich der Abscheidungsprozess mittels $Fe(CO)_5$ als nicht selektiv, d.h. eine beträchtliche Menge an Eisen wurde durch katalytische und autokatalytische Zersetzung des Präkursors ohne Elektronenwechselwirkung auf der ganzen Oberfläche bereits bei Raumtemperatur abgeschieden. Im Gegensatz dazu war der Abscheidungsprozess auf strukturell nicht „perfekten“ Rh(110) Proben bedingt selektiv, d. h. nur eine kleine Menge Eisen wurde im nicht belichteten Bereich abgeschieden. Eine hohe Selektivität wurde durch die Bedeckung einer sauberen und geordneten Rh(110)-Oberfläche mit einer dünnen Titanoxid-Schicht erreicht; die katalytische Zersetzung von $Fe(CO)_5$ wurde hierdurch vollständig unterbunden. Unabhängig von dem spezifischen Oberflächenzustand war die Reinheit der erzeugten Strukturen stets sehr hoch ($\geq 87\%$). Zusätzlich wurde beobachtet, dass die Qualität der Oberfläche die laterale Größe der erzeugten Strukturen beeinflusst. In diesem Zusammenhang wurde gezeigt, dass kleinere und besser definierte Strukturen (laterale Größe $< 25\text{ nm}$) auf einer „raueren“ Oberfläche erzeugt werden können.

Die räumlich gut definierten Strukturen, die auf einer rauen Oberfläche hergestellt wurden, waren thermisch stabil bis zu 500 K. Längeres Heizen bei 600 K führte zu Veränderung der Form der Strukturen, was vermutlich auf die Diffusion von Eisen auf der Oberfläche zurückzuführen ist. Weiterhin konnte gezeigt werden, dass die Eisenstrukturen durch die Dosierung von O_2 bei erhöhten Temperaturen selektiv zu Eisenoxid oxidiert werden können. Ein weiteres Ergebnis, welches nicht direkt mit EBID in Beziehung steht, war die Möglichkeit der Beobachtung und Erzeugung von Wasserstoff-Reduktionsfronten auf einer sauerstoffbedeckten Rh(110) Oberfläche mittels SEM.

EBID mit $Fe(CO)_5$ auf Silizium Einkristall-Oberflächen

Die elektronenstrahlinduzierte Abscheidung mit Eisenpentacarbonyl auf Si(100) bei Raumtemperatur führte zu diskontinuierlichen Strukturen bestehend aus reinen Eisen-Clustern (Eisen-Reinheit $> 96\%$). Eine identische Morphologie der Strukturen wurde auf Si(111) ebenfalls beobachtet, auch wenn die Reinheit der Abscheidungen auf dieser Oberfläche etwas niedriger war. Die typische Größe dieser Cluster war $< 10\text{ nm}$, was deutlich unter der minimalen Größe von Abscheidungen liegt, die mit unserer Apparatur im „klassischen“

EBID-Prozess erreicht werden kann (~ 20 nm). Die Erzeugung der Fe-Cluster wurde auf eine Fehlanpassung zwischen dem abgeschiedenen Eisen und einer vor dem Beginn des Cluster-Wachstums gebildeten Schicht zurückgeführt. Der entsprechende Prozess der Clusterbildung basiert demnach auf einer ausreichenden Mobilität der beteiligten Molekülfragmente. Diese Hypothese wurde bestätigt durch die Durchführung von EBID auf Si(100) bei einer Proben temperatur von 200 K, was zur Erzeugung von kontinuierlichen Strukturen führte, die auch bei Raumtemperatur stabil waren. In diesem Fall wurde eine Reinheit der Strukturen von ~ 79 % erreicht. Kontinuierliche Abscheidungen mit einem höheren Eisen-Gehalt (~ 92 %) konnten bei einer Proben temperatur von 200 K mit einer modifizierten Belichtungsstrategie, d. h. der wiederholten Belichtung desselben Bereichs, erzeugt werden. Die Dichte der bei Raumtemperatur erzeugten Eisen-Cluster erwies sich als abhängig von der angewandten Elektronendosis. Für Punkt-, Flächen- und Linien-Strukturen wurde nach einer spezifischen Mindestelektronendosis für die Erzeugung der Cluster ein zumindest teilweise linearer Verlauf zwischen der Anzahl an hergestellten Clustern und der Elektronendosis beobachtet. Verschiedene Experimente zur Herstellung von Punkt-Abscheidungen zeigten eine ähnliche Steigung des linearen Verlaufs, während die Mindestelektronendosis allerdings stark variierte. Diese Abweichungen der Dosis wurden lokalen Unterschieden in der Elektronendichte zugeschrieben, die aus der jeweiligen Dichte der Strukturen in den verwendeten Mustern resultierten. Ein weiterer, wichtiger Parameter, der das Wachstum der Eisen-Cluster bei Raumtemperatur beeinflusst, war die Reinheit des Präkursor-Gases. Die Verwendung eines intensiv aufgereinigten Gases führte zur Erzeugung einer hohen Dichte reiner Eisen-Cluster (~ 96 %), wohingegen mit einem wenig gereinigtem $\text{Fe}(\text{CO})_5$ sowohl die Menge als auch die Reinheit (~ 83 %) der erzeugten Cluster reduziert wurde. Diese Ergebnisse demonstrieren die Bedeutung der Qualität des Präkursor-Gases für den EBID-Prozess und die Notwendigkeit seine Zusammensetzung zu kontrollieren.

Die bei Raumtemperatur in einer hohen Dichte erzeugten Eisen-Cluster waren thermisch stabil bis 680 K. Heizen auf 780 K führte entweder zur Bildung von größeren Eisenstrukturen als Ergebnis einer Ostwald-Reifung oder zur Bildung einer kontinuierlichen, Kohlenstoff und Eisen enthaltenden Schicht, abhängig von der lokalen Zusammensetzung der Abscheidung. Im Gegensatz dazu waren individuelle, getrennt liegende Eisen-Cluster zumindest bis 780 K stabil. Einen möglichen Anwendungsbereich der Eisen-Abscheidungen auf Silizium stellt das lokalisierte katalytische Wachstum von Kohlenstoff-Nanoröhren mittels eines CVD-Prozesses dar, wobei die Eisenstrukturen als katalytische Keime dienen.

Die Ergebnisse die in dieser Arbeit gewonnen werden konnten zeigen, dass EBID unter UHV-Bedingungen zu einer Reihe neuartiger Erkenntnisse mit Anwendungspotential führt. Speziell mit dem Präkursor $\text{Fe}(\text{CO})_5$ konnten Eisen-Reinheiten von über 87 % auf Rh(110) und über 96 % auf Si(100) bei Raumtemperatur erreicht werden. Dies stellt eine der höchsten Metallreinheiten dar, welche bisher mittels EBID erzielt werden konnten. Eine Schlüsselrolle spielte dabei die Reinheit des gesamten Prozesses, d. h. eine Umgebung frei von Restgasen und die Verwendung von reinen und wohl definierten Oberflächen und Präkursor-Verbindungen. Die Anwendung von EBID auf einer katalytisch aktiven Oberfläche eröffnet neue Möglichkeiten im Bereich der elektronenstrahlinduzierten Prozesse, da die katalytische Aktivität der Oberfläche durch die Abscheidung einer dünnen Schicht lokal verändert werden könnte. In dieser Hinsicht erweitert der beschriebene Ansatz zur Durchführung von EBID unter UHV-Bedingungen deutlich die Möglichkeiten zur Herstellung von Nanostrukturen.

9 Appendixes

9.1 Appendix to Chapter 3

9.1.1 Electron filament setup in the preparation chamber

Schematic drawings of the electron filament, which was attached to the preparation chamber, are depicted in Fig. 9.1. For this design three vacuum feedthroughs were incorporated into a CF 35 flange at an angle of 120° with respect to the neighboring contacts and the center of the flange (see Fig. 9.1 (a)). Integrated on the vacuum side of the feedthroughs is a stainless steel rod with 3 mm diameter. A linear connector couples this rod to a second one, with the filaments being spot welded at the end of the latter (see Fig. 9.1 (b)). By changing the length of this second rod the distance between the filament and the sample can be tuned.

The applied filaments were fabricated from a 0.125 mm thick thoriated tungsten wire (Goodfellow / W145300/2). Measurements acquired at the vacuum feedthroughs resulted in a resistance between 0.6 and 0.8Ω for each filament.

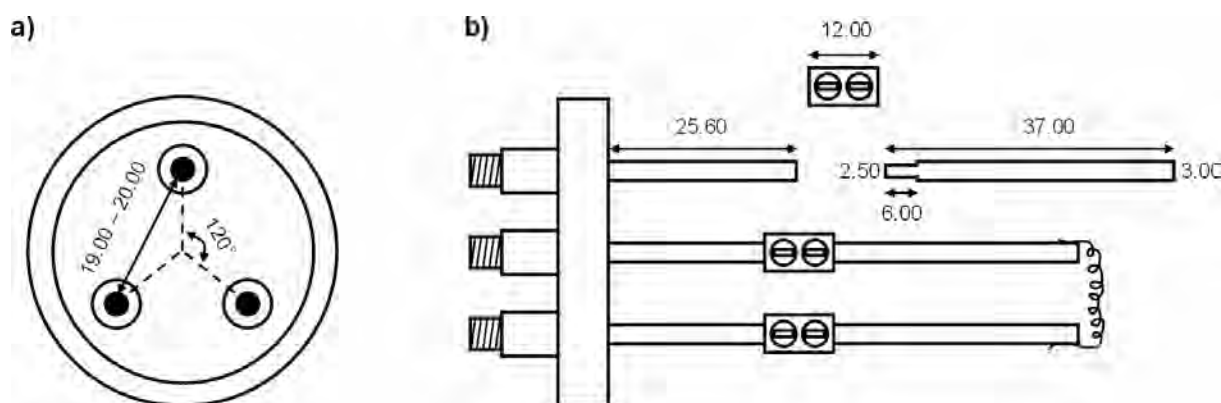


Fig. 9.1: Drawings of the filament setup, from a) top view and b) side view.

9.1.2 Characteristics of the different sample holder setups

The system utilizes a set of different sample holders. Their most important characteristics are the heating and cooling capabilities in the preparation and analysis chamber. But also the geometry of the mounted specimen plays an important role for the choice of the specific sample holder, since it influences the results of the AES measurements (strong influence on the effectiveness of the octopol correction system).

Table 9.1 summarizes the heating and cooling possibilities of the different sample holder setups. The given temperature values were mostly taken from the manuals of the system. Two values were determined via a pyrometer (Impac Elektronik / *IP 120*) through a quartz window. Since this measurement technique is rather imprecise (e.g., influence of the quartz window on the light radiation of the hot sample, pyrometer position not perpendicular to the specimen surface), an error value of roughly 50 K can be assumed for the given temperatures. Additionally listed is the compatibility of the sample position towards an octopol correction table that was generated with a sample mounted below a standard sample plate (e.g., Au covered mica sample) or in a VT sample holder.

		Heating in Prep. Chamber	Cooling in Prep. Chamber	Heating in Ana. Chamber	Cooling in Ana. Chamber	AES: Octopol Compatibility
Standard Sample Plate	Without Window	~ 1230 K ^{1,2} (Electr. Bomb.)	~ 160 K ³ (Liqu. N ₂)	N/A	N/A	No
	With Window / Mounted Top	~ 1250 K ⁴ (Electr. Bomb.)	~ 160 K ³ (Liqu. N ₂)	N/A	N/A	No
	With Window / Mounted Below	N/A	N/A	N/A	N/A	Yes
Variable Temperature (VT) Sample Plate	Direct Current Heating	> 1500 K ⁵	~ 160 K ³ (Liqu. N ₂)	~ 1000 K ⁶	70 K ⁶ (Liqu. He)	Yes
	PBN Heater	~ 1080 K ⁶	~ 160 K ³ (Liqu. N ₂)	~ 650 K ⁶	70 K ⁶ (Liqu. He)	Yes
	Integrated Filament	> 1500 K ⁷	~ 160 K ³ (Liqu. N ₂)	U/V	70 K ⁶ (Liqu. He)	Yes
	Special Cooling Setup	U/V	~ 160 K ³ (Liqu. N ₂)	N/A	70 K ⁶ (Liqu. He)	Yes

Table 9.1: Maximum heating and cooling temperatures of samples mounted on different sample holders and octopol compatibility of the setups, so far known. ¹⁾ Temperature of sample plate without specimen. ²⁾ Value taken from reference [107]. ³⁾ Value taken from reference [107], as measured for a PBN sample holder. ⁴⁾ Value measured via pyrometer on a Rh(110) sample. ⁵⁾ Value measured via pyrometer on a Si(100) sample. ⁶⁾ Value taken from reference [108]. ⁷⁾ Value measured via a thermocouple attached to a Rh(110) sample. N/A means that the corresponding process is not available with this type of sample holder. U/V means that the corresponding value has not been determined yet.

9.1.3 Scheme of the preparation chamber with port designation

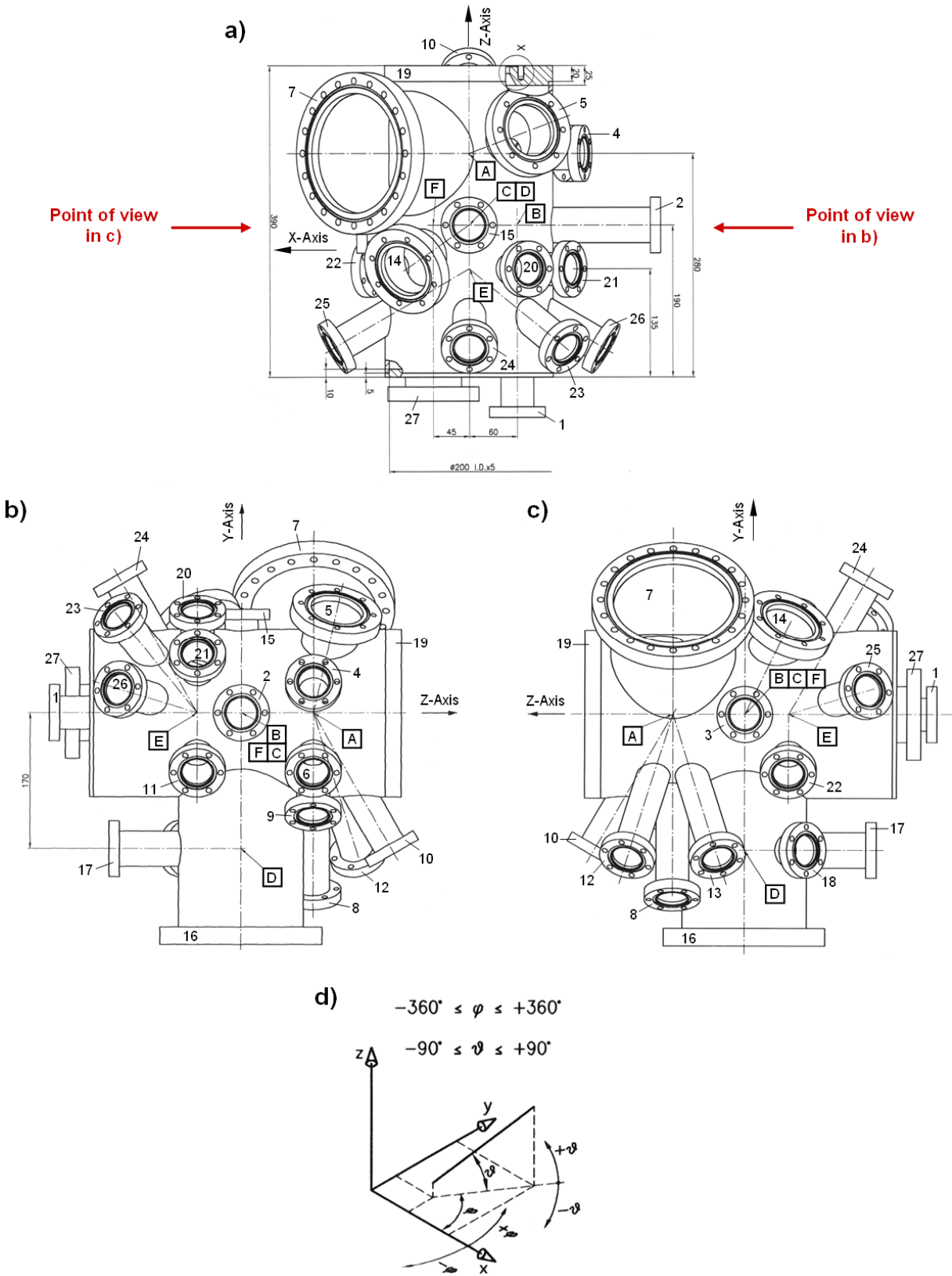


Fig. 9.2: Drawings of the preparation chamber from a) top view and b), c) two side views. Focal points are denoted by a letter in a square. d) Coordinate system for the drawings.

Port	Use	Focal Point	Flange Type	Distance Flange – Focal Point	$\varphi \pm 0.5^\circ$	$\theta \pm 0.5^\circ$
1	FEL chamber	B	CF40 (R)	240	—	- 90
2	Ana. Chamb.	C	CF40	240	180	0
3	Probe Transf.	C	CF40	140	0	0
4	Flood Gun	A	CF40	150	165	0
5	Viewport	A	CF63	155	121	11
6	Blank	A	CF40	150	210	0
7	LEED	A	CF160	203	45	0
8	Blank	A	CF40 (R)	254	294	0
9	Microbalance	A	CF40 (R)	150	240	0
10	Blank	A	CF40	203	270	30
11	Blank	E	CF40	150	210	0
12	Evaporator	A	CF40 (R)	254	- 47	13
13	Viewport	A	CF40 (R)	254	- 47	- 13
14	Viewport	C	CF63	155	50	- 22
15	Sputter Optics	C	CF40 (R)	130	90	0
16	Pumping	C	CF160	290	270	0
17	Ion Gauge	D	CF40	165	—	- 90
18	Vent Valve	D	CF40	110	0	- 45
19	Manipulator	—	—	—	—	90
20	Blank	E	CF40 (R)	150	120	0
21	Blank	E	CF40 (R)	150	150	0
22	Leak Dosage	E	CF40	150	- 30	0
23	Blank	E	CF40	200	135	- 30
24	QMS	E	CF40	200	90	- 30

25	Blank	E	CF40	200	10	- 30
26	Blank	E	CF40	200	170	- 30
27	Viewport	F	CF63	220	—	- 90

Table 9.2: Legend for the ports marked in Fig. 9.2. (R) in the column “Flange Type” represents a rotatable flange. For a definition of the given angles see Fig. 9.2 (d).

Fig. 9.2 shows drawings of the preparation chamber from different point of views. The assignment of the ports together with the corresponding focal points, flange types and mounting geometries at the chamber are listed in Table 9.2. The two angles φ and ϑ in Table 9.2 are related to the coordinate system in Fig. 9.2 (d).

9.1.4 Modification of the preparation chamber manipulator

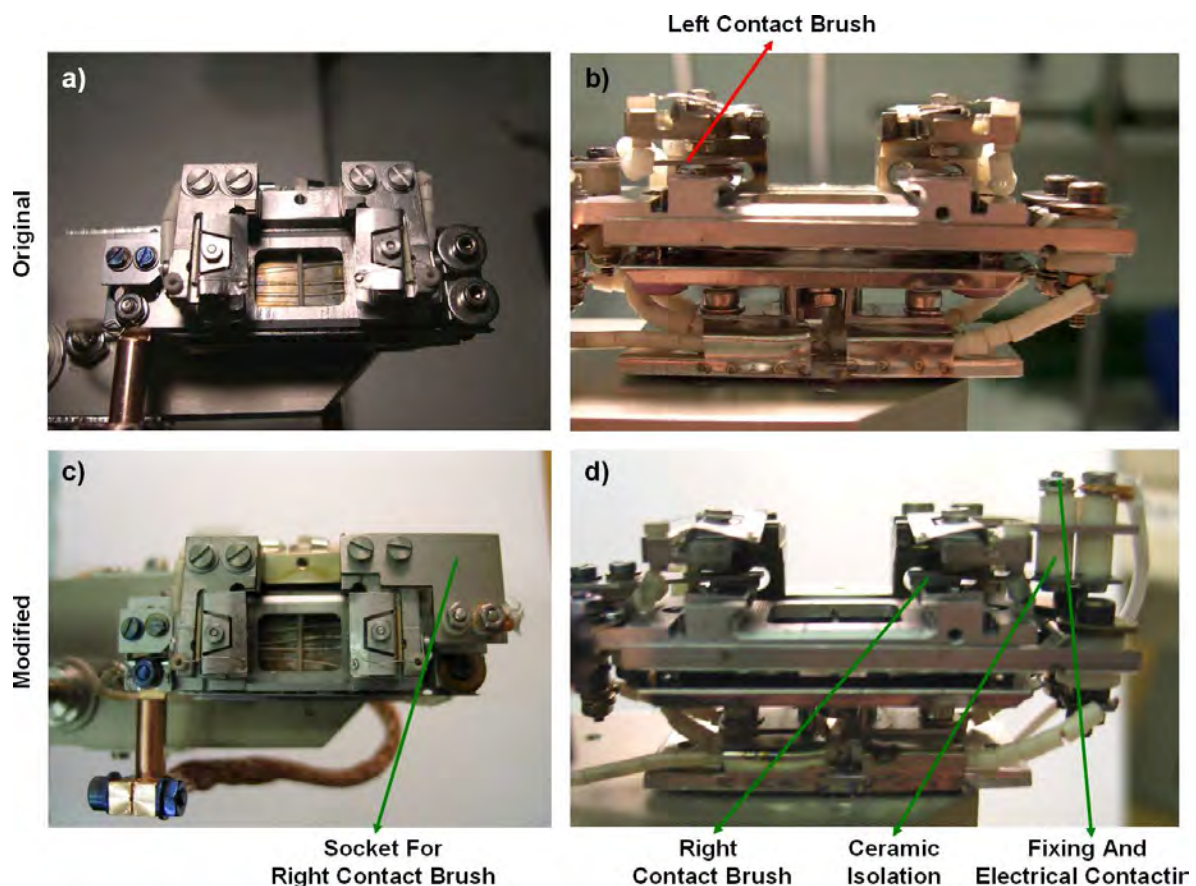


Fig. 9.3: Pictures of the manipulator head of the preparation chamber in its original design from a) top view and b) side view and of the modified setup from c) top view and b) side view.

M2 screws were used to fix the contact brush to the socket by two drill holes (see Fig. 9.3 (d)). Electric insulation from the rest of the manipulator and adjustment of the position of the brush was realized via four ceramic tubes.

The electrical contact to the outside of the chamber is performed via a vacuum feedthrough, originally used to ground the sample stage. The corresponding wire was extended by a copper cable that was insulated from the manipulator head by a glass fiber tubing and connected to one of the M2 screws of the contact brush, as illustrated in Fig. 9.3 (d). Grounding of the sample stage is now realized within the system by a wire attached to the body of the manipulator.

9.1.5 Scheme of the analysis chamber with port designation

Fig. 9.5 shows drawings of the analysis chamber from different point of views. The assignment of the ports together with the corresponding focal points, flange types and mounting geometries at the chamber are listed in Table 9.3. The two angles φ and ϑ in Table 9.3 are related to the coordinate system in Fig. 9.5 (d).

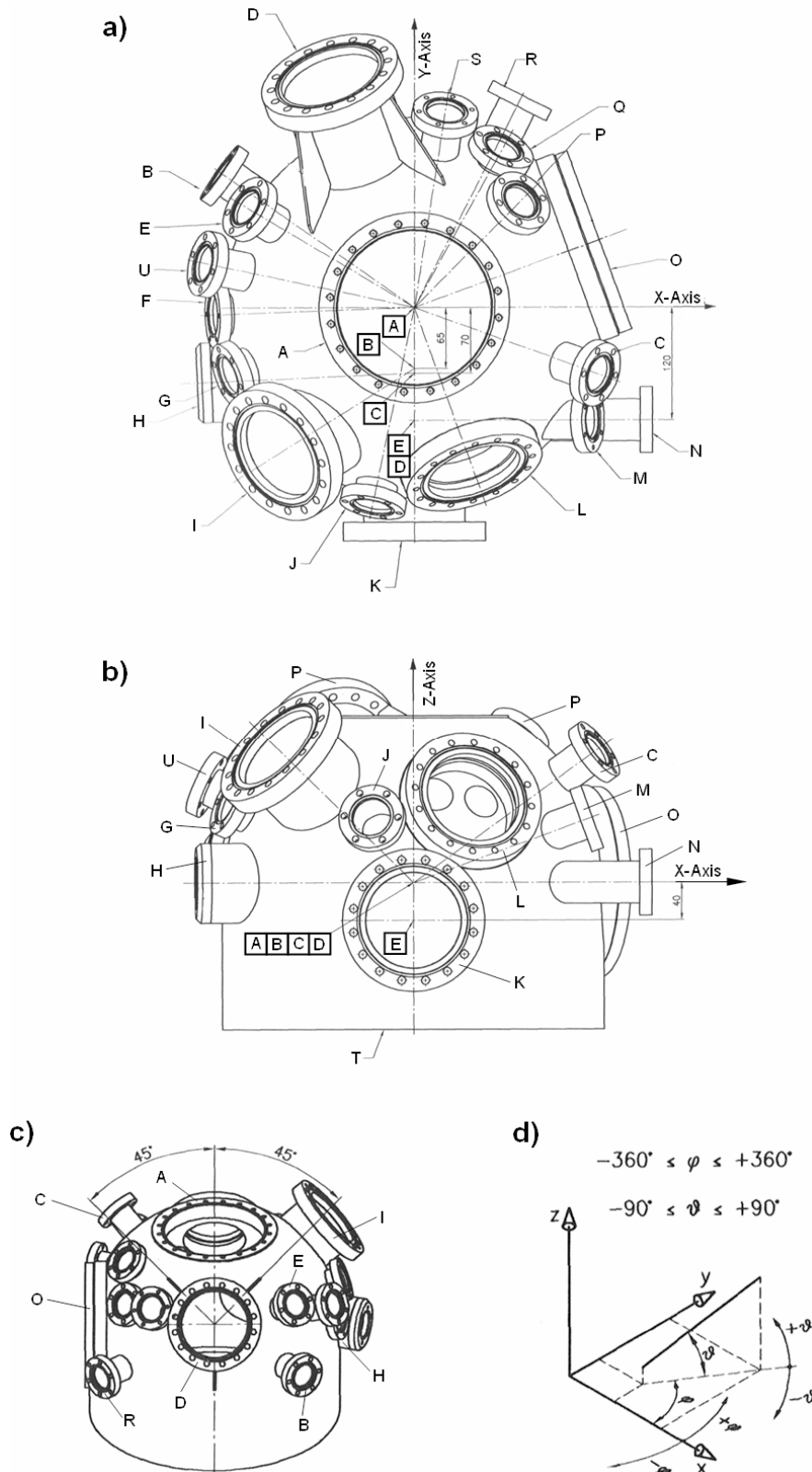


Fig. 9.5: Drawings of the analysis chamber from a) top view, b) side view and c) perspective view. Focal points are denoted by a letter in a square. d) Coordinate system for the drawings.

Port	Use	Focal Point	Flange Type	Distance Flange – Focal Point	$\varphi \pm 0.5^\circ$	$\vartheta \pm 0.5^\circ$
A	SEM	A	—	—	0	90
B	Ex. SED	A	CF40 (R)	254	145	5
C	Viewport	A	CF40 (R)	254	340	34
D	Ener. Anal.	A	—	305	110	30
E	Blank	A	CF40 (R)	247	149	32
F	Blank	A	CF40 (R)	220.5	182	13
G	Viewport	A	CF 40	228	200	22
H	Wobblestick	C	—	231	182.5	0
I	Viewport	B	CF100	226	212	40
J	Viewport	A	CF40	228	258	18
K	Carousel	E	CF100	128	270	0
L	Gas Doser	A	CF100	208	290	26
M	Viewport	D	CF40	203	0	20
N	Prep. Chamb.	D	CF40	254	0	0
O	STM	A	—	210	20	0
P	Bypass Pump.	A	CF40	228	45	45
Q	Viewport	A	CF40	226	61	30
R	Blank	A	CF40 (R)	254	63	0
S	Bypass Pump.	A	CF40 (R)	254	81	33
T	Pumping	A	—	—	0	-90
U	QMS	A	CF40 (R)	254	168	25

Table 9.3: Legend for the ports marked in Fig. 9.5. (R) in the column “Flange Type” stands for a rotatable flange. For a definition of the given angles see Fig. 9.5 (d).

9.1.6 Gas doser design

Fig. 9.6 shows schematic drawings of the dosing nozzle and the adapter flange, attached to the analysis chamber. For the nozzle design two tubes with an outer diameter of 4.0 mm and 0.5 mm thick walls were integrated into a CF 40 flange. Additionally, a 5 mm thick stainless steel rod (“Support” in Fig. 9.6 (a)) was attached for the mechanical stabilization of the tubes.

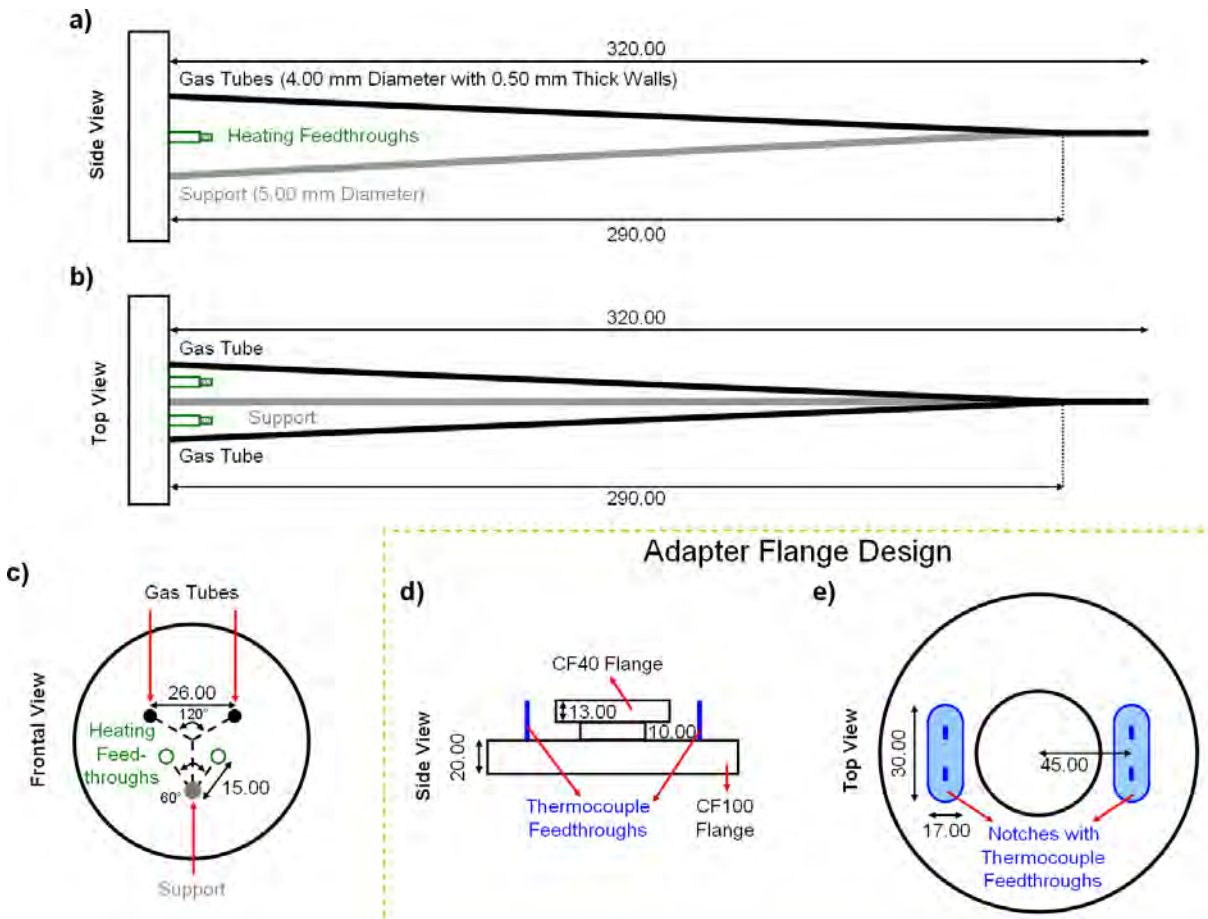


Fig. 9.6: Schematic drawings of the dosing nozzle from a a) side view, b) top view, c) frontal view and of the adapter flange from a d) side view, e) top view. All the values are given in mm.

All three parts were fixed at an angle of 120° with respect to the middle of the flange and the respective other two components (see Fig. 9.6 (c)). They were mounted in a way that they are connecting at a position perpendicular from the center of the flange at a distance of 290 mm (see Fig. 9.6 (a)). At that position the two separated tubes are merged into a single tube; this geometry is important for the nozzle exit to reach the specimen position (due to the focal point of the corresponding analysis chamber port). Two electrical feedthroughs were also integrated in the flange. They are connected to a special heating wire wrapped around the

dosing nozzle (Thermocoax). The wire has a resistance of 27.5Ω and can be heated with a maximum heating power of $\sim 100 \text{ W}$.

Drawings of the adapter flange are depicted in Fig. 9.6 (d) and (e). It consists of a CF 40 flange mounted concentric on a blank CF 100 flange with a 10 mm long tube as spacer. Two notches were included on the CF 100 flange. Each of them is surrounding two thermocouple feedthroughs for the contacting of thermocouples attached to the dosing nozzle.

9.1.7 Precursor storage device

A schematic drawing of the bottom part of the precursor storage device is depicted in Fig. 9.7. It consists of a 59.7 mm long cylinder with an outer diameter of 34 mm and 1.5 mm thick walls. Both ends were closed by 3 mm thick steel plates, which results in a cylinder with an inner volume of 40.5 ml. A tube with an outer diameter of 10 mm and 1 mm thick walls was concentrically attached to the top plate and connects the cylinder to a CF16 flange.

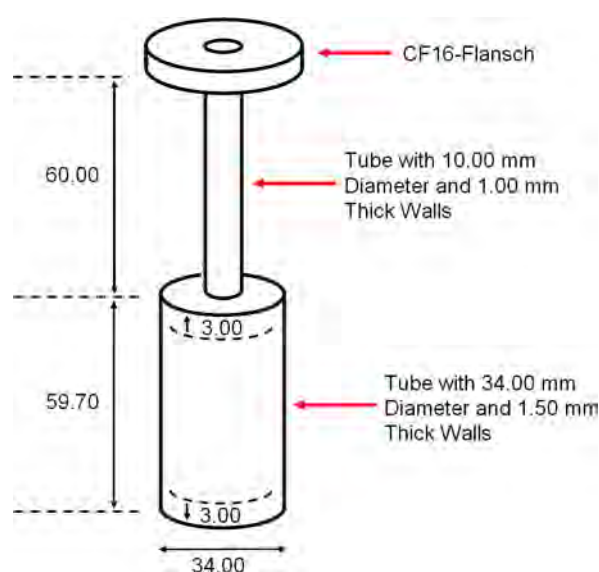


Fig. 9.7: Schematic drawing of the lower part of the precursor storage device. All the values are given in mm.

9.1.8 Images of GPM-chamber

As it was described in Chapter 3.1.4, an additional vacuum chamber was constructed during the final stage of the work at hand. The main purpose of this GPM chamber (**G**as **P**urification and **M**onitoring chamber) is to improve and monitor the composition of the applied precursor compounds. Fig. 9.8 shows drawings of this chamber with descriptions of the most important

parts; the images were generated by Bernd Kress with the program *Autodesk Inventor Professional 2010* (Autodesk, Inc.).

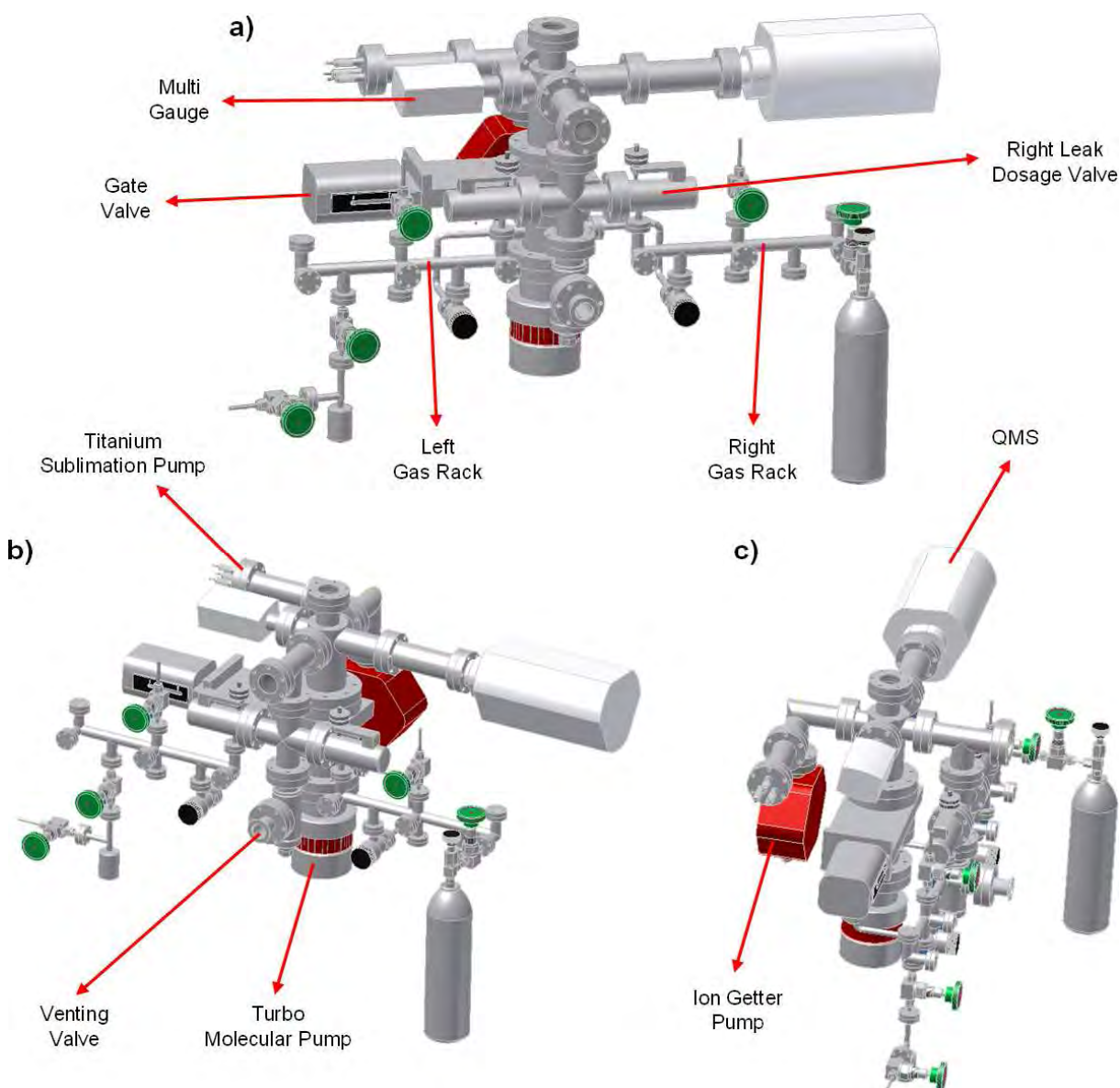


Fig. 9.8: Drawings of the GPM chamber from different points of view. The images were generated by Bernd Kress with the program *Autodesk Inventor Professional 2010*.

9.1.9 Manipulator positions in the preparation chamber

Sample access to the attached instruments in the preparation chamber is performed via a X,Y,Z – Φ, φ manipulator (Omicron NanoTechnology / *RX1515*). A coordination system with respect to the manipulator head is depicted in Fig. 3.5 (a). The manipulator has one rotary drive that allows turning the manipulator 360° around the Z axis (Φ) and another one for the rotation of the manipulator head in the X / Z plane with $\pm 90^\circ$ (φ). In the following, typical

manipulator positions for different applications in the preparation chamber are listed (Table 9.4).

Application	X (mm)	Y (mm)	Z (mm)	Φ (°)	φ (°)
Transport	7.855	12.600	54.50	0.0	12.2
LEED	6.500	10.350	142.00	45.0	12.2
Sputtering	5.000	12.675	55.00	0.0	12.2
Evaporation	19.900	21.000	144.50	138.0	12.2
Pyrometer Measurement	6.840	12.000	20.00	43.0	12.2

Table 9.4: Typical manipulator positions in the preparation chamber for specific applications. Note, that $\varphi = 12.2^\circ$ corresponds to a parallel alignment of the manipulator head with respect to the Z-axis.

9.1.10 Experimental parameters

In the following, typical parameters used for the different analysis techniques and for the low temperature experiments are listed (compare Chapter 3.4). If not mentioned otherwise, these parameters were applied for the work in hand.

Settings for AES measurements via EIS

- **Sweeps:** 1
- **Mag Mode:** High
- **Step Size:** 0.5 eV
- **Dwell time:** 0.2 s
- **Mode CRR:** 5 for energies between 0 – 990 eV; 10 for energies between 1000 – 1987 eV.

To perform an “area scan”, a measurement has to be initiated via *ISEM* and stopped again after the start of *EIS*, in order to load the octopol correction table properly. Afterwards, the measurement area is defined via *SmartSEM* and the scan is directly initiated in *EIS*.

Settings for the acquisition of SAM images via ISEM

- **Image resolution:** 512 x 384
- **Menu “Acquisition Mode”:** Line by Line (measurement of the peak energy counts at each point in a horizontal line, followed by the acquisition of the background energy counts of the same line)
- **Transmission Mode CRR:** 5 for energies between 0 – 990 eV; 10 for energies between 1000 – 1987 eV
- **Mag Mode:** High
- **No Counters:** 7
- **Menu “Data Schema”:** Peak – Background (subtraction of the count value of the background energy from the count value of the peak energy).

Settings for the acquisition of Auger line scans via ISEM

- **Menu “Acquisition Mode”:** Point by Point (one by one measurement of the peak energy counts and background energy counts for all elements at each point)
- **Transmission Mode CRR:** 5 for energies between 0 – 990 eV; 10 for energies between 1000 – 1987 eV
- **Mag Mode:** High
- **No Counters:** 7
- **Menu “Intensity Calculation”:** Peak – Background (subtraction of the count value of the background energy from the count value of the peak energy).

LEED parameters

- **I_{Filament}**: 1.678 A
- **I_{Emission}**: 0.1 – 0.3 mA
- **U_{Wehnelt}**: - 10.4 V
- **U_{Suppressor}**: - 2.5 V for beam
energy = 50.2 eV
- **Lens 1 / 3**: Offset: 14 V
Gain: 1786 V
- **Lens 2**: Offset: 29 V
Gain: 753 V

PID controller settings for experiments at 200 K

- **P**: 300
- **I**: 39.5
- **D**: 0
- **MHP (Manual Heater Power)**: 40 %
- **Heater Range**: Medium
- **T(Set)**: 127.0 K

The PID controller regulated the temperature at the heater position (measured via a silicon diode; denoted as T_A in the controller display; error of ± 1 % of temperature above 100 K) with respect to a given set-point temperature $T(\text{Set})$. The corresponding sample temperature was estimated from the temperature measured via a PT 100 resistor (error of ± 5 K; denoted as T_B in the controller display; ~ 181.0 K at $T(\text{Set}) = 127.0$ K), situated at the cryo spring coupling of the sample stage (compare Fig. 3.10 (b)); according to reference [108] an offset temperature of 22 K has to be taken into account to determine the absolute sample temperature. The relation between the set-point temperature and the temperature measured at the PT 100 resistor was determined via previously performed calibration measurements.

9.1.11 Reference values for carbon and oxygen contaminations

As described in Chapter 3.4, for the determination of the composition of the generated deposits two reference values for carbon and oxygen were self-determined.

For carbon the reference value was acquired from a spectrum of a thick carbon layer on a SiO_x (300 nm) / Si support. The raw data file of the corresponding spectrum is “081014_14_AES_Black_Specks.aes” (region 13 and 14); note, that the substrate signals

were in this case completely damped due to the overlaying carbon. The carbon peak intensity (area) determined from this spectrum was 196,740.

In the case of oxygen, a reference value was estimated from the damping of the Fe Auger signal in the iron oxidation experiment presented in Chapter 5.9. Thereby, a reference value for the oxygen intensity of 109,964 could be calculated.

9.2 Appendix to Chapter 5

9.2.1 Auger line scans on Sample III and Sample III-Ti

The elemental distribution of Sample III (clean and well ordered) and Sample III-Ti (clean and titanium precovered) of the rhodium surface after $\text{Fe}(\text{CO})_5$ dosage is confirmed via Auger line scans (Fig. 9.9). Fig. 9.9 (a) shows an SEM image of a non irradiated area after the dosing process; again the titanium covered area appears bright compared to the formerly free rhodium surface, which is now covered with iron (e.g., top left region).

Auger line scans for the elements Fe, O, Ti and Rh were acquired along the path marked in Fig. 9.9 (a), starting on a clean rhodium area and scanning into a titanium covered region. The corresponding iron (green spectrum in Fig. 9.9 (b)) and oxygen (brown) spectra decrease significantly upon reaching the titanium covered area, while the situation is reverse for the titanium (blue) and rhodium (violet) spectra. For the oxygen and titanium spectra the change in signal intensity is smaller compared to the one of the other two elements; this effect represents differences in the coverage of the respective elements, which is also confirmed via local Auger spectra depicted in Chapter 5.6. Close to the transition between the two regions (clean and titanium covered area) the iron and rhodium spectra display significant local variations in the signal intensities. This is mainly attributed to an increased roughness and local differences of the iron coverage in this area, resulting in a higher noise of the measured spectra. Indications for the change of the iron layer morphology are also visible in the SEM image in Fig. 9.9 (a); the respective region of the clean rhodium surface close to the titanium covered area shows pronounced hollows in the iron layer, leading even to the observation of separated iron particles at certain positions.

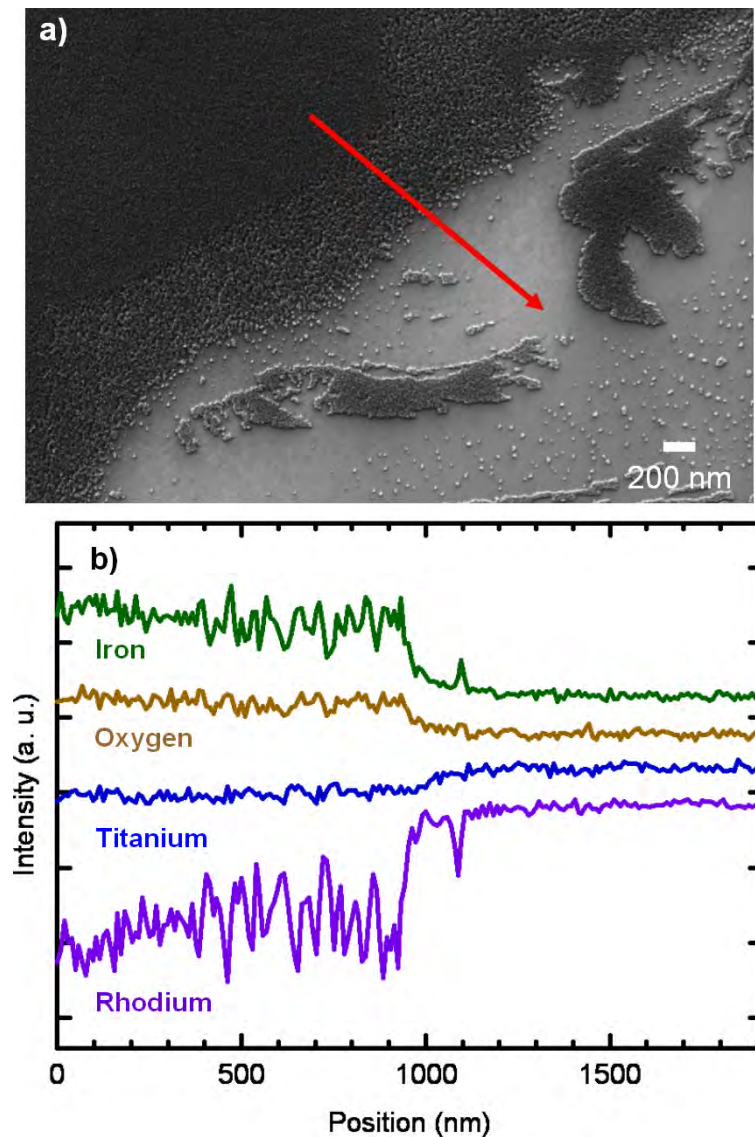


Fig. 9.9: Auger line scans acquired across the transition between a clean and titanium covered region on rhodium after $\text{Fe}(\text{CO})_5$ dosage. a) SEM image of the corresponding region. The red arrow marks the position where the line scans were acquired. ($U = 15 \text{ kV}$; $I = 3 \text{ nA}$; tilted sample) b) Auger line scans of the elements iron (green; $E_{\text{Peak}} = 702.5 \text{ eV}$; $E_{\text{Bkg}} = 739.5 \text{ eV}$), oxygen (brown; $E_{\text{Peak}} = 514.5 \text{ eV}$; $E_{\text{Bkg}} = 529.0 \text{ eV}$), titanium (blue; $E_{\text{Peak}} = 418.0 \text{ eV}$; $E_{\text{Bkg}} = 442.0 \text{ eV}$) and rhodium (purple; $E_{\text{Peak}} = 301.0 \text{ eV}$; $E_{\text{Bkg}} = 328.0 \text{ eV}$). All spectra were acquired with 200 points and a dwell time of 0.5 s.

9.3 List of applied data

- Fig. 2.7 060119_SAM_Titan.Titan.SAM.bmp
060119_15kV_3nA_SAM_TiOxNT16.tif
- Fig. 2.13 091007_01_Si_15kV_beam_diameter_3nm_#electron200000_#displ500.cas
091007_03_Si_8kV_beam_diameter_3p6nm_#electron200000_#displ500.cas
100126_01_Rh_15kV_beam_diameter_3nm_#electron200000_#displ500.cas
100126_02_Rh_8kV_beam_diameter_3p8nm_#electron200000_#displ500.cas
- Fig. 3.21 060323_LEED_Si(100)_49.7eV_RT.jpg
060316_LEED_Si(111)_34p1eV.jpg
- Fig. 4.4 051108_Lithogr_Test_PMMA01.tif
051108_Lithogr_Test_PMMA12.tif
051108_Lithogr_Test_PMMA02.tif
051108_Lithogr_Test_PMMA05.tif
- Fig. 4.6 060804_Si111_Feld2802.tif
060825_Si111_Feld23_01.tif
- Fig. 4.7 051122_15kV_400pA_Si_EBID_RA03.tif
051122_15kV_400pA_Si_EBID_RA05.tif
- Fig. 4.8 091007_01_Si_15kV_beam_diameter_3nm_#electron200000_#displ500.cas
091007_02_Si_3kV_beam_diameter_4p9nm_#electron200000_#displ500.cas
- Fig. 4.9 060825_Si111_Feld16_01.tif
060825_Si111_Feld21_01.tif
060825_Si111_Feld22_01.tif
060825_Si111_Feld23_01.tif
060825_Si111_Feld24_01.tif
- Fig. 5.4 060412_Rh(110)_vorReinigung03.tif
060418_LEED_Rh(110)_80_4eV_1.jpg
- Fig. 5.5 060413_MPS_Rh(110)_vorReinigung Fokussiert.aes
060516_Rh110_reineOberflaeche Point 1.aes
060911_MPS_Rh110_Stelle1 Stelle_1.aes
061206_MPS1_Freie Flaeche Free Area.aes
- Fig. 5.6 060518_Rh110_EBID_vorher14.tif
060516_Rh110_O2Dosierung_no40.tif
060912_Rh110_15kV_400pA_EBID02.tif
060906_Rh100_nSputtern01.tif
061207_15kV_400pA_Rh110_03.tif
061206_15kV_3nA_Rh110_02.tif
- Fig. 5.7 061107_Rh110_74p1.jpg
061107_Rh110_72p0_6x8_02.jpg
061107_Rh110_72p0_1x7_2.jpg
- Fig. 5.8 060515_Rh(110)_einigeZyklen06.tif
060515_Rh(110)_einigeZyklen07.tif
060515_Rh(110)_einigeZyklen10.tif
- Fig. 5.9 060516_Rh110_O2Dosierung_no02.tif
060516_Rh110_O2Dosierung_no04.tif
060516_Rh110_O2Dosierung_no08.tif
- Fig. 5.10 060516_Rh110_O2Dosierung_no18.tif
060516_Rh110_O2Dosierung_no24.tif
060516_Rh110_O2Dosierung_no25.tif

	060516_Rh110_O2Dosierung_no28.tif
	060516_Rh110_O2Dosierung_no30.tif
	060516_Rh110_O2Dosierung_no32.tif
	060516_Rh110_O2Dosierung_no36.tif
	060516_Rh110_O2Dosierung_no38.tif
Fig. 5.12	060515_Rh(110)_einigeZyklen35.tif
	060515_Rh(110)_einigeZyklen37.tif
	060515_Rh(110)_einigeZyklen44.tif
Fig. 5.13	060523_Rh110_FeldC01.tif
	060523_Rh110_ZusatzfeldC01.tif
	060523_Rh110_FeldC02.tif
	060524_Rh110_ZusatzfeldC02.tif
Fig. 5.14	060519_Rh110_MPS_FeldC_2 Schreibungfeld.aes
	060523_Rh110_MPS_FeldC_2 Schreibungfeld.aes
	060524_Rh110_MPS_ZusatzfeldC_2 Schreibungfeld.aes
Fig. 5.15	060524_Rh110_ZusatzfeldA01.tif
	060519_Rh110_FeldE02.tif
	060919_Rh110_15kV_3nA_FeldP_06.tif
	060919_Rh110_15kV_3nA_FeldU_03.tif
	061208_FeldT_11.tif
Fig. 5.16	060516_Rh110_reineOberflaeche Point 1.aes
	060519_Rh110_MPS_ZusatzfeldA_1 Schreibungfeld.aes
	060519_Rh110_MPS_ZusatzfeldA_2 Oberflaeche.aes
	060911_MPS_Rh110_Stelle1 Stelle_1.aes
	060918_MPS1_Rh110_FeldP_DarkCentre Dark_Centre.aes
	060918_MPS3_Rh110_FeldP_OutArea Out_Area.aes
	061206_MPS1_Freie Flaeche Free Area.aes
	061208_MPS_FeldT_Square20 Square_dose_20.aes
	061208_MPS_FeldT_surface Surface.aes
Fig. 5.17	061128_15kV_3nA_Rh110_02.tif
	061128_15kV_3nA_Rh110_27.tif
	061128_15kV_3nA_Rh110_28.tif
	061128_MPS_Stelle4 Bright Area.aes
	061128_MPS_Stelle3 Dark Area.aes
	061128_Oxidiert_dunkel_manuell.aes
Fig. 5.18	061130_15kV_400pA_Rh110_09.tif
	061201_15kV_3nA_Rh110_02.tif
	061201_MPS_Bereich1_Feld1_S3 Square3.aes
	061201_MPS_Bereich1_Feld1_Umgebung1 Surrounding1.aes
	061201_MPS_Bereich1_Feld1_Umgebung2 Surrounding2.aes
Fig. 5.19	061201_15kV_3nA_Rh110_06.tif
	061201_MPS_Bereich2_Feld1_S4 Square4.aes
	061201_MPS_Bereich2_Feld1_Umgebung Surrounding.aes
Fig. 5.20	061211_Rh110_Dreck_15.tif
	061211_SAM_Eisen.Eisen.SAM.bmp
	061211_SAM_Titan.Titan.SAM.bmp
Fig. 5.22	060918_Rh110_15kV_3nA_FeldT_01.tif
	060918_Rh110_15kV_3nA_FeldP_05.tif
	060918_Rh110_15kV_3nA_FeldS_06.tif
Fig. 5.24	060918_MPS4_Rh110_FeldS_DarkCentre Dark_Centre.aes

- 060918_MPS5_Rh110_FeldS_FeCluster Iron_Cluster.aes
060918_MPS1_Rh110_FeldP_DarkCentre Dark_Centre.aes
060918_MPS2_Rh110_FeldP_FeCluster Iron_Cluster.aes
060918_MPS7_Rh110_FeldT_DarkCentre Dark_Centre.aes
060918_MPS8_Rh110_FeldT_FeCluster Iron_Cluster.aes
- Fig. 5.25 060601_Rh110_FeldF02.tif
060601_Rh110_FeldF09.tif
060601_Rh110_FeldF15.tif
060601_Rh110_FeldF22.tif
060601_Rh110_FeldF23.tif
- Fig. 5.26 060523_Rh110_ZusatzfeldC01.tif
060601_Rh110_ZusatzfeldC01.tif
060519_Rh110_MPS_ZusatzfeldC_1 Schreibfeld.aes
060519_Rh110_MPS_ZusatzfeldC_2 Oberflaeche.aes
060601_Rh110_MPS_ZusatzfeldC_6 weisser Punkt.aes
060601_Rh110_MPS_ZusatzfeldC_7 dunkler Punkt.aes
060601_Rh110_MPS_ZusatzfeldC_5 Oberflaeche.aes
- Fig. 5.27 060919_Rh110_15kV_3nA_FeldP_07.tif
060920_Rh110_15kV_3nA_FeldP_02.tif
060920_Rh110_15kV_3nA_FeldP_05.tif
060919_MPS_FeldP_Innen Kreis_Mitte.aes
060919_MPS_FeldP_Oberflaeche Oberflaeche.aes
060920_MPS_FeldP_Innen Kreis_Mitte.aes
060920_MPS_FeldP_Oberflaeche Oberflaeche.aes
060920_MPS_FeldP_Innen_2 Kreis_Innen.aes
060920_MPS_FeldP_Oberflaeche_2 Oberflaeche.aes
- Fig. 6.3 default_2005Jun29-092246_Standard-STM_Basic_0001.mtrx
- Fig. 6.5 060303_15kV_400pA_Si_EBID_Sc01.tif
060303_8kV_400pA_Si_EBID_Sc03.tif
- Fig. 6.6 091007_01_Si_15kV_beam_diameter_3nm_#electron200000_#displ500.cas
091007_03_Si_8kV_beam_diameter_3p6nm_#electron200000_#displ500.cas
- Fig. 6.7 060612_Si100_FeldB02.tif
060612_Si100_FeldB03.tif
060612_Si100_FeldB04.tif
070212_Si100_FeldC_a_C_C_02.tif
060612_Si100_FeldG02.tif
- Fig. 6.8 060714_Si100_FeldA01.tif
060714_Si100_FeldD01.tif
- Fig. 6.9 060714_MPS_Si100_Fe_FeldD_Oberflaeche Oberflaeche.aes
060714_MPS_Si100_Fe_FeldD_Rechteck Rechteck.aes
060714_MPS_Si100_Fe_FeldA_Rechteck2 Rechteck_Dosis_3.aes
060714_MPS_Si100_Fe_FeldA_Rechteck_Dosis2_manuell.aes
- Fig. 6.11 070208_qms_waehrend_dosierung_0-50_nach_spuelen_30min.sac
070207_qms_waehrend_dosierung_0-50.sac
- Fig. 6.12 070205_Si100_FeldS_a_C_A_06.tif
070205_Si100_FeldS_a_C_C_03.tif
070209_15kV_3nA_Si100_SACA_01.tif
070209_15kV_3nA_Si100_SACC_01.tif
- Fig. 6.13 070205_MPS_FeldS_a_C_C Square_Dosis_30.aes
070209_MPS6_SACC_Square30 Square30.aes

- Fig. 6.14 070219_Si100_FeldD_K_02.tif
070216_Si100_FeldC_C_A_01.tif
070216_Si100_FeldC_C_B_01.tif
070216_Si100_FeldS_a_C_B_01.tif
070216_Si100_Feldin_situ_05.tif
- Fig. 6.15 070216_MPS_FeldS_a_C_B Square_Dosis_20.aes
070216_MPS_Feldin_situ In_Situ.aes
070216_MPS_Feldin_situ_surface Surface.aes
- Fig. 6.16 060726_Si111_FeldO01.tif
060726_Si111_FeldO03.tif
070223_Si111_FeldS_a_C_A_02.tif
060726_Si111_FeldV02.tif
- Fig. 6.17 060810_Si111_FeldE03.tif
default_2006Jul27-103614_STM-STM_Spectroscopy--15_1_Z.mtrx
- Fig. 6.18 060613_Si100_FeldA02.tif
060613_Si100_FeldB02.tif
060613_Si100_FeldC02.tif
- Fig. 6.20 060713_Si100_FeldH04.tif
- Fig. 6.22 060613_Si100_FeldG02.tif
060704_Si100_FeldG23.tif
060704_Si100_FeldG24.tif
060704_Si100_FeldG30.tif
060622_Si100_FeldI01.tif
060704_Si100_FeldI01.tif
- Fig. 6.23 060623_SAM_Si100_Eisen_FeldG.Eisen.SAM.bmp
060623_SAM_Si100_Sauerstoff_FeldG.Sauerstoff.SAM.bmp
060623_SAM_Si100_Silizium_FeldG.Silizium.SAM.bmp
060623_SAM_Si100_unb_Signal_FeldG.unb_Peak.SAM.bmp
060705_SAM_Si100_Fe_FeldG_Eisen.Eisen.SAM.bmp
060705_SAM_Si100_Fe_FeldG_Sauerstoff.Sauerstoff.SAM.bmp
060706_SAM_Si100_Fe_FeldG_Silizium.Silizium.SAM.bmp
060705_SAM_Si100_Fe_FeldG_unb_Signal.unb_Signal.SAM.bmp
- Fig. 6.25 070216_Si100_FeldS_a_C_A_01.tif
070216_Si100_FeldS_a_C_B_01.tif
070621_CNT_FeldSaC_A_01.tif
070621_CNT_FeldSaC_B_01.tif
070621_CNT_FeldSaC_A_02.tif
070621_CNT_FeldSaC_B_02.tif
070621_CNT_FeldSaC_A_04.tif
- Fig. 6.26 070219_Si100_FeldD_O_01.tif
070620_CNT_FeldD_O_01.tif
070620_CNT_FeldD_O_04.tif
- Fig. 6.27 070620_Si100_CNT_04.tif
070620_Si100_CNT_05.tif
070620_Si100_CNT_07.tif
070705_Si100_CNT_04.tif
070706_Si100_CNT_01.tif
070906_Si100_CNT_Katja_II_15.tif
- Fig. 9.9 061214_LS_Rh110_Rand_Titan.sid

References

- [1] G. E. Moore, *Electronics* **38**, 114 (1965).
- [2] R. P. Feynman, *Eng. Sci.* **23**, 22 (1960).
- [3] N. Taniguchi, *Proc. Intl. Conf. Prod. Eng. Tokyo, Part II, Japan Society of Precision Engineering* (1974).
- [4] B. Bhushan, *Introduction to Nanotechnology in Handbook of Nanotechnology* (Springer, Berlin, 2004).
- [5] A. L. Rogach, N. Gaponik, J. M. Lupton, C. Bertoni, D. E. Gallardo, S. Dunn, N. L. Pira, M. Paderi, P. Repetto, S. G. Romanov, C. O'Dwyer, C. M. S. Torres and A. Eychmuller, *Angew. Chem.-Int. Edit.* **47**, 6538 (2008).
- [6] F. Buchner, K. Comanici, N. Jux, H. P. Steinrück and H. Marbach, *J. Phys. Chem. C* **111**, 13531 (2007).
- [7] A. E. Ennos, *Brit. J. Appl. Phys.* **4**, 101 (1953).
- [8] A. G. Baker and W. C. Morris, *Rev. Sci. Instr.* **32**, 458 (1961).
- [9] M. Takeguchi, M. Shimojo, K. Mitsubishi, M. Tanaka, R. Che and K. Furuya, *J. Mater. Sci.* **41**, 4532 (2006).
- [10] M. Shimojo, M. Takeguchi and K. Furuya, *Nanotechnology* **17**, 3637 (2006).
- [11] H. W. P. Koops, R. Weiel, D. P. Kern and T. H. Baum, *J. Vac. Sci. Technol., B* **6**, 477 (1988).
- [12] W. F. van Dorp, B. van Someren, C. W. Hagen and P. Kruit, *Nano Lett.* **5**, 1303 (2005).
- [13] P. C. Hoyle, M. Ogasawara, J. R. A. Cleaver and H. Ahmed, *Appl. Phys. Lett.* **62**, 3043 (1993).
- [14] M. Shimojo, K. Mitsubishi, A. Tameike and K. Furuya, *J. Vac. Sci. Technol., B* **22**, 742 (2004).
- [15] S. Matsui and K. Mori, *J. Vac. Sci. Technol., B* **4**, 299 (1986).
- [16] Y. M. Lau, P. C. Chee, J. T. L. Thong and V. Ng, *J. Vac. Sci. Technol., A* **20**, 1295 (2002).
- [17] M. Weber, H. W. P. Koops, M. Rudolph, J. Kretz and G. Schmidt, *J. Vac. Sci. Technol., B* **13**, 1364 (1995).
- [18] H. W. P. Koops, C. Schössler, A. Kaya and M. Weber, *J. Vac. Sci. Technol., B* **14**, 4105 (1996).
- [19] H. W. P. Koops, J. Kretz, M. Rudolph and M. Weber, *J. Vac. Sci. Technol., B* **11**, 2386 (1993).
- [20] I. Utke, P. Hoffmann, B. Dwir, K. Leifer, E. Kapon and P. Doppelt, *J. Vac. Sci. Technol., B* **18**, 3168 (2000).
- [21] A. Botman, J. J. L. Mulders and C. W. Hagen, *Nanotechnology* **20**, 1 (2009).
- [22] I. Utke, P. Hoffmann, R. Berger and L. Scandella, *Appl. Phys. Lett.* **80**, 4792 (2002).
- [23] H. W. P. Koops, C. Schössler, A. Kaya and M. Weber, *J. Vac. Sci. Technol., B* **14**, 4105 (1996).

- [24] F. Cicoira, P. Hoffmann, C. O. A. Olsson, N. Xanthopoulos, H. J. Mathieu and P. Doppelt, *Appl. Surf. Sci.* **242**, 107 (2005).
- [25] A. Perentes, G. Sinicco, G. Boero, B. Dwir and P. Hoffmann, *J. Vac. Sci. Technol., B* **25**, 2228 (2007).
- [26] T. Bret, I. Utke, A. Bachmann and P. Hoffmann, *Appl. Phys. Lett.* **83**, 4005 (2003).
- [27] O. Yavas, C. Ochiai, M. Takai, A. Hosono and S. Okuda, *Appl. Phys. Lett.* **76**, 3319 (2000).
- [28] I. Utke, B. Dwir, K. Leifer, F. Cicoira, P. Doppelt, P. Hoffman and E. Kapon, *Appl. Phys. Lett.* **53**, 261 (2000).
- [29] K. L. Lee and M. Hatzakis, *J. Vac. Sci. Technol., B* **7**, 1941 (1989).
- [30] Y. Ochiai, J.-i. Fujita and S. Matsui, *J. Vac. Sci. Technol., B* **14**, 3887 (1996).
- [31] A. Perentes, T. Bret, I. Utke, P. Hoffmann and M. Vaupel, *J. Vac. Sci. Technol., B* **24**, 587 (2006).
- [32] W. F. van Dorp and C. W. Hagen, *J. Appl. Phys.* **104**, 081301/1 (2008).
- [33] R. R. Kunz and T. M. Mayer, *J. Vac. Sci. Technol., B* **6**, 1557 (1988).
- [34] R. R. Kunz and T. M. Mayer, *Appl. Phys. Lett.* **50**, 962 (1987).
- [35] W. Zhang, M. Shimojo, M. Takeguchi, R. C. Che and K. Furuya, *Adv. Eng. Mater.* **8**, 711 (2006).
- [36] G. Hochleitner, H. D. Wanzenboeck and E. Bertagnolli, *J. Vac. Sci. Technol., B* **26**, 939 (2008).
- [37] M. Shimojo, M. Takeguchi, M. Tanaka, K. Mitsuishi and K. Furuya, *Appl. Phys. A-Mater. Sci. Process.* **79**, 1869 (2004).
- [38] G. Boero, I. Utke, T. Bret, N. Quack, M. Todorova, S. Mouaziz, P. Kejik, J. Brugger, R. S. Popovic and P. Hoffmann, *Appl. Phys. Lett.* **86**, (2005).
- [39] R. R. Kunz, T. E. Allen and T. M. Mayer, *J. Vac. Sci. Technol., B* **5**, 1427 (1987).
- [40] I. Utke, P. Hoffman and J. Melngailis, *J. Vac. Sci. Technol., B* **24**, 1197 (2008).
- [41] N. Silvis-Cividjian and C. W. Hagen, *Electron-beam-induced nanometer-scale deposition in Advances in Imaging and Electron Physics, Vol 143* (Elsevier Academic Press Inc., San Diego, 2006).
- [42] S. J. Randolph, J. D. Fowlkes and P. D. Rack, *Crit. Rev. Solid State Mater. Sci.* **31**, 55 (2006).
- [43] M. Knoll, *Z. Tech. Phys.* **16**, 467 (1935).
- [44] M. von Ardenne, *Zeit. Phys.* **109**, 553 (1938).
- [45] M. von Ardenne, *Z. Tech. Phys.* **19**, 407 (1938).
- [46] D. Meschede, *Gerthsen Physik* (Springer, Heidelberg, 2006).
- [47] M. Henzler and W. Göpel, *Oberflächenphysik des Festkörpers* (Teubner, Stuttgart, 1994).
- [48] L. Reimer, *Scanning Electron Microscopy* (Springer-Verlag, Heidelberg, 1998).
- [49] eaps4.iap.tuwien.ac.at/~werner/qes_tut_interact.html in January 2010, Research Group of the Institut für Allgemeine Physik, TU Wien, 2009.

- [50] J. F. Watts and J. Wolstenholme, *An Introduction to Surface Analysis by XPS and AES* (Wiley-VCH, Weinheim, 2003).
- [51] H. Seiler, *J. Appl. Phys.* **54**, R1 (1983).
- [52] G. Wedler, *Lehrbuch der Physikalischen Chemie* (Wiley-VCH, Weinheim, 2004).
- [53] en.wikipedia.org/wiki/Auger_electron_spectroscopy in January 2010, Wikipedia, 2009.
- [54] D. Briggs and M. P. Seah, *Practical Surface Analysis by Auger and X-ray Photoelectron Spectroscopy* (John Wiley & Sons, Chichester, 1983).
- [55] L. C. Feldman, *Fundamentals of surface and thin film analysis* (North-Holland, New York, 1986).
- [56] K. Oura, V. G. Lifshits, A. A. Saranin, A. V. Zotov and M. Katayama, *Surface Science - An Introduction* (Springer-Verlag, Berlin, 2003).
- [57] H.-P. Steinrück, *Physikalische Chemie an Oberflächen*, Lecture (Friedrich-Alexander-Universität Erlangen-Nürnberg, **2004**).
- [58] Physical Electronics, *Handbook of Auger electron spectroscopy* (Eden Prairie (USA), 1995).
- [59] Jeol Ltd., *Handbook of Auger electron spectroscopy* (Tokyo, 1982).
- [60] R. P. Lindner, *Modifikation des Wachstums von Kupfer auf Ni(111) untersucht mit dem Rastertunnelmikroskop*, PhD Thesis (Friedrich-Alexander-Universität Erlangen-Nürnberg, **2004**).
- [61] P. K. Hansma and J. Tersoff, *J. Appl. Phys.* **61**, R1 (1987).
- [62] T. Staudt, *TiO₂ auf Pt(111)-Einkristalloberflächen: Anwendungen von Ceroxid-Zwischenschichten*, Diploma Thesis (Heinrich Heine Universität Düsseldorf, **2007**).
- [63] en.wikipedia.org/wiki/Scanning_tunneling_microscope in January 2010, Wikipedia, 2010.
- [64] www.in-process.com/massenspektrometrie-quadrupol-ms.html?PHPSESSID=01aa0da4ee37ef83b29b407fc0021212 in January 2010, InProcess Instruments, 1999.
- [65] N. Schmidt, *LEED-Untersuchungen an organischen Adsorbatmolekülen auf Metall-Einkristallen*, Diploma Thesis (Friedrich-Alexander-Universität Erlangen-Nürnberg, **2003**).
- [66] H. Adachi, H. Nakane and M. Katamoto, *Appl. Surf. Sci.* **76-77**, 11 (1994).
- [67] S. Kiyohara, H. Takamatsu and K. Mori, *Semicond. Sci. Technol.* **17**, 1096 (2002).
- [68] L. Rotkina, J. F. Lin and J. P. Bird, *Appl. Phys. Lett.* **83**, 4426 (2003).
- [69] W. Li and D. C. Joy, *J. Vac. Sci. Technol., A* **24**, 431 (2006).
- [70] S. Matsui, T. Ichihashi and M. Mito, *J. Vac. Sci. Technol., B* **7**, 1182 (1989).
- [71] S. H. Kim and G. A. Somorjai, *J. Phys. Chem. B* **106**, 1386 (2002).
- [72] T. Bret, I. Utke, C. Gaillard and P. Hoffmann, *J. Vac. Sci. Technol., B* **22**, 2504 (2004).
- [73] F. Cicoira, K. Leifer, P. Hoffmann, I. Utke, B. Dwir, D. Laub, P. A. Buffat, E. Kapon and P. Doppelert, *J. Cryst. Growth* **265**, 619 (2004).

- [74] G. C. Gazzadi and S. Frabboni, *J. Vac. Sci. Technol.*, B **23**, L1 (2005).
- [75] K. L. Lee, D. W. Abraham, F. Secord and L. Landstein, *J. Vac. Sci. Technol.*, B **9**, 3562 (1991).
- [76] Y. Akama, E. Nishimura, A. Sakai and H. Murakami, *J. Vac. Sci. Technol.*, A **8**, 429 (1990).
- [77] P. C. Hoyle, J. R. A. Cleaver and H. Ahmed, *J. Vac. Sci. Technol.*, B **14**, 662 (1996).
- [78] K. Edinger, H. Becht, J. Bihl, V. Boegli, M. Budach, T. Hofmann, H. W. P. Koops, P. Kuschnerus, J. Oster, P. Spies and B. Weyrauch, *J. Vac. Sci. Technol.*, B **2**, 2902 (2004).
- [79] H. W. P. Koops, *Innovation* **16**, 46 (2005).
- [80] T. Liang, E. Frendberg, B. Lieberman and A. Stivers, *J. Vac. Sci. Technol.*, B **23**, 3101 (2005).
- [81] C. Schoessler and H. W. P. Koops, *J. Vac. Sci. Technol.*, B **16**, 862 (1998).
- [82] I. Utke, T. Bret, D. Laub, P. Buffat, L. Scandella and P. Hoffmann, *Microel. Eng.* **73-74**, 553 (2004).
- [83] I. Utke, J. Michler, P. Gasser, C. Santschi, D. Laub, M. Cantoni, P. t. A. Buffat, C. Jiao and P. Hoffmann, *Adv. Eng. Mater.* **7**, 323 (2005).
- [84] W. F. van Dorp, *Sub-10 nm focused electron beam induced deposition*, PhD Thesis (Technische Universitat Delft, **2008**).
- [85] P. Rowntree, *Chemical Processes of Electron Beam Induced Deposition*, Presented at the First International EBID Workshop, Delft, **2006**.
- [86] M. A. Henderson, R. D. Ramsier and J. T. J. Yates, *Surf. Sci.* **259**, 173 (1991).
- [87] N. Silvis-Cividjian, C. W. Hagen, L. H. A. Leunissen and P. Kruit, *Microel. Eng.* **61-62**, 693 (2002).
- [88] J. D. Fowlkes, S. J. Randolph and P. D. Rack, *J. Vac. Sci. Technol.*, B **23**, 2825 (2005).
- [89] K. Mitsuishi, Z. Q. Liu, M. Shimojo, M. Han and K. Furuya, *Ultramicroscopy* **103**, 17 (2005).
- [90] B. C. Ibanescu, O. May, A. Monney and M. Allan, *PCCP* **9**, 3163 (2007).
- [91] S. Massey, P. Cloutier, M. Bazin, L. Sanche and D. Roy, *J. Appl. Polym. Sci.* **108**, 3163 (2008).
- [92] D. Drouin, A. R. Couture, D. Joly, X. Tastet, V. Aimez and R. Gauvin, *Scanning* **29**, 92 (2007).
- [93] T. Bret, *Physico-chemical study of the focused electron beam induced deposition process*, PhD Thesis (EPFL Lausanne, **2005**).
- [94] T. Bret, I. Utke, P. Hoffmann, M. Abourida and P. Doppelt, *Microel. Eng.* **83**, 1482 (2006).
- [95] K. Molhave, D. N. Madsen, S. Dohn and P. Boggild, *Nanotechnology* **15**, 1047 (2004).
- [96] V. V. Aristov, N. A. Kislov and I. I. Khodos, *Microsc. Microanal. Microstruct.* **3**, 313 (1992).

- [97] H. Hiroshima and M. Komuro, *Nanotechnology* **108** (1998).
- [98] W. F. van Dorp, S. Lazar, C. W. Hagen and P. Kruit, *J. Vac. Sci. Technol., B* **25**, 1603 (2007).
- [99] A. F. Holleman and N. Wiberg, *Lehrbuch der Anorganischen Chemie* (Walter de Gruyter Verlag, Berlin, 1985).
- [100] Strem Chemicals, *Material Safety Data Sheet Iron pentacarbonyl* (Newburyport, 2006).
- [101] Sigma Aldrich Chemie, *Sicherheitsdatenblatt Eisenpentacarbonyl* (Steinheim, 2004).
- [102] C. Elschenbroich, *Organometallchemie* (B.G. Teubner Verlag, Wiesbaden, 2003).
- [103] W. Zhang, M. Shimojo, M. Takeguchi and K. Furuya, *J. Mater. Sci.* **41**, 2577 (2006).
- [104] M. Tanaka, F. Chu, M. Shimojo, M. Takeguchi, K. Mitsuishi and K. Furuya, *J. Mater. Sci.* **41**, 2667 (2006).
- [105] M. Tanaka, F. Chu, M. Shimojo, M. Takeguchi, K. Mitsuishi and K. Furuya, *Appl. Phys. Lett.* **86**, 183104 (2005).
- [106] M. Takeguchi, M. Shimojo and K. Furuya, *Nanotechnology* **16**, 1321 (2005).
- [107] Omicron NanoTechnology, *Multiprobe Surface Science Systems User's Guide* (Taanusstein, 2005).
- [108] Omicron NanoTechnology, *Multiscan STM VT User's Guide* (Taanusstein, 2005).
- [109] Omicron NanoTechnology, *Advertisement flyer for Gemini column (3 nm UHV SEM)* (Taanusstein, 2003).
- [110] Zeiss, *Handbuch für die Rasterelektronenmikroskope SUPRA(VP) und ULTRA* (Oberkochen, 2004).
- [111] Omicron, *Presentation*, Taanusstein, **2005**.
- [112] Omicron NanoTechnology, *NanoSAM User Guide* (Taanusstein, 2005).
- [113] Raith, *Product Info ELPHY Plus, ELPHY Quantum and laser interferometer stage* (Dortmund, 2006).
- [114] Raith, *Software Reference Manual Version 4.0* (Dortmund, 2004).
- [115] A. Schaak, S. Shaikhutdinov and R. Imbihl, *Surf. Sci.* **421**, 191 (1999).
- [116] H. Marbach, G. Lilienkamp, H. Wei, S. Günther, Y. Suchorski and R. Imbihl, *PCCP* **5**, 2730 (2003).
- [117] F. Mertens and R. Imbihl, *Chem. Phys. Lett.* **242**, 221 (1995).
- [118] P. J. Cumpson and M. P. Seah, *Surf. Interface Anal.* **25**, 430 (1997).
- [119] W. F. v. Dorp and C. W. Hagen, *J. Appl. Phys.* **104**, 081301/1 (2008).
- [120] I. Jungwirthova, J. Eklund, Y. Sun and J. M. White, *Rev. Sci. Instr.* **73**, 3302 (2002).
- [121] O. Guise, H. Marbach, J. Levy, J. Ahner and J. T. Yates, *Surf. Sci.* **571**, 128 (2004).
- [122] M. Schirmer, *Lithographic Fabrication of Nanostructures by Means of Electron-Beam Induced Deposition (EBID)*, Master Thesis (Friedrich-Alexander-University Erlangen-Nuremberg, **2006**).

- [123] M. A. McCord and M. J. Rooks, *Electron Beam Lithography in Handbook of Microlithography, Micromachining, and Microfabrication; Volume 1: Microlithography* (SPIE Press, Bellingham, 1997).
- [124] B. Ziaie, A. Baldi and M. Atashbar, *Introduction to Micro/Nanofabrication in Springer Handbook of Nanotechnology* (Springer, Berlin, 2007).
- [125] A. del Campo and E. Arzt, *Chem. Rev.* **108**, 911 (2008).
- [126] M. J. Bowden, *The Lithographic Process: The Physics in Introduction to Microlithography* (ACS Professional Reference Book, Washington, 1994).
- [127] C. G. Willson, *Organic Resist Materials in Introduction to Microlithography* (ACS Professional Reference Book, Washington, 1994).
- [128] V. M. Bermudez, *J. Vac. Sci. Technol., B* **17**, 2512 (1999).
- [129] A. N. Broers, W. W. Molzen, J. J. Cuomo and N. D. Wittels, *Appl. Phys. Lett.* **29**, 596 (1976).
- [130] H. G. Craighead and P. M. Mankiewich, *J. Appl. Phys.* **53**, 7186 (1982).
- [131] Air Liquide, *EG-Sicherheitsdatenblatt Ethen Version 1.70* (Düsseldorf, 2005).
- [132] A. Streitwieser, C. H. Heathcock and E. M. Kosower, *Organische Chemie* (VCH, Weinheim, 1994).
- [133] L. Reimer and C. Tollkamp, *Scanning* **3**, 35 (1980).
- [134] Kohlmann-von Platen, J. K. T. Chlebek, M. Weiss, K. Reimer, H. Oertel and W. H. Brunger, *J. Vac. Sci. Technol., B* **11**, 2219 (1993).
- [135] D. Beaulieu, Y. Ding, Z. L. Wang and W. J. Lackey, *J. Vac. Sci. Technol., B* **23**, 2151 (2005).
- [136] U. Hübner, R. Plontke, M. Blume, A. Reinhardt and H. W. P. Koops, *Microel. Eng.* **57-58**, 953 (2001).
- [137] A. Perentes, A. Bachmann, M. Leutenegger, I. Utke, C. Sandu and P. Hoffman, *Microel. Eng.* **73-74**, 412 (2004).
- [138] J. D. Barry, M. Ervin, J. Molstad, A. Wickenden, T. Brintlinger, P. Hoffman and J. Meingailis, *J. Vac. Sci. Technol., B* **24**, 3165 (2006).
- [139] F. Mertens and R. Imbihl, *Nature* **370**, 124 (1994).
- [140] M. Kiskinova, *Chem. Rev.* **96**, 1431 (1996).
- [141] S. Günther, R. Hoyer, H. Marbach, R. Imbihl, F. Esch, C. Africh, G. Comelli and M. Kiskinova, *J. Chem. Phys.* **124**, 014706/1 (2006).
- [142] T. Schmidt, A. Schaak, S. Günther, B. Ressel, E. Bauer and R. Imbihl, *Chem. Phys. Lett.* **318**, 549 (2000).
- [143] S. Sato, Y. Ukisu, H. Ogawa and Y. Takasu, *J. Chem. Soc., Faraday Trans.* **89**, 4387 (1993).
- [144] M. Xu and F. Zaera, *J. Vac. Sci. Technol., A* **14**, 415 (1996).
- [145] F. Zaera, *Surf. Sci.* **255**, 280 (1991).
- [146] F. Zaera, *Langmuir* **7**, 1188 (1991).
- [147] P. W. Murray, F. M. Leibsle, Y. Li, Q. Guo, M. Bowker, G. Thornton, V. R. Dhanak, K. C. Prince and R. Rosei, *Phys. Rev. B* **47**, 12976 (1993).

- [148] G. Comelli, V. R. Dhanak, M. Kiskinova, N. Pangher, G. Paolucci, K. C. Prince and R. Rosei, *Surf. Sci.* **269/270**, 360 (1992).
- [149] G. Comelli, V. R. Dhanak, M. Kiskinova, N. Pangher, G. Paolucci, K. C. Prince and R. Rosei, *Surf. Sci.* **260**, 7 (1992).
- [150] M. Bowker, Q. Guo and R. Joyner, *Surf. Sci.* **253**, 33 (1991).
- [151] H. Marbach, *Der Einfluss von Alkalimetallen auf musterbildende Reaktionen auf einer Rh(110) Oberfläche*, PhD Thesis (University Hannover, **2002**).
- [152] V. R. Dhanak, G. Comelli, G. Cautero, G. Paolucci, K. C. Prince, M. Kiskionva and R. Rosei, *Chem. Phys. Lett.* **188**, 237 (1992).
- [153] G. Comelli, V. R. Dhanak, M. Kiskinova, K. C. Prince and R. Roseil, *Surf. Sci. Rep.* **32**, 165 (1998).
- [154] E. Schwarz, J. Lenz, H. Wohlgemuth and K. Christmann, *Vacuum* **41**, 167 (1990).
- [155] K. Christmann, *Introduction to Surface Physical Chemistry* (Springer, New York, 1991).
- [156] H. Niehus and W. Losch, *Surf. Sci.* **111**, 344 (1981).
- [157] J. M. Heras and L. Viscido, *J. Vac. Sci. Technol., A* **15**, 2051 (1997).
- [158] A. Makeev and R. Imbihl, *J. Chem. Phys.* **113**, 3854 (2000).
- [159] T. Fink, R. Imbihl and G. Ertl, *J. Chem. Phys.* **91**, 5002 (1989).
- [160] J. Wolff, A. G. Papathanasiou, I. G. Kevrekidis, H. H. Rotermund and G. Ertl, *Science* **294**, 134 (2001).
- [161] L. Reimer and M. Wächter, *Ultramicroscopy* **3**, 169 (1978).
- [162] M. Amman, J. W. Sleight, D. R. Lombardi, R. E. Welser, M. R. Deshpande, M. A. Reed and L. J. Guido, *J. Vac. Sci. Technol., B* **14**, 54 (1996).
- [163] M. A. Henderson, R. D. Ramsier and J. T. Yates, Jr., *J. Vac. Sci. Technol., A* **9**, 2785 (1991).
- [164] O. Dulub, M. Batzill, S. Solovev, E. Loginova, A. Alchagirov, T. E. Madey and U. Diebold, *Science* **317**, 1052 (2007).
- [165] T. Block and H. Pfnür, *J. Appl. Phys.* **103**, 064303/1 (2008).
- [166] M. L. Knotek and P. J. Feibelman, *Phys. Rev. Lett.* **40**, 964 (1978).
- [167] Jeol, *A Guide to Scanning Microscope Observation* (USA, 2006).
- [168] F. Qin, N. P. Magtoto, M. Garza and J. A. Kelber, *Thin Solid Films* **444**, 179 (2003).
- [169] V. S. Smentkowski and J. T. J. Yates, *Surf. Sci.* **232**, 102 (1990).
- [170] M. Seo, J. B. Lumsden and R. W. Staehle, *Surf. Sci.* **50**, 541 (1975).
- [171] M. Tanaka, M. Han, M. Takeguchi, F. Chu, M. Shimojo, K. Mitsuishi and K. Furuya, *Jpn. J. Appl. Phys.* **44**, 5635 (2005).
- [172] en.wikipedia.org/wiki/Diamond in October 2009, Wikipedia, 2009.
- [173] www.old.uni-bayreuth.de/departments/didaktikchemie/umat/rekorde_ac1/rekorde.htm in October 2009, University Bayreuth, 1999.
- [174] K. Takayanagi, Y. Tanishiro, S. Takahashi and M. Takahashi, *Surf. Sci.* **164**, 367 (1985).

- [175] www.fkp.uni-erlangen.de/methoden/stmtutor/stmex.html in October 2009, Lehrstuhl für Festkörperphysik of the FAU Erlangen-Nürnberg, 2005.
- [176] www.chem.qmul.ac.uk/surfaces/scc/scat1_6a.htm in October 2009, Queen Mary University of London, 2003.
- [177] N. Silvis-Cividjian, C. W. Hagen and P. Kruit, *J. Appl. Phys.* **98**, (2005).
- [178] J. S. Foord and R. B. Jackman, *Chem. Phys. Lett.* **112**, 190 (1984).
- [179] H. Brune, M. Giovannini, K. Bromann and K. Kern, *Nature* **394**, 451 (1998).
- [180] I. N. Stranski and L. von Krastanov, Presented at the Acad. Wiss. Lit. Mainz Math.-Natur Kl. 11b 146 797, **1939**.
- [181] K. Rührschopf, D. Borgmann and G. Wedler, *Thin Solid Films* **280**, 171 (1996).
- [182] J. M. Gallego and R. Miranda, *J. Appl. Phys.* **69**, 1377 (1990).
- [183] I. Utke, V. Friedli, M. Purrucker and J. Michler, *J. Vac. Sci. Technol., B* **25**, 2219 (2007).
- [184] W. Ding, D. A. Dikin, X. Chen, R. D. Piner, R. S. Ruoff, E. Zussman, X. Wang and X. Li, *J. Appl. Phys.* **98**, (2005).
- [185] K. T. Kohlmann-von Platen, L.-M. Buchmann, H.-C. Petzold and W. H. Brunger, *J. Vac. Sci. Technol., B* **10**, 2690 (1992).
- [186] M. A. Bruk, E. N. Zhikharev, E. I. Grigor'ev, A. V. Spirin, V. A. Kal'nov and I. E. Kardash, *High Energy Chem.* **39**, 65 (2005).
- [187] W. Ostwald, *Z. physik. Ch.* **34**, 495 (1900).
- [188] B. K. Chakraverty, *J. Phys. Chem. Solids* **28**, 2401 (1967).
- [189] B. K. Chakraverty, *J. Phys. Chem. Solids* **28**, 2413 (1967).
- [190] M. Petersen, A. Zangwill and C. Ratsch, *Surf. Sci.* **536**, 55 (2003).
- [191] S. Iijima, *Nature* **354**, 56 (1991).
- [192] H. Allouche and M. Monthieux, *Carbon* **43**, 1265 (2005).
- [193] H. Allouche, M. Monthieux and R. L. Jacobsen, *Carbon* **41**, 2897 (2003).
- [194] J. P. Salvétat-Delmotte and A. Rubio, *Carbon* **40**, 1729 (2002).
- [195] P. G. Collins and P. Avouris, *Sci. Am.* **283**, 62 (2000).
- [196] Y. Maeda, M. Kanda, M. Hashimoto, T. Hasegawa, S. Kimura, Y. F. Lian, T. Wakahara, T. Akasaka, S. Kazaoui, N. Minami, T. Okazaki, Y. Hayamizu, K. Hata, J. Lu and S. Nagase, *J. Am. Chem. Soc.* **128**, 12239 (2006).
- [197] D. Chattopadhyay, L. Galeska and F. Papadimitrakopoulos, *J. Am. Chem. Soc.* **125**, 3370 (2003).
- [198] T. L. Sun, H. Tan, D. Han, Q. Fu and L. Jiang, *Small* **1**, 959 (2005).
- [199] A. P. Graham, G. S. Duesberg, R. V. Seidel, M. Liebau, E. Unger, W. Pamler, F. Kreupl and W. Hoenlein, *Small* **1**, 382 (2005).
- [200] M. I. H. Panhuis, S. Gowrisanker, D. J. Vanesko, C. A. Mire, H. P. Jia, X. Hui, R. H. Baughman, I. H. Musselman, B. E. Gnade, G. R. Dieckmann and R. K. Draper, *Small* **1**, 820 (2005).

- [201] W. B. Choi, D. S. Chung, J. H. Kang, H. Y. Kim, Y. W. Jin, I. T. Han, Y. H. Lee, J. E. Jung, N. S. Lee, G. S. Park and J. M. Kim, *Appl. Phys. Lett.* **75**, 3129 (1999).
- [202] K. Balasubramanian and M. Burghard, *Anal. Bioanal. Chem.* **385**, 452 (2006).
- [203] X. Yu, B. Munge, V. Patel, G. Jensen, A. Bhirde, J. D. Gong, S. N. Kim, J. Gillespie, J. S. Gutkind, F. Papadimitrakopoulos and J. F. Rusling, *J. Am. Chem. Soc.* **128**, 11199 (2006).
- [204] I. Firkowska, M. Olek, N. Pazos-Perez, J. Rojas-Chapana and M. Giersig, *Langmuir* **22**, 5427 (2006).
- [205] R. A. MacDonald, B. F. Laurenzi, G. Viswanathan, P. M. Ajayan and J. P. Stegemann, *J. Biomed. Mater. Res. Part A* **74A**, 489 (2005).
- [206] R. Krajcik, *Funktionalisierte Kohlenstoffnanoröhren als neuartiges Transfektionsmittel für effizientes gene silencing in Rattenkardiomyozyten*, PhD Thesis (Friedrich-Alexander-Universität Erlangen-Nürnberg, **2008**).
- [207] S. Farhat, M. L. de La Chapelle, A. Loiseau, C. D. Scott, S. Lefrant, C. Journet and P. Bernier, *J. Chem. Phys.* **115**, 6752 (2001).
- [208] T. Guo, P. Nikolaev, A. Thess, D. T. Colbert and R. E. Smalley, *Chem. Phys. Lett.* **243**, 49 (1995).
- [209] M. J. Bronikowski, P. A. Willis, D. T. Colbert, K. A. Smith and R. E. Smalley, *J. Vac. Sci. Technol., A* **19**, 1800 (2001).
- [210] C. B. Xu and J. Zhu, *Nanotechnology* **15**, 1671 (2004).
- [211] P. Moodley, J. Loos, J. W. Niemantsverdriet and P. C. Thune, *Carbon* **47**, 2002 (2009).
- [212] C. L. Cheung, A. Kurtz, H. Park and C. M. Lieber, *J. Phys. Chem. B* **106**, 2429 (2002).

Danksagung

An dieser Stelle möchte ich mich bei allen bedanken, ohne die das Gelingen dieser Arbeit nicht möglich gewesen wäre.

Prof. Hans-Peter Steinrück, der mir die Möglichkeit gegeben hat diese Arbeit an seinem Lehrstuhl durchzuführen und das damit verbundene Vertrauen. Danken möchte ich Ihnen weiterhin für die vielen wissenschaftlichen Diskussionen und die kollegiale und sehr angenehme Atmosphäre, die Sie in Ihrer Arbeitsgruppe geschaffen haben.

Dr. Hubertus Marbach für die Betreuung meiner Arbeit und die große Unterstützung während dieser Zeit. Vielen Dank auch für die sehr interessanten und oftmals erheiternden Gespräche über die Wissenschaft und auch darüber hinaus.

Prof. Oliver Diwald für die Übernahme der Zweitkorrektur und der schnellen Durchführung dieser, obwohl es sich um ein sehr langes Schriftstück handelte.

Der EBID-Crew, Michael Schirmer, Marie-Madeleine Walz und Florian Vollnhals, die mir in diesen Jahren immer als hilfsbereite Kollegen und gute Freunde zur Seite gestanden haben. Danke für die schöne Zeit mit euch.

Hans-Peter Bäumler, für seinen Ideenreichtum bei der Umsetzung von elektronischen Fragestellungen und seine stets hilfsbereite Art bei der Lösung von Problemen.

Friedhold Wölfel und seinen Mitarbeitern aus der mechanischen Werkstatt für die oftmals hervorragende Umsetzung von neuen Bauteilen für die Apparatur, auch wenn diese teilweise bereits in fünf Minuten gebraucht wurden.

Bernd Kress, für die Planung und Unterstützung beim Bau der Gasdosierkammer.

Stefan Tampier und Dr. Matthias Moll für die Hilfe bei der Handhabung des Eisenpentacarbonyls.

Allen Mitarbeitern, die im Rahmen eines Praktikums zu dieser Arbeit beigetragen haben.

Den anderen Kellerkindern, Markus Happel, Thorsten Staudt, Marek Sobota, Dr. Matthias Laurin und Aine Desikusumastuti, für die freundliche Nachbarschaft.

Allen weiteren Mitarbeitern des AK Steinrücks, für die gute Zusammenarbeit in diesen Jahren. Vor allem Florian Buchner für die freundliche Unterstützung zum Ende dieser Arbeit.

Abschließend möchte ich mich besonders bei meiner Familie und Carola Ganzmann bedanken, die mich in so mancher schweren Zeit aufgefangen und wieder aufgebaut haben.

Lebenslauf

Persönliche Daten

Name : Lukasczyk
Vorname : Thomas
Geburtsdatum : 03.07.1979
Geburtsort : Erlangen
Familienstand : Ledig
Nationalität : Deutsch

Hochschulbildung

Seit 10/2005 : Wissenschaftlicher Mitarbeiter und Doktorand am Lehrstuhl für Physikalische Chemie II der Universität Erlangen-Nürnberg (Arbeitsgruppe Prof. Hans-Peter Steinrück): *Generation of pure iron nanostructures via electron-beam induced deposition in UHV*
04/2005 – 09/2005 : Diplomarbeit am Lehrstuhl für Physikalische Chemie II der Universität Erlangen-Nürnberg: *Adsorption und Reaktion von Metalloporphyrinen auf einer Ag(111)-Oberfläche*
02/2005 : Diplomprüfung
10/2000 – 09/2005 : Studium der Chemie an der Universität Erlangen-Nürnberg

Schulbildung

09/1990 – 06/1999 : Mathematisch-Naturwissenschaftliches Gymnasium in Herzogenaurach
09/1986 – 07/1990 : Grundschule Herzogenaurach

Sonstige Tätigkeiten

12/2002 – 10/2004 : Studentische Hilfskraft im Computer-Chemie-Centrum (CCC) der Universität Erlangen-Nürnberg
12/1999 – 10/2000 : Zivildienst beim ASB Kreisverband Erlangen-Höchstadt
09/1998 – 09/2006 : Teilnahme an diversen Wahlen als Schriftführer und Beisitzer

Publikationen und Konferenzteilnahmen

Veröffentlichungen in Fachzeitschriften („peer-reviewed“)

- (1) M. Schirmer, M.-M. Walz, F. Vollnhals, T. Lukasczyk, C. Chen, H.-P. Steinrück, H. Marbach: "Addressing Proximity Effects in Electron Beam Induced Deposition: Fabrication of Clean Titanium Oxide Nanostructures on Silicon", **2010**, *to be published*.
- (2) M.-M. Walz, M. Schirmer, F. Vollnhals, T. Lukasczyk, H.-P. Steinrück, H. Marbach: "Electrons as Invisible Ink - Generation of Iron Nanostructures on 300 nm SiO_x", **2010**, *submitted*.
- (3) T. Lukasczyk, M. Schirmer, H.-P. Steinrück, H. Marbach *Langmuir*, **2009**, 25, S. 11930 – 11939.
- (4) T. Lukasczyk, M. Schirmer, H.-P. Steinrück, H. Marbach *Small*, **2008**, 4 (6), S. 841 – 846.
- (5) K. Comanici, F. Buchner, K. Flechtner, T. Lukasczyk, J. M. Gottfried, H.-P. Steinrück, H. Marbach *Langmuir*, **2008**, 24 (24), S. 1897 – 1901.
- (6) T. Lukasczyk, K. Flechtner, L. R. Merte, N. Jux, F. Maier, J. M. Gottfried, H.-P. Steinrück *J. Phys. Chem. C*, **2007**, 111(7), S. 3090 – 3098.
- (7) J. M. Gottfried, K. Flechtner, A. Kretschmann, T. Lukasczyk, H.-P. Steinrück *J. Am. Chem. Soc.*, **2006**, 128 (17), S. 5644 – 5645.

Sonstige Veröffentlichungen

- (1) T. Lukasczyk, M. Schirmer, M.-M. Walz, F. Vollnhals, H.-P. Steinrück, H. Marbach *Omicron Pico*, **2008**, 12 (2), S. 6 – 8.

Tagungsbeiträge (Auswahl)

- (1) „Frühjahrstagung der Sektion Kondensierte Materie der Deutschen Physikalischen Gesellschaft“ in Dresden (**2009**)
- (2) „34th International Conference on Micro and Nanoengineering“ in Athen (**2008**)
- (3) „25th European Conference on Surface Science“ in Liverpool (**2008**)
- (4) „72. Jahrestagung der Deutschen Physikalischen Gesellschaft“ in Berlin (**2008**)
- (5) „Chemical Nanotechnology Talks VIII“ in Frankfurt (**2007**)
- (6) „Jahrestagung der Deutschen Physikalischen Gesellschaft“ in Regensburg (**2007**)
- (7) „Frühjahrstagung des Arbeitskreises Festkörperphysik der Deutschen Physikalischen Gesellschaft“ in Dresden (**2006**)